Modelling of 3D Anisotropic Turbulent Flow in Compound Channels

Keyur Vyas

Department of Civil and Building Engineering

Loughborough University

A Doctoral Thesis Submitted for the Degree of

Doctor of Philosophy

April 2007

Abstract

The present research focuses on the development and computer implementation of a novel threedimensional, anisotropic turbulence model not only capable of handling complex geometries but also the turbulence driven secondary currents. The model equations comprise advanced algebraic Reynolds stress models in conjunction with Reynolds Averaged Navier-Stokes equations. In order to tackle the complex geometry of compound meandering channels, the body-fitted orthogonal coordinate system is used. The finite volume method with collocated arrangement of variables is used for discretization of the governing equations. Pressure-velocity coupling is achieved by the standard iterative SIMPLE algorithm. A central differencing scheme and upwind differencing scheme are implemented for approximation of diffusive and convective fluxes on the control volume faces respectively. A set of algebraic equations, derived after discretization, are solved with help of Stones implicit matrix solver.

The model is validated against standard benchmarks on simple and compound straight channels. For the case of compound meandering channels with varying sinuosity and floodplain height, the model results are compared with the published experimental data. It is found that the present method is able to predict the mean velocity distribution, pressure and secondary flow circulations with reasonably good accuracy. In terms of engineering applications, the model is also tested to understand the importance of turbulence driven secondary currents in slightly curved channel. The development of this unique model has opened many avenues of future research such as flood risk management, the effects of trees near the bank on the flow mechanisms and prediction of pollutant transport.

Key words: Compound meandering channel flows, Turbulence modelling, Collocated finite volume method, Body-fitted orthogonal grids

Acknowledgements

I would like to thank my supervisors Dr. Cecil Scott and Prof. Koji Shiono for their assistance, encouragement and guidance during all stages of my research.

I would like to thank Department of Civil and Building Engineering of Loughborough University, UK for providing me the financial support for this work.

I am sincerely thankful to Postgraduate Research Administrator, Helen Newbold, for all her support during my research. I am also thankful to department IT administrators Stephen Grieve and John Salisbury for their invaluable support.

Thanks to my research colleagues Ben, Masoud, Rene, Tingting, Xin, and Zul for valuable discussions and making the workplace lively. Special thanks to Fiona for her constructive comments on the thesis.

I am grateful to Prof. Milovan Perić for providing the computer code, which is a base for this work and suggestions on my research approach.

I would also like to thank my friends and housemates Bala, Maninder, Ning, Rajesh, Rushabh, and Udit for making my stay easy and enjoyable.

Special thanks to Atmanand, Deepak, Mukesh, Navraj and Sachin for their wonderful *funde.*

Finally, I am thankful to my parents, my brother Mayur, sister Trusha and grandfather Mukund dada for their support and encouragement.

Contents

List of Tables

List of Figures

Nomenclature

Greek Symbols

α	Under-relaxation factor
δ_{ij}	Kronecker delta function
η	Orthogonal coordinate
ε	Turbulent energy dissipation
Γ	Generalised diffusivity
λ	Interpolation factor
μ_t	Turbulent viscosity
ν	Kinematic viscosity
ν_{ij}	Eddy viscosity
ϕ	Generic variable
ρ	Fluid density
σ_k	Constant in $k-\varepsilon$ model equal to 1.0
σ_ε	Constant in $k-\varepsilon$ model equal to 1.3
τ_w	Wall shear stress

θ Channel inclination

κ von Karmen constant equal to 0.41

ξ Orthogonal coordinate

ζ Orthogonal coordinate

Other Symbols

$\bar{u}$ Instantaneous velocity component in x direction

$\bar{v}$ Instantaneous velocity component in y direction

$\bar{w}$ Instantaneous velocity component in z direction

A Square coefficient matrix

a Coefficient in the discretized equation

B Channel width L

C' Constant in LY model equal to 0.0325

C'_k Constant in LY model equal to 0.522

C_3 The model constant in NR model equal to 0.1

C_D The model constant in NLKE model equal to 1.68

C_E The model constant in NLKE model equal to 1.68

C_μ Constant in $k-\varepsilon$ model equal to 0.09

$C_{\varepsilon 1}$ Constant in $k-\varepsilon$ model equal to 1.44

$C_{\varepsilon 2}$ Constant in $k-\varepsilon$ model equal to 1.92

D Diffusive coefficient

E Roughness parameter in the log law equal to 9.0

f Distortion function

f_1 The wall proximity function in NR model

f_2 The surface proximity function in NR model

g Gravitational acceleration

g_{ij} Matric tensor

u Gravitational acceleration

H Channel height

h_η Scale factor in η direction

h_ξ Scale factor in ξ direction

H Channel height L

H Water depth

i and j Standard tensor indices varying between 1 and 3

$\underline{\mathbf{J}}$ Jacobian matrix

$\underline{\mathbf{J}}^{-1}$ Inverse of Jacobian matrix

k Turbulent kinetic energy

l Neighbouring coefficients

$\dot{m}$ Mass flux

P Mean static pressure

p Wetted perimeter

NOMENCLATURE

P_k Turbulent kinetic energy production

P_x Inhomogeneous source term in x direction

Q Vector matrix

Q_y Inhomogeneous source term in y direction

R Hydraulic radius

r Expansion factor for the computational grid

S Source term

S Energy slope

U Mean velocity component in x direction

U^+ Dimensionless velocity in the log law

u_* Frictional velocity

U_τ Shear velocity in the log law

U_r Resultant velocity in the log law

U_s Mean velocity

z^+ Normalised in the log law

$u_i\bar{u}_j$ Turbulent Reynolds stresses

V Mean velocity component in y direction

W Mean velocity component in z direction

x Longitudinal direction

y Lateral direction

y'	Distance from the side wall in the log law
z	Vertical direction

Abbreviations and Acronyms

1D	One-Dimensional
2D	Two-Dimensional
3D	Three-Dimensional
AR	Aspect ratio of orthogonal grid
CFD	Computational Fluid Dynamics
LDA	Laser Doppler Velocimeters
LY	Launder and Ying
NLKE	Non-linear $k-\varepsilon$
NR	Noat and Rodi
RANS	Reynolds Averaged Navier Stokes
RSM	Reynolds Stress Models

CHAPTER 1

Introduction

1.1 Introduction

The ability to determine the overbank flow behaviour of rivers and their associated flood plains is a vital prerequisite in the design of flood prediction, warning and alleviation schemes as well as for the planning of river/floodplain management strategies. Global warming and climate change has increased the frequency and severity of flooding in the UK and in other parts of the world. This has added to the urgency in developing a better understanding of two-stage river/floodplain flows. The investigation and analysis of these flows leads to the requirement for a design tool that is capable of predicting the flow field crucial for the prediction of flooding.

In traditional one-dimensional (1D) methods, only the discharge, or section-averaged velocity, is calculated for a given flow depth. Thus, only one value is provided for the whole section or subsection. The calculation is performed via a flow resistance equation with empirical corrections for energy dissipation other than boundary friction (Rameshwaran and Willetts (1999)). The accuracy of such 1D methods is restricted by the assumptions they make about the channel geometry, flow interaction, boundary roughness and vegetation. Given these

limitations, higher dimensional methods are required to successfully address the river engineering issues associated with two-stage channels.

In recent years, two-dimensional (2D) and three-dimensional (3D) computational fluid dynamic (CFD) methods have been increasingly used in river engineering in order to improve understanding of turbulent flow behaviour and develop design tools for predicting the flow field and bed shear stress (Morvan *et al.* (2002), Rameshwaran and Shiono (2002), Rameshwaran and Shiono (2003)).

Shiono and Knight (1989) and Shiono and Knight (1990) presented a 2D method for calculating the variation in depth-averaged velocity across a two-stage channel, based upon approximate forms of the Reynolds Averaged Navier-Stokes (RANS) equations and using a simplified eddy viscosity model. Such 2D solutions are particularly important when detailed main channel and floodplain flow distributions are required, as in the prediction of sediment transport. In compound channels with overbank flow, turbulence anisotropy drives secondary circulation; a phenomenon that is particularly noticeable in the region of the main channel/floodplain interface. A number of 3D turbulence models have been applied to this, notably algebraic stress models (Krishnappa and Lau (1986), Naot *et al.* (1993b), Cokljat and Younis (1995)), non-linear $k-\varepsilon$ models (Shiono and Lin (1995), Pezzinga (1994)), a non-linear $k-\omega$ model (Sofialidis and Prinos (1999)) and large eddy simulation (Thomas and Williams (1995)).

Until today, little efforts had been made to simulate turbulent flow in curved compound channels numerically. Wilson *et al.* (2002) recently used a 2D depth-averaged finite element method, which predicted lateral free surface elevations and depth-averaged velocity for reach-scale flows in meandering compound channels with straight floodplain banks. They pointed out that 3D and secondary current effects may also become important for velocity prediction, particularly in the case of meandering channels, but did not rule out the possibility that a more finely resolved 2D code would be sufficient to incorporate these effects.

1.2 Identifying the Research Gap

Further effort is yet to be expended to use various turbulence models to predict turbulent flows in curved channels with compound cross-sections. Most turbulence models applied thus for have been particularly tuned to predict correctly the magnitude of the secondary currents in simple cross-section (e.g. square) duct flow or a straight compound open-channel flow. A model that is well tested for duct flow may however need further investigation before being applied to predict flows, where either the channel curvature or the cross-section configuration is changing.

Since the Reynolds stress model is based on a set of differential transport equations, which increase the complexity of the simulation, simple algebraic stress models have often been chosen for numerical modeling of 3D, curved compound channel flows for reasons of computational economy. Among these models, the Launder and Ying (1973) algebraic stress model (LY model) has been favoured especially for calculation of the flow in channels with complex geometrical cross-sections. The nonlinear $k-\varepsilon$ (NLKE) model (Speziale (1987)) was applied in a curved simple crosssection duct flow calculation by Hur *et al.* (1990) and generally agrees with measured secondary flows; and the NR model (Naot and Rodi (1982)) was used by Naot *et al.* (1993b) for flow in an asymmetric compound channel.

The use of a boundary-fitted orthogonal curvilinear coordinate system can take into account the impact of channel curvature in a mathematical way without using additional terms in the governing equations and turbulence stress models. Though generation of 3D orthogonal grid is challenging, if done it offers distinct advantages over finite element and unstructured grid. Due to the simplicity in computer programming, it is also easier to incorporate higher order turbulence models like LY, NR and NLKE to simulate compound meandering channel flow with orthogonal grids.

1.3 Aims and Objectives

The principal aim of this research is to develop a hydraulic simulation model for open channel flows using the collocated Finite Volume Method as a numerical technique and an orthogonal coordinate system to tackle complex geometries. The detailed research objectives are:

- Develop a 3D, fast and efficient model to simulate flow mechanisms within rectangular, compound and compound meandering open channels.
- Incorporate existing anisotropic algebraic stress models to capture the secondary currents in straight, rectangular and compound channels.
- Simulate the velocity profiles and secondary currents in straight as well as meandering channels with varying sinuosity and relative depth.
- Validate the developed model for various scenarios with the help of available experimental data.
- Investigate the effects of anisotropic turbulence in the compound meandering channel.

1.4 Thesis Structure

The scope of the thesis is outlined as follows:

- In Chapter 2, the current knowledge of the flow characteristics for complex channel geometries such as straight channels with rectangular and compound cross sections and meandering channels is reviewed. Various aspects of numerical modelling including recent trends are also covered.
- The governing equations and boundary conditions describing the flow phenomena within open channels are discussed in Chapter 3.

- In Chapter 4, a solution technique for the Reynolds Averaged Navier Stokes equations, a finite volume numerical method and relevant issues are discussed in detail.

- The process of mathematical mapping from the physical plane to a computational plane, the governing equations in an orthogonal coordinate system and simulation strategy on the transformed plane are discussed in Chapter 5.

- In Chapter 6, different test cases of model development are presented, which cover rectangular and compound channels and compound meandering channels flow simulations.

- In Chapter 7, the conclusions of the present work are summarised and possible future enhancements of the work are also discussed.

CHAPTER 2

Literature Survey

2.1 Introduction

To date, an extensive investigation has been carried out to understand the complex phenomena of turbulent channel flows. However, it is still far from reaching definitive conclusions. This is due to the complexities involved in turbulent flows which depend on various geometries as well as hydraulic conditions.

In this section, a brief and the latest literature review is presented covering following points to create a base for the present research:

- Flow mechanisms in rectangular channels,
- Flow mechanisms in compound channels,
- Flow mechanisms in meandering channels; and
- Numerical modeling of compound meandering channels.

In each of these sections, issues such as distribution of longitudinal velocity, secondary circulations, main channel/floodplain interaction and boundary shear stress are discussed. In the last, recent developments in numerical modelling of compound meandering channels are also presented.

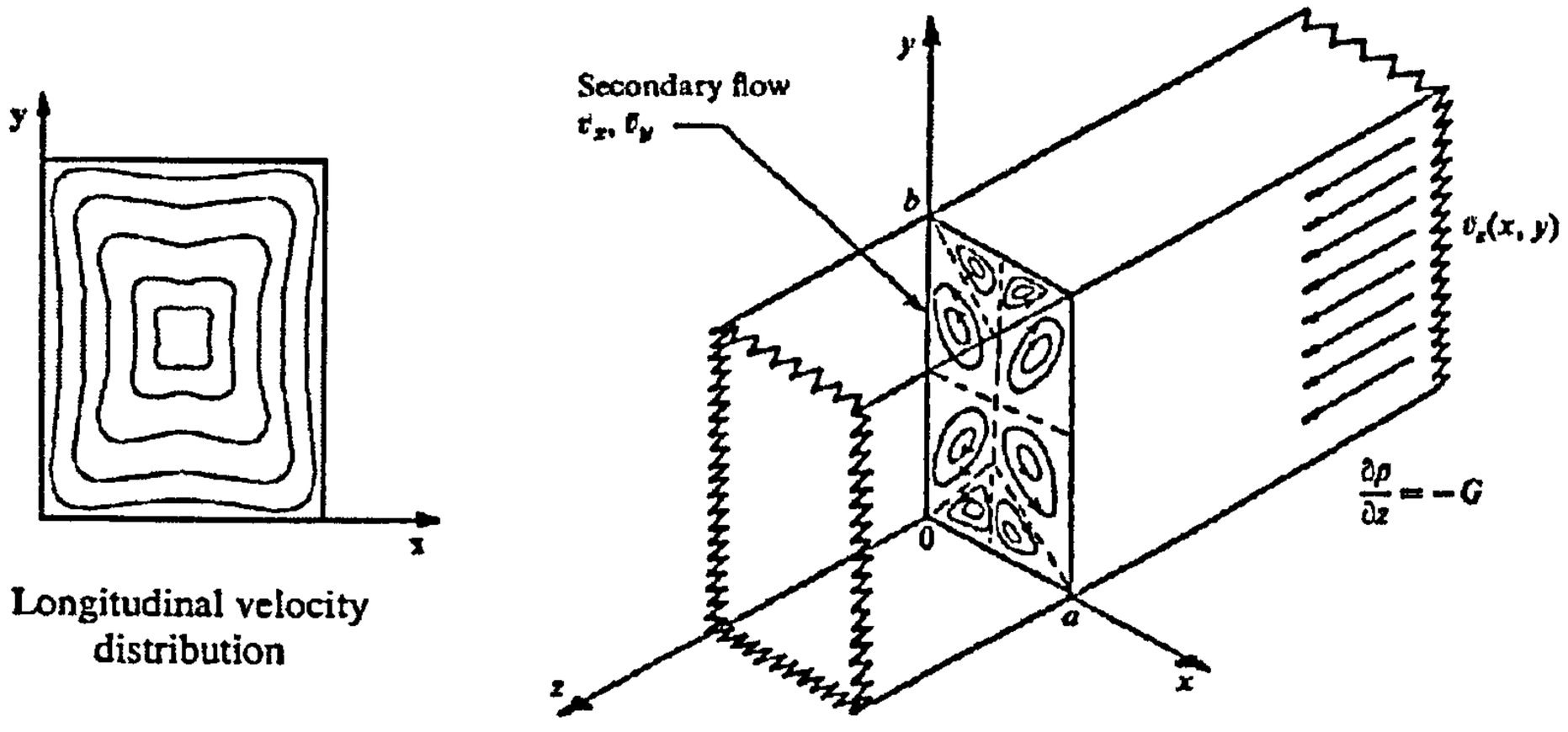

Figure 2.1: Longitudinal velocity distribution and secondary flow pattern in a closed duct. The secondary currents cause bulging of velocity contours in the corner of duct. (after Speziale (1987))

2.2 Rectangular Channels

Before understanding complicated flow mechanisms in a meandering channel, its vital to gain a foothold in a straight channel with rectangular cross section and compound channel with closed and open free surface. The following section discusses the flow distribution within rectangular closed and open channels.

2.2.1 Closed Channel

In fully developed turbulent flow through a closed channel (see Figure 2.1), a pair of vortices is formed in each corner of the duct and their orientation is from the corner towards the wall bisector. At this position, due to the plane of symmetry, the secondary currents is deflected and changes direction, moving low momentum fluid from the wall region towards the center of the channel. This occurrence has a direct effect on the longitudinal velocity distribution.

To illustrate this effect of secondary currents on the longitudinal velocity distribution, a sketch of the longitudinal velocity distribution is shown in Figure

2.1. As would be expected, the maximum velocity occurs at the center of the duct. Due to the presence of secondary currents, high momentum fluid is carried from the core region towards the corner of the duct, causing the velocity contour to bulge towards the corner.

This type of currents is known as Praudtl's second kind which is turbulence-driven and resulting from the anisotropy of the turbulent stresses. Its magnitude has been observed to be mostly between $1-4\%$ of the bulk mean velocity in most straight ducts with non-circular crosssection. However, its effects on wall shear stress distribution and heat transfer rates are quite significant.

This behavior, known as corner flow has been observed by many researchers (Speziale (1987), Nikuradse (1933), Launder and Ying (1973) and many others). A comprehensive review on the subject is given by Bradshaw (1987).

2.2.2 Open Channel

For rectangular open channels, Nezu and Rodi (1993) found that secondary flow circulation patterns are different from those observed in closed channel flows, due to the presence of the free surface. In case of non-circular conduits, the secondary flow circulations transports high momentum fluid towards the corners, leading to a bulging of velocity contour lines towards the corner. This clearly demonstrates the effect of secondary flow circulations on the primary flow behavior.

In simple open channel flows, secondary motions cause the maximum primary flow velocity to lie below the free surface. This phenomenon is widely referred to as *velocity dip effect* (Nezu and Nakagawa (1993)). The secondary flow circulations near the free surface is directed away from the bank and it transports the fluid with relatively low longitudinal momentum towards the centre point of the channel, leading to the velocity dip effect (Naot and Rodi (1982)).

Figure 2.2(a & b) show the typical secondary flow circulations observed by Nezu and Nakagawa (1993) in rectangular closed and open channel with aspect ratio (B/H) approximately equal to 2.0, where B is width and H is height of the

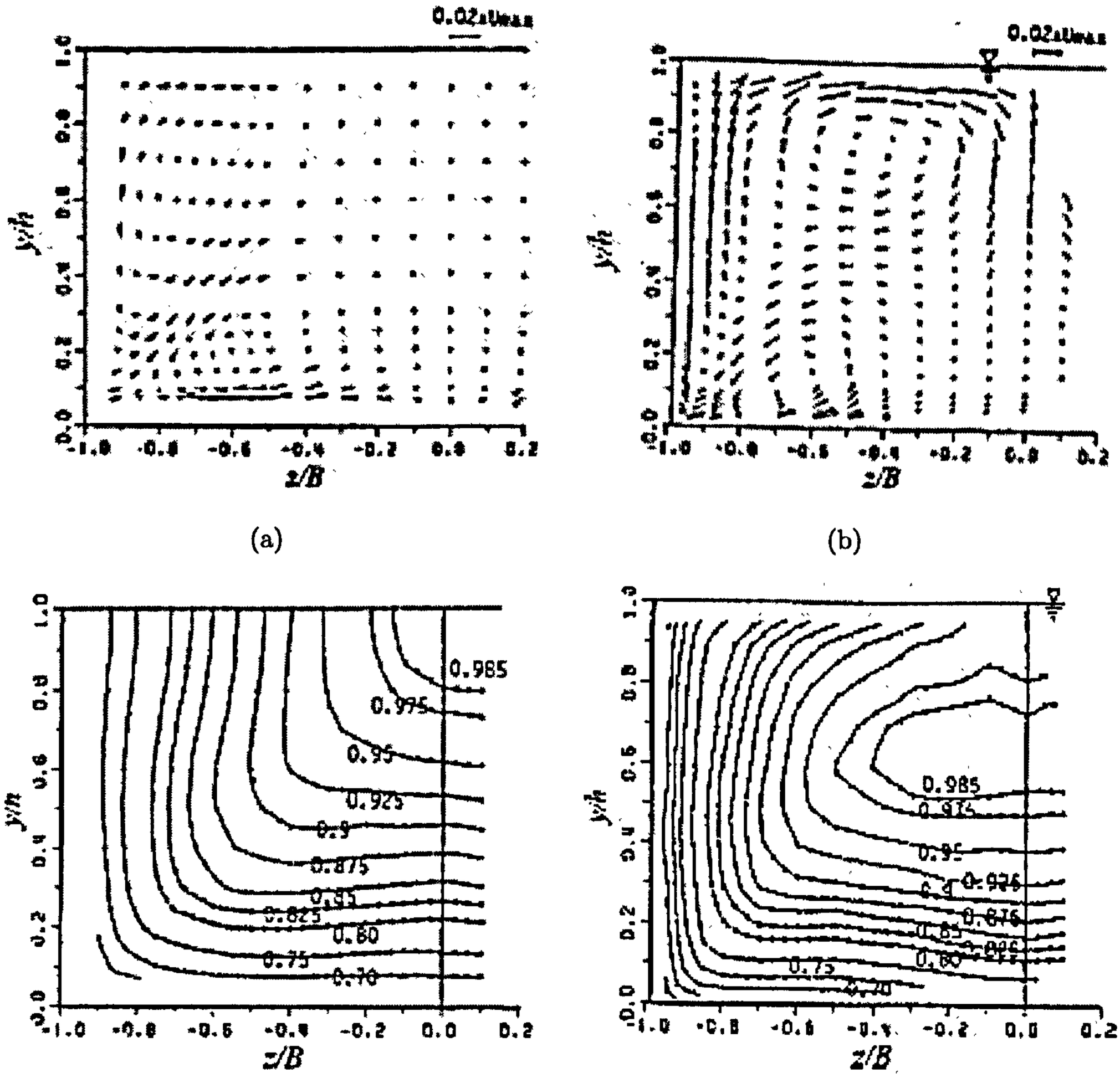

Figure 2.2: Flow patterns in closed and open straight channels. (a) & (b) Secondary currents; (c) & (d) Longitudinal velocity isovels for closed and open channel respectively. In closed duct flows, the secondary currents causes the bulging of mean velocity towards the corner bisector. In open channel flows, the presence of a free surface causes the maximum primary flow velocity lie below the free surface. (after Nezu and Nakagawa (1993))

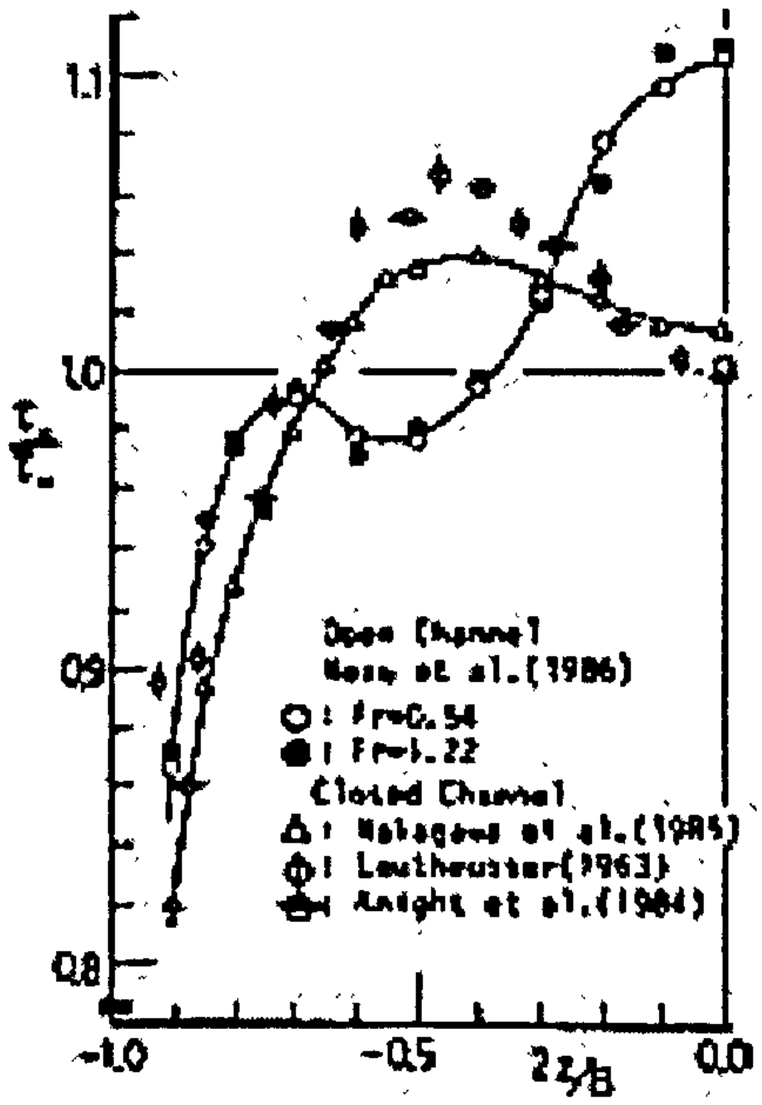

Figure 2.3: Bed shear stress distribution in closed and open channels (after Tominaga and Nezu (1990)). Secondary circulations cause wavy distribution of bed shear stress in transverse direction. An increase in bed shear stress implies the downward flow and vice versa.

channel. The corresponding isovels of the primary velocity fields which demonstrate the velocity dip effect (for open channel) and the bulging of velocity contour (for closed non-circular conduit) are also shown in Figure 2.2(c & d).

Nezu (2005) explain the effect of secondary flow circulations on the bed shear stress. Nezu (2005) stated that secondary flow circulations cause a wavy distribution of bed shear stress in the transverse direction. An increase in bed shear stress implies downward flow whereas a decrease implies up-flow. This is also clear from Figure 2.3, which shows that at the centre line of a duct, bed shear stress attains a local minimum whereas, in case of open channel, bed shear stress attains a local maximum at the same location.

In simple open channels, the small magnitude (1 to 3 % of the primary mean velocity) of secondary velocity components (transverse and vertical components of velocity) makes it very difficult to measure them accurately (Tominaga and Nezu (1990)).

Tominaga *et al.* (1989) used a calibrated hot-film anemometer to measure secondary flow circulations and three-dimensional turbulent structures in rectangular and trapezoidal open channels. Their research aimed at investigating particularly the effects of free surface, channel shape and boundary roughness on secondary flow circulations. They stated that secondary flow circulations in rectangular open channel comprise of free-surface vortex and bottom vortex, separated at about y/H $\cong$ 0.6 where y is height and h is water depth, when B/H equal to 2. They attribute the velocity dip effect to the free surface vortex, as demonstrated by previous researchers like Nezu and Rodi (1993).

They further confirmed that the circulations patterns are different between rectangular and trapezoidal cross-sections and that the velocity dip effect is not seen in the trapezoidal cross-section. The uniform boundary roughness condition of the channel was found not to change significantly the pattern of secondary flow circulations.

In general, the secondary flow circulations were found to affect the distribution of primary mean velocity, turbulence intensities and Reynolds stresses and the spanwise distribution of the boundary shear stress.

2.3 Compound Channels

Many rivers and estuaries by their nature or design are classified as compound channels. A compound channel is composed of a main channel and a floodplain. Turbulent flow in a compound channel is characterised by a shear layer generated due to the velocity difference between the usually faster flow in the main channel and the slower flow on the flood-plain. In the shear layer, there exist a not only vortices in the vertical direction but also in the longitudinal direction. These vortices affect the mean velocity profile and mixing process considerably.

Shiono and Knight (1991) illustrated the overall flow mechanism that contribute to the transport and mixing processes in compound channel flow which is shown in Figure 2.4.

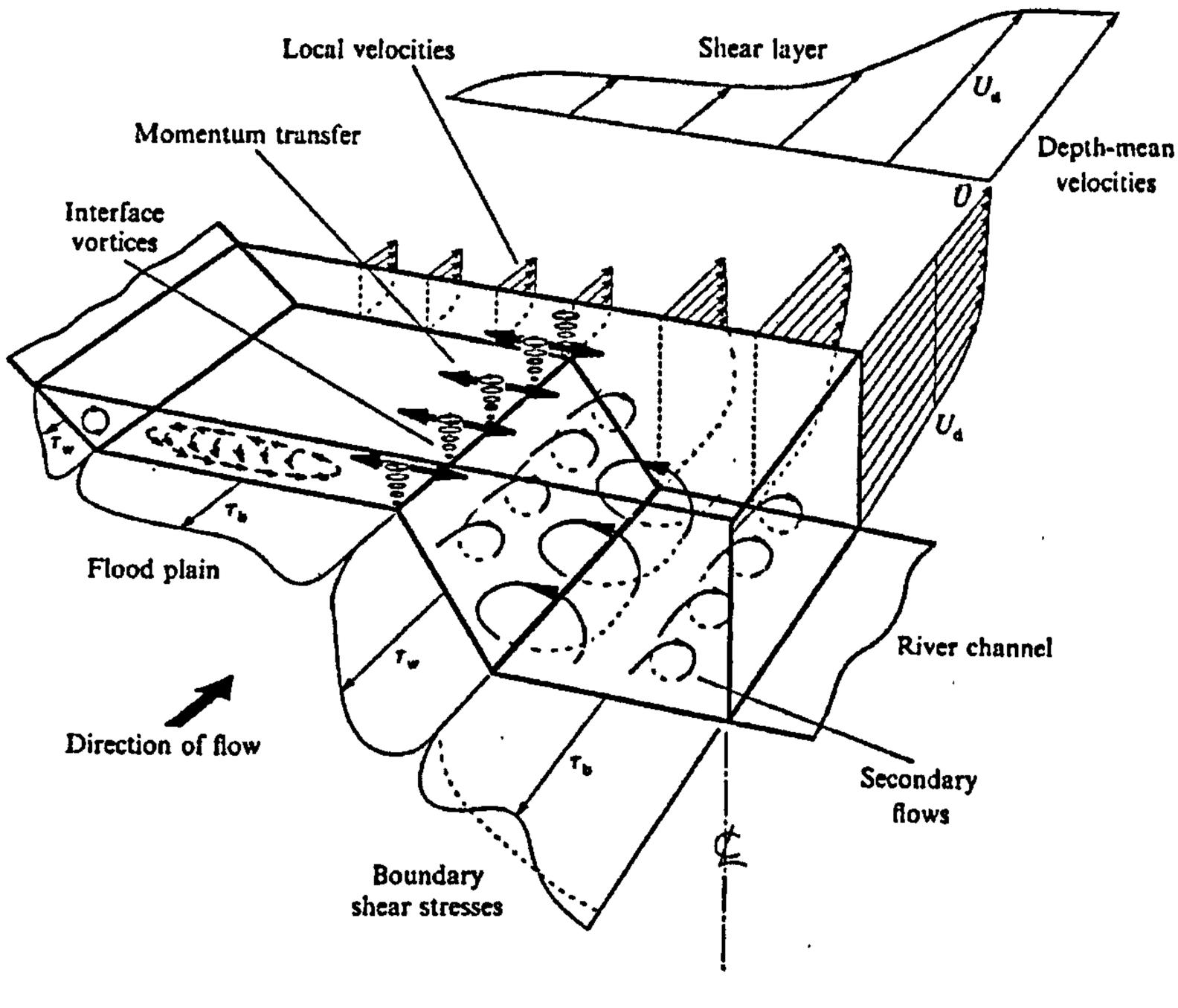

Figure 2.4: Sketch of the compound channel flow with trapezoidal cross section showing the overall flow mechanism that contribute to the transport and mixing processes. (after Shiono and Knight (1991))

2.3.1 Longitudinal Velocity Distribution

The modification of the longitudinal velocity distribution due to horizontal vortices created by the turbulent interaction between the main channel and the floodplain was first recognised by Sellin (1964) followed by Rajaratnam and Ahmadi (1979).

Tominaga *et al.* (1989) described the flow behaviour as:

"The isovel lines of the longitudinal velocity bulge upward in the vicinity of junction the main channel with the flood plain. The velocity in this region is decelerated due to low-momentum transport by the secondary currents away from the wall. On both sides of this decelerated region, the isovel lines bulge toward the wall due to high-momentum

transport by the secondary currents."

To illustrate the longitudinal velocity distribution in a compound open channel, the results obtain by Tominaga and Nezu (1991) are shown in Figure 2.5.

2.3.2 Secondary Currents

As shown in Figure 2.5, strong upflow, which is associated with a pair of longitudinal vortices, is generated in the main channel/flood-plain junction area. Existence of this strong secondary flow around the main channel/flood-plain junction area in a compound channel is demonstrated by Knight and Shiono (1990) and is recognised by many other researchers (Cokljat and Younis (1995), Lin and Shiono (1994) and others).

Shiono and Knight (1989) identified two major secondary flow circulation cells in the compound straight channels as shown in Figure 2.6. A strong upflow inclined towards the main channel from the top edge of the floodplain and downflow in the corner of the main channel. They stated that these secondary flow circulation cells change strength as the main channel side slope changes. In the floodplain region only one large secondary flow circulation cell was observed, which extends laterally to a considerable distance.

2.3.2.1 Generation of Secondary Currents

The streamwise vorticity equation is often used by researchers to explain the generation mechanisms for Prandtl's first and second kinds of secondary flow circulations.

During the early research, Brundrett and Baines (1964), Gessner and Jones (1965) and Perkins (1970) have shown that, in theory, it is mainly the inequality between the normal turbulent stresses and the gradients of this inequality that induces the secondary flow circulations (Naot and Rodi (1982)). This anisotropy of turbulence is caused by boundary roughness conditions of the bed, sidewall

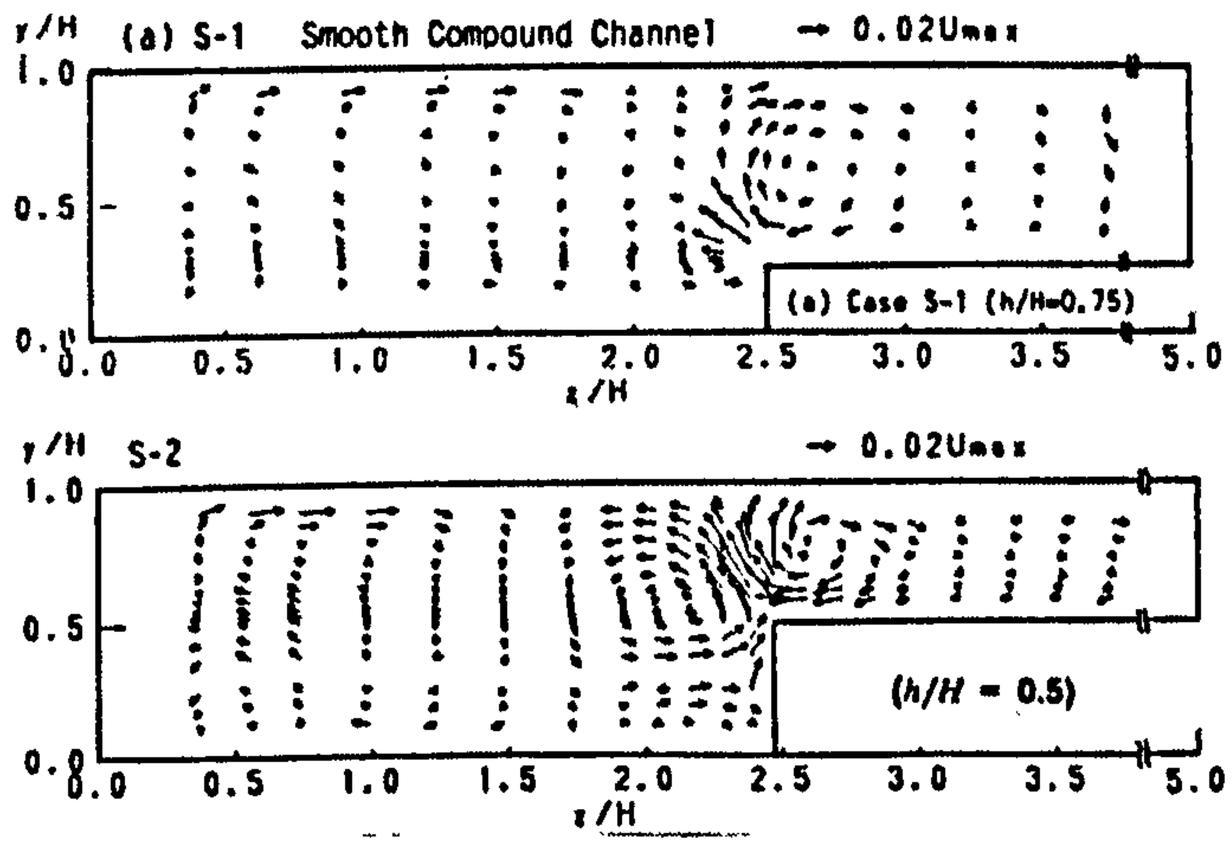

(a)

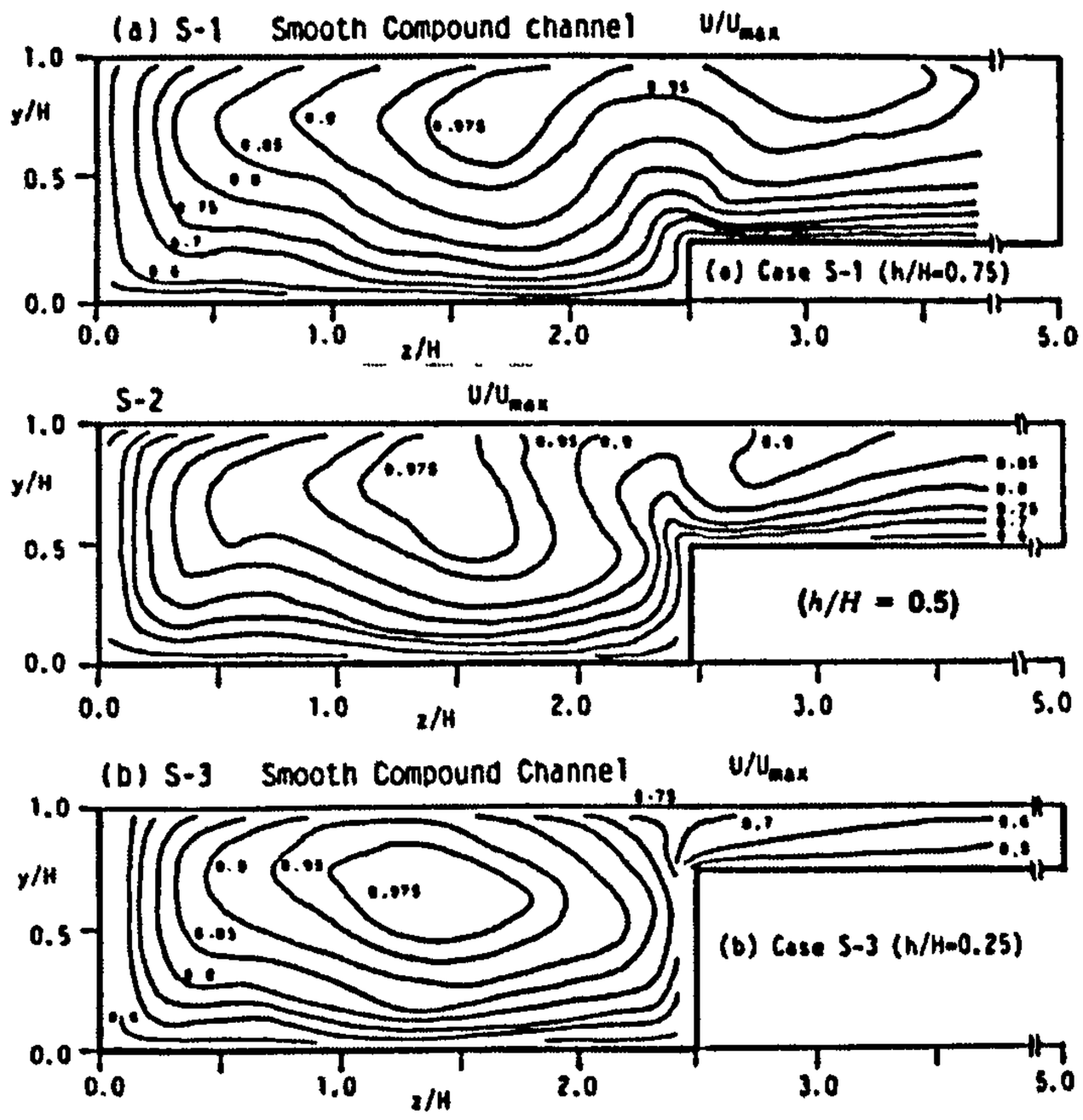

(b)

Figure 2.5: Compound channel flow profiles for different relative depths (h/H): (a) Secondary currents; (b) Longitudinal velocity contours. As relative depth decreases the interaction between main channel and flood plain decreases. This leads to less bulging of longitudinal velocity at floodplain/main channel junction. (after Tominaga and Nezu (1990))

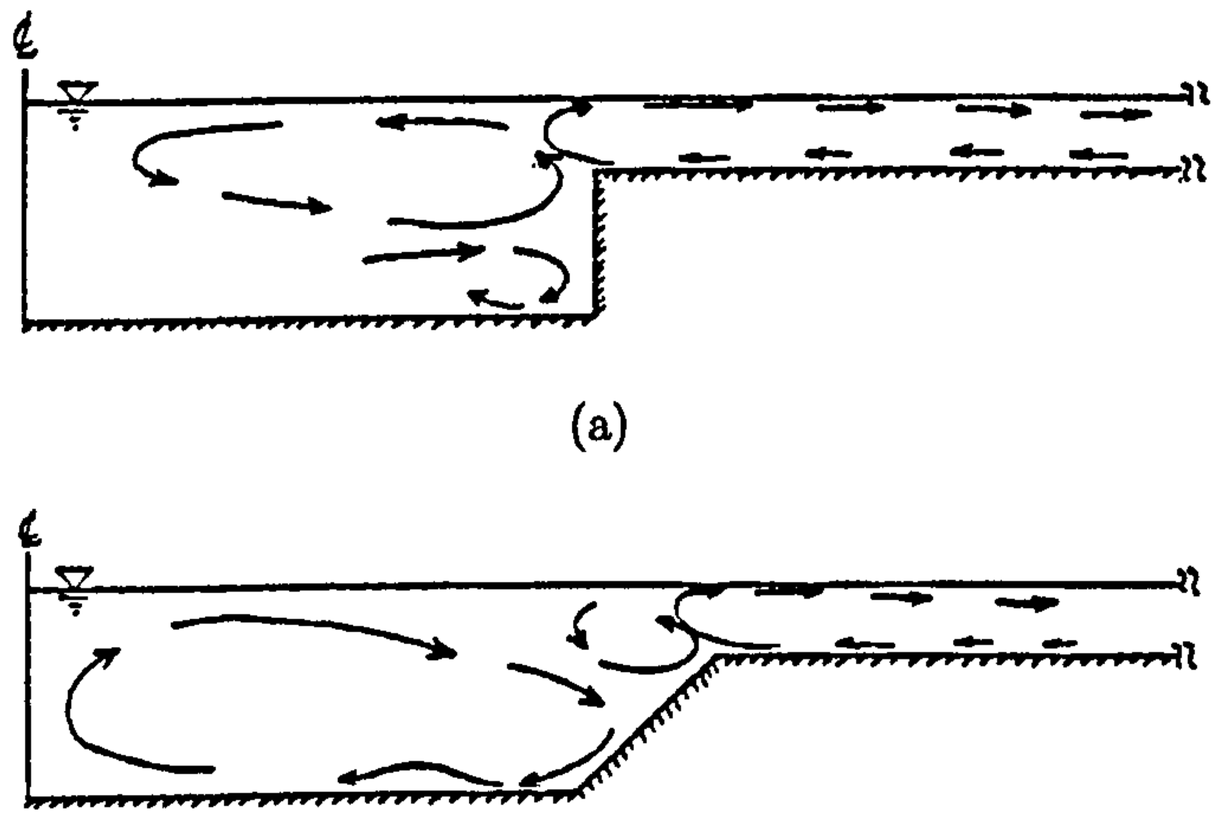

Figure 2.6: Illustration of secondary circulations in compound channels (a) with rectangular cross section (b) with trapezoidal cross section. Secondary flow circulation cells strength increases as the main channel side slope increases (after Shiono and Knight (1989)).

and free surface, as well as the aspect ratio of the channel and channel geometry (Tominaga *et al.* (1989)).

Tominaga and Nezu (1990) stated that the magnitude of difference in the normal Reynolds stresses was found to be the most important term of the streamwise vorticity, which is responsible for the production of turbulence-induced secondary flow circulations.

2.3.3 Effect of Relative Depth on Flow Behavior

Lai and Knight (1988) analysed the distribution of longitudinal velocity in compound ducts, and found that flows in compound channels are strongly related to the relative depth. The relative width was found to be a less significant parameter.

Nezu *et al.* (1999) found that the isovel lines of the longitudinal velocity are changed by the upflow in the main channel flood plain junction area. This effect increases with an increase of the flow depth on the flood plain.

Cokljat (1991) shows that with the decrease in the relative depth, all the characteristics of the flow remain but the interaction between main channel and flood plain is not so strong any more, and the bulging of the mean velocity distribution becomes weaker. These findings are also confirmed by the numerical simulation of Sofialidis and Prinos (1999).

2.4 Meandering Channels

Investigation into flows in channel bends has been one of the most important topic in water engineering. Thomson (1876) observed the characteristic spiral motion of the flow in a channel bend and concluded that the essential source of this phenomenon is the centrifugal force generated due to the curved flow path. The resulting spiral motions, i.e. secondary flows, have significant effect on engineering matters such as flow resistance, sediment transport, erosion and deposition, and so on.

Shukry (1949) investigated the flow through closed **U** bend by using specially designed pitot tube capable of recording the three components of velocity. This study was first to present the detailed behaviour of flow around the bend. Shukry (1949) observed that due to the centrifugal force, the secondary circulations along the bend showed a continuous tendency to deviate from the original pattern of the straight approach flume and to form a new one.

As a result of extensive research activities for more than a hundred years, lots of literature is available dealing with bend flows and related issues. In this section primary flow, secondary flow, bed shear stress and different aspects of numerical modelling pertaining to a meandering channel are discussed briefly.

2.4.1 Primary Flow

In meandering channels (see Figure 2.7), the maximum velocity core travels towards the outer bank as flow reaches the middle of the cross-over region. At the

next bend apex section, this maximum velocity core again occupies its position near the inner bank of the main channel showing that the main channel flow follows the shortest path of travel. Shiono and Muto (1998) stated that the primary main channel velocity below the floodplain level follows the channel sides, whereas above floodplain level it follows the floodplain direction as the floodplain depth increases. The flow pattern observed in a meandering channel is totally different from those observed in a straight channel.

Patra *et al.* (2004), in their investigation on the flow and velocity distribution in a compound meandering channel, found that the flow and velocity distributions in meandering compound channels are strongly governed by the interaction between the flow in the main channel and that in the floodplain.

2.4.2 Secondary Flow

2.4.2.1 Circulation Pattern

As discussed earlier in Section 2.3, in straight compound channels the secondary flow circulations are generated mainly due to the anisotropy of the turbulence. However, in the case of curved or meandering channels, secondary flow circulations are generated due to the curvature effects of planform geometry. These types of circulations are called as *geometry or pressure driven* secondary flow circulations or Prandtl's first kind of circulations which has magnitude $10-40\%$ of the bulk streamwise velocity. The strength of these types of circulations is much higher as compared to that of Prandtl's second kind.

In compound meandering channels, a helical secondary circulation cell occupying most of the main channel cross-sectional area is present at the bend apex section. Toebes and Sooky (1967) found the patterns of secondary flow circulations to be significantly different between inbank and overbank flows in compound meandering channels.

For overbank flows, the circulations were found to be stronger and with opposite sense of rotation as compared to those in inbank flow. Shiono *et al.* (1994)

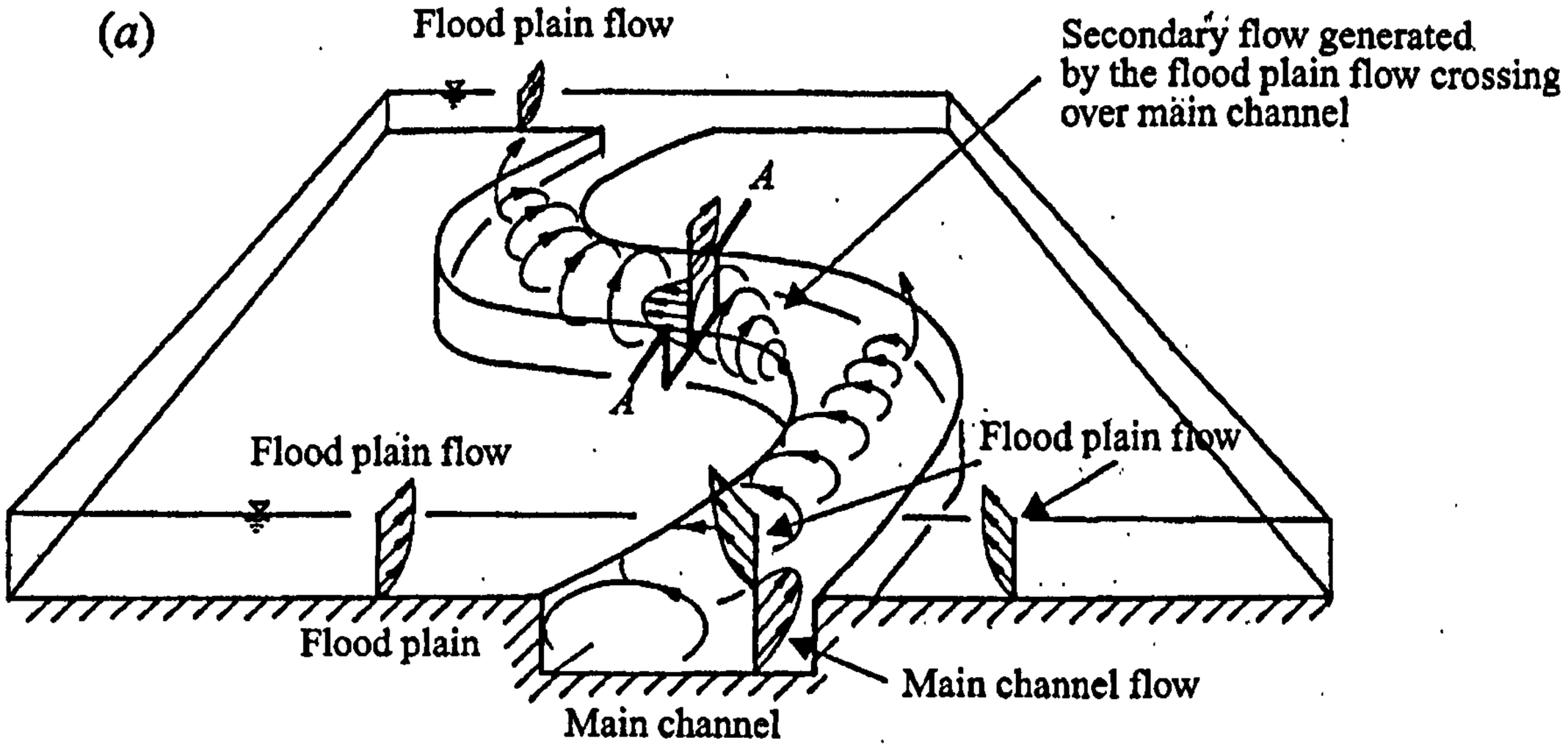

Figure 2.7: Conceptual sketch of complex 3D flow structures associated with a compound meandering channels: (a) Secondary flow pattern in compound meandering channel with rectangular cross-section. Anticlockwise circulation cell is present at bend apex which losses its strength as flow reaches just upstream of crossover region. New clockwise circulation cell starts to generate from here due to the impingement of floodplain flow into the main channel. (b) Contributions of flow mechanisms (turbulent shear, secondary flows and anisotropy of turbulence) towards the production of turbulence energy (after Shiono and Muto (1998)).

and Imamoto *et al.* (1982) carried out experiments on a meandering channel with meandering floodplain walls (usually straight in most of the studies) and reported that the dominant cell for the overbank case rotated in the same direction as that for the inbank cases. This clearly indicated the effect of meandering floodplain walls on the secondary flow circulations.

Different mechanisms behind the generation of secondary flow circulations for inbank and overbank flows were identified during previous studies. Ervine and Ellis (1987) stated that the meander bend with outward centrifugal pressure generates transverse secondary currents occupying most of the main channel cross-sectional area.

Selling *et al.* (1993) gave a conceptual presentation of the mechanisms behind the generation of the secondary flow circulations as shown in Figure 2.8. As can be seen from the figure, the vortex is initiated approximately from the start of the cross-over region mainly due to the floodplain flow plunging into the main channel.

Willetts and Hardwick (1993) through dye injection experiments demonstrated that the flow structures in the main channel with trapezoidal cross-section are different from those observed in meandering channels with natural cross-section. Ervine and Jasem (1995), based on their experiments on the skewed compound channels illustrated the effect of the main channel aspect ratio and the channel bank side slope on the patterns of secondary flow circulations. This is shown in Figure 2.9.

The secondary flow circulations in compound meandering channels are studied extensively in the past by many researchers [e.g. Toebes and Sooky (1967), Mckeogh and Kiely (1989), Sellin (1991), Sellin et al. (1993), Willetts and Hardwick (1993), Shiono and Muto (1993; 1998) and many others].

2.4.2.2 Complex Turbulent Flow Structures

Shiono and Muto (1998) undertook detailed turbulence and secondary flow measurements using a two-component Laser Doppler Anemometer in meandering

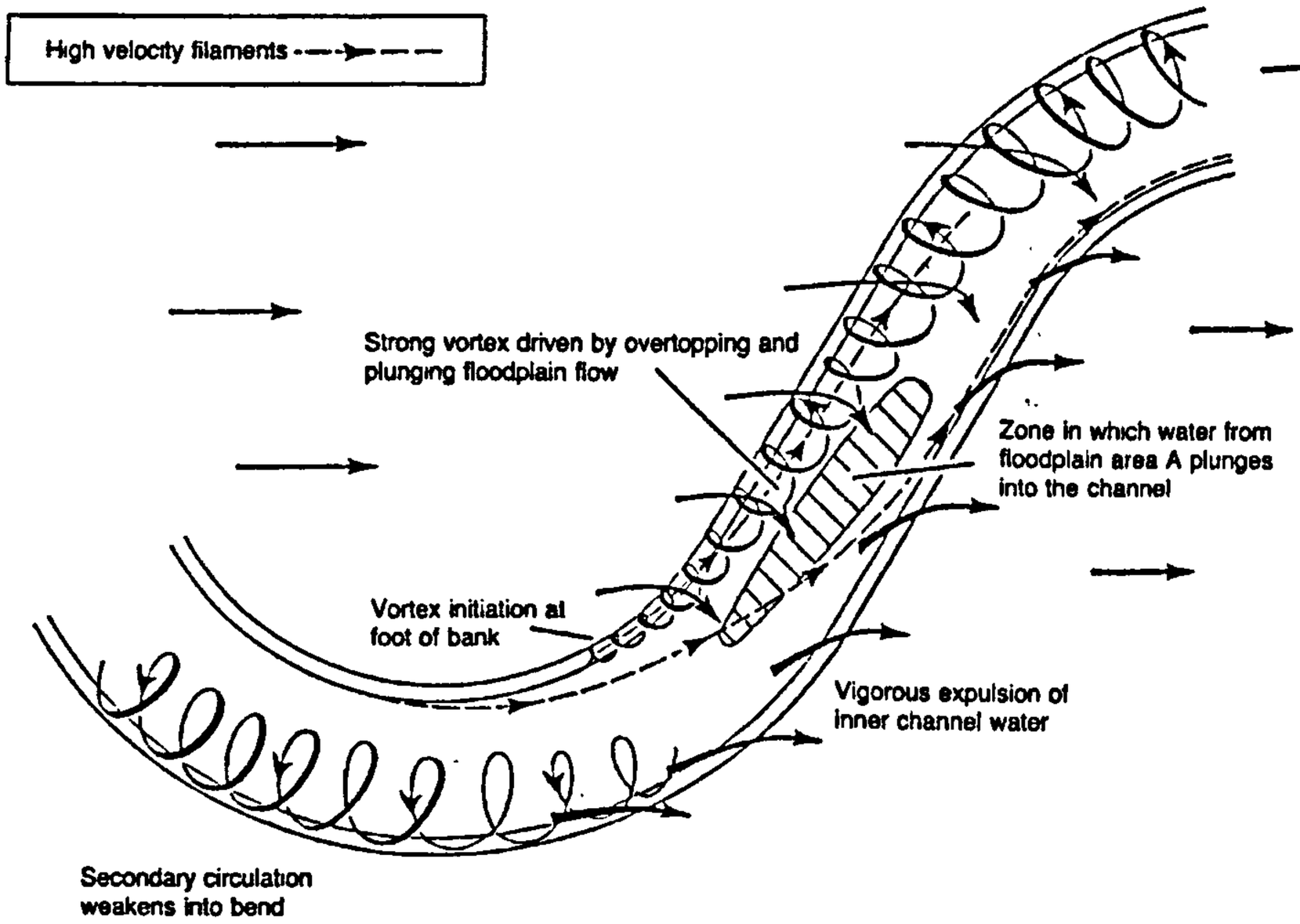

Figure 2.8: Conceptual sketch of the generation and destruction of secondary currents within compound meandering channels with trapezoidal cross-section. Overtopping and plunging of overbank flow into the main channel creates and drives the strong vortex (after Selling *et al.* (1993)).

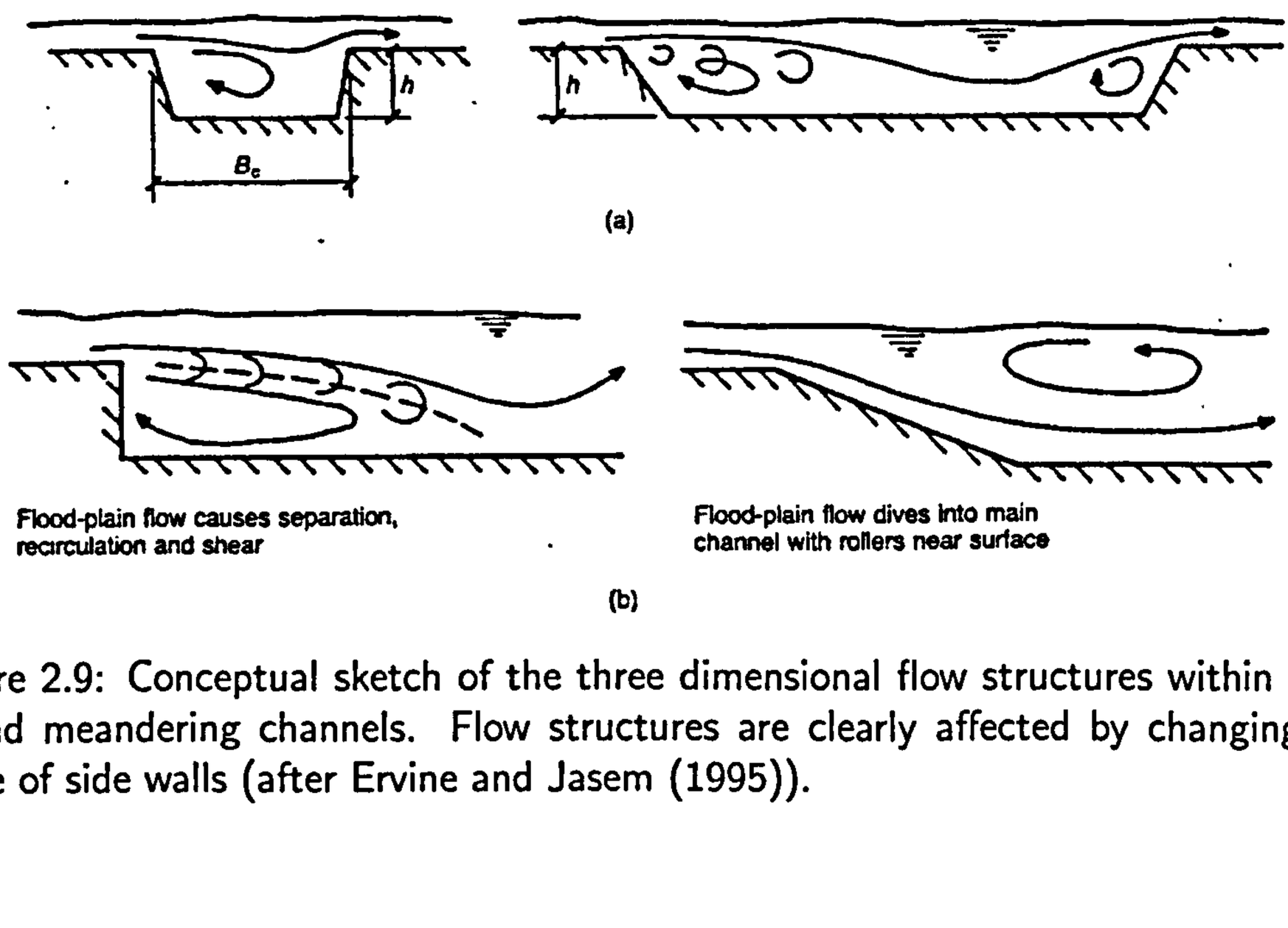

Figure 2.9: Conceptual sketch of the three dimensional flow structures within compound meandering channels. Flow structures are clearly affected by changing the slope of side walls (after Ervine and Jasem (1995)).

channels having a rectangular cross-section and straight floodplain walls. Based on these measurements, they conceptually presented the overall flow structures in a meandering channel for the overbank flows, as shown in the Figure 2.10.

As shown in this figure, a dominant anti-clockwise secondary circulation is present at the bend apex, which losses its strength as flow travels along the meander till the upstream edge of cross-over region. From here a new clockwise circulation cell occurs and gains strength as the floodplain flow plunges into and over the main channel in the cross-over region. The floodplain flow plunging into the main channel causes interfacial shear stress at around the bankfull level. They reported that this large interfacial shear stress induced at around the bankfull level, especially in the cross-over region and was found to be larger than the bed shear stress. They further stated that the strong shear layer generated by the floodplain flow crossing over the main channel flow is controlled by the angle between the meandering channel and the floodplain wall together with the depth of the water.

The pattern of floodplain flow plunging into the main channel varies with the floodplain flow depth. This is shown in Figure 2.7. The figure shows the flow visualisation for different relative depths as conducted by Shiono and Muto (1998). For shallower floodplain depth, the main channel flow is still seen to be dominant and as the floodplain flow depth increases the floodplain flow dominates the main channel flow direction above the bankfull level (see $Dr \cong 0.25$ in Figure 2.7).

In case of straight channels the shear is normally generated due to the differential velocity between the main channel and floodplain flows. Thus the mechanisms behind shear generation are significantly different between compound straight and meandering channels. Shiono and Muto (1998) stated that for the inbank flow cases, the clockwise secondary circulation cell at the bend apex gains strength due to the stretching of vortices, which is caused due to the centrifugal effect of the bend or the curvature. As this cell reaches the cross-over section it starts weakening as centrifugal forces or bend effect weakens. However, for the overbank

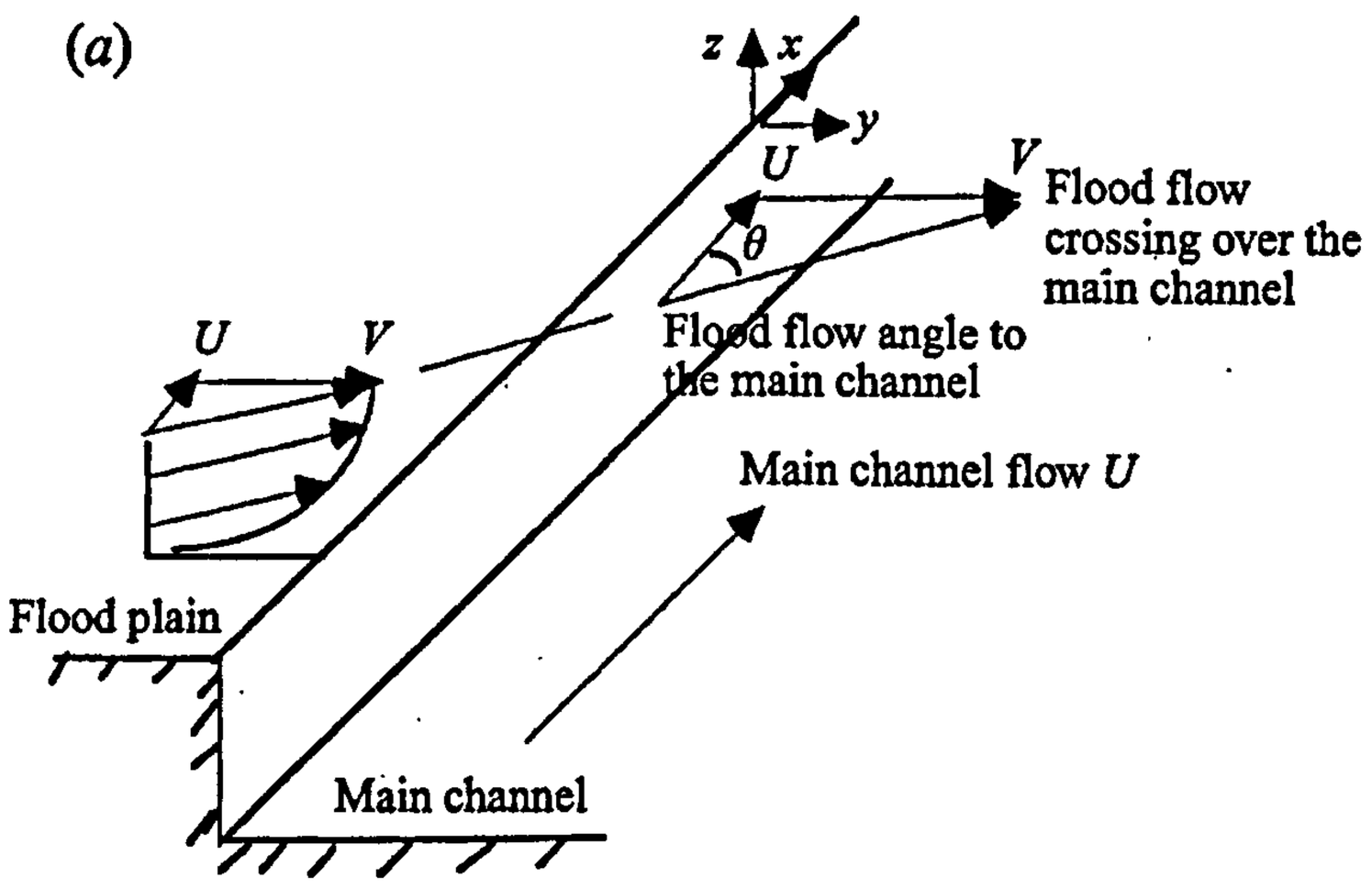

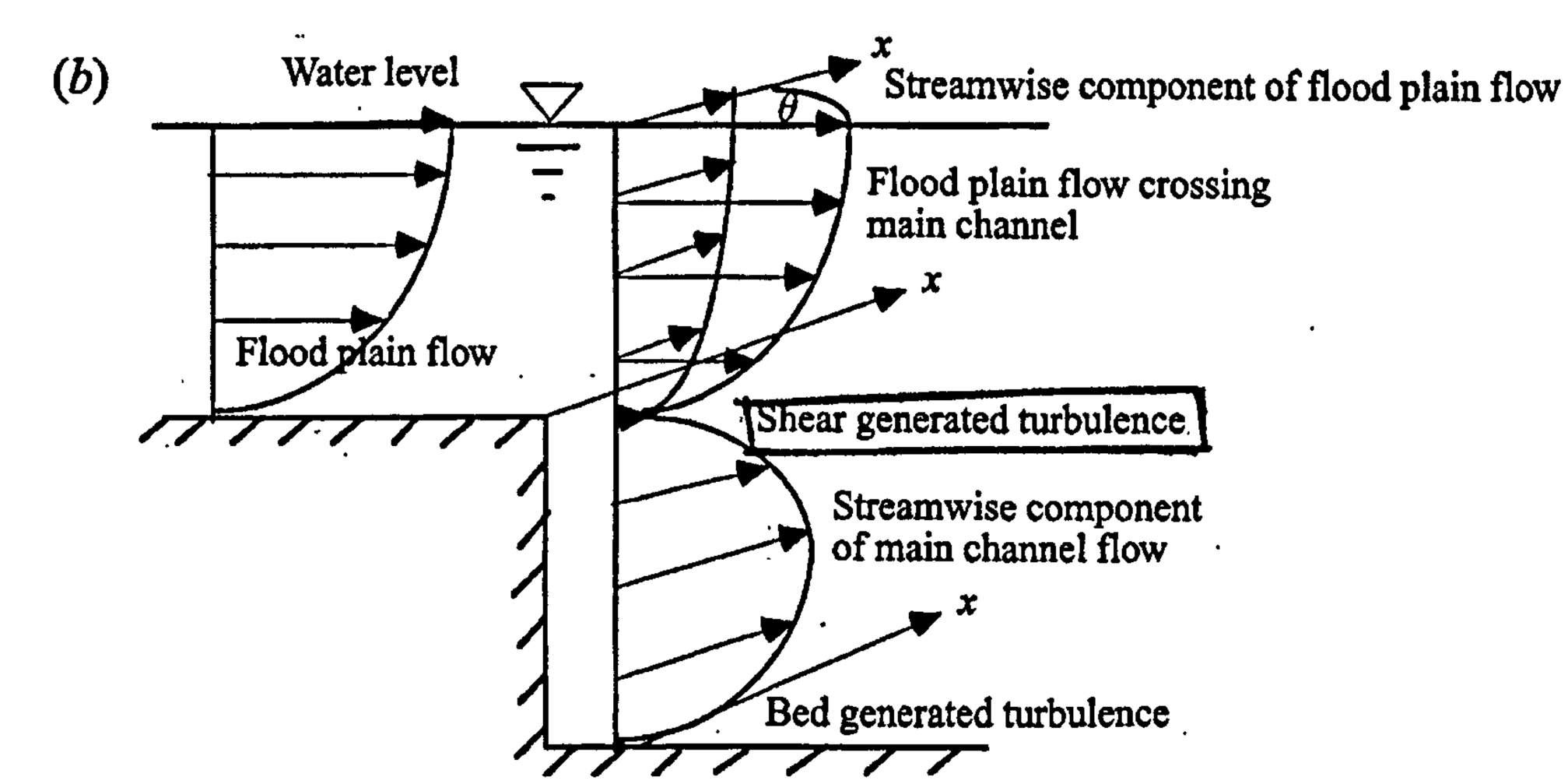

Figure 2.10: Illustration of the floodplain flows resolved in streamwise direction representing the effect of meander channel angel on flood plain flow and turbulence structures (after Shiono and Muto (1998)).

flow cases, the clockwise secondary circulations cells are generated just near the upstream edge of the cross-over region by the floodplain flow plunging into the main channel. Thus for inbank flows, the bed- and wall-generated turbulence are the most dominating feature whereas, for overbank flows the turbulent intensities just below the bankfull level become more important.

From the Reynolds stress analysis, Shiono and Muto (1998) found that the main contribution of shear stresses to the turbulence production in the strong secondary flow region come from term generated by the secondary flows. Figure 2.11 shows the main contributions to the turbulence energy production in the cross-over region. As can be seen from the figure, the main contribution to the turbulence production is from the secondary flow and due to the shear generated by the main channel and floodplain flow interaction.

2.4.3 Bed Shear Stress

The bed shear stress is usually measured using a Preston tube technique (Preston (1954)). Moreover, Ghosh and Kar (1975), Knight *et al.* (1992), Lorena (1992), Muto (1997) and many others measured the bed shear stress in compound meandering channels.

The distribution of boundary shear stress around the wetted perimeter of an open channel is normally affected by the existence of secondary flow circulations. Knight *et al.* (1992) measured the boundary shear stress in strong secondary flow regions in a large-scale meandering compound channel at the FCF. Their results indicated that an undulation of the boundary shear stress distribution is closely related to secondary flow structures. The downward motion of secondary flow is generally related to larger boundary shear stress whereas; the upward motion is related to smaller boundary shear stress. Shiono *et al.* (1999) confirmed this later while comparing the bed shear stresses measured by both a Preston tube and a heated thin film sensor in small-scale meandering channels.

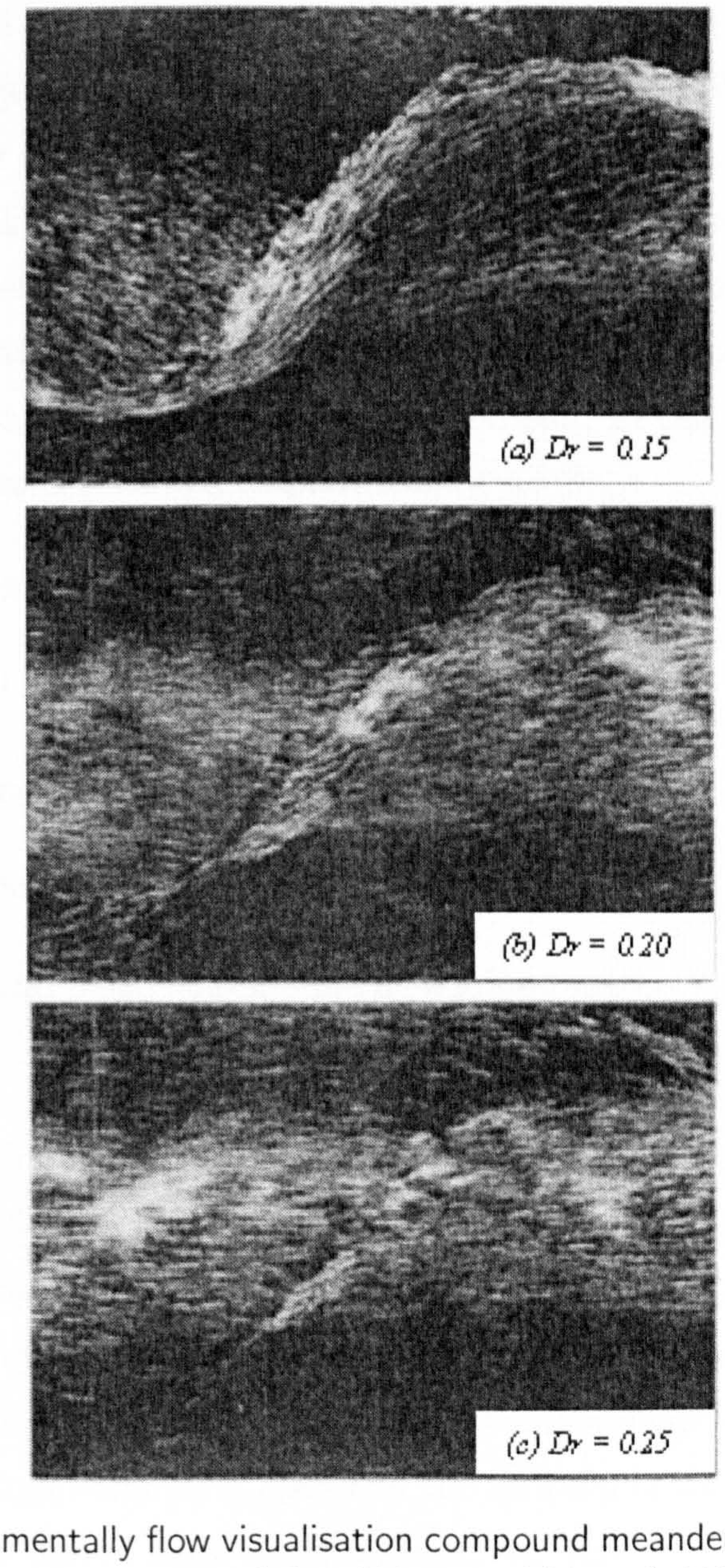

Figure 2.11: Experimentally flow visualisation compound meandering channel flow for relative depth 0.15, 0.20 and 0.25 (after Shiono and Muto (1998)).

2.4.4 Numerical Modeling of Meandering Channel Flow

Extensive research work to model the flow behaviour within meandering channels has been done since early 1989. A few of the researcher who have tried to simulate complex geometries include Stein and Rouv (1989), Wenka *et al.* (1992), Jenkins and Keller (1992), Rameshwaran and Shiono (2003), Rameshwaran and Naden (2004), Shukla (2006) and others. Major challenges faced whilst modeling meandering channel flows are complicated geometry of the meandering channel and the determination of factors influencing the flow behaviour e.g. established model constants, capturing free surface variation etc.. In this section, work done by other researchers is reviewed emphasizing:

- ◇ Method adopted to tackle the meandering channel geometry,
- ◇ Types of grid considered,
- ◇ Turbulence modeling,
- ◇ Pressure velocity coupling algorithm; and
- ◇ Advantages and disadvantages of the adopted method.

Sugiyama *et al.* (1999) carried out a study of turbulent flow developing in a meandering open-channel with rectangular cross sections using an algebraic stress model. In the calculation, governing equations are transformed from the physical plane to the computational plane by using boundary-fitted non-orthogonal coordinate system. They reported that the adopted numerical method could predict well the features of streamwise velocity, i.e. the maximum streamwise velocity generated at the inner bank bend apex and the location of the maximum velocity moved to the other side of bank along meandering channel. They also suggested that meandering channel flow is featured by unsteady movement of the secondary flow pattern.

Sugiyama and Saito (2002) performed the numerical analysis for the developing turbulent flow in a compound meandering open-channel using an algebraic Reynolds stress model. Again, the boundary fitted coordinate system was adopted to handle the complicated geometry of the compound meandering channel so that the transport equation were converted from the physical plane to the computational plane. Figure 2.12 shows the body fitted grid used by the author for the numerical simulations. They studied the flow behaviour in meandering channel under the influence of centrifugal force, pressure driven force and shear stress generated between the main channel and flood plain. Though the proposed method able to reproduce the characteristic features, the agreement with the experimental data was not perfect quantitatively.

Ye and McCorquodale (1998) presented a 3D model of turbulent flows developed for a body-fitted curvilinear coordinate system and applied it to simulate the flow through curved channels. In the horizontal plane, a channel-fitted curvilinear coordinate system were used, whereas in vertical plane, the σ transformation was applied to track the free surface and bed topography.

The modified standard $k-\varepsilon$ model, in which eddy viscosity in the horizontal and vertical directions were formulated algebraically, was considered to take into account the streamline curvature and damping effects as well as solid walls effects appearing in the shallow curved channel. The governing equations were solved in a collocated grid system by a fractional three-step implicit algorithm (Ye and McCorquodale (1997)). The model was applied to two typical curved open channel flows:

1. A single 270^0 channel bend with a sloped outer bank,

2. A meandering channel with pollutant transport.

They reported that the strength of secondary currents were much stronger in a single bend than that in meanders due to the opposite spiral motion generated by the alternate bends of the meandering channels. The lateral mass transport due to secondary currents in curved channel could be considerable.

Lai *et al.* (2003) proposed a 3D non-hydrostatic numerical method based on an unstructured grid technology to solve flow problems in hydraulic engineering. The model solved 3D turbulent flow equations and utilised a collocated and cell-centered storage scheme with a finite-volume discretization. The model adopted the general framework of an unstructured grid technology with arbitrarily shaped cells so that both structured and unstructured grid could be used.

The model was tested on an S-shaped open-channel flow with the use of hexahedral, tetrahedral and prismatic cells. Authors reported that a prismatic mesh was as efficient and accurate as a hexahedral mesh, and it might be a good choice for flows in natural rivers. They also found that high aspect ratio or highly stretched tetrahedral meshes produced less accurate solutions and should be avoided.

Rameshwaran and Naden (2004) presented a 3D numerical study for the calculation of turbulent free surface flow in a meandering channel. In the calculation Reynolds Averaged Navier Stoke's equations with the standard $k-\varepsilon$ model for steady flow was used. Moreover, a free surface treatment for spatial variation was also employed. They analysed the distribution of water free surface elevation, bed shear stress, streamwise and transverse velocities to check the model performance by comparing the results with experimental data obtained from UK FCF for inbank flow. Results showed that the free surface treatment for the spatial variation of the water surface was vital for the accurate prediction of bed shear stress.

Shao *et al.* (2003) proposed a model based on orthogonal curvilinear system in conjunction with algebraic stress models to simulate the secondary currents in helically coiled channel. They used various combinations of cross sections and channel curvature for a helically coiled compound channel to examine the effects of anisotropy on the secondary motion and other turbulence properties. They reported that for primary velocity profiles, both the LY model and the NLKE model captured the stronger flows near the side-wall of the main channel (concave side) in curved channels. The LY model properly produced the low velocity zone

that extends from the junction edge to the free surface whilst the NLKE model predicted a shorter extension of the low velocity zones.

For the case of rectangular channel, primary velocity predicted by the NLKE and the LY models were better in agreement compared to the NR model. However, Shao *et al.* (2003) compared numerical predictions of flow through a helically coiled channel with a straight channel which makes the performance check of the model very difficulty quantitatively as well as qualitatively.

In a recent numerical investigation, Wormleaton and Ewunetu (2006) used a standard 3D $k - \varepsilon$ turbulence model SSIIM (Olsen (2002), Olsen (2003)) to compare the experimental data collected on overbank flow in a mobile bed meandering channels carried out on the UK FCF at HR Wellingford. In the model, the RANS equations were discretized using the control volume approach. A second order upwind scheme was used to determine the fluxes. The pressure velocity coupling in the solution was accomplished using the SIMPLE algorithm. The body fitted non orthogonal grid used by the authors is shown in Figure 2.12.

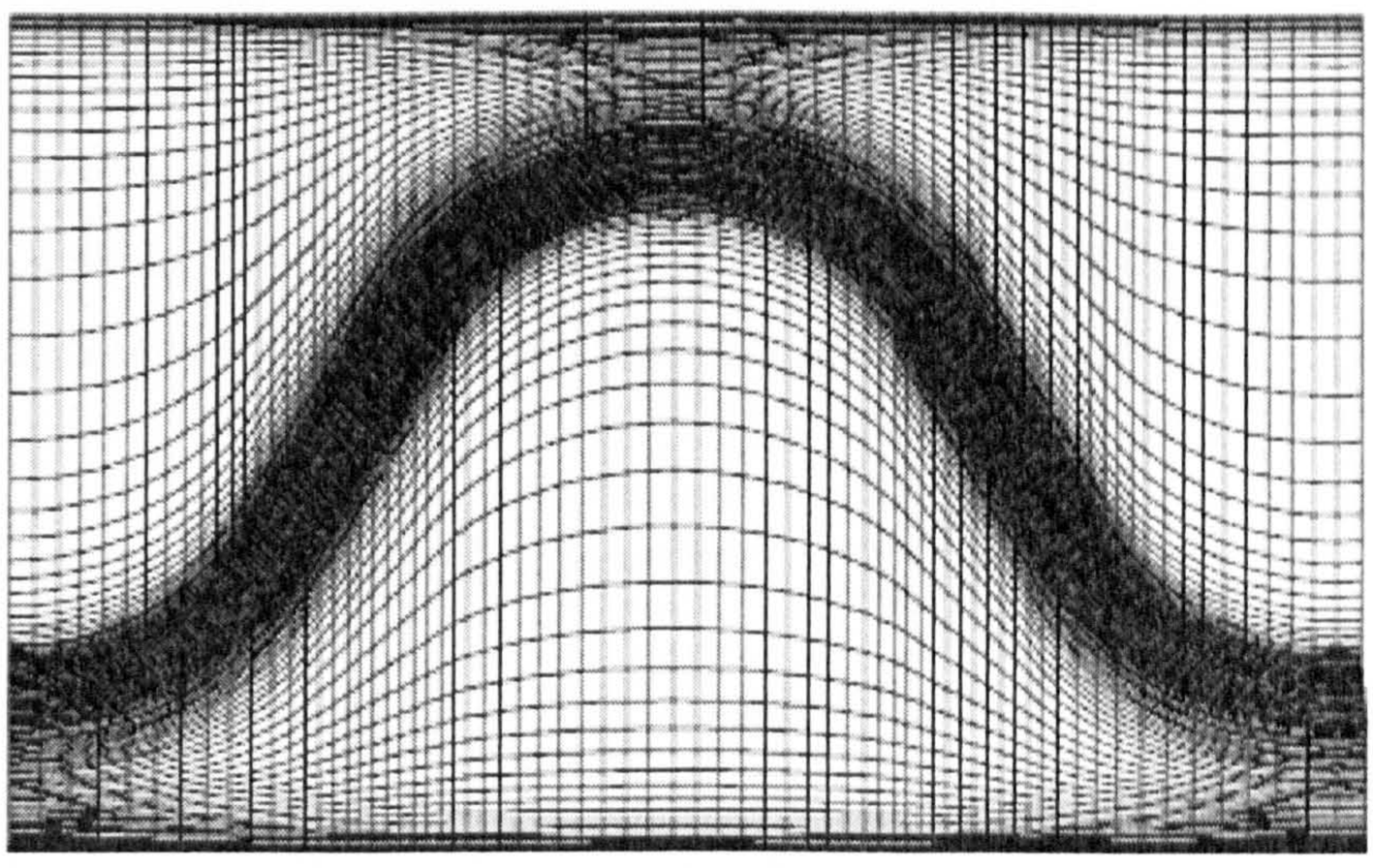

Figure 2.12: Plane view of a non-orthogonal body fitted grid adopted for numerical simulations by Sugiyama and Saito (2002) and Wormleaton and Ewunetu (2006). The grid represents one channel meander.

The model was used to compare with overbank meandering channel data from

the UK FCF for different flood plain depths, roughness and planforms. They reported that the standard $k-\varepsilon$ model provides good agreement between total main channel flows and their variation through a meander wavelength. However, they also concluded that the model underestimates the outward secondary flows which is very important for the prediction of boundary shear, bed morphology development and sediment transport.

Shukla (2006) used 3D finite element model to handle the complicated geometry of compound meandering channel and considered isotropic $k-\varepsilon$ turbulence model in conjunction with the Reynolds Averaged Navier Stoke's equations to investigate the flow mechanism. They reported that the horizontal shear layer at the inner bankfull level generated secondary flow circulations. As the depth of flow increased, the point of generation of secondary flow circulations moved downstream. They noticed that in terms of the generation of secondary currents, the secondary flow shear stress significantly contributed towards the generation of streamwise vorticity and the production of turbulent kinetic energy.

Shukla (2006) also noticed that the rate of turbulence kinetic energy production was higher than the rate of its dissipation in the crossover region. The turbulence extracts more energy from the mean flow than what is actually dissipated. It was also found that the strength of geometry induced secondary flow circulation increases with the increase in the relative depth.

2.5 Concluding Remarks

This chapter has presented the review of work carried out by other researchers to understand the the flow mechanisms occurring in straight rectangular channels, compound channels and meandering channels with and without floodplains. The flow behaviour in these channels is summarized as follow:

- In simple open channel flows, the secondary currents (*Prandtl's second kind*) are generated due to the wall and bed shear stresses, which have magnitude

of $1-4\%$ of the bulk mean velocity. The secondary circulations cause the maximum primary flow velocity to lie below the free surface, which is widely referred as *the velocity dip effects.*

- In compound channels, the shear layers are generated due to the velocity difference between usually faster flow in the main channel and slower flow on the floodplain. In these layers a strong vortex exists which affects the mean velocity profile and mixing process considerably.

- The flow mechanism is in compound meandering channels are affected by the channel sinuosity (responsible for the centrifugal forces) and plunging of floodplain flow into the main channel. The secondary currents are, generally, pressure or geometry driven and known as *the Prandlt's first kind* of circulations which have magnitude of $10-40\%$ of the bulk mean velocity.

Important aspects of the numerical modeling of open channel flows are also covered, concentrating types of grid used, turbulence modelling and accuracy of the method which can be summarized as:

- The traditional 1D models used for prediction of the discharge and sectional average velocity have limitations due to the assumptions made for the channel geometry, flow interaction and boundary roughness. 2D models, based on RANS equations and iso-tropic turbulence models, are only sufficient to calculate the detailed variation in dept-averaged velocity and sediment transport. A number of 3D anisotropic models such as algebraic stress models have been developed and used to predict the detailed flow mechanism of open channel flows.

- Beside conventional time averaging approach (RNAS modelling), Large Eddy Simulations and Direct Numerical Simulations are also adopted for open channel flow simulation, which have increased the accuracy of numerical accuracy considerably. But these methods are very time and computational energy intensive.

- Finite element, unstructured finite volume and non-orthogonal types of numerical discretization have been used to handle the 3D geometry of compound meander channels. However, only isotropic models have used for these methods.

CHAPTER 3

Governing Equations

3.1 Introduction

To predict the behaviour of mean flow properties and turbulence parameters within open channels, the governing equations must be solved. These equations are based on the conservation laws of mass, momentum and energy. The 3D, steady state, incompressible, turbulent flow through open channels can be described by the Reynolds Averaged Navier Stokes equations, generally known as RANSe, which are adopted as the governing equations in the present research. These equations are the result of time averaging of the Navier Stokes equations, which can be found from Versteeg and Malalasekera (1995), Rodi (1993), Abott and Basco (1989) and Ferziger and Perić (1995).

This section describes the governing equations in a Cartesian coordinate system, considered for the flow through simple channels and compound channels shown in Figure 3.1. The formation and derivation of equations in the orthogonal coordinate system, for the case of meandering channels, is discussed in Chapter 5.

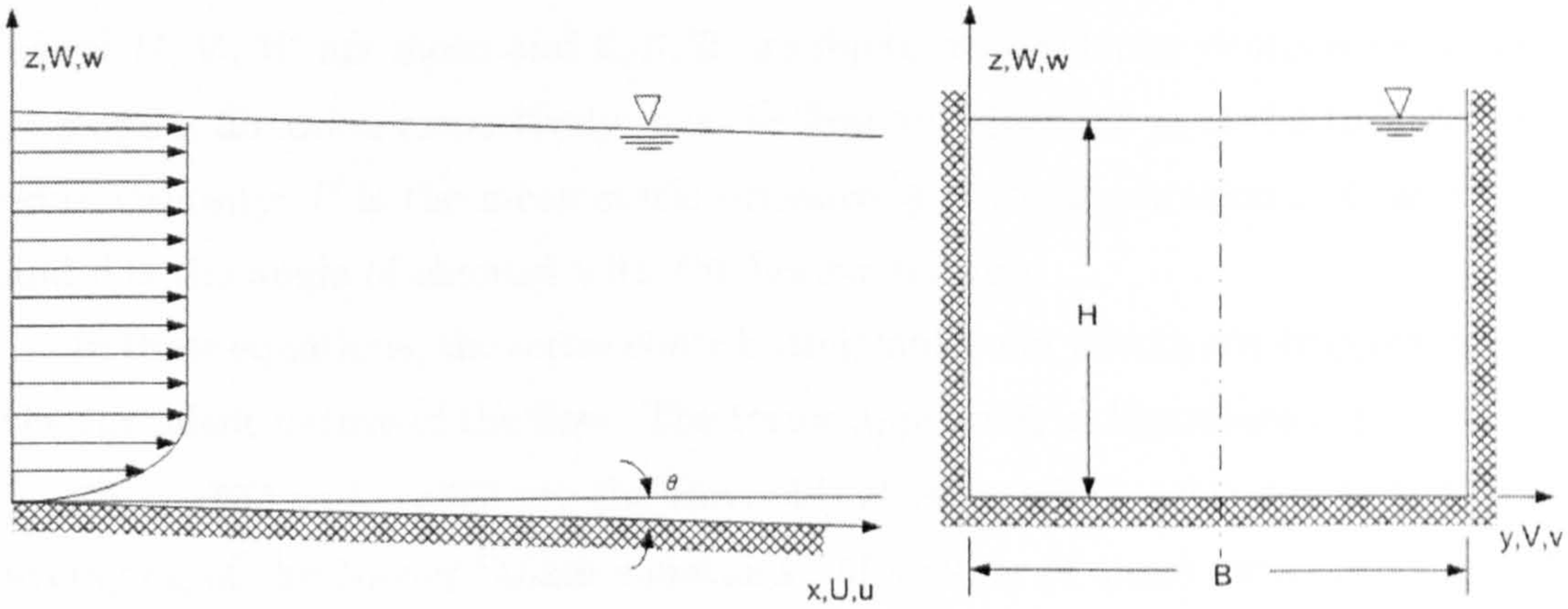

Figure 3.1: Typical sketch of an open channel flow configuration. B and H are the channel width and height respectively. The primary flow direction is x while secondary flow direction occurs in the y and z planes. U, V and W are primary velocity components and u, v and w are components of secondary velocity in the x, y and z directions respectively.

3.2 Reynolds Averaged Navier-Stokes Equations

The continuity equation is expressed as

$$\frac{\partial U}{\partial x} + \frac{\partial V}{\partial y} + \frac{\partial W}{\partial z} = 0. \tag{3.1}$$

The momentum equations in the longitudinal (x), lateral (y) and vertical (z) directions are given by Equations 3.2, 3.3 and 3.4 respectively as follow:

$$U\frac{\partial}{\partial x}(\rho U) + V\frac{\partial}{\partial y}(\rho U) + W\frac{\partial}{\partial z}(\rho U) = -\frac{\partial P}{\partial x} + \mu_t\frac{\partial^2 U}{\partial x^2} + \mu_t\frac{\partial^2 U}{\partial y^2} + \mu_t\frac{\partial^2 U}{\partial z^2} + \rho g \sin\theta, \tag{3.2}$$

$$U\frac{\partial}{\partial x}(\rho V) + V\frac{\partial}{\partial y}(\rho V) + W\frac{\partial}{\partial z}(\rho V) = -\frac{\partial P}{\partial y} + \mu_t\frac{\partial^2 V}{\partial x^2} - \frac{\partial}{\partial y}(\rho\overline{vv}) - \frac{\partial}{\partial z}(\rho\overline{vw}) \tag{3.3}$$

$$U\frac{\partial}{\partial x}(\rho W) + V\frac{\partial}{\partial y}(\rho W) + W\frac{\partial}{\partial z}(\rho W) = -\frac{\partial P}{\partial z} + \mu_t\frac{\partial^2 W}{\partial x^2} - \frac{\partial}{\partial y}(\rho\overline{vw}) - \frac{\partial}{\partial z}(\rho\overline{ww}) \tag{3.4}$$

where U, V, W are mean and $\overline{u}$, $\overline{v}$, $\overline{w}$ are fluctuating velocity components in the x, y and z direction respectively; ρ is the fluid density; and μ_t is the turbulent or eddy viscosity; P is the mean static pressure, g is the gravitational acceleration and θ is the angle of channel with the horizontal axis.

In these equations, the terms contributing molecular effects are dropped due to the turbulent nature of the flow. The terms appearing in Equations 3.3) and (3.4 [$-\rho\overline{vv}$, $-\rho\overline{ww}$ and $-\rho\overline{vw}$] are the Reynolds stresses which arise due to the time averaging of the Navier Stokes equations. Modelling of these terms is discussed in the following sections.

3.2.1 Eddy Viscosity Concept

The eddy viscosity concept proposed by Boussinesq (1887) is one of the oldest concepts for modelling the turbulent or Reynolds stresses. It assumes that in analogy to the viscous stresses in laminar flows, the turbulent stresses are proportional to the mean-velocity gradients. For general flow situations, this concept may be expressed in tensor form as

$$-\overline{u_i u_j} = \nu_t \left(\frac{\partial U_i}{\partial x_j} + \frac{\partial U_j}{\partial x_i} \right) - \frac{2}{3} k \delta_{ij} \quad \begin{cases} \delta = 0 & \text{if } i = j \\ \delta = 1 & \text{if } i \neq j \end{cases}. \tag{3.5}$$

Here, ν_t is the turbulent or eddy viscosity which, in contrast to the molecular viscosity μ, is not a fluid property but depends strongly on the state of the turbulence and δ is the Kronecker delta.

Equation 3.5 provides the framework for constructing turbulence models if the distribution of ν_t is known. This is discussed in following section.

3.3 The Standard $k-\varepsilon$ Turbulence Model

The two transport equations for turbulent kinetic energy (k) and kinetic energy dissipation (ε), described by Rodi (1993) are considered here to calculate the distribution of turbulent viscosity (μ_t).

The turbulent kinetic energy equation is expressed as

$$U\frac{\partial}{\partial x}(\rho k)+V\frac{\partial}{\partial y}(\rho k)+W\frac{\partial}{\partial z}(\rho k)=\frac{\partial}{\partial x}\left(\frac{\mu_t}{\sigma_k}\frac{\partial k}{\partial x}\right)+\frac{\partial}{\partial y}\left(\frac{\mu_t}{\sigma_k}\frac{\partial k}{\partial y}\right)+\frac{\partial}{\partial z}\left(\frac{\mu_t}{\sigma_k}\frac{\partial k}{\partial z}\right)+P_k-\rho\varepsilon. \tag{3.6}$$

The turbulent energy dissipation equation is given by

$$U\frac{\partial}{\partial x}(\rho\varepsilon)+V\frac{\partial}{\partial y}(\rho\varepsilon)+W\frac{\partial}{\partial z}(\rho\varepsilon)=\frac{\partial}{\partial x}\left(\frac{\mu_t}{\sigma_\epsilon}\frac{\partial \varepsilon}{\partial x}\right)+\frac{\partial}{\partial y}\left(\frac{\mu_t}{\sigma_\epsilon}\frac{\partial \varepsilon}{\partial y}\right)+\frac{\partial}{\partial z}\left(\frac{\mu_t}{\sigma_\epsilon}\frac{\partial \varepsilon}{\partial z}\right)+\frac{\varepsilon}{k}\left(C_{\epsilon 1}P_k-C_{\epsilon 2}\rho\varepsilon\right) \tag{3.7}$$

where P_k is the production of kinetic energy by the mean velocity gradients expressed as:

$$P_k=\mu_t\left(\frac{\partial U}{\partial y}\right)^2+\mu_t\left(\frac{\partial U}{\partial z}\right)^2 \tag{3.8}$$

and μ_t is the turbulent viscosity defined as

$$\mu_t=C_\mu\rho\frac{k^2}{\varepsilon} \quad . \tag{3.9}$$

The model constants, proposed by Rodi (1993) are given by $(C_{\epsilon 1}, C_{\epsilon 2}, \sigma_k, \sigma_\epsilon, C_\mu)$ = (1.44, 1.92, 1.0, 1.3, 0.09).

3.4 Algebraic Stress Models

The linear or standard $k-\varepsilon$ model has been shown to be incapable of accurately predicting the normal Reynolds stresses, hence making the description of secondary flows by these type of models impossible (Speziale (1987)).

In the present thesis, instead of solving the complete set of equations describing the Reynolds stresses, three different algebraic stress models are adopted. In these models, algebraic expressions are used to predict the normal as well as cross Reynolds stresses.

3.4.1 Launder and Ying Model

Launder and Ying (1973) derived algebraic expressions for the Reynolds stresses by simplifying the transport equations of the Reynolds stresses. They modelled the Reynolds stresses as a function of longitudinal velocity gradients, which are expressed as follows:

$$\rho\overline{vv} = -C'\mu_t\frac{k}{\varepsilon}\left(\frac{\partial U}{\partial y}\right)^2 + C'_k\rho k, \tag{3.10}$$

$$\rho\overline{ww} = -C'\mu_t\frac{k}{\varepsilon}\left(\frac{\partial U}{\partial z}\right)^2 + C'_k\rho k, \tag{3.11}$$

and

$$\rho\overline{vw} = \rho\overline{wv} = -C'\mu_t\frac{k}{\varepsilon}\left(\frac{\partial U}{\partial y}\right)\left(\frac{\partial U}{\partial z}\right). \tag{3.12}$$

The values of empirical constants are $C'_k = 0.522$ and $C' = 0.0325$ and it is these that governs the magnitude of the secondary currents.

3.4.2 Noat and Rodi Model

Naot and Rodi (1982) refined the LY model by introducing wall and surface proximity functions, which are quadratic in nature, to take boundary effects into account. The model, known as the advanced algebraic stress model, is expressed by the following equations for Reynolds stresses:

$$\overline{v^2} = \frac{k}{C_1 + 2C_3 f_2}\left[\frac{2}{3}\left(\alpha - \frac{1}{2}\beta + C_1 - 1\right) + \frac{\beta}{\epsilon}\left(\overline{uv}\frac{\partial U}{\partial y} - \overline{uw}\frac{\partial U}{\partial z}\right)\right] - 2\nu_t\frac{\partial V}{\partial y}, \tag{3.13}$$

$$\overline{w^2} = \frac{k}{C_1}\left[\frac{2}{3}\left(\alpha - \frac{1}{2}\beta + C_1 - 1\right) + C_3 f_2\frac{\overline{v^2}}{\rho k}\frac{\beta}{\epsilon}\left(\overline{uw}\frac{\partial U}{\partial w} - \overline{uv}\frac{\partial U}{\partial y}\right)\right] - 2\nu_t\frac{\partial W}{\partial z}, \tag{3.14}$$

$$\overline{vw} = \overline{wv} = \frac{k}{C_1 + \frac{3}{2}C_3 f_2}\left(\overline{uw}\frac{\partial U}{\partial y} + \overline{uv}\frac{\partial U}{\partial z}\right) - \nu_t\left[\left(\frac{\partial W}{\partial y}\right) + \left(\frac{\partial V}{\partial z}\right)\right]. \quad (3.15)$$

The empirical values are $\alpha = 0.7636 f_1$, $\beta = 0.1091 + 0.06 f_1$, $C_1 = 1.50 - 0.5 f_1$ and $C_3 = 0.1$.

The wall proximity function, f_1, was taken as the absolute value of the gradient of the length scale, l, as suggested by Ilegbusi (1985) and f_2 was determined by the Naot and Rodi (1982)'s formula as presented in Cokljat (1991).

3.4.3 Speziale's Non-linear $k - \varepsilon$ Model

Speziale (1987) demonstrated a special case of the complex non-linear eddy viscosity model obtained by Yoshizawa (1984), namely the non-linear $k - \epsilon$ (NLKE) model. The approach is based on the derivation of asymptotic expansions of the Reynolds stresses, which maintain terms that are quadratic in velocity gradients. Like the algebraic stress models (ASM), this model can account for the secondary flows in fully developed non-circular duct flow. The normal and cross Reynolds stresses are expressed as follows.

$$-\overline{w^2} = -\sqrt{k}l\frac{\partial W}{\partial z} - C_D l^2\left[\frac{1}{12}\left(\frac{\partial U}{\partial z}\right)^2 - \frac{1}{6}\left(\frac{\partial U}{\partial y}\right)^2\right] - C_E l^2 \frac{1}{3}\left[\left(\frac{\partial U}{\partial z}\right)^2 + \left(\frac{\partial U}{\partial y}\right)^2\right] \quad (3.16)$$

$$-\overline{v^2} = -\sqrt{k}l\frac{\partial V}{\partial y} - C_D l^2\left[\frac{1}{12}\left(\frac{\partial U}{\partial y}\right)^2 - \frac{1}{6}\left(\frac{\partial U}{\partial z}\right)^2\right] - C_E l^2 \frac{1}{3}\left[\left(\frac{\partial U}{\partial y}\right)^2 + \left(\frac{\partial U}{\partial z}\right)^2\right] \quad (3.17)$$

$$\overline{vw} = \overline{wv} = -\frac{1}{2}\sqrt{k}l\left(\frac{\partial V}{\partial z} + \frac{\partial W}{\partial y}\right) - \frac{1}{4}C_D l^2\left(\frac{\partial U}{\partial z}\right)\left(\frac{\partial U}{\partial y}\right) \quad (3.18)$$

where, $l = 2C_\mu k^{3/2}\epsilon^{-1}$ and $C_\mu = 0.09$. C_D and C_E are coefficients determined from experimental data. Both have been found to be 1.68 using duct flow data.

To evaluate the turbulent length scale l, k and ε equations as discussed in Section 3.3 are solved. Naot and Rodi (1982) suggested coefficients for Equations 3.6 and 3.7 as $(C_{\varepsilon 1}, C_{\varepsilon 2}, \sigma_k, \sigma_\varepsilon) = (1.44, 1.92, 1.225, 1.225)$.

3.5 Boundary Conditions

3.5.1 Inlet and Outlet Boundaries

In the present calculations, the fully developed values of U, k and ε are imposed at the inlet boundary. As the region is sufficiently long downstream it may be assumed that the flow is fully developed at the outlet which implies that the gradients of all of the variables are negligible, i.e.

$$\frac{\partial \phi}{\partial x} = 0, \qquad \phi = U_i, P, k, \varepsilon, \overline{u_i u_j}. \tag{3.19}$$

3.5.2 Free Surface Boundary

In the case of duct flow, symmetrical boundary conditions are applied at the axisymmetric planes, in which gradients of fluxes, k and ε are considered to be zero.

In the case of open channel flows, the secondary current near the free surface is directed away from the bank, which transfers the fluid with relatively low momentum towards the centre of the channel. The influence of the free surface on the turbulence can be explained in two ways:

- The presence of the free surface serves to damp turbulent fluctuations in the vertical direction. According to continuity therefore, fluctuations in the horizontal plane increases.
- The reduction of the length scale of turbulence due to the geometrical redistribution. This consequently, increases the dissipation of energy.

The effect of the free surface leads to a reduction in the eddy viscosity near the surface resulting in the parabolic distribution of eddy viscosity. Since, it is the difference in the normal stresses that drives the secondary motion, the redistribution effect of the free surface must be modelled correctly in order to obtain a realistic distribution.

In the present work, the formula proposed by Naot and Rodi (1982) is used to model the turbulent energy dissipation at the free surface, expressed as:

$$\varepsilon_s = \frac{C_\mu^{3/4}}{\kappa} k_s^{3/2} \left(\frac{1}{y'} + \frac{1}{0.07H} \right) \tag{3.20}$$

where κ is the von Karmen constant, H is the depth of water and y' is the distance from the side wall.

3.5.3 Wall Boundary

Near the wall, viscous effects become dominant and the local Reynolds number is very low, which makes turbulence models inadequate to apply. Moreover, there is a steep variations of properties near the wall, which needs a very refined grid to be resolved. To overcome both of these effects a special treatment, called *the law of the wall function* proposed by Launder and Spalding (1974) is adopted in which the boundary conditions are not specified right at the wall, but at the first grid point that lies outside the viscous sublayer in a region where the logarithmic law of the wall prevails and the turbulence is nearly in local equilibrium. Figure 3.2 shows the node arrangement at the bottom wall boundary in which T, P and B represent the top, the P and bottom nodes.

The log law is expressed as:

$$U^+ = \frac{U_r}{U_\tau} = \frac{1}{\kappa} (\ln E z^+) \tag{3.21}$$

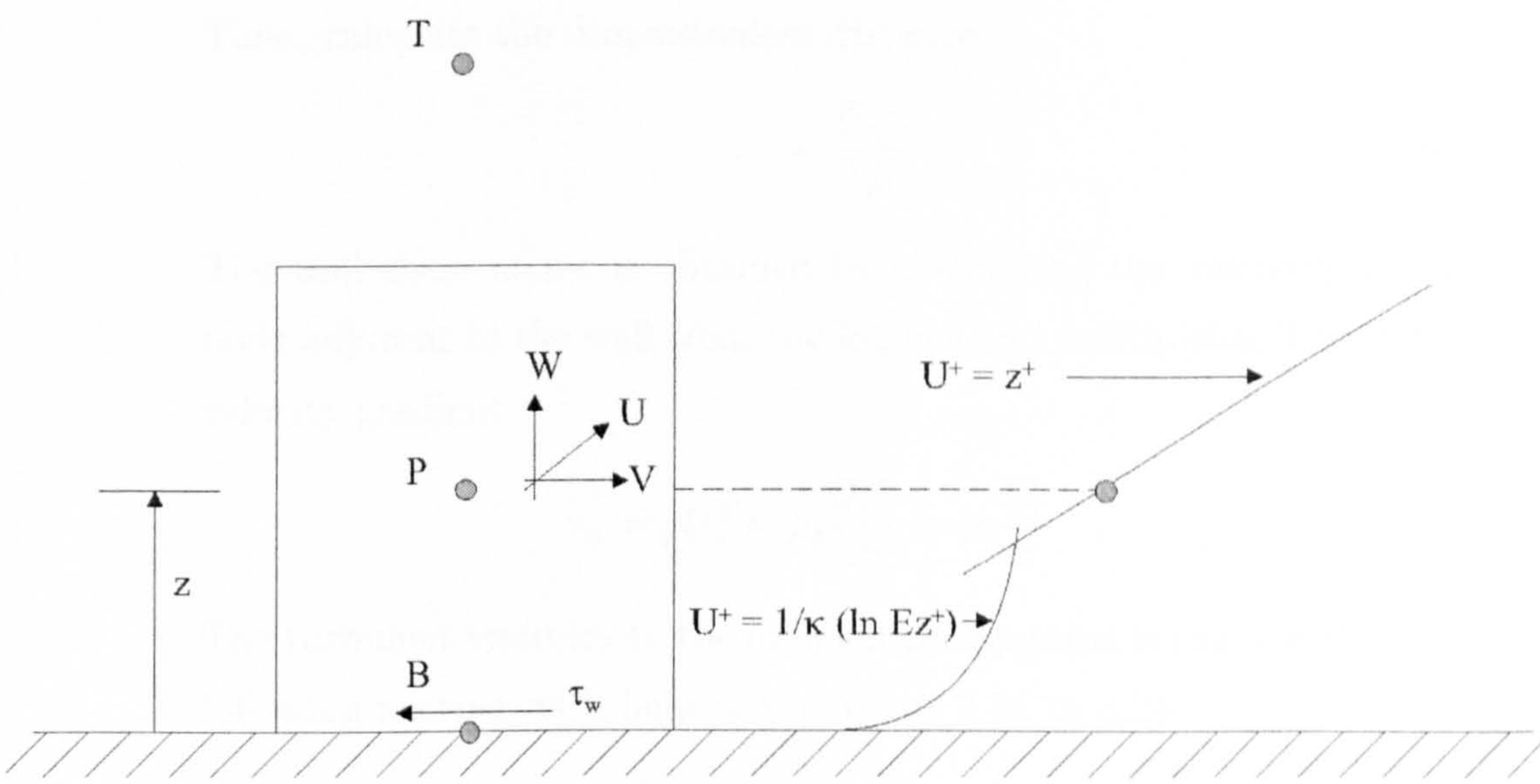

Figure 3.2: Illustration of the node arrangement at wall boundary on the cross sectional (y, z) plane. T, P, and B are the top, the first node from wall and the bottom node. U^+ and z^+ are the dimensionless velocity and the dimensionless distance of a first node from the wall. They are connected by the wall function as $U^+ = 1/\kappa(\ln Ez^+)$.

where U^+ is the dimensionless velocity, U_r is the resultant velocity, U_τ is the shear velocity, z^+ is the normalised distance defined as $z^+ = U_\tau z\rho/\mu$, E is the roughness parameter, which is taken 9.0 for smooth surfaces and $\kappa(=0.41)$ is the von Karmen constant.

This law is employed in following way:

- *For* $z^+ \geq 30.0$, *where* $\mu_t/\mu \gg 1, \tau \approx \tau_w$:

1. Incorporation of the log law into computer code is based on the concept of the turbulent viscosity (Peric (2004), Farhanieh and Davidson (1993)), which is calculated in following way. First, calculate the shear velocity based on an initial guess of k as:

$$U_\tau = C_\mu^{1/4}\sqrt{k}. \tag{3.22}$$

Then, calculate the dimensionless distance:

$$z^+ = \frac{U_\tau z \rho}{\mu}. \tag{3.23}$$

The wall shear stress is obtained by calculating the viscosity at the node adjacent to the wall from the log law and multiplying it with the velocity gradient.

$$\tau_w = \rho U_\tau^2 = \mu_t \frac{\partial U_r}{\partial z} \approx \mu_t \frac{U_r}{z} \quad . \tag{3.24}$$

The turbulent viscosity in the momentum equation is calculated in the following manner with help of Equations 3.21 to 3.24:

$$\mu_t = \rho U_\tau^2 \frac{z}{U_r} = \mu \left(\frac{\rho U_\tau z}{\mu}\right) \left(\frac{U_\tau}{U_r}\right) = \mu z^+ \frac{\kappa}{\ln(E z^+)} \quad . \tag{3.25}$$

2. We can also write the turbulent kinetic energy as:

$$k = \frac{U_\tau^2}{\sqrt{C_\mu}}. \tag{3.26}$$

3. The turbulent energy dissipation is:

$$\varepsilon = \frac{U_\tau^3}{\kappa z}. \tag{3.27}$$

- *For* $z^+ \leq 30.0$, *where* $\mu_t/\mu \ll 1, \tau \approx \tau_w$:
  Here, U_τ is obtained from

$$\frac{U_r}{U_\tau} = \frac{\rho U_\tau z}{\mu}, \tag{3.28}$$

which gives,

$$\tau_w = \rho U_\tau^2 = \mu \frac{U_r}{z}. \tag{3.29}$$

3.6 Concluding Remarks

In this chapter, equations describing the flow in open channels and boundary conditions are discussed, which can be summarized as follow:

- The 3D anisotropic, turbulent flow in open channels are modelled with RANS equations. The Reynolds averaging of Navier Stokes equations leads to additional source terms, which are known as Reynolds stresses. These terms are modelled isotropically (constant eddy viscosity concept) as well as anisotropically (LY, NR and nonlinear $k-\varepsilon$ models).

- The k and ε equations contain source terms, which are function of underlying variables. These makes the equations non-linear and very difficult to converge hence require linearisation.

- Anisotropic models of LY, NR and non-linear $k-\varepsilon$ provide the algebraic approximation (second order polynomial) of Reynolds stresses, each with different capabilities. NR model incorporates the wall and surface proximity functions while in non-linear $k-\varepsilon$ model quadratic longitudinal velocity gradients in vertical and transverse directions are used.

- The only difference between closed and open channel simulation is the boundary condition posed at free surface. In the closed channel symmetric boundary condition is applied while for the open channel free surface condition is used, which considers the reduction in turbulent length scale near free surface. The steep variation of velocity gradient is tackled by the law of wall function at first grid point from the wall. In this research, the normalised distance (y^+) is taken equal to 9.0.

CHAPTER 4

Numerical Implementation

4.1 Introduction

The set of governing equations discussed in Chapter 3 are parabolic in type and non-linear in nature (Patankar and Spalding (1972)). Hence, an exact solution of these equations, which can give the distribution of dependent variables in the domain of interest is not possible. These equations can be solved with help of numerical techniques.

In this research, the computer model developed by Lilek *et al.* (1995) is adopted as a starting point. The model was created to simulate the 3D lid-driven cavity flow and offered following advantages:

- The governing equations comprised of 3D Navier-Stokes equations and the continuity equation, which can be easily modified to 3D Reynolds-Averaged Navier-Stokes equations for compound meandering channel flows.

- The discretization schemes used such as upwinding scheme for convection terms and central differencing scheme for diffusion terms can also be adopted for turbulent flow computations (Peric *et al.* (1989)).

- In terms of computing, arrays were created with 1D indexing instead of 3D indexing, which makes computations faster and parallel computing possible.
- Multigrid convergence accelerator is used for faster and efficient computations.

In this chapter, the discretization of the governing equations with the finite volume method (FVM), the pressure velocity coupling algorithm, the formulation of a set of algebraic equations and the iterative solutions of those equations is discussed.

4.2 Finite Volume Formulation

The governing equations, described in previous section are discretized using the FVM, which is based on the principal of the conservation of properties across the control volume (CV) (Ferziger and Perić (1995),Versteeg and Malalasekera (1995),Patankar (1980)). All the governing equations, discussed in Chapter 3, can be expressed in a general form as

$$\frac{\partial(\rho U\phi)}{\partial x}+\frac{\partial(\rho V\phi)}{\partial y}+\frac{\partial(\rho W\phi)}{\partial z}=\frac{\partial}{\partial x}\left(\Gamma_\phi\frac{\partial\phi}{\partial x}\right)+\frac{\partial}{\partial y}\left(\Gamma_\phi\frac{\partial\phi}{\partial y}\right)+\frac{\partial}{\partial z}\left(\Gamma_\phi\frac{\partial\phi}{\partial z}\right)+S_\phi. \tag{4.1}$$

In Equation 4.1, ϕ is the conserved quantity, U, V and W are the mean velocities in x, y and z directions respectively, ρ is the fluid density and Γ is the generalized diffusivity. The terms on the left hand side of the equation represent the convective fluxes, on the right hand side first three terms represent the fluxes

due to diffusion and the last term is source term. Equation 4.1 is integrated over the 3D CV, shown in Figure 4.1.

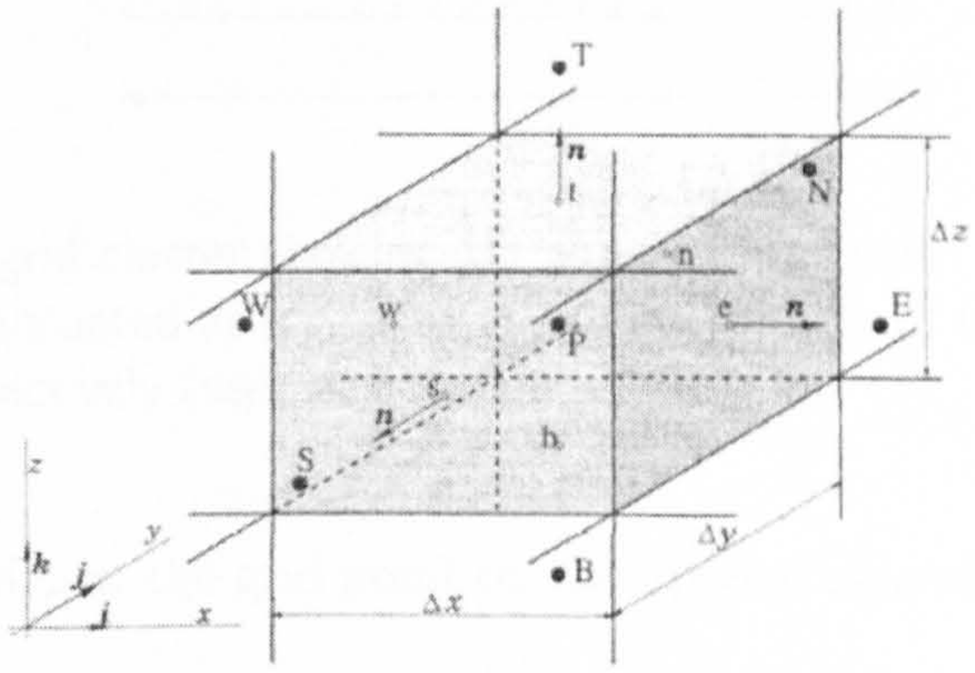

Figure 4.1: Illustration of a 3D Cartesian CV showing different faces like north(n), south(s), east(e), west(w), top(t), bottom(b) and CV center(P). Δx, Δy and Δz are dimensions of the CV in x, y and z directions respectively.

The CV surface consists of 6 plane faces denoted by lower case letters corresponding to their direction i.e. east (e), west (w), north (n), south (s), top (t) and bottom (b) with respect to the central node P. In following section, the discretization of convective and diffusive fluxes and the linearisation of the source term are described.

4.3 Approximation of Fluxes

4.3.1 Convective Fluxes

The convective terms are discretized using an *upwind differencing scheme* (UDS). Consider Figure 4.2, which shows the node arrangement in the x direction, for example.

To evaluate the net convective fluxes through a CV it is necessary to find out the properties at the CV faces. In UDS, the value of of ϕ at an interface is set

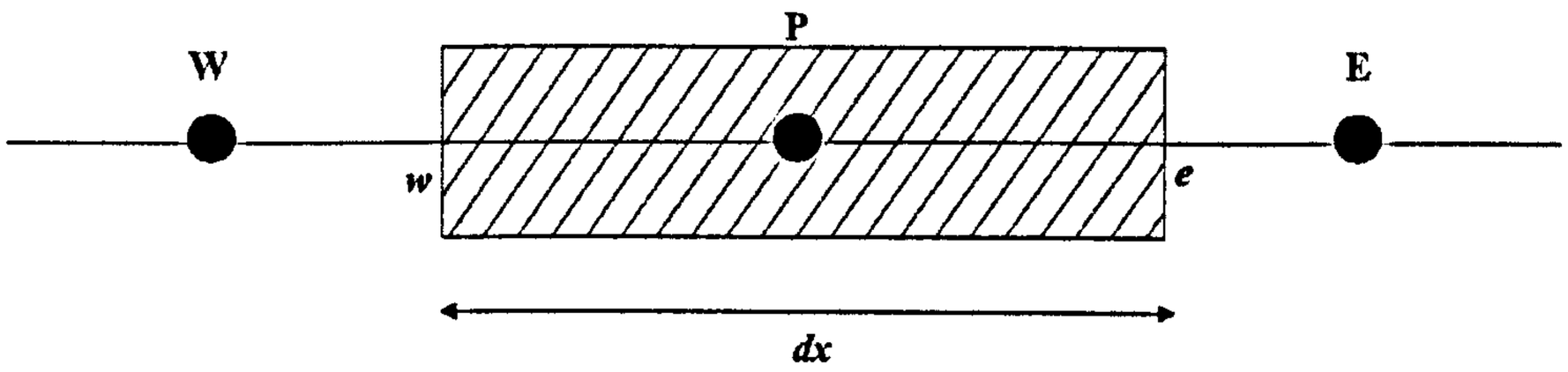

Figure 4.2: Typical grid cluster showing 1D node arrangement. The convective and diffusive fluxes are evaluated at CV faces w and e with help of UDS and CDS differencing schemes respectively (see Section 4.3).

equal to the value of ϕ at the grid point on the upwind side of the face depending on the flow direction.

So, the value of conserved property at east face ϕ_e is approximated with help of upwind difference scheme as:

$$\phi_e = \phi_P \qquad \text{if} \qquad (\rho U) > 0 \tag{4.2}$$

and

$$\phi_e = \phi_E \qquad \text{if} \qquad (\rho U) < 0 \tag{4.3}$$

The approximation of mass flux, $(\rho U = \dot{m})$, at the CV faces is given by:

$$(\dot{m}\phi)_e = \max(\dot{m}_e, 0.)\phi_P + \min(\dot{m}_e, 0.)\phi_E, \tag{4.4}$$

and

$$(\dot{m}\phi)_w = \max(\dot{m}_w, 0.)\phi_W + \min(\dot{m}_w, 0.)\phi_P. \tag{4.5}$$

Expressions for convective fluxes at the north, south, top and bottom faces can be derived in the same manner.

4.3.2 Diffusive Fluxes

To evaluate the diffusive terms, a *central differencing scheme* (CDS) has been adopted to approximate the value at the CV face centre. The scheme is a straightforward approximation and is based on linear interpolation between the two nearest nodes.

With the help of CDS, ϕ at east face of the CV (Figure 4.2) can be obtained as

$$\phi_e = \phi_E \lambda_e + \phi_P(1 - \lambda_e), \tag{4.6}$$

where, the linear interpolation factor λ_e , is defined as

$$\lambda_e = \frac{x_e - x_P}{x_E - x_P}. \tag{4.7}$$

The above derivation is based on the Taylor series expansion of the gradient $\frac{\partial \phi}{\partial x}$, which is second order accurate. The assumption of a linear profile between the P and E nodes also offers the simplest approximation of the gradient, which is needed for the evaluation of diffusive fluxes, so that:

$$\Gamma_w \left(\frac{\partial \phi}{\partial x}\right)_w = \Gamma_w \left(\frac{\phi_P - \phi_W}{x_P - x_W}\right)_w = D_w(\phi_P - \phi_W) \tag{4.8}$$

and

$$\Gamma_e \left(\frac{\partial \phi}{\partial x}\right)_e = \Gamma_e \left(\frac{\phi_P - \phi_E}{x_P - x_E}\right)_e = D_e(\phi_P - \phi_E) \tag{4.9}$$

In above equations, $D_e = (\Gamma_e / x_P - x_E)$ and $D_w = (\Gamma_w / x_P - x_W)$ are the diffusion coefficients. We can simplify the rest of the diffusive terms in a similar way.

4.4 The Discretized Equation and It's Solution

After inserting the convective and diffusive approximations into Equation 4.1 and on simplifying further, we find a discretized algebraic equation in following form:

$$a_P \phi_P = a_E \phi_E + a_W \phi_W + a_N \phi_N + a_S \phi_S + a_T \phi_T + a_B \phi_B + S_\phi \Delta x \Delta y \Delta z, \tag{4.10}$$

where,

$$a_E = (D_e + \max(\dot{m}_e, 0.))\Delta y \Delta z \tag{4.11}$$

$$a_W = (D_w + \min(\dot{m}_w, 0.))\Delta y \Delta z \tag{4.12}$$

$$a_N = (D_n + \max(\dot{m}_n, 0.))\Delta x \Delta z \tag{4.13}$$

$$a_S = (D_s + \min(\dot{m}_s, 0.))\Delta x \Delta z \tag{4.14}$$

$$a_T = (D_t + \max(\dot{m}_t, 0.))\Delta x \Delta y \tag{4.15}$$

$$a_B = (D_b + \min(\dot{m}_b, 0.))\Delta x \Delta y \tag{4.16}$$

$$a_P = a_E + a_W + a_N + a_S + a_T + a_B. \tag{4.17}$$

After evaluating the above coefficients and linearizing the source terms, the discretized equation for each variable attains the following form

$$A_P^\phi \phi_P + \sum_l A_l^\phi \phi_l = S_P^\phi \tag{4.18}$$

where P denotes the node at which the partial differential equation is approximated and index l represents the neighboring nodes. The coefficients A_l depend on the fluid properties and geometric quantities. S_P^ϕ contains all the terms which do not contain unknown variables values and its presumed to be known.

The system of equation can be written in the form of matrix notation as

$$A\phi = Q, \tag{4.19}$$

where A is a square coefficient matrix, ϕ is a vector or column matrix containing the variable values at the grid nodes and Q is the vector containing the terms on the right hand side or the known values.

In the present research, the system of equations has been solved with the strongly implicit method (SIP) (Ferziger and Perić (1995)).

4.5 Source Term Linearisation

- *Source term of k equation:* In the k equation (Section 3.3), the source term is expressed as $P_k - \rho\varepsilon$, which is a function of one of the dependent variables ε and hence make the source term nonlinear. Linearisation of the source term is achieved by adding P_k to S_ϕ and $\rho\varepsilon$ to a_p of Equation 4.10 in following way

$$S_\phi = S_\phi + P_k$$

and

$$a_p = a_p + \rho\varepsilon/k.$$

- *Source term of ε equation:* The ε equation source term is expressed as $\frac{\varepsilon}{k}(c_{\varepsilon 1}P_k - c_{\varepsilon 2}\rho\varepsilon)$. This term is also highly non-linear in nature. As with the k equation linearization is achieved as follows:

$$S_\phi = S_\phi + \frac{\varepsilon}{k}(c_{\varepsilon 1}P_k)$$

and

$$a_p = a_p + \frac{\varepsilon}{k}(c_{\varepsilon 2}\rho).$$

- *Source terms due to Reynolds stresses:* The Reynolds stresses, which appear in the V and W momentum equations, are calculated from the LY model implicitly. The gradients of these Reynolds stresses are coupled to momentum equations by adding them to source the term, in the following way:

$$S_V = S_V - \frac{\partial}{\partial y}(\rho\overline{vv}) - \frac{\partial}{\partial z}(\rho\overline{vw})$$

$$S_W = S_W - \frac{\partial}{\partial y}(\rho\overline{vw}) - \frac{\partial}{\partial z}(\rho\overline{ww}).$$

These gradients of the Reynolds stresses are added to the source terms from node 3 instead of node 2. Here, node 2 represent a first node from the wall boundary. At node 2, the Reynolds stresses are calculated isotropically in the form of turbulent viscosity, obtained from the log law as explained in Section 3.5.3.

4.6 Pressure Velocity Coupling

4.6.1 SIMPLE Algorithm

For the RANS equations there is no direct method of specifying an equation for pressure. Instead, pressure is determined indirectly using the continuity equation. If the correct pressure field is used to solve the momentum equations then the continuity equation will also be satisfied. In the present research, the Semi-Implicit Method for Pressure-Linked Equations (SIMPLE) of Patankar and Spalding (1972) is used to handle the pressure-velocity coupling.

The steps involved in the SIMPLE algorithm can be summarized as follows:

1. Initially a pressure field is guessed, P^*, which is used in the discretized momentum equations to find the guessed velocity field.

2. An equation is solved for the pressure correction, P', which gives the pressure difference between the guessed pressure and the pressure necessary to satisfy the continuity condition.

3. The pressure and velocity fields are then updated based on the pressure correction (with some under-relaxation).

4. Other scalar transport equations are solved (e.g. k and ε) and eddy viscosity is updated.

5. Steps $1-4$ are repeated (using the pressure field from the previous step as the initial guess) until the calculation has converged.

The complete simulation model is shown in Figure 4.3.

4.6.2 Under-Relaxation

Under-relaxation is a means of slowing down the updating process of the variables and is necessary for convergence of coupled non-linear equations. Variables are updated in the following manner:

1. Model Construction & Parameter Input

- Construct FV grid (Cartesian or orthogonal) based on the hydraulic conditions
- Read input details: Convergence parameters, under-relaxation factors, No. of iterations, fluid properties, boundary conditions, turbulence model to be used and other details
- Read coordinates of the FV grid from input grid file
- Calculate the scale factors for meandering channel simulations

↓

2. Computation

1. Initialise the computational domain
2. With initial guessed pressure solve pressure correction equations to obtain approximate solution of velocity components
3. Update pressure and velocities with some under-relaxation
4. Solve k and ε equations; update eddy viscosity
5. Calculate the Reynolds stresses with either LY, NR or NLKE model
6. If convergence is achieved then stop else go back to step 1

↓

3. Analysis of Results

- Write variables values of converged solution in separate file for analysis

Figure 4.3: Flowchart explaining the model construction, computational algorithm and post processing. The *computation* part is based on the SIMPLE algorithm for pressure velocity coupling proposed by Patankar (1980).

$$\phi_P^{new} = \alpha\phi_P^{calc} + (1-\alpha)\phi_P^{old} \tag{4.20}$$

where ϕ_P^{old} is the value of ϕ from the previous iteration and ϕ_P^{calc} is the result of the current calculation. Applying the above formula to the discretized transport Equation 4.10 gives:

$$\frac{a_P}{\alpha}\phi_P^{new} = \sum a_{nb}\phi_{nb} + S_P^{\phi} + (1-\alpha)\frac{a_P}{\alpha}\phi_P^{old}. \tag{4.21}$$

In practice, under-relaxation involves the modification of the coefficient a_P and source S_ϕ:

$$(a_P)_{new} = \frac{a_P}{\alpha} \tag{4.22}$$

$$(S_\phi)_{new} = S + (1-\alpha)(a_P)_{new}\phi_P^{old} \tag{4.23}$$

Its effect, therefore, is to increase the diagonal dominance of the coefficient matrix and add in a source term. Since the pressure is updated by means of a pressure correction, its under-relaxation takes the form:

$$P_P^{new} = P_P^{*} + \alpha P_P' \tag{4.24}$$

where P' is the pressure correction.

If the under-relaxation factor, α, in the above equations is set to unity there is no under-relaxation and the new value is equivalent to the calculated value. Typical values for the under-relaxation factors used in the case of straight rectangular and compound channel are 0.7 for U and 0.4 for P.

4.7 Numerical Grid

The numerical solution of partial differential equations requires discretization of the computational domain into a collection of points or elemental volumes

(cells). This discretion or sub-division of a domain into a number of smaller, non-overlapping sub-domains is known as numerical grid or mesh generation.

Numerical grids can be categorised into structured (regular) grids, block structured grids and unstructured grids depending on the shape of the domain and the elemental volumes. Based on the discrete locations at which the variables are to be calculated, the grid can further be classified as a staggered grid and non-staggered or collocated grid.

4.7.1 Staggered Grid

In a Cartesian coordinate system, Harlow and Welsh (1965) introduced a staggered grid arrangement. This arrangement for a 2D grid is shown in Figure 4.4 (a). In the staggered grid, the velocity components are calculated for the points that lie on the faces of control volumes while the scalar quantities are being evaluated at the control volume centre.

From Figure 4.4 (a) it can be seen that both pressure and diffusive terms, which are stored at a control volume centre, are easily approximated without interpolation by central difference approximations. The velocity components required to evaluate diffusive terms are readily computed at the control volume faces. Most importantly, the evaluation of mass fluxes in the continuity equation on the faces of a pressure CV is also straightforward.

The biggest advantage of staggered grids is the strong coupling of pressure and velocity components. This coupling helps to overcome the problem of convergence and oscillation in the pressure and velocity fields.

Despite the fact that it is easy to handle pressure-velocity coupling, the staggered approach can be used only in generalised coordinate systems, when other grid oriented components of vectors and tensors are the working variables. The curvature effect is difficult to treat as the curvature terms are difficult to treat numerically and may create non-conservative errors when the grid is not smooth. It is also difficult to implement the multigrid procedure with a staggered grid

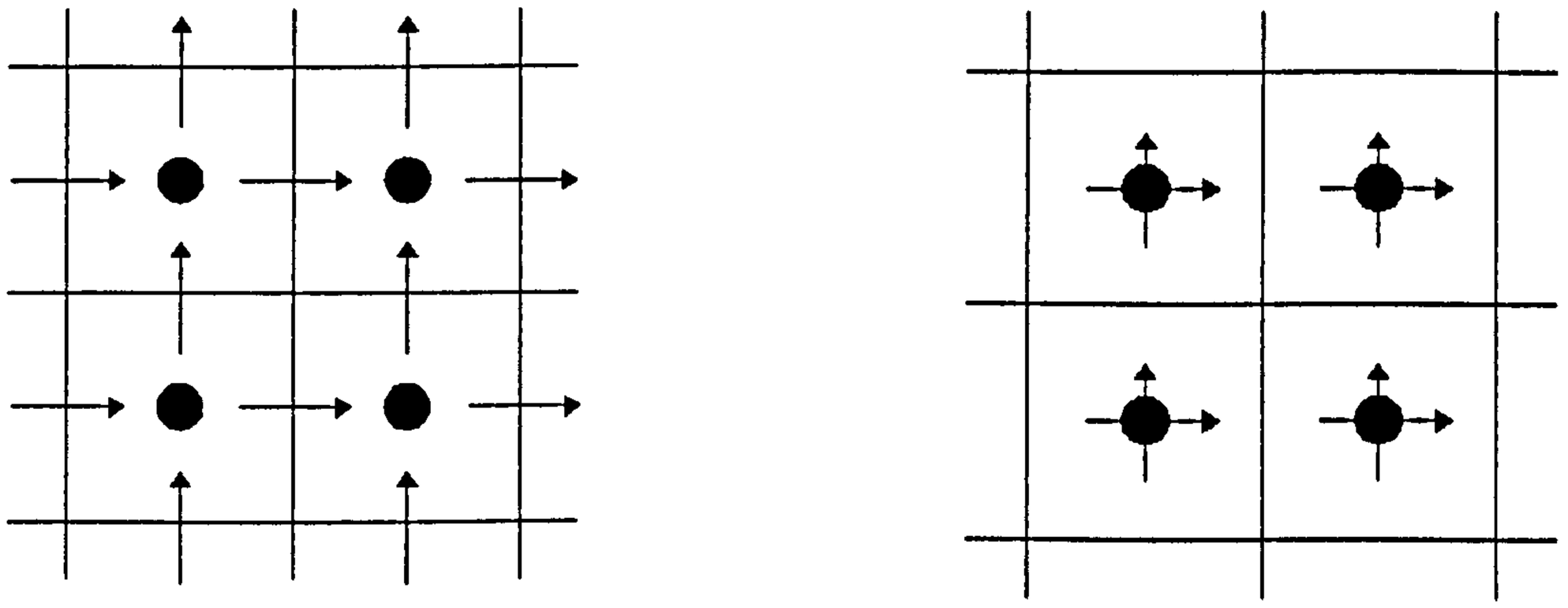

(a) (b)

Figure 4.4: (a) Staggered Grid arrangements; (b) Collocated Grid arrangements. Here, → and • represent storage locations of velocity components and pressure respectively. In the staggered grid pressure is computed at CV faces and velocities at CV centre. For collocated grids, both pressure and velocities are calculated at CV centre which makes the transfer of residuals (in multigrids) and the handling of grid discontinuity (e.g. meander channels) easier.

arrangement. These problems are very well tackled with the collocated grid approach.

4.7.2 Collocated Grid

In the collocated grid arrangement, all the variables are stored at the same grid point of the same control volume as shown in Figure 4.4(b). In a collocated grid, the number of coefficients, which are generated after discretization and must be computed and stored are minimised and the programming is simplified. The significant advantage of collocated grid is its compatibility with the multigrid method. When multigrid procedures are used to accelerate convergence, the same restriction and prolongation operators for transfer of information between the various grids can be used for all variables.

Furthermore, when the solution domain is complicated and the boundaries

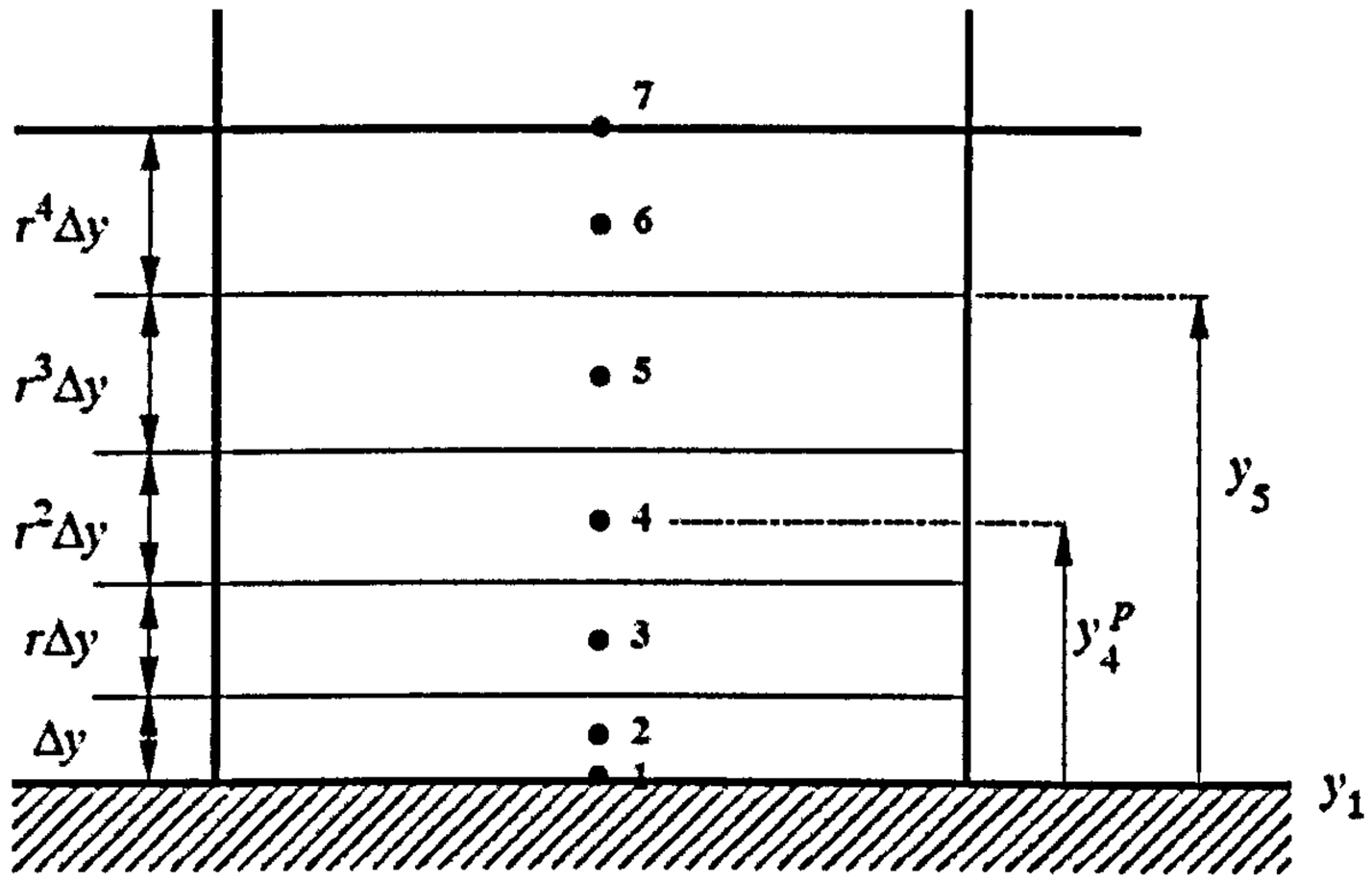

Figure 4.5: 2D Cartesian mesh showing node numbers and cell widths. The expansion of a mesh follows a geometric series expansion, which helps to generate a refined grid near the walls where variable gradients are steep.

have slope discontinuities, or the boundary conditions are discontinuous, the collocated grid proves very advantageous. A set of control volumes can be designed to fit the boundary, including the discontinuity.

The major drawback of the collocated grid arrangement is pressure-velocity coupling. However, this can be tackled by use of the improved pressure-velocity coupling algorithm, which is discussed in Section 4.6

4.7.3 Grid Generation

For rectangular and compound straight channels, governing equations are solved on cartesian grid whilst for meandering channels orthogonal grids are used. In this section, the generation of cartesian and body-fitted orthogonal grids are discussed.

4.7.3.1 Cartesian Grids

The governing equations described in Chapters 3 and 5 are solved over an algebraically generated grid for the entire domain of interest. In order to obtain sufficient resolution of the dependent variables, it is necessary to use a refined grid in the vicinity of the wall. A schematic diagram of a simple 2D Cartesian grid is given in Figure 4.5, which represents the non-uniform arrangement of computational nodes. The locations of the bottom and top of the grid (locations y_1 and y_7) are already defined. Between nodes $i = 1$ to $i = 7$, the grid is expanded with a given ratio, r, according to

$$\Delta y_i = r\Delta y_{i-1}$$

where Δy_i is the cell width for node i. The distance between the first and last boundary locations consists of the sum of the control volume widths:

$$\begin{aligned} y_n - y_1 &= \Delta y + r\Delta y + r^2\Delta y + \ldots + r^{(n-3)}\Delta y \\ &= \sum_{m=0}^{n-3} r^m \Delta y \end{aligned}$$

where n is the number of nodes, in this case $n = 7$. The width of the smallest control volume ($\Delta = y_2 - y_1$) is then given by:

$$\Delta y = \frac{y_n - y_1}{\sum_{m=0}^{n-3} r^m}.$$

The position of the cell faces then can be calculated in recursive fashion as

$$y_m = y_{m-1} + r^{(m-2)}\Delta y \quad \text{for } m = 2, 3, 4, \ldots (n-2). \tag{4.25}$$

The coordinates of the CV centered nodes can be calculated from the coordinates of the CV faces in the following way:

$$y_m^p = \frac{y_m + y_{m-1}}{2} \quad \text{for } m = 2, 3, 4, \ldots (n-2).$$

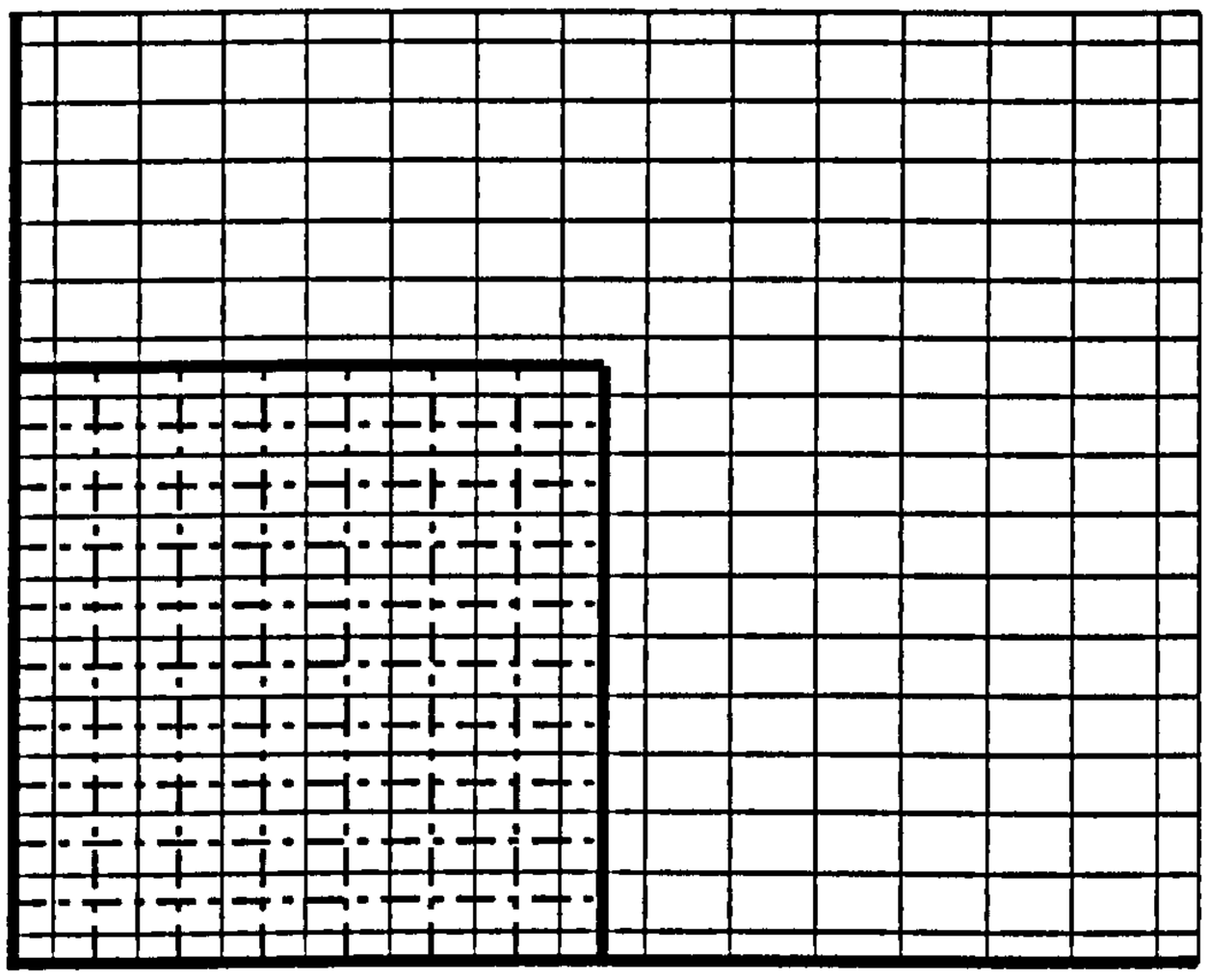

Figure 4.6: Typical sketch of a 2D Cartesian mesh for compound channel geometry. In the highlighted bottom left corner, computational arrays are "*blocked-off*", which represents the solid wall. During computations, the source term and the variables are set to zero, while the term a_P is set equal to one (see Section 4.7.3.2).

4.7.3.2 Grids for Compound Channels

In the present research, the computer program as written for a regular Cartesian grid is modified to handle compound channel domains. This is done by "blocking-off" some of the control volumes of the regular grid so that the remaining active control volumes form the desired irregular domain. Figure 4.6 shows a grid for a compound channel where the highlighted area (bottom left) represent the inactive control volumes.

As such, the inactive region represents the stationary solid boundary, the velocity components in that region are set equal to zero. The desired values in the inactive region are set, with help of the Equation 4.18 in following way:

1. Set all neighbouring coefficients equal to zero, i.e. $\sum_l A_l^\phi = 0$.

2. Impose $A_P^\phi = 1$.

3. Fix S_P^ϕ equal to the desired value, which is zero.

Finally, the wall boundary condition is imposed to the cells next to the blocked-off cells. The method of applying the boundary condition (the log law) to these cells is same as discussed in Section 3.5.3.

4.7.3.3 Orthogonal Grids

In the case of meandering channels, the successful numerical calculation of the solution to a set of partial differential equations is strongly dependent on the quality of grid especially the grid orthogonality. Extensive literature is available on 2D orthogonal grid generators (Eca (1996), Thompson *et al.* (1985)). In the present research, the algorithm proposed by Akcelik *et al.* (2001) has been adopted to generate 2D orthogonal grids for compound channel domains. This also uses a forcing function to control grid aspect ratio.

The 2D orthogonal grid generation system is based on following system of equations:

$$\frac{\partial}{\partial \xi}\left(f\frac{\partial x}{\partial \xi}\right)+\frac{\partial}{\partial \eta}\left(f\frac{\partial x}{\partial \eta}\right)+P_x(h_\xi)+Q_x(h_\eta)=0, \tag{4.26}$$

$$\frac{\partial}{\partial \xi}\left(f\frac{\partial y}{\partial \xi}\right)+\frac{\partial}{\partial \eta}\left(f\frac{\partial y}{\partial \eta}\right)+P_y(h_\xi)+Q_y(h_\eta)=0. \tag{4.27}$$

where x and y are coordinates in the physical space while ξ and η are orthogonal curvilinear coordinates. In above equations, $f(x(\xi,\eta),y(\xi,\eta))$ is the distortion function, which is defined as the ratio of the scale factor in the η-direction to that in the ξ-direction, i.e.

$$f=\frac{h_\eta}{h_\xi}, \tag{4.28}$$

where the scale factors h_ξ and h_η are defined by:

$$h_\eta=\sqrt{\left(\frac{\partial x}{\partial \eta}\right)^2+\left(\frac{\partial y}{\partial \eta}\right)^2} \tag{4.29}$$

$$h_\xi = \sqrt{\left(\frac{\partial x}{\partial \xi}\right)^2 + \left(\frac{\partial y}{\partial \xi}\right)^2}. \tag{4.30}$$

Formulas to evaluate the distortion function, f, are given in Eca (1996). In Equations 4.26 and 4.27, $P(h_\xi)$ and $Q(h_\eta)$ are inhomogeneous source terms that alter the solution (x, y) in such a way as to control the scale factors h_ξ and h_η favorably, and hence the aspect ratio of the resulting grid. Evaluations of these source terms are described in Akcelik *et al.* (2001).

Because the presented system of Equations 4.26 and 4.27 is nonlinear, an iterative algorithm is used to solve it numerically:

1. Choose four corner points of the physical domain that serve as the corner points of the grid in computational domain. Calculate x and y values of the other boundary grid points by dividing physical boundaries into equal segments.

2. Determine an initial approximation for the interior grid points by bilinear interpolation (see Figure 4.7 (a)).

3. Calculate distortion function, f, from Equation 4.28.

4. Solve the system of Equations 4.26 and 4.27 with fixed f values calculated in Step 3 using SOR iterative method. Calculate source terms P and Q in following way (Akcelik *et al.* (2001)):

$$P(h_\xi) = c\left(h_\xi - \frac{\bar{h}_\xi^2}{h_\xi}\right), \tag{4.31}$$

$$Q(h_\eta) = c\left(h_\eta - \frac{\bar{h}_\eta^2}{h_\eta}\right), \tag{4.32}$$

where c is a force constant and $\bar{h}_\xi$ and $\bar{h}_\eta$ are mean scale factors. By changing the magnitude of force constant, it is possible to change the intensities of P and Q. The functions P and Q act like distributed forces proportional to the deviation of the local scale factors from the mean scale factors.

5. Adjust boundary conditions; if Dirichlet boundaries are applied nothing is done, if sliding boundaries are applied (Neumann-Dirichlet), relocate boundary nodes to satisfy orthogonality.

6. If convergence criteria on orthogonality are not satisfied, return to step 3. The orthogonality condition is expressed by Equation 5.16 and discussed in detail in Section 5.2.3.

The results obtained after implementing the algorithm, are shown in Figure 4.7. The computation starts with the initial grid approximation shown in Figure 4.7 (a). In the absence of pseudo forcing functions $P(h_\xi)$ and $Q(h_\eta)$, several grid lines tends to collapse onto each other at the curved boundary which may cause convergence problems. This result is shown in Figure 4.7 (b). However, the introduction of pseudo-force prevents the grid lines collapsing and imposes some control on grid spacing which is represented in Figure 4.7 (c) and (d) for forcing function values of 0.001 and 0.2 respectively.

This algorithm was applied to create orthogonal grids for compound meandering channels with three different values of sinuosity; 1.093, 1.370 and 1.570. For each of this case the forcing function values used are 0.15, 0.2 and 0.25 respectively. Figure 4.8 shows the orthogonal grids for one bank with different sinuosities. In all grids, boundary conditions are fixed at all boundaries except at the bottom where a sliding boundary condition is specified.

4.8 Concluding Remarks

In this chapter, the finite volume discretization of a generalised governing equation, handling the non-linearity of governing equations as well as source terms and different type of numerical grid generation are discussed. The discussion can be summarised as follows:

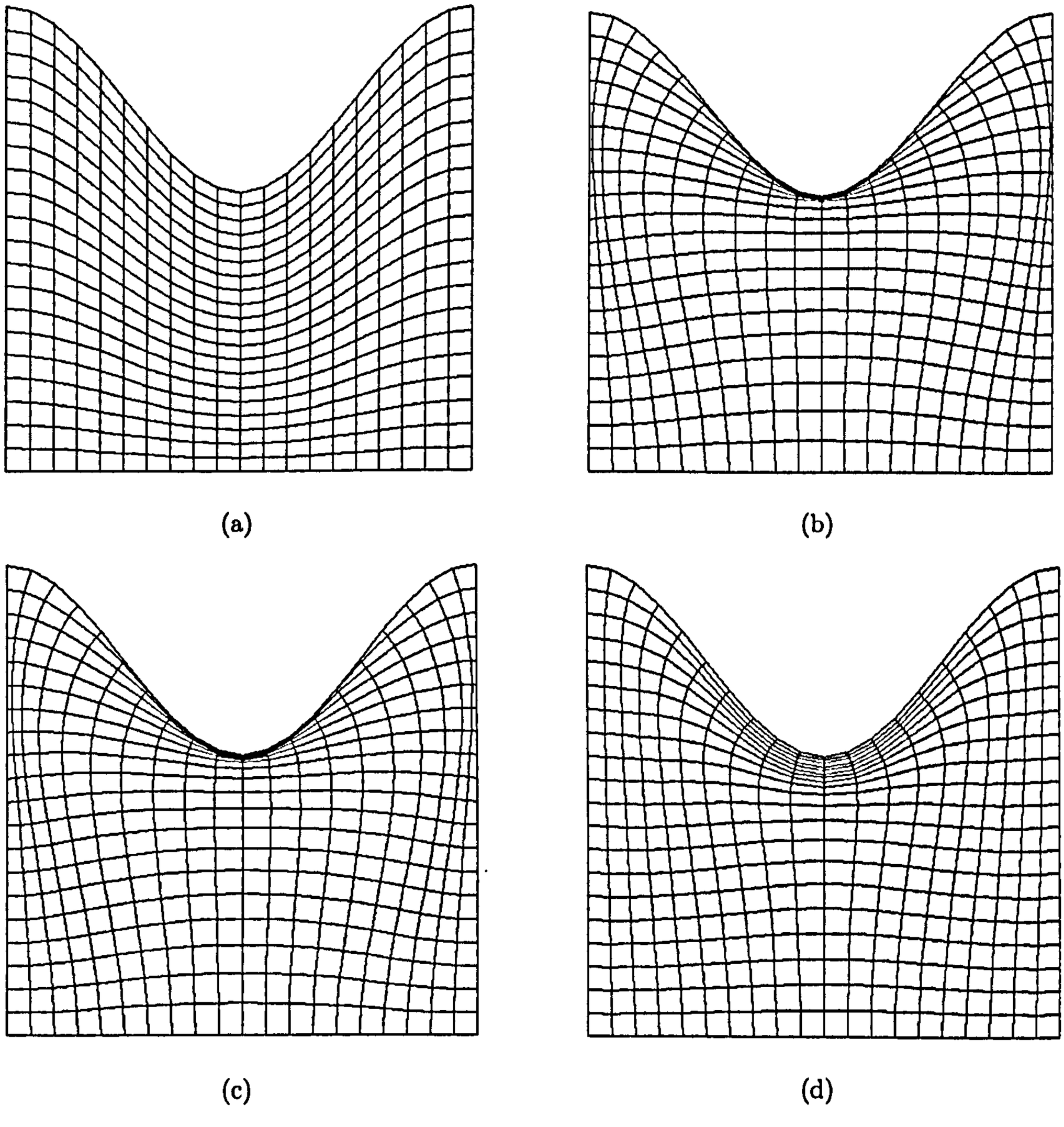

Figure 4.7: Illustration of initial and orthogonal grids for the domain (24×24) limited by $x = 0$, $x = 1$, $y = 1$ and $y = 0.85 + 0.15\cos(\pi x)$. Grid (a) represents the initial approximation of the grid. Force constants are 0 in grid (b) 0.001 in grid (c) and 0.2 in grid (d). Boundary conditions are specified or fixed at all boundaries.

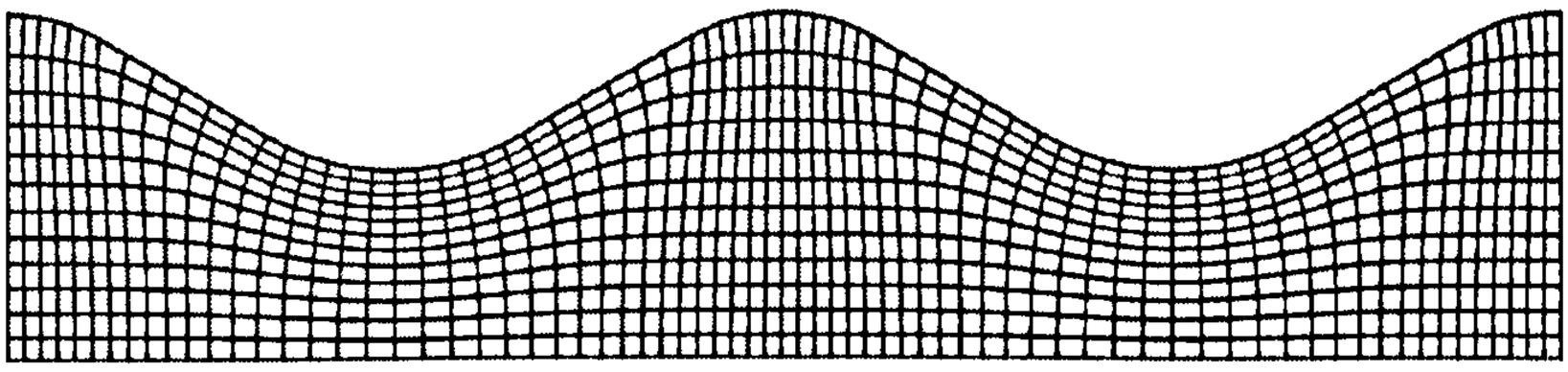

(a)

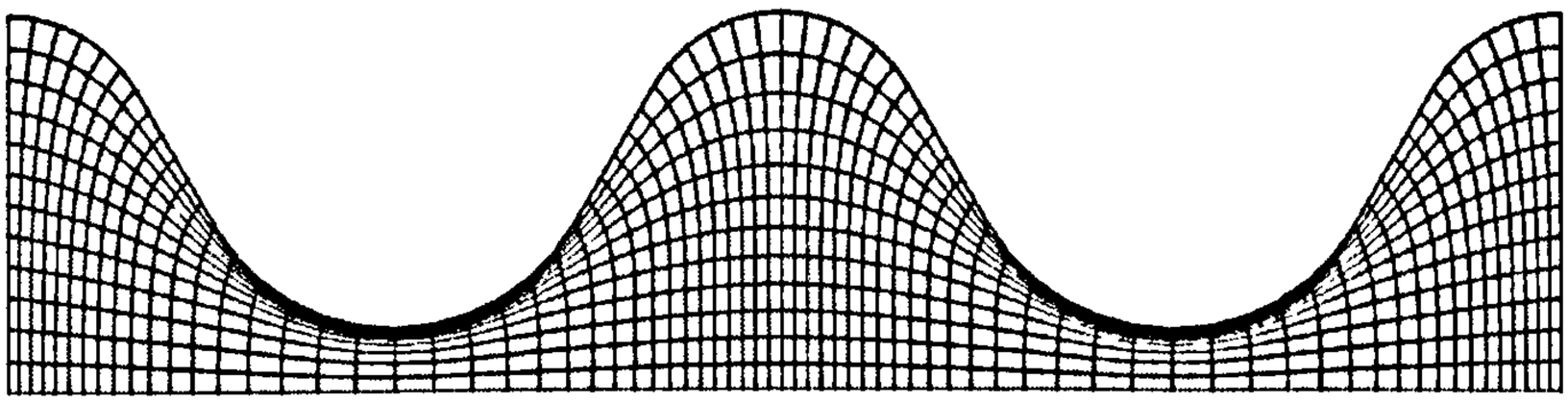

(b)

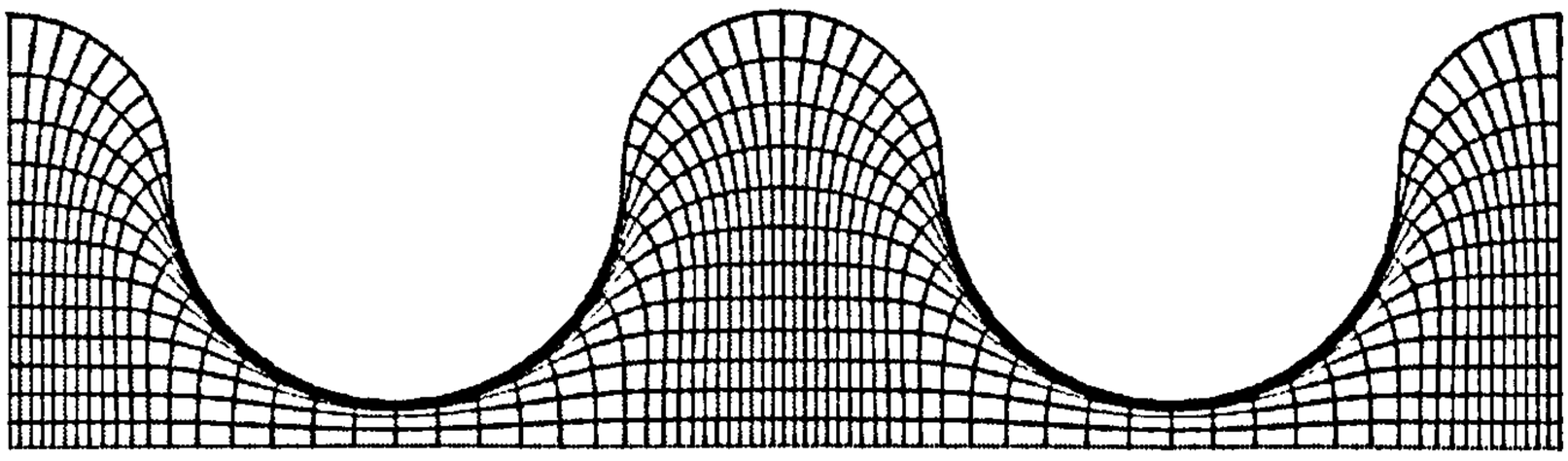

(c)

Figure 4.8: Orthogonal grids for different geometries: (a) sinuosity = 1.093 (b) sinuosity = 1.370 and (c) sinuosity = 1.570. These grids represent one part of the complete overbank grid, which is shown in Section 6.4. It can be seen that by increasing the curvature, the grid lines tends to bulge near the curved boundary.

- The finite volume formulation with the help of UDS for convective terms and CDS for diffusive terms leads to a set of algebraic equations which are solved using SIP solver.

- The numerical solution becomes stable and converges if source terms are linearised. The SIMPLE algorithm with predetermined under-relaxation factor is used to couple the pressure and velocity, which are updated in each inner iteration while in outer iteration solution of all governing equations is updated.

- The geometric expansion of a cartesian grid gives better control on grid refinement wherever it is desired. Implemented algorithm for orthogonal grid generation works well for different sinuosities. The forcing function gives better command over the grid aspect ratio. However, as sinuosity increases the orthogonal grid lines start to bulg near the curvature peak.

CHAPTER 5

Body-fitted Coordinate System for Meandering Channel Simulations

5.1 Introduction

For 3D flows involving complex geometries, it is desirable to employ a numerical technique in such a way that the flow in the wall layer can be accurately resolved with a reasonable number of grid points. Where the shape of the physical domain and the numerical grid is complex, such as a meandering channel, boundary conditions must be described precisely. The boundary-fitted curvilinear coordinate technique has been developed to meet these requirements (Thompson *et al.* (1985)). This technique transforms the coordinates in the physical plane to coordinates in a computational plane, which helps to specify the boundary conditions with sufficient accuracy.

Once such a coordinate system is selected for a given geometry, the equation of motion must be formulated in that system. One option is to transform the equations completely, including the independent and the dependent variables. In

this case, the use of *contra-variant* velocity components, which follow the grid lines, allows a much more accurate resolution of the boundary-layer flow near a solid surface.

However, the fully-transformed equations involve many geometric coefficients and their higher-order derivatives, which increases the computational time and complicates the programming. Sometimes the arrangement of variables on the grid affects the accuracy and efficiency of the numerical algorithm.

Despite these disadvantages, as already discussed in Section 2.4.4, the body-fitted coordinate system is one of the most popular techniques for simulation of meander channel flows (Wormleaton and Ewunetu (2006), Shao *et al.* (2003), Sugiyama and Saito (2002), Ye and McCorquodale (1998)) due to the ease of handling complicated geometries. In this study also, a body-fitted grid is considered for simulation purposes.

This chapter focuses on the basic methodology involved in coordinate transformation from the physical plane to the computational plane, transformation parameters and their evaluations. The governing equations are subsequently converted from cartesian to orthogonal coordinates. The numerical implementation of the converted equations for simulations of meandering channel flows are discussed briefly at the end.

5.2 Method of Coordinate Transformation

The use of a generalised coordinate system, as explained by Fletcher (1989), comprises the following steps:

1. A distorted or complicated physical (x, y, z) space is mapped into a rectangular region in the generalised coordinate (ξ, η, ζ) space as shown in Figure 5.1.

2. The governing equations are then converted or expressed in terms of the generalised coordinates as independent variables.

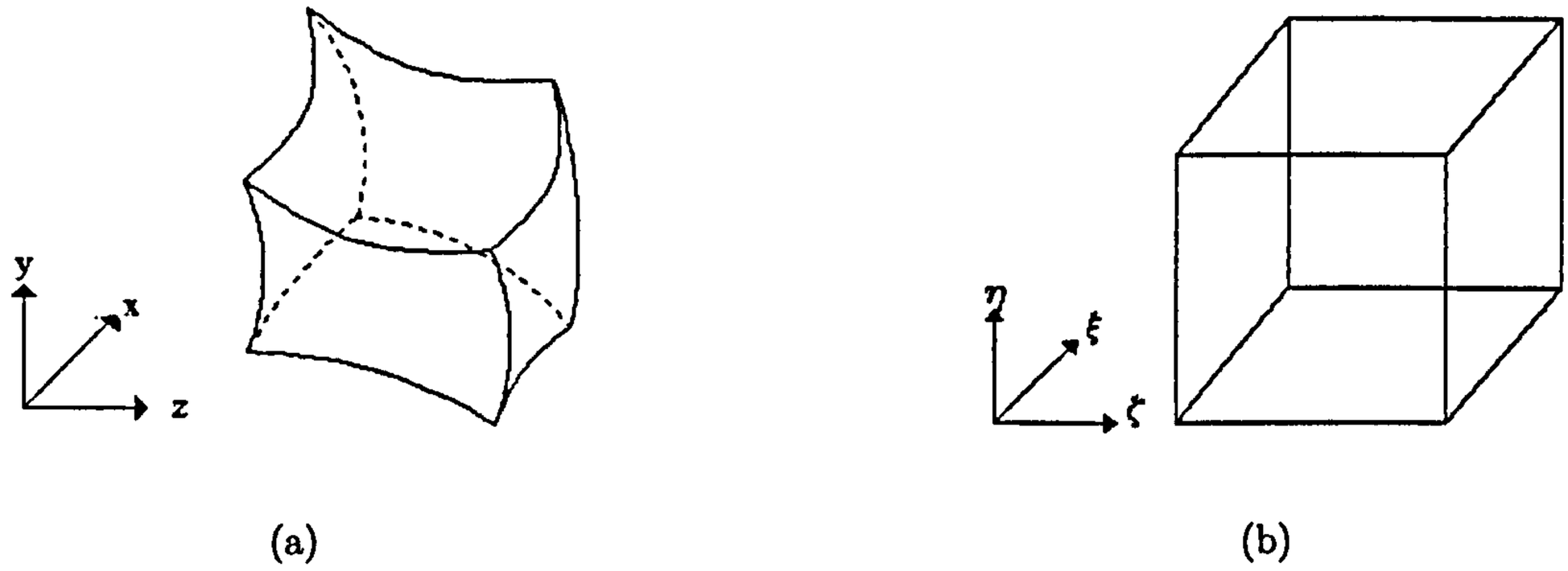

(a) (b)

Figure 5.1: Illustration of (a) physical domain and (b) generalised or computational coordinate domain. This shows the correspondence of the physical domain characterized by (x, y, z) coordinates and the generalised domain represented by (ξ, η, ζ) coordinates.

3. The equations are discretized into generalised coordinate space.

4. Computation is performed on generalised space.

To understand the mapping of physical space into computational space, consider a two dimensional curved duct as shown in Figure 5.2. Here, it would be appropriate to construct a grid lines coinciding well with the curvature of physical geometry. The location along the duct wall, say from A to B or D to C, correspond to a specific value of ξ in the computational domain. Similarly, a location on A to D or B to C corresponds to a specific value of η.

Points on AB and CD, connected by a particular η line, will have the same value ξ_i but different η values (η_1 on $A'B'$ and η_{JMAX} on $C'D'$). The same applies to points on AD and BC, connected by a particular ξ line, which will have the same value η_j but different ξ values (ξ_1 on $A'D'$ and ξ_{IMAX} on $B'C'$). At a particular point (i, j), highlighted in the figure, $\xi = \xi_i$ and $\eta = \eta_j$. A corresponding point, $x = x(\xi_i, \eta_j)$ and $y = y(\xi_i, \eta_j)$, exists in the physical domain.

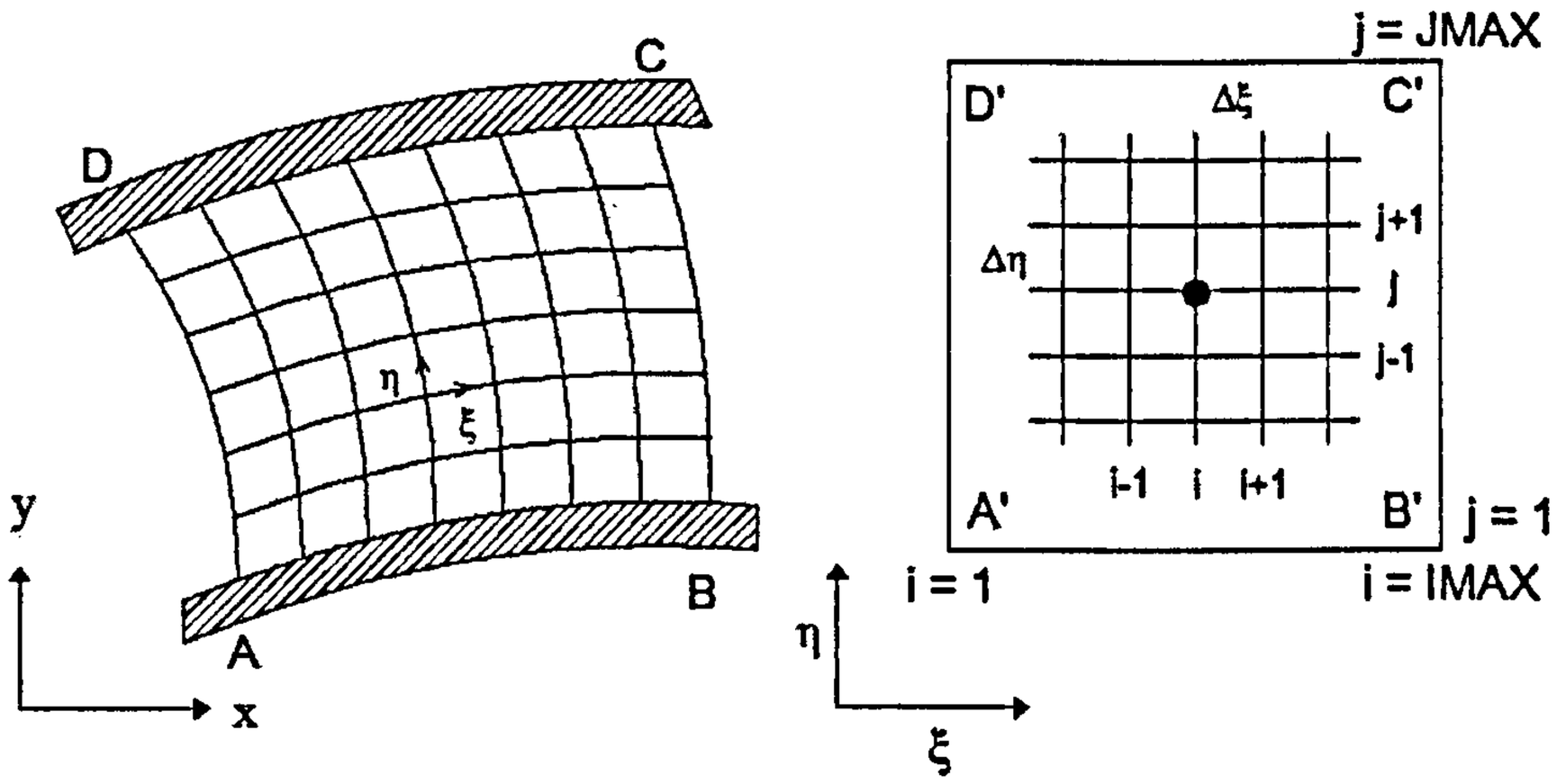

Figure 5.2: Illustration of 2D curved duct in (x, y) plane and transformed (ξ, η) plane. Domain $ABCD$ represents the physical domain and $A'B'C'D'$ represents the computational domain. The constant η and ξ lines are constructed coinciding with wall duct. The computational domain is created with uniform spacing of ξ and η generally keeping $\Delta\xi = \Delta\eta = 1$.

5.2.1 Transformation Relationship

In this section 2D relations between the physical (x, y) and computational (ξ, η) coordinates are established. It is assumed that there exists a unique, single-valued relationship between the generalised coordinates and the physical coordinates which can be written as

$$\xi = \xi(x, y), \quad \text{and} \quad \eta = \eta(x, y)$$

and by implication, $x = x(\xi, \eta)$ and $y = y(\xi, \eta)$. The specific relation can be established once the physical grid is generated as discussed in previous section.

Once, the functional relationship is known the governing equations can be transformed into corresponding equations containing partial derivatives with respect to ξ and η. For example, the first derivatives of the velocity components u and v with respect to x and y become

$$\begin{bmatrix} \frac{\partial u}{\partial x} & \frac{\partial u}{\partial y} \\ \frac{\partial v}{\partial x} & \frac{\partial v}{\partial y} \end{bmatrix} = \begin{bmatrix} \frac{\partial u}{\partial \xi} & \frac{\partial u}{\partial \eta} \\ \frac{\partial v}{\partial \xi} & \frac{\partial v}{\partial \eta} \end{bmatrix} \begin{bmatrix} \frac{\partial \xi}{\partial x} & \frac{\partial \xi}{\partial y} \\ \frac{\partial \eta}{\partial x} & \frac{\partial \eta}{\partial y} \end{bmatrix}. \tag{5.1}$$

Here, the Jacobian matrix, $\underline{\mathbf{J}}$, of the transformation can be defined as

$$\underline{\mathbf{J}} = \begin{bmatrix} \frac{\partial \xi}{\partial x} & \frac{\partial \xi}{\partial y} \\ \frac{\partial \eta}{\partial x} & \frac{\partial \eta}{\partial y} \end{bmatrix}. \tag{5.2}$$

If an analytic relationship $\xi = \xi(x, y)$ is available then the elements of $\underline{\mathbf{J}}$ can be evaluated directly. In practice, an explicit analytical relationship is not available hence, it becomes more convenient to work with the inverse of the Jacobian matrix, $\underline{\mathbf{J}}$, given by

$$\underline{\mathbf{J}}^{-1} = \begin{bmatrix} \frac{\partial x}{\partial \xi} & \frac{\partial x}{\partial \eta} \\ \frac{\partial y}{\partial \xi} & \frac{\partial y}{\partial \eta} \end{bmatrix}. \tag{5.3}$$

The determinant of the inverse Jacobian matrix, $|\underline{\mathbf{J}}^{-1}|$ is given by

$$|\underline{\mathbf{J}}^{-1}| = x_\xi y_\eta - x_\eta y_\xi \tag{5.4}$$

where $x_\xi \equiv \partial x/\partial \xi$, etc. Now, the elements of $\underline{\mathbf{J}}$ can be expressed as

$$\underline{\mathbf{J}} = \frac{\text{Transpose of Cofactors } (\underline{\mathbf{J}}^{-1})}{|\underline{\mathbf{J}}^{-1}|}, \tag{5.5}$$

or

$$\xi_x = \frac{y_\eta}{|\underline{\mathbf{J}}^{-1}|}, \quad \xi_y = \frac{-x_\eta}{|\underline{\mathbf{J}}^{-1}|}, \quad \eta_x = \frac{-y_\xi}{|\underline{\mathbf{J}}^{-1}|}, \quad \text{and} \quad \eta_y = \frac{x_\xi}{|\underline{\mathbf{J}}^{-1}|}. \tag{5.6}$$

Once a grid representing the complicated domain is constructed, the discretized form of the elements, e.g. x_ξ of the inverse Jacobian are evaluated. Equation 5.6 can then be used to evaluate the elements, e.g. ξ_x, of the Jacobian matrix of Equation 5.3. This helps the discretization of the governing equations in generalised coordinates.

5.2.2 Matric Tensor and the Physical Features of Transformations

In order to link the coordinates of the physical domain and the generalised coordinates the matric tensor g_{ij} is introduced, which is related to the Jacobian matrix $\underline{\mathbf{J}}$.

As already assumed, the physical domain, shown in Figures 5.1 and 5.2, is represented by Cartesian coordinates $x^i(\equiv x, y)$ and the computational domain by generalised coordinates $\xi^i(\equiv \xi, \eta)$.

The small distance Δs between two points in physical space can be written in terms of coordinate displacement as

$$\Delta s^2 = \sum_{k=1}^{2} \Delta x^k \Delta x^k. \tag{5.7}$$

The increments in the physical coordinates Δx^k can be related to the change in generalised coordinates $\Delta \xi^i$ by

$$\Delta x^k = \frac{\partial x^k}{\partial \xi^i} \Delta \xi^i \qquad \text{(summation over } i \text{ implied)}. \tag{5.8}$$

Consequently the small distance Δs in physical coordinates can be related to generalised coordinates by:

$$\begin{aligned} \Delta s^2 &= \sum_{k=1}^{2} \left(\frac{\partial x^k}{\partial \xi^i} \Delta \xi^i \right) \left(\frac{\partial x^k}{\partial \xi^j} \Delta \xi^j \right) \\ &= g_{ij} \Delta \xi^i \Delta \xi^j \qquad \text{(summation over } i \text{ and } j \text{ implied)}, \end{aligned} \tag{5.9}$$

where

$$g_{ij} = \sum_{k=1}^{2} \frac{\partial x^k}{\partial \xi^i} \frac{\partial x^k}{\partial \xi^j}. \tag{5.10}$$

It is also convenient to express Equation 5.10 as a matrix

$$\underline{\mathbf{g}} = \begin{bmatrix} (x_\xi^2 + y_\xi^2) & (x_\xi x_\eta + y_\xi y_\eta) \\ (x_\xi x_\eta + y_\xi y_\eta) & (x_\eta^2 + y_\eta^2) \end{bmatrix}. \tag{5.11}$$

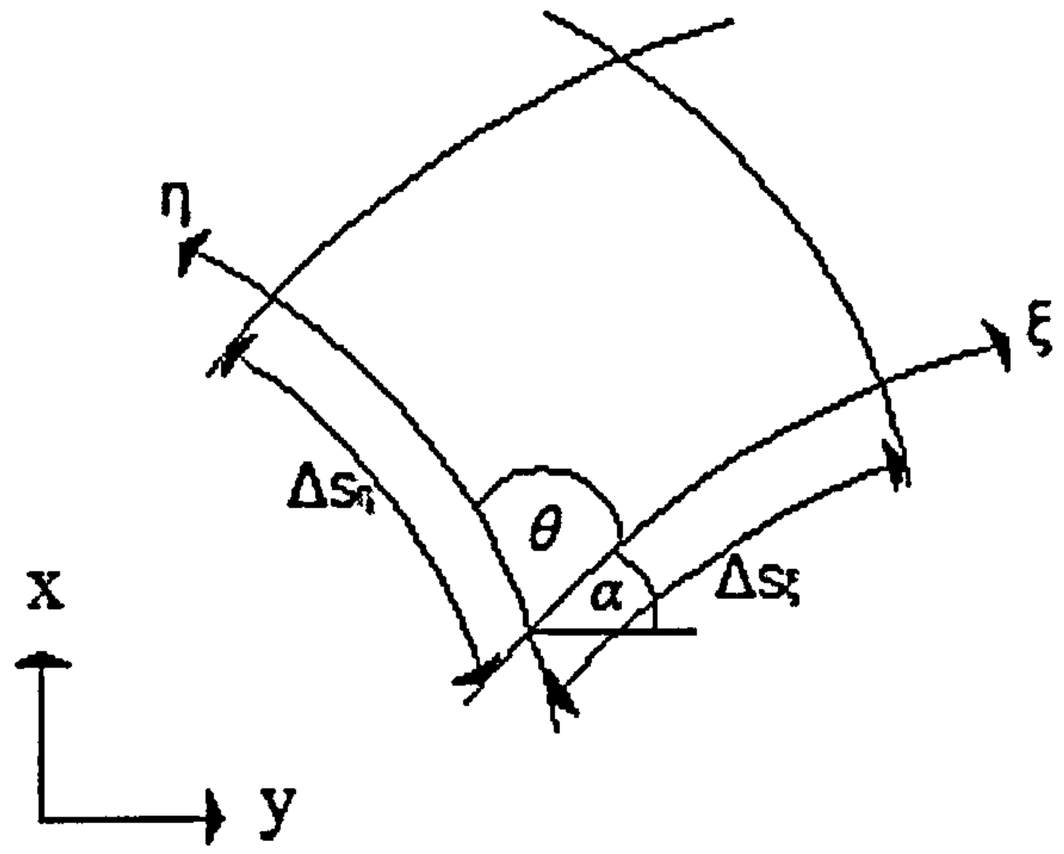

Figure 5.3: Illustration of physical features of the computational domain. Length of the sides: $\Delta S_\eta = (\sqrt{x_\eta^2 + y_\eta^2})\Delta\eta$ and $\Delta S_\xi = (\sqrt{x_\xi^2 + y_\xi^2})\Delta\xi$; The grid Aspect Ratio: $\mathbf{AR} = \Delta s_\eta / \Delta s_\xi$; The angle θ between the coordinate lines: $\cos\theta = g_{12}/\sqrt{(g_{11}g_{22})}$. Symbols are explained in Section 5.2.2.

The matric tensor g_{ij} relates the contribution to the distance Δs to small changes in the generalised coordinates $\Delta\xi^i$. In two dimensions the distance measured along ξ and η grid lines is given by

$$\Delta s_\xi = g_{11}^{1/2}\Delta\xi \qquad \text{and} \qquad \Delta s_\eta = g_{22}^{1/2}\Delta\eta \tag{5.12}$$

respectively, as shown in Figure 5.3.

The metric tensor g_{ij} and the various transformation parametcrs, x_ξ etc., on which it depends can be interpreted in relation to the physical features of the computational grid. The transformation parameters are evaluated in Section 5.3. The other properties of the physical grid in connection with generalised coordinates can be expressed in following way:

Cell Area: The grid cell area is given by

$$\text{Area} = |\underline{\mathbf{g}}|^{1/2}\Delta\xi\Delta\eta, \tag{5.13}$$

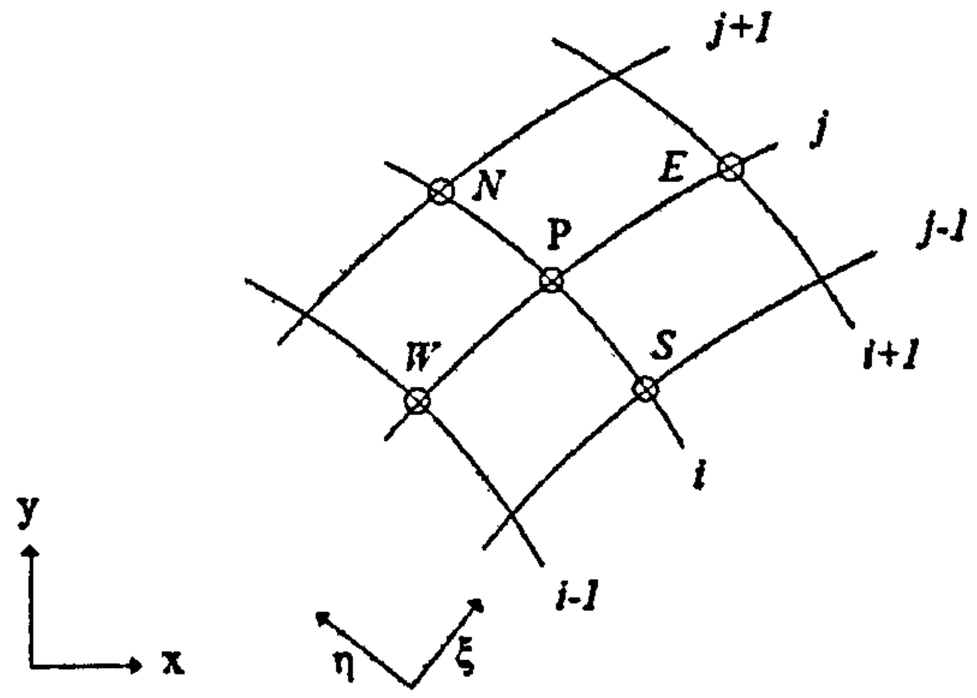

Figure 5.4: Illustration of node arrangement in a computational grid equivalent to the physical domain. At node P the evaluation of transformation parameters (x_ξ, for example) is given by $x_\xi = (x_{i+1,j} - x_{i-1,j})/(\xi_{i+1,j} - \xi_{i-1,j})$.

which gives a physical interpretation of the inverse Jacobian determinant. Here, $|\underline{\mathbf{g}}|^{1/2} = |\underline{\mathbf{J}}|^{-1}$.

Aspect Ratio: The grid aspect ratio **AR** is given by the ratio of the magnitude of the tangent vectors (with $\Delta\xi = \Delta\eta$)

$$\mathbf{AR} = \frac{\Delta s_\eta}{\Delta s_\xi} = \left(\frac{g_{22}}{g_{11}}\right)^{1/2}. \tag{5.14}$$

Local Distortion: The local distortion of the grid is determined by the angle θ between the ξ and η coordinate lines. Thus

$$\cos\theta = \frac{g_{12}}{(g_{11}g_{22})^{1/2}}. \tag{5.15}$$

5.2.3 Simplification Due to Orthogonal Coordinates

The use of generalised coordinates permits arbitrary geometries to be considered. However, it is well known that the accuracy of the solution is degraded by grid distortion. For high accuracy, the grid should be orthogonal or nearly orthogonal. For orthogonal systems some of the transformation terms disappear and the equations simplify further.

For 2D orthogonal systems the grid must have $\theta = 90^0$ (see Figure 5.3) or from Equation (5.15) the orthogonality condition for the 2D plane is

$$g_{12} = x_\xi x_\eta + y_\xi y_\eta = 0. \tag{5.16}$$

In three dimensions the orthogonality condition becomes

$$g_{ij} = 0, \quad i \neq j. \tag{5.17}$$

For 2D orthogonal coordinates, the matric tensor contains only diagonal terms g_{ij}, hence we can define

$$h_1 = h_\xi = (g_{ii})^{1/2} = (x_\xi^2 + y_\xi^2)^{1/2} \qquad \text{and} \qquad h_2 = h_\eta = (g_{jj})^{1/2} = (x_\eta^2 + y_\eta^2)^{1/2}. \tag{5.18}$$

The terms h_i can be interpreted as "*scale factors*", which are already defined in Section 4.7.3.3.

The maximum deviation (MDO) and mean deviation (ADO) from orthogonality are calculated from

$$\text{MDO} = \max(|90^\circ - \theta_{i,j}|) \tag{5.19}$$

$$\text{ADO} = \frac{1}{n_x - 2}\frac{1}{n_y - 2}\sum_{i-2}^{n_x}\sum_{j-2}^{n_y}(|90^\circ - \theta_{i,j}|), \tag{5.20}$$

where

$$\theta = \arccos\left(\frac{g_{12}}{h_\xi h_\eta}\right). \tag{5.21}$$

A small change in the ξ^i coordinate, in the orthogonal grid, produces a scaled overall movement given by

$$\Delta s_1 = h_1 \Delta \xi \qquad \text{and} \qquad \Delta s_2 = h_2 \Delta \eta. \tag{5.22}$$

For computational convenience purposes some additional terms are defined as

$$\frac{1}{r_\xi} = \frac{1}{h_1 h_2} \frac{\Delta h_1}{\Delta \eta} \qquad \text{and} \qquad \frac{1}{r_\eta} = \frac{1}{h_1 h_2} \frac{\Delta h_2}{\Delta \xi}. \tag{5.23}$$

These terms are used extensively in the derivation of working equations for the simulations of compound meandering channels.

5.3 Evaluation of Transformation Parameters

Once the mapping is defined at grid points, we have to evaluate the transformation parameters numerically. Here, a central difference scheme is considered, which is discussed in following section.

5.3.1 Central-Difference Scheme

The evaluation of the transformation parameters (x_ξ, y_η etc.) is carried out with the help of a central-difference scheme. Hence, for the point P as shown in Figure 5.4 a central difference evaluation of the parameters gives

$$x_\xi = \frac{x_{i+1,j} - x_{i-1,j}}{\xi_{i+1,j} - \xi_{i-1,j}}, \qquad y_\xi = \frac{y_{i+1,j} - y_{i-1,j}}{\xi_{i+1,j} - \xi_{i-1,j}},$$
$$\text{and} \tag{5.24}$$
$$x_\eta = \frac{x_{i,j+1} - x_{i,j-1}}{\eta_{i,j+1} - \eta_{i,j-1}}, \qquad y_\eta = \frac{y_{i,j+1} - y_{i,j-1}}{\eta_{i,j+1} - \eta_{i,j-1}}.$$

Similarly, second order transformation parameters are evaluated as

$$x_{\xi\xi} = \frac{x_{i-1,j} - 2x_{i,j} + x_{i+1,j}}{\Delta\xi^2}, \qquad y_{\xi\xi} = \frac{y_{i-1,j} - 2y_{i,j} + y_{i+1,j}}{\Delta\xi^2},$$
$$\text{and} \tag{5.25}$$
$$x_{\eta\eta} = \frac{x_{i,j-1} - 2x_{i,j} + x_{i,j+1}}{\Delta\eta^2}, \qquad y_{\eta\eta} = \frac{y_{i,j+1} - 2y_{i,j} + y_{i,j-1}}{\Delta\eta^2}.$$

Here, a uniform (ξ, η) grid is assumed, i.e. $\Delta\xi = \xi_{i+1,j} - \xi_{i,j} = \Delta\eta = \eta_{i,j+1} - \eta_{i,j} = 1$. Once the basic parameters have been evaluated as discussed above, the transformed parameters ξ_x etc., can be obtained with help of Equations 5.6.

5.4 Equations Governing the Flow Through Meandering Channels

The 3D steady, incompressible, turbulent flow in meandering channels (see Figure 5.5) is governed by continuity, momentum balance, turbulent kinetic energy and energy dissipation equations as already discussed in Section 3.

In this section, the governing equations are derived in an orthogonal curvilinear coordinate system. The detailed derivation of the governing equations in generalised coordinate systems can be found in Ye and McCorquodale (1997), Ye and McCorquodale (1998), Warsi (1998) and Shao *et al.* (2003).

5.4.1 Continuity Equation

The continuity equation for meandering channels in orthogonal coordinates may be expressed as

$$\frac{1}{h_1 h_2}\left[\frac{\partial}{\partial\xi}(h_2 U) + \frac{\partial}{\partial\eta}(h_1 V) + \frac{\partial}{\partial z}(h_1 h_2 W)\right] = 0 \tag{5.26}$$

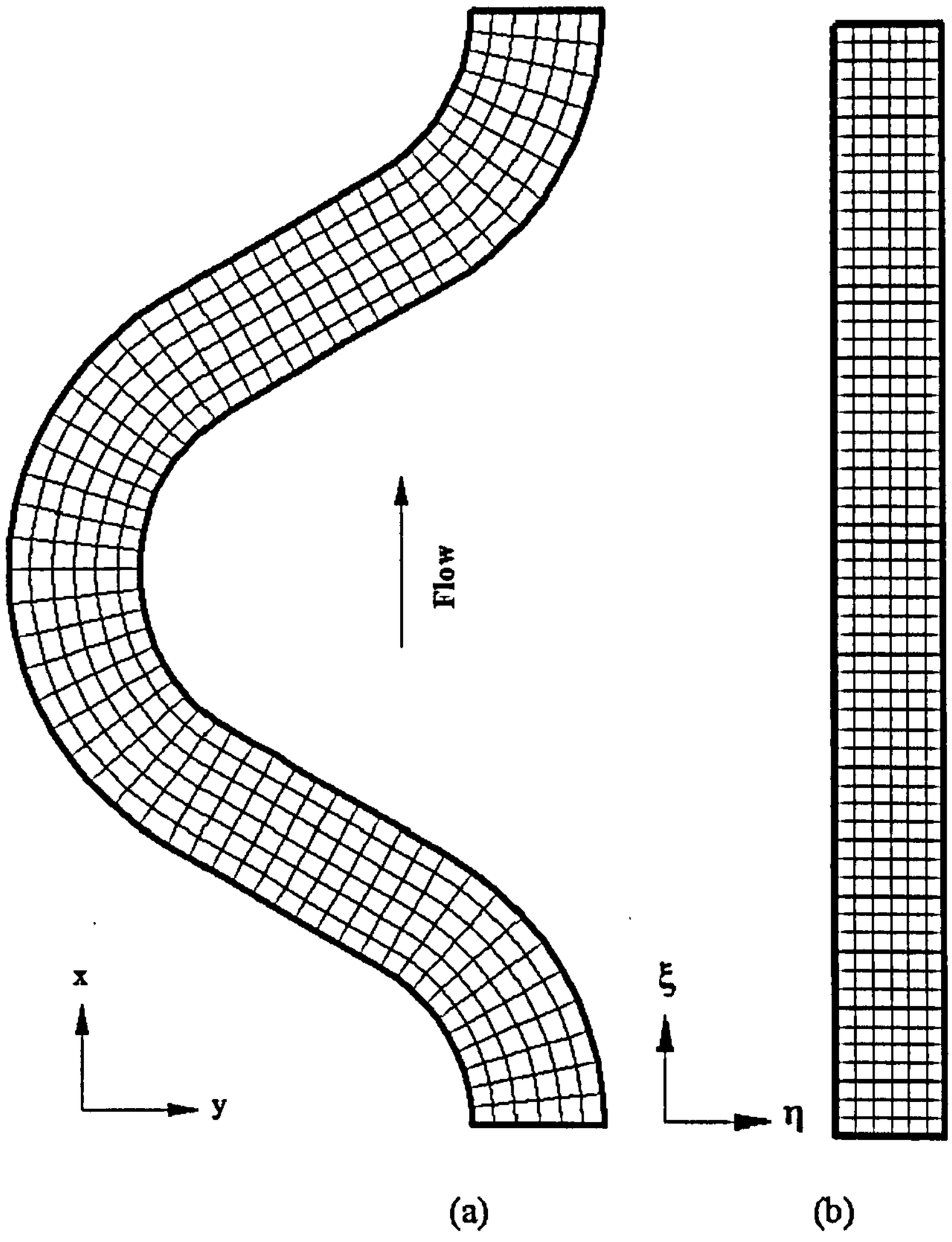

Figure 5.5: 2D numerical grids of a meandering channel: (a) physical domain in (x,y) plane (b) computational domain in (ξ, η) plane. Physical domain represents the single meander of a channel with sinuosity = 1.370. Number of CVs have to be same both in physical and computational grids.

where h_1 and h_2 are the scale factors defined in Equations 5.18; U, V and W are velocity components aligned with grid lines in x, y and z directions.

After applying the chain rule of differentiation and using Equations 5.22 and 5.23, we get:

$$\frac{\partial U}{\partial s_1} + \frac{\partial V}{\partial s_2} + \frac{\partial W}{\partial z} + \frac{U}{r_\eta} + \frac{V}{r_\xi} = 0 \tag{5.27}$$

5.4.2 Momentum Equations

The momentum equations are expressed in the following sections.

5.4.2.1 Streamwise Direction

The streamwise, x-direction momentum equation may be described as

$$\frac{U}{h_1}\frac{\partial U}{\partial \xi} + \frac{V}{h_2}\frac{\partial U}{\partial \eta} + W\frac{\partial U}{\partial z} + \frac{UV}{h_1 h_2}\frac{\partial h_1}{\partial \eta} - \frac{V^2}{h_1 h_2}\frac{\partial h_2}{\partial \xi} = -\frac{1}{h_1}\frac{\partial}{\partial \xi}\left(\frac{P}{\rho}\right) + \frac{1}{\rho h_1 h_2}\left[\frac{\partial}{\partial \xi}(h_2\tau_{xx}) + \frac{\partial}{\partial \eta}(h_1\tau_{xy}) + \frac{\partial}{\partial z}(h_1 h_2 \tau_{xz})\right] + \frac{\tau_{xy}}{\rho h_1 h_2}\frac{\partial h_1}{\partial \eta} - \frac{\tau_{yy}}{\rho h_1 h_2}\frac{\partial h_2}{\partial \xi} \tag{5.28}$$

which, on simplification, leads to

$$\begin{aligned} U\frac{\partial U}{\partial s_1} + V\frac{\partial U}{\partial s_2} + W\frac{\partial U}{\partial z} + \frac{UV}{r_\xi} - \frac{V^2}{r_\eta} &= -\frac{\partial}{\partial s_1}\left(\frac{P}{\rho}\right) \\ &+ \frac{1}{\rho}\left(\frac{\partial \tau_{xx}}{\partial s_1} + \frac{\partial \tau_{xy}}{\partial s_2} + \frac{\partial \tau_{xz}}{\partial z}\right) \\ &+ \frac{1}{\rho}\left(\frac{2\ \tau_{xy}}{r_\xi}\right) + \frac{1}{\rho}\left(\frac{\tau_{xx} - \tau_{yy}}{r_\eta}\right). \end{aligned} \tag{5.29}$$

5.4.2.2 Lateral Direction

The lateral or y-direction momentum equation may be expressed as

$$\frac{U}{h_1}\frac{\partial V}{\partial \xi}+\frac{V}{h_2}\frac{\partial V}{\partial \eta}+W\frac{\partial V}{\partial z}+\frac{UV}{h_1h_2}\frac{\partial h_2}{\partial \xi}-\frac{U^2}{h_1h_2}\frac{\partial h_2}{\partial \eta}=-\frac{1}{h_2}\frac{\partial}{\partial \eta}\left(\frac{P}{\rho}\right)+$$
$$\frac{1}{\rho h_1h_2}\left[\frac{\partial}{\partial \xi}(h_2\tau_{yx})+\frac{\partial}{\partial \eta}(h_1\tau_{yy})+\frac{\partial}{\partial z}(h_1h_2\tau_{yz})\right]+\frac{\tau_{yx}}{\rho h_1h_2}\frac{\partial h_2}{\partial \xi}-\frac{\tau_{xx}}{\rho h_1h_2}\frac{\partial h_1}{\partial \eta}. \tag{5.30}$$

After doing further simplification, we get

$$U\frac{\partial V}{\partial s_1}+V\frac{\partial V}{\partial s_2}+W\frac{\partial V}{\partial z}+\frac{UV}{r_\eta}-\frac{U^2}{r_\xi}=-\frac{\partial}{\partial s_2}\left(\frac{P}{\rho}\right)$$
$$+\frac{1}{\rho}\left(\frac{\partial \tau_{yx}}{\partial s_1}+\frac{\partial \tau_{yy}}{\partial s_2}+\frac{\partial \tau_{xz}}{\partial z}\right)$$
$$+\frac{1}{\rho}\left(\frac{2\,\tau_{yx}}{r_\eta}\right)+\frac{1}{\rho}\left(\frac{\tau_{yy}-\tau_{xx}}{r_\xi}\right). \tag{5.31}$$

5.4.2.3 Vertical Direction

Similarly, for z-direction we may write

$$\frac{U}{h_1}\frac{\partial W}{\partial \xi}+\frac{V}{h_2}\frac{\partial W}{\partial \eta}+W\frac{\partial W}{\partial z}=-\frac{\partial}{\partial z}\left(\frac{P}{\rho}\right)$$
$$+\frac{1}{\rho h_1h_2}\left[\frac{\partial}{\partial \xi}(h_2\tau_{zx})+\frac{\partial}{\partial \eta}(h_1\tau_{zy})+\frac{\partial}{\partial z}(h_1h_2\tau_{zz})\right] \tag{5.32}$$

which leads to

$$U\frac{\partial W}{\partial s_1}+V\frac{\partial W}{\partial s_2}+W\frac{\partial W}{\partial z}=-\frac{\partial}{\partial z}\left(\frac{P}{\rho}\right)+\frac{1}{\rho}\left(\frac{\partial \tau_{zx}}{\partial s_1}+\frac{\partial \tau_{zy}}{\partial s_2}+\frac{\partial \tau_{zz}}{\partial z}\right)$$
$$+\frac{1}{\rho}\left(\frac{\tau_{zx}}{r_\eta}+\frac{\tau_{zy}}{r_\xi}\right). \tag{5.33}$$

5.4.2.4 Reynolds Stresses

In Equations 5.28 to 5.33, the term τ_{ij} is the shear stress. In open channel flow, these stress are modelled with help of Boussinesq's approximation (Boussinesq (1887)), which in orthogonal coordinates, takes the following form:

$$\frac{\tau_{xx}}{\rho} = 2\,\nu'\left(\frac{\partial U}{\partial s_1} + \frac{V}{r_\xi}\right); \qquad \frac{\tau_{yy}}{\rho} = 2\,\nu'\left(\frac{\partial V}{\partial s_2} + \frac{U}{r_\eta}\right); \qquad \frac{\tau_{zz}}{\rho} = 2\,\nu'\frac{\partial W}{\partial z};$$

$$\frac{\tau_{xy}}{\rho} = \frac{\tau_{yx}}{\rho} = \nu'\left[\left(\frac{\partial U}{\partial s_2} - \frac{V}{r_\eta}\right) + \left(\frac{\partial V}{\partial s_1} + \frac{U}{r_\xi}\right)\right];$$

$$\frac{\tau_{yz}}{\rho} = \frac{\tau_{zy}}{\rho} = \nu'\left(\frac{\partial V}{\partial z} + \frac{\partial W}{\partial s_2}\right); \qquad \frac{\tau_{xz}}{\rho} = \frac{\tau_{zx}}{\rho} = \nu'\left(\frac{\partial U}{\partial z} + \frac{\partial W}{\partial s_1}\right) \tag{5.34}$$

where ν' is the eddy viscosity.

5.4.3 Momentum Balance Equations in Their Final Form

After considering the expressions for the Reynolds stresses expressed in Equation 5.34 and performing some mathematical manipulation, we can express the momentum balance equations as:

U Momentum

$$U\frac{\partial U}{\partial s_1}+V\frac{\partial U}{\partial s_2}+W\frac{\partial U}{\partial z}=-\frac{\partial}{\partial s_1}\left(\frac{P}{\rho}\right)+\nu'\left(\frac{\partial^2 U}{\partial s_1^2}\right)+\nu'\left(\frac{\partial^2 U}{\partial s_2^2}\right)+\nu'\left(\frac{\partial^2 U}{\partial z^2}\right)+\underbrace{\frac{1}{\rho}\left(\frac{2\,\tau_{xy}}{r_\xi}\right)+\frac{1}{\rho}\left(\frac{\tau_{xx}-\tau_{yy}}{r_\eta}\right)+\frac{V^2}{r_\eta}-\frac{\mathbf{UV}}{\mathbf{r}_\xi}}\tag{5.35}$$

V Momentum

$$U\frac{\partial V}{\partial s_1}+V\frac{\partial V}{\partial s_2}+W\frac{\partial V}{\partial z}=-\frac{\partial}{\partial s_2}\left(\frac{P}{\rho}\right)+\nu'\left(\frac{\partial^2 V}{\partial s_1^2}\right)+\nu'\left(\frac{\partial^2 V}{\partial s_2^2}\right)+\nu'\left(\frac{\partial^2 V}{\partial z^2}\right)+\underbrace{\frac{1}{\rho}\left(\frac{2\,\tau_{yx}}{r_\eta}\right)+\frac{1}{\rho}\left(\frac{\tau_{yy}-\tau_{xx}}{r_\xi}\right)-\frac{UV}{r_\eta}+\frac{\mathbf{U^2}}{\mathbf{r}_\xi}}\tag{5.36}$$

W Momentum

$$U\frac{\partial W}{\partial s_1}+V\frac{\partial W}{\partial s_2}+W\frac{\partial W}{\partial z}=-\frac{\partial}{\partial z}\left(\frac{P}{\rho}\right)+\nu'\left(\frac{\partial^2 W}{\partial s_1^2}\right)+\nu'\left(\frac{\partial^2 W}{\partial s_2^2}\right)+\nu'\left(\frac{\partial^2 W}{\partial z^2}\right)+\underbrace{\frac{1}{\rho}\left(\frac{\tau_{zx}}{r_\eta}+\frac{\tau_{zy}}{r_\xi}\right)}\tag{5.37}$$

In Equations 5.35 to 5.37, the underbrace terms are the additional source terms, which arise due to the coordinate transformation. In the U and V momentum equations, the last highlighted terms represent source terms, which are responsible for the centrifugal effects.

5.4.4 The Standard $k - \varepsilon$ Turbulence Model

The k and ε equations in Cartesian coordinates are already noted in Section 3.3. In this section, the model equations are derived for an orthogonal coordinate system.

5.4.4.1 The k Equation

$$\frac{U}{h_1}\frac{\partial k}{\partial \xi} + \frac{V}{h_2}\frac{\partial k}{\partial \eta} + W\frac{\partial k}{\partial z} = \frac{(\nu_t/\sigma_k)}{h_1 h_2}\left[\frac{\partial}{\partial \xi}\left(\frac{h_2}{h_1}\frac{\partial k}{\partial \xi}\right) + \frac{\partial}{\partial \eta}\left(\frac{h_1}{h_2}\frac{\partial k}{\partial \eta}\right) + \frac{\partial}{\partial z}\left(h_1 h_2 \frac{\partial k}{\partial z}\right)\right] + S_k \tag{5.38}$$

where, $S_k = P_k + \varepsilon$, P_k is the turbulent production term and $\nu_t = C_\mu \frac{k^2}{\varepsilon}$ is the eddy viscosity. After further simplification, we get

$$U\frac{\partial k}{\partial s_1} + V\frac{\partial k}{\partial s_2} + W\frac{\partial k}{\partial z} = \frac{\nu_t}{\sigma_k}\left[\frac{\partial^2 k}{\partial s_1^2} + \frac{\partial^2 k}{\partial s_2^2} + \frac{\partial^2 k}{\partial z^2}\right] + \frac{\nu_t}{\sigma_k}\left(\frac{1}{r_\eta}\frac{\partial k}{\partial s_1} + \frac{1}{r_\xi}\frac{\partial k}{\partial s_2}\right) + S_k \tag{5.39}$$

5.4.4.2 The ε Equation

$$\frac{U}{h_1}\frac{\partial \varepsilon}{\partial \xi} + \frac{V}{h_2}\frac{\partial \varepsilon}{\partial \eta} + W\frac{\partial \varepsilon}{\partial z} = \frac{(\nu_t/\sigma_\varepsilon)}{h_1 h_2}\left[\frac{\partial}{\partial \xi}\left(\frac{h_2}{h_1}\frac{\partial \varepsilon}{\partial \xi}\right) + \frac{\partial}{\partial \eta}\left(\frac{h_1}{h_2}\frac{\partial \varepsilon}{\partial \eta}\right) + \frac{\partial}{\partial z}\left(h_1 h_2 \frac{\partial \varepsilon}{\partial z}\right)\right] + S_\varepsilon \tag{5.40}$$

where, $S_\varepsilon = (C_{\varepsilon 1} P_k - C_{\varepsilon 2}\varepsilon)\varepsilon/k$. Further simplification leads to

$$U\frac{\partial \varepsilon}{\partial s_1} + V\frac{\partial \varepsilon}{\partial s_2} + W\frac{\partial \varepsilon}{\partial z} = \frac{\nu_t}{\sigma_\varepsilon}\left[\frac{\partial^2 \varepsilon}{\partial s_1^2} + \frac{\partial^2 \varepsilon}{\partial s_2^2} + \frac{\partial^2 \varepsilon}{\partial z^2}\right] + \frac{\nu_t}{\sigma_\varepsilon}\left(\frac{1}{r_\eta}\frac{\partial \varepsilon}{\partial s_1} + \frac{1}{r_\xi}\frac{\partial \varepsilon}{\partial s_2}\right) + S_\varepsilon \tag{5.41}$$

5.4.4.3 Kinetic Energy Production Terms

In Cartesian coordinates, the rate of production of turbulent kinetic energy (TKE) is expressed with help of Boussinesq's eddy viscosity approximation as

$$P_k \approx \mu_t \left(\frac{\partial \overline{u}_i}{\partial x_j} + \frac{\partial \overline{u}_j}{\partial x_i}\right)\frac{\partial \overline{u}_i}{\partial x_j}. \tag{5.42}$$

In orthogonal coordinates the TKE production term can be expressed in vector notation with the help of the Reynolds stresses as expressed in Section 5.4.2.4.

For $i = 1, 2, 3$ and $j = 1$

$$2\left(\frac{\partial U}{\partial s_1} + \frac{V}{r_\xi}\right)^2;\quad \left[\left(\frac{\partial V}{\partial s_1} + \frac{U}{r_\xi}\right) + \left(\frac{\partial U}{\partial s_2} - \frac{V}{r_\eta}\right)\right]\left(\frac{\partial V}{\partial s_1} + \frac{U}{r_\xi}\right);$$

$$\left(\frac{\partial W}{\partial s_1} + \frac{\partial U}{\partial z}\right)\frac{\partial W}{\partial s_1};$$

For $i = 1, 2, 3$ and $j = 2$

$$\left[\left(\frac{\partial U}{\partial s_2} - \frac{V}{r_\eta}\right) + \left(\frac{\partial V}{\partial s_1} + \frac{U}{r_\xi}\right)\right]\left(\frac{\partial U}{\partial s_2} - \frac{V}{r_\eta}\right);\quad 2\left(\frac{\partial V}{\partial s_2} + \frac{U}{r_\eta}\right)^2;$$

$$\left(\frac{\partial W}{\partial s_2} + \frac{\partial V}{\partial z}\right)\frac{\partial W}{\partial s_2};$$

For $i = 1, 2, 3$ and $j = 3$

$$\left(\frac{\partial U}{\partial z} + \frac{\partial W}{\partial s_1}\right)\frac{\partial U}{\partial z};\quad \left(\frac{\partial V}{\partial z} + \frac{\partial W}{\partial s_2}\right)\frac{\partial V}{\partial z};\quad 2\left(\frac{\partial W}{\partial z}\right)^2. \tag{5.43}$$

5.4.5 Reynolds Stress Models

In this section, the ASM equations discussed in Section 3.4 are transformed in an orthogonal coordinate system. For this derivations, the shear stresses terms discussed in Section 5.4.2.4 are used to evaluate the gradients.

5.4.5.1 LY Model

Primary flow direction:

$$\tau_{xx} = -\rho\overline{uu} = \rho\nu_t \left(\frac{\partial U}{\partial s_1} + \frac{V}{r_\xi}\right) \tag{5.44}$$

$$\tau_{xy} = -\rho\overline{uv} = \rho\nu_t \left(\frac{\partial U}{\partial s_2} - \frac{V}{r_\eta}\right) \tag{5.45}$$

$$\tau_{xz} = -\rho\overline{uw} = \rho\nu_t \left(\frac{\partial U}{\partial z}\right) \tag{5.46}$$

Secondary flow direction:

$$\tau_{yy} = -\rho\overline{vv} = -C_1\frac{\rho\nu_t k}{\epsilon}\left(\frac{\partial U}{\partial s_2} + \frac{V}{r_\xi}\right) - C_k\rho k \tag{5.47}$$

$$\tau_{zz} = -\rho\overline{ww} = -C_1\frac{\rho\nu_t k}{\epsilon}\left(\frac{\partial U}{\partial z}\right) - C_k\rho k \tag{5.48}$$

$$\tau_{yz} = \tau_{zy} = -\rho\overline{vw} = -C_1\frac{\rho\nu_t k}{\epsilon}\left(\frac{\partial U}{\partial z}\right)\left(\frac{\partial U}{\partial s_2} + \frac{V}{r_\xi}\right) \tag{5.49}$$

Here, C_1 and C_k are the dimensionless constants discussed in Section 3.4.1. This transformation has given additional terms, particularly V/r_ξ, which take care of centrifugal effects on Reynolds stresses.

5.4.5.2 NR algebraic stress model

Primary flow direction:

$$\tau_{xx} = -\rho\overline{uu} = \rho\nu_t \left(\frac{\partial U}{\partial s_1} + \frac{V}{r_\xi}\right) \tag{5.50}$$

$$\tau_{xy} = -\rho\overline{uv} = \rho\nu_{t2} \left(\frac{\partial U}{\partial s_2} - \frac{V}{r_\eta}\right) \tag{5.51}$$

$$\tau_{xz} = -\rho\overline{uw} = \rho\nu_{t3} \left(\frac{\partial U}{\partial z}\right) \tag{5.52}$$

where ν_{t2} and ν_{t3} are equal to the same quantities in Cartesian coordinates, as discussed in Section 3.4.2.

Secondary flow direction:

$$\begin{aligned}\tau_{yy} &= -\rho\overline{vv} \\ &= \frac{-\rho k}{c_1} \\ &\quad \left\{\frac{2}{3}\left(\alpha - \frac{1}{2}\beta + c_1 - 1\right) + c_3 f_2 \frac{\overline{ww}}{k} + \frac{\beta}{\epsilon}\left[\overline{uw}\left(\frac{\partial U}{\partial z}\right) - \overline{uv}\left(\frac{\partial U}{\partial s_2} - \frac{V}{r_\eta}\right)\right]\right\} \\ &\quad + 2\rho\nu_t \left(\frac{\partial V}{\partial s_2} + \frac{U}{r_\eta}\right)\end{aligned} \tag{5.53}$$

$$\begin{aligned}\tau_{zz} &= -\rho\overline{ww} \\ &= \frac{-\rho k}{c_1 + 2c_3 f_2} \\ &\quad \left\{\frac{2}{3}\left(\alpha - \frac{1}{2}\beta + c_1 - 1\right) + \frac{\beta}{\epsilon}\left[\overline{uv}\left(\frac{\partial U}{\partial s_2} - \frac{V}{r_\eta}\right) - \overline{uw}\left(\frac{\partial U}{\partial s_2} - \frac{V}{r_\eta}\right)\right]\right\} \\ &\quad + 2\rho\nu_t \left(\frac{\partial W}{\partial z}\right)\end{aligned} \tag{5.54}$$

$$\begin{aligned}\tau_{yz} = \tau_{zy} &= -\rho\overline{vw} \\ &= \frac{-\rho\beta}{c_1 + \frac{3}{2}c_3 f_2} \frac{k}{\epsilon}\left\{\overline{uw}\left(\frac{\partial U}{\partial s_2} - \frac{V}{r_\eta}\right) + \overline{uv}\left(\frac{\partial U}{\partial z}\right)\right\} + \rho\nu_t \left(\frac{\partial W}{\partial s_2} + \frac{\partial V}{\partial z}\right)\end{aligned} \tag{5.55}$$

Similar to LY model, the transformation has raised additional terms, which might influence the secondary current behaviour in meandering channels.

5.4.5.3 Nonlinear $k-\varepsilon$ Model

Primary flow direction:

$$\tau_{xx} = -\rho\overline{uu} = \rho\nu_t\left(\frac{\partial U}{\partial s_1} + \frac{V}{r_\xi}\right) \tag{5.56}$$

$$\tau_{xy} = -\rho\overline{uv} = \rho\nu_t\left(\frac{\partial U}{\partial s_2} - \frac{V}{r_\eta}\right) \tag{5.57}$$

$$\tau_{xz} = -\rho\overline{uw} = \rho\nu_t\left(\frac{\partial U}{\partial z}\right) \tag{5.58}$$

Secondary flow direction:

$$\begin{aligned}\tau_{yy} &= -\rho\overline{vv} \\ &= -\frac{2}{3}\rho k + \rho k^{1/2} l\left(\frac{\partial V}{\partial s_1} + \frac{U}{r_\eta}\right) + C_D\rho l^2\left(\frac{1}{12}\left(\frac{\partial U}{\partial s_2} - \frac{V}{r_\eta}\right)^2 - \frac{1}{6}\left(\frac{\partial U}{\partial z}\right)^2\right) \\ &\quad + \frac{1}{3}C_E\rho l^2\left(\left(\frac{\partial U}{\partial s_2} - \frac{V}{r_\eta}\right)^2 + \left(\frac{\partial U}{\partial z}\right)^2\right)\end{aligned} \tag{5.59}$$

$$\begin{aligned}\tau_{zz} &= -\rho\overline{ww} \\ &= -\frac{2}{3}\rho k + \rho k^{1/2} l\left(\frac{\partial W}{\partial z}\right) + C_D\rho l^2\left(\frac{1}{12}\left(\frac{\partial U}{\partial z}\right)^2 - \frac{1}{6}\left(\frac{\partial U}{\partial s_2} - \frac{V}{r_\eta}\right)^2\right) \\ &\quad + \frac{1}{3}C_E\rho l^2\left(\left(\frac{\partial U}{\partial z}\right)^2 + \left(\frac{\partial U}{\partial z} - \frac{V}{r_\eta}\right)^2\right)\end{aligned} \tag{5.60}$$

$$\begin{aligned}\tau_{yz} = \tau_{zy} &= -\rho\overline{vw} \\ &= \frac{1}{2}\rho k^{1/2} l\left(\frac{\partial V}{\partial z} + \frac{\partial W}{\partial s_2}\right) + \frac{1}{4}C_D\rho l^2\left(\frac{\partial U}{\partial s_2} - \frac{V}{r_\eta}\right)\left(\frac{\partial U}{\partial z}\right).\end{aligned} \tag{5.61}$$

It can be noticed from ASM models in transformed coordinates that, the conversion process has created in stress terms also for longitudinal direction. As discussed in Chapter 3, the Reynolds stresses are treated as additional source terms and handled explicitly.

5.5 Numerical Implementation of Orthogonal Coordinates

Once the governing equations are converted into orthogonal coordinates, their numerical discretization is carried out with help of the FVM. As the FVM is based on the principal of global conservation of quantities inside the computational domain, the discretization process remains similar for orthogonal coordinates and cartesian coordinates (Ferziger and Perić (1995)). Hence, coding becomes more easy.

The discretization of convective and diffusive fluxes, the SIMPLE algorithm and the set of derived algebraic equations in orthogonal coordinates remains the same as for Cartesian coordinates as discussed in Section 4. The only change is the area of the CV and volume of the CV.

5.5.1 The System Equations and Their Solution

Here, CV areas can be expressed in the computational domain as:

$$\Delta s_1 \Delta s_2 = h_1 h_2 \Delta\xi \Delta\eta$$

$$\Delta s_1 \Delta z = h_1 \Delta\xi \Delta z$$

$$\Delta s_2 \Delta z = h_2 \Delta\eta \Delta z$$

and the volume ($\Delta\Omega$) can be expressed as

$$\Delta s_1 \Delta s_2 \Delta z = h_1 h_2 \Delta\xi \Delta\eta \Delta z = \Delta\Omega.$$

The discretized algebraic equation is expressed as:

$$a_P\phi_P = a_E\phi_E + a_W\phi_W + a_N\phi_N + a_S\phi_S + a_T\phi_T + a_B\phi_B + S_\phi\Delta\Omega \qquad (5.62)$$

where,

$$a_E = (D_e + \max(\dot{m}_e, 0.))\Delta s_2\Delta z$$

$$a_W = (D_w + \min(\dot{m}_w, 0.))\Delta s_2\Delta z$$

$$a_N = (D_n + \max(\dot{m}_n, 0.))\Delta s_1\Delta z$$

$$a_S = (D_s + \min(\dot{m}_s, 0.))\Delta s_1\Delta z$$

$$a_T = (D_t + \max(\dot{m}_t, 0.))\Delta s_1\Delta s_2$$

$$a_B = (D_b + \min(\dot{m}_b, 0.))\Delta s_1\Delta s_2$$

$$a_P = a_E + a_W + a_N + a_S + a_T + a_B.$$

5.5.2 Source Terms

The source term UV/r_ξ is a function of the dependent variable U in the U momentum equations and hence makes the source term non-linear. This source term is linearised by adding it to the a_P in following way:

$$a_P = \frac{UV}{r_\xi}\frac{1}{U} = V/r_\xi$$

Other source terms are treated explicitly, i.e. they are evaluated with the help of values from the previous iteration.

5.6 Concluding Remarks

The basic mechanism of coordinate transformation from physical to computational plane, derivation of governing equations including RANS equations and ASM equations, and their numerical implementation are discussed in this section, which can be summarised as follows:

- Important aspects of relationship between physical and computational coordinates including grid cell ares, grid aspect ratio and local distortion are established.

- The orthogonality condition, mean and maximum deviation from orthogonality and scale factors are discussed in detail. These terms play a vital role in the orthogonal grid generation and in the transformation of governing equations.

- Momentum balance and continuity equations, the k and ε equations with kinetic energy production terms and algebraic stress models of LY, NR and non-linear $k-\varepsilon$ are derived in curvilinear coordinates. This transformation from cartesian to curvilinear leads to additional source terms in equations, which take care of the centrifugal effects.

- Numerical implementation of converted equations remains similar to that of the original equations. The only difference is in the evaluation of control volume surface areas, which are multiplied by scale factors in the case of curvilinear coordinates. This, in fact, provides ease of computer implementations for numerical simulations.

CHAPTER 6

Results and Discussions

6.1 Introduction

The 3D RANS equations have been solved numerically in conjunction with the continuity equation to predict the flow mechanisms in a simple channel, a compound channel and compound meandering channels. The objectives of this chapter are to:

- investigate the flow by examining the effects of isotropic and anisotropic turbulence on it
- reproduce flow mechanisms with the help of the model
- validate the model by comparing the computed results with experimental data
- investigate the impact of anisotropy in a compound meandering channel of low sinuosity (s=1.093).

These objectives are achieved in four phases. In each phase, the complexity of the channel geometry is gradually increased.

1. **Simple channel**: The simple channel geometry is the most straightforward case considered here. Therefore, the simple channel flow simulation can be considered to be the first step towards the simulation of complex compound meandering channel flow. In this section, closed and open channel flow conditions are simulated to validate the model when the symmetry and free-surface boundary conditions are considered in conjunction with the rigid lid approximation at the surface. The ASMs discussed in Section 3.4 are tested to reproduce the secondary currents and their effects on the mean flow behaviour. The computed results are also compared with the published literature in this section (Section 6.2).

2. **Compound channel**: The performance of the masking array concept is thoroughly tested by simulating turbulent flows in a compound channel during the second phase of validation. In this section (Section 6.3), as in phase one, the effects of boundary conditions are tested in conjunction with the masking arrays concept whilst simulating the compound duct and open channels.

3. **Compound meandering channels**: In this phase of model validation (Section 6.4) , the model is applied to simulate the flows in compound meandering channels. The performance of the orthogonal coordinate system coupled with masking arrays are checked by simulating three different types of meandering channels (s = 1.093, 1.37 and 1.57). For each of the meandering channels, three different relative depths (Dr=0.0, 0.15 and 0.5) are also simulated.

4. **Anisotropy in compound meandering channel**: Finally, the LY model is applied for less sinuous compound meandering channel case (s=1.093) to investigate the effects of anisotropy on flow mechanism. For meandering channels, generally, the secondary currents are pressure driven, however in less sinuous channels, the secondary currents may be generated due to the

turbulence anisotropy (similar to simple channels) or due to the centrifugal forces (similar to meandering channel). In this section (Section 6.5), the effect of anisotropy on the secondary current generation mechanism is investigated.

While performing the simulations for a simple channel, compound channel and a compound meandering channel cases, fully developed flow is achieved using the periodic boundary conditions. This was achieved by checking the profiles at inlet and exit. For simple and compound channels, uniform flow was assumed to have established when the profiles became almost identical, proving that the shear forces on the walls of a flow domain is balanced by the force which drive the flow as follow:

$$-\left(\frac{\partial P}{\partial x}+\rho g sin\theta\right)\cdot Area=\int \tau_{wall}\quad dp \tag{6.1}$$

where the integral expresses integrated shear stress (τ_{wall}) over wetted perimeter (p). The convergence criteria was set to be achieved once the difference between the variable values of two successive iterations dropped below 0.1%. This optimum value was decided based on numerical experiments with different convergence criteria such as 0.01% and 1.0%. In presented results (Figures 6.1 to 6.70), the lateral axis represents the lateral distance y normalised by the channel depth h. The vertical axis expresses the vertical distance z normalised by h, which is taken from the channel bed. The velocities are normalised by the section averaged velocity $U_s = Q/A$, where Q is the total discharge and A is the cross sectional area at the inlet.

6.2 Simple Channel

The aim of this section is to judge the performance of the LY, NR and NLKE models by checking their ability to reproduce the turbulence driven secondary currents and their effect on the mean velocity profile. In this section, the predicted mean

velocity distributions, secondary currents and Reynolds stresses obtained from these models are presented and compared with published data in the literature (Section 2.2) for closed and open channel flows.

6.2.1 Closed Channel

A sketch of the closed channel duct is shown in Figure 6.1, which shows the axis configurations and respective velocity components. The geometry is axisymmetric in the y as well as z directions, hence only the bottom left quadrant is simulated. This geometries with aspect ratio of one for closed channel and two for open channel are widely adopted for benchmarking of computation for open channel flows. Figure 6.2 shows the non-uniform numerical grid of the bottom left quadrant adopted for the simulations. The number of control volumes used in the present study are 40, 40 and 100 in lateral, vertical and longitudinal direction respectively. During simulations, non-dimensional parameters (shown in Table 6.1) are used and the value of Reynolds number ($Re = 4U_*R/\nu$) is kept equal to 50000, where R is the hydraulic radius, θ is the bed slope and ν is the molecular viscosity. In Figure 6.3 (a) secondary currents and (b) longitudinal velocity contours for closed duct flow captured experimentally by Nezu and Nakagawa (1993) are presented, which will be used to validate the model.

Table 6.1: Non-dimensional hydraulic parameters considered for simple channel flow simulations

	Closed channel	Open channel
Height (H)	1.0	0.5
Width (B)	1.0	1.0
Aspect Ratio (B/H)	1.0	2.0
Reynolds number (Re ($\times 10^4$))	5.0	5.0
Channel slope (θ)	0	1/2000

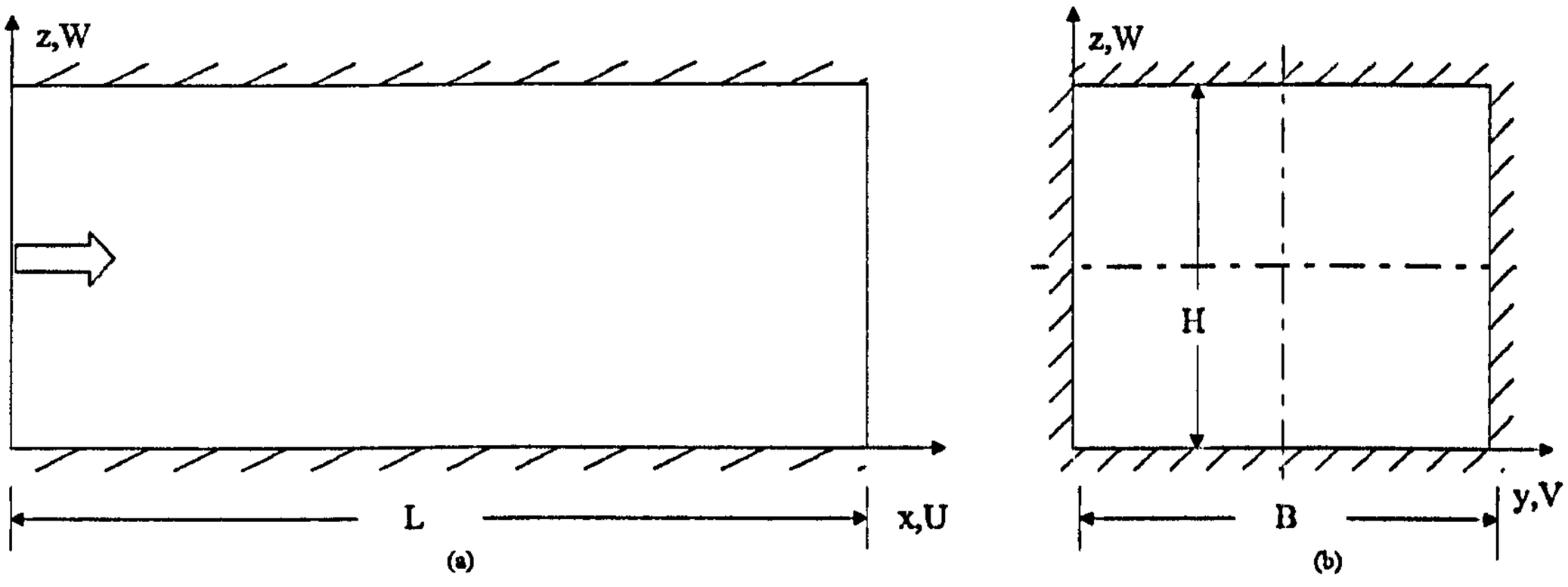

Figure 6.1: Typical sketch of a computational duct: (a) Longitudinal view (b) Cross sectional view, where L = length, B = breadth, H = height of the duct. U, V and W are mean velocities in x, y and z coordinates respectively. For simulations, only the bottom left quarter is considered due to the effects of axisymmetry.

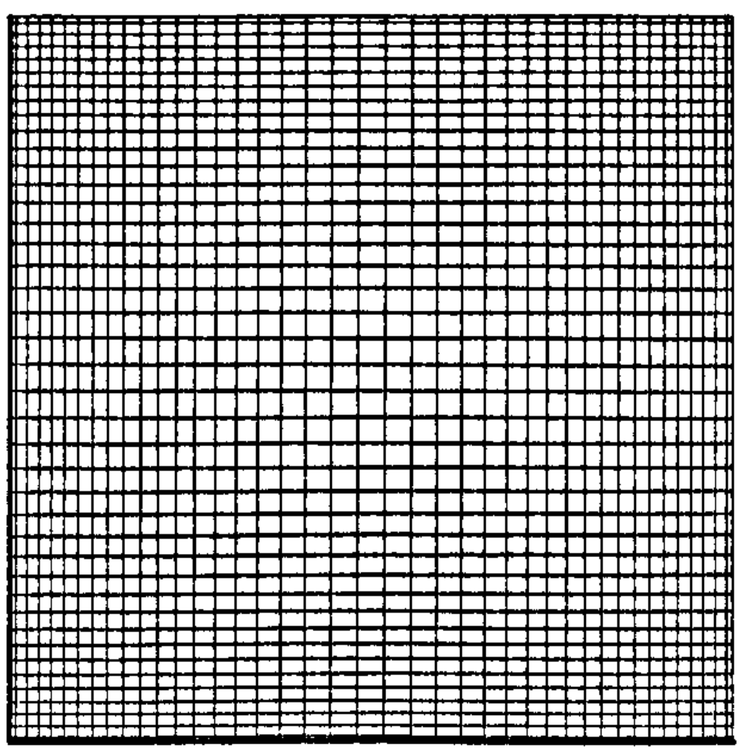

Figure 6.2: Non-uniform computational grid of one quadrant of the duct. The geometrical expansion factor (r) used for non-uniform grid generation is 1.05 (section 4.7.3). The number of CVs are (y, z) = (40,40).

The objective behind the simulation of closed channel flow is to validate the model with data from the literature when symmetry boundary conditions are imposed at the right and top boundaries (see Figure 6.2) of the domain. The symmetry or the zero gradient boundary condition is applied, in conjunction with the rigid lid boundary condition, for all the computed variables, including the Reynolds stresses in following way:

$$\left(\frac{\partial \phi}{\partial y}\right)_{right} = \left(\frac{\partial \phi}{\partial z}\right)_{top} = 0. \tag{6.2}$$

Figure 6.4 shows the isovel lines of the mean primary velocity normalised by the section averaged velocity calculated using (a) linear $k-\varepsilon$ model, (b) LY model, (c) NLKE model and (d) NR model respectively. It can be seen that for the LY, NLKE and NR models the isovel lines bulge markedly toward the corner along the corner bisector and slightly toward the core along the axes of symmetry. However, no bulging effect is observed in the case of $k-\varepsilon$ model, due to model's inability to calculate the difference in the Reynolds stresses responsible to generate the secondary currents. Naturally, the maximum velocity is predicted at the centre of channel. The predicted results from the ASMs are in close agreement with the experimental observations (see Figure 6.3 (a)), which display the the distortion of the contours towards the corner as a result of movement of high momentum fluid near the centre outwards along the diagonals.

Figure 6.5 shows the secondary currents predicted using (a) LY model (b) NLKE model and (c) NR model. It can be observed that the direction of secondary currents are from the centre towards the corner, from the corner towards the midpoint of adjacent walls and back to the centre parallel to the bisector of the wall. This phenomenon causes the bulging of the mean velocity isovels towards the corners and towards the centre of the channel. The maximum magnitude of secondary currents is observed to be 2% of the cross-sectional mean velocity. Again, the predicted secondary currents from all ASMs are well in agreement

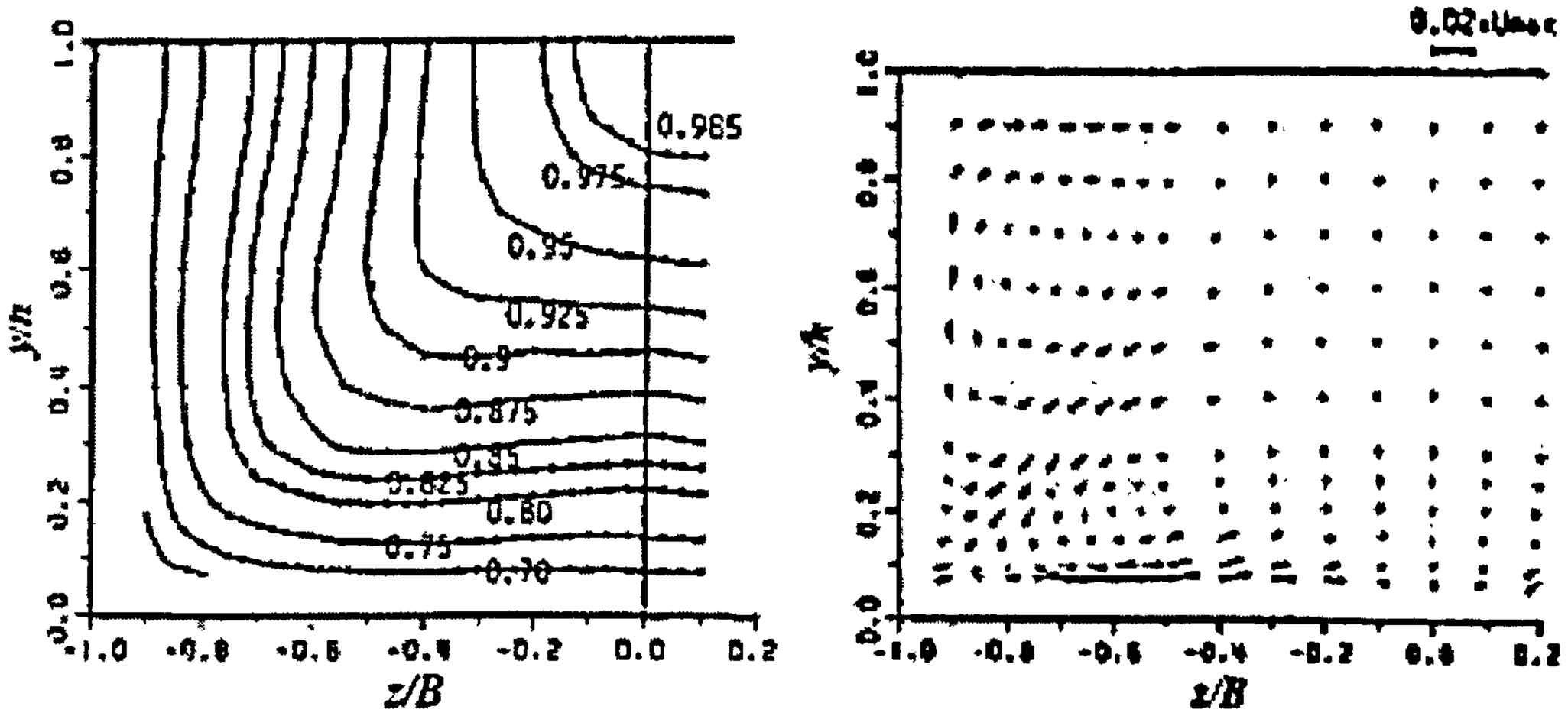

(a) (b)

Figure 6.3: Flow patterns in closed channel observed experimentally by Nezu and Nakagawa (1993): (a) Longitudinal velocity (U/U_s) isovels (b) Secondary currents.

with the experimental data as shown in Figure 6.3 (b) in terms of secondary circulation direction and magnitude.

From close observation, it can be seen that the locations and the pattern of secondary currents are slightly different for the LY, NLKE and NR models. The origins of currents in the LY model case are closer to the side walls compared to the NLKE and NR model cases, which causes a strong flow near the wall at $y/B = z/H = 0.3$. This also causes the bulging of velocity contours away from the side wall at same the location for the LY model. In the case of NLKE model, the mean velocity bulging is less intense towards the centre away from the walls along the axis of symmetry compared to the previous literature. Hence, NR model seems to have captured the secondary currents and its effect on mean velocity distribution in the best manner amongst all the implemented ASMs compared to the experiments.

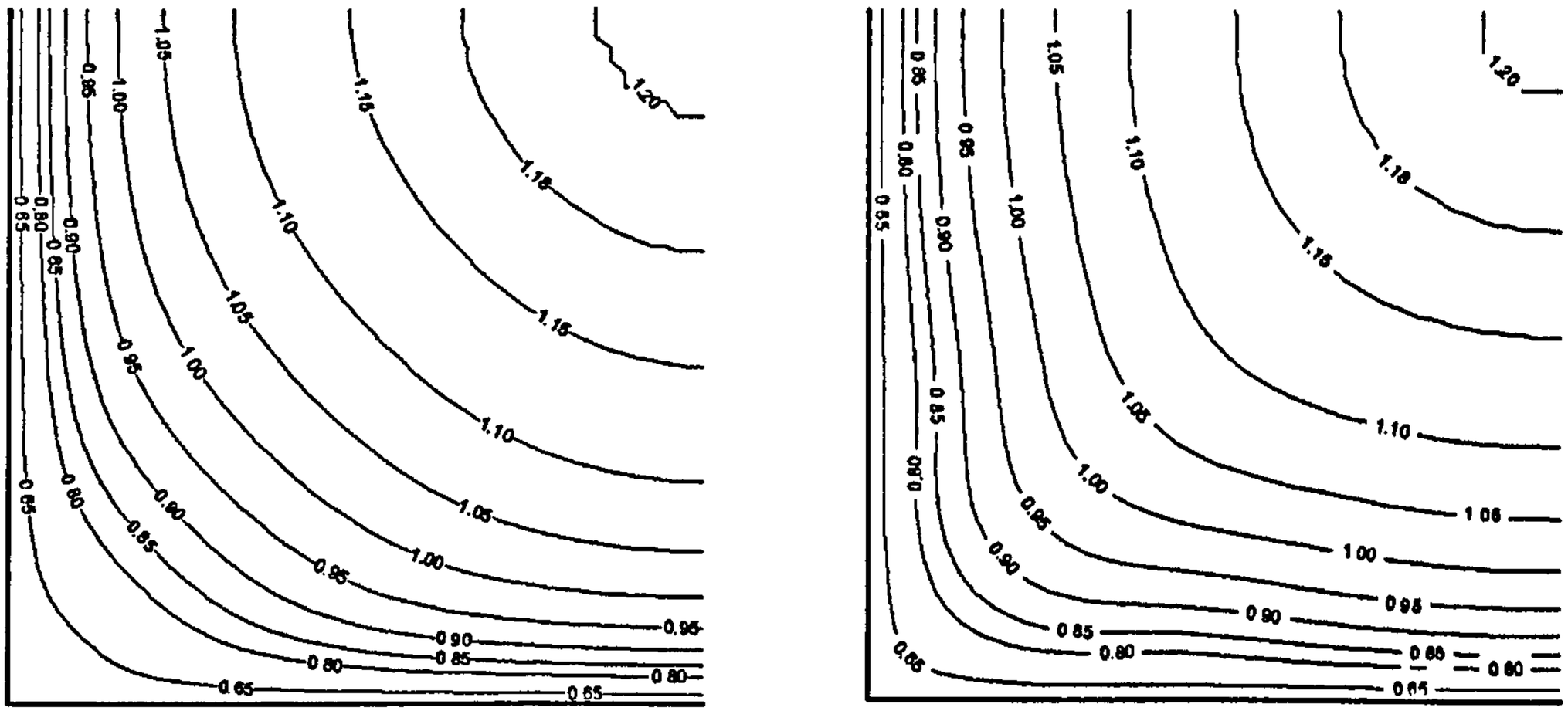

Figure 6.4: Prediction of the mean primary velocity distribution $U(y,z)/U_s$ using (a) $k-\varepsilon$ model (b) LY model (c) NLKE model and (d) NR model in a closed duct. The implemented anisotropic models are capable of predicting the bulging of isovel lines towards corner bisectors unlike the isotropic $k-\varepsilon$ model (Section 2.2). Mean velocity U is normalised with cross sectional averaged velocity U_s instead of maximum velocity. This leads to $(U(y,z)/U_s) > 1$ near channel core.

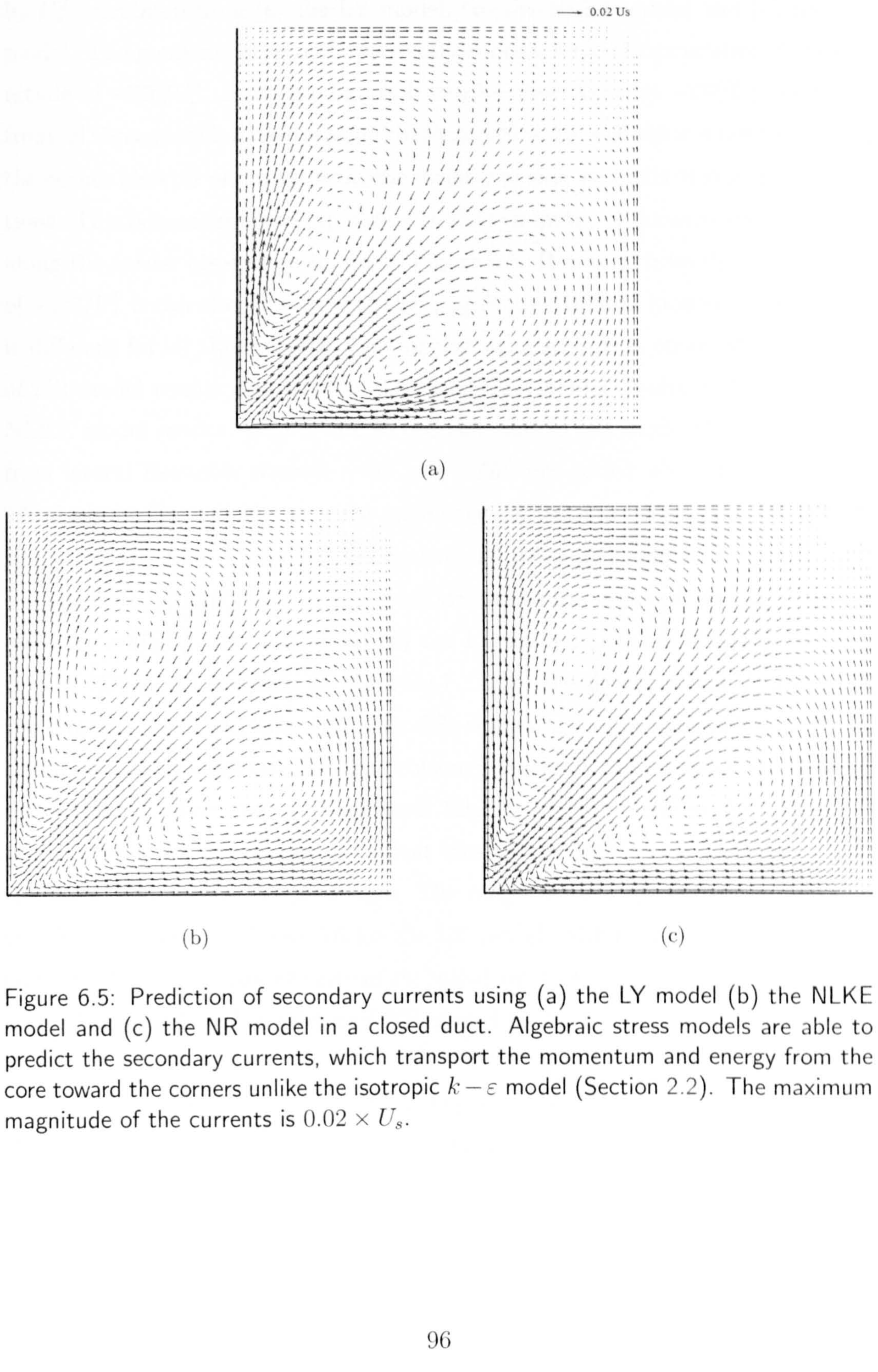

(a)

(b)

(c)

Figure 6.5: Prediction of secondary currents using (a) the LY model (b) the NLKE model and (c) the NR model in a closed duct. Algebraic stress models are able to predict the secondary currents, which transport the momentum and energy from the core toward the corners unlike the isotropic $k-\varepsilon$ model (Section 2.2). The maximum magnitude of the currents is $0.02 \times U_s$.

Figure 6.6 shows the distribution of turbulent Reynolds stresses $\overline{vw}$ normalised by U_*^2 calculated from (a) the LY model, (b) the NLKE model and (c) the NR model. The gradients of secondary velocity contribute to the generation and magnitude of $-\overline{vw}/U_*^2$. From the figure, it can be observed that $-\overline{vw}/U_*^2$ predicted from all three models have the same characteristics, i.e. the value is negative along the corner bisector and positive in the vicinity of side wall axis of symmetry junctions. This behaviour is corresponding to the symmetry of the secondary currents along the corner bisector as shown in Figure 6.5. However, from the distribution of $-\overline{vw}/U_*^2$ it can also be seen that the magnitude, size and location of the origin is different for all three ASMs. The highest value of 0.08 is observed in the case of NR model results compared to 0.01 in the LY model results and 0.02 for the NLKE model results. This is due to the fact that in NR model the contribution from lateral Reynolds stresses ($-\overline{uv}$ and $-\overline{uw}$) are added while calculating the $\overline{vw}$ algebraically, which makes the secondary current stronger as predicted from the NR model than LY model (see Section 3.4 for model equations).

The distribution of normal Reynolds stresses or the square of lateral turbulent intensity $-\overline{vv}/U_*^2$ computed from (a) the LY model, (b) the NLKE model and (c) the NR model is shown in Figure 6.7. From the figure, it can be seen that the intensity predicted from all the models is highest on the channel bed, steadily becoming lower as distance from the bottom increases, until the symmetry boundary is reached where the value is lowest. Slightly higher values are found close to the side wall. In general, the turbulent intensity is higher near the walls where the turbulence kinetic energy is high. The range of $-\overline{vv}/U_*^2$ is observed from 1.8 to 0.8, 2.0 to 1.0 and 2.0 to 0.6 for the LY model, NLKE model and NR model respectively. The square of vertical turbulent intensity $-\overline{ww}/U_*^2$ computed from the LY model, NLKE model and NR model is illustrated in Figure 6.8. The highest intensity occurs at the channel wall, as opposed to the bed, where the high lateral intensity occurred. This suggests that the intensity is reduced by the solid boundaries running perpendicular to the vertical plane. Moreover, the profile of $-\overline{ww}/U_*^2$ is mirror image of $-\overline{vv}/U_*^2$ at corner bisector, which is due

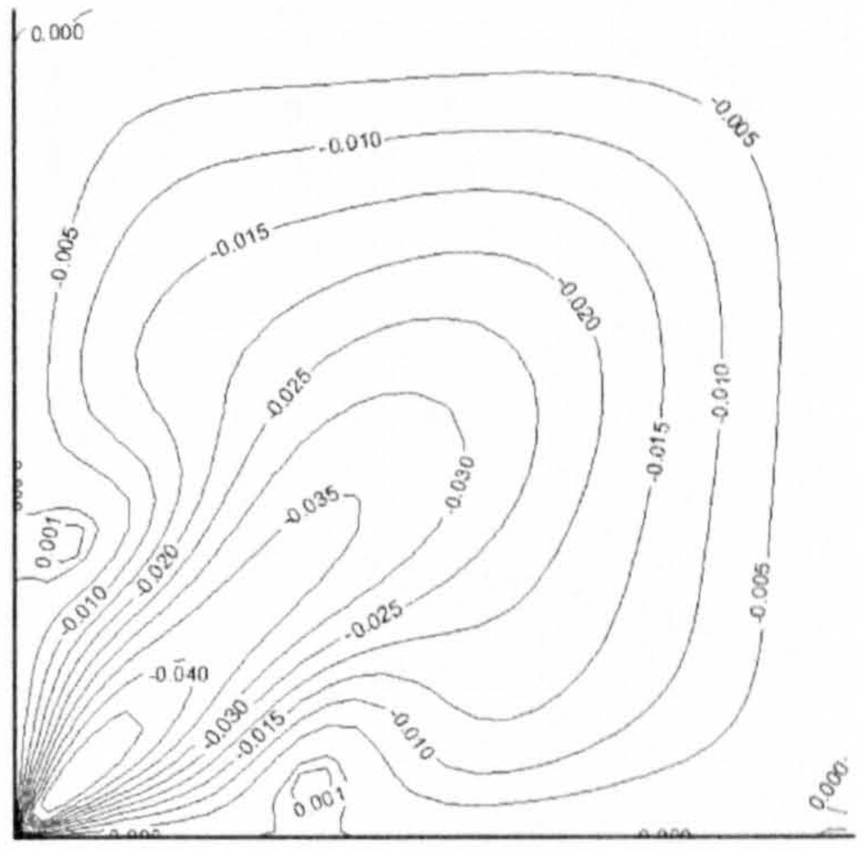

(a)

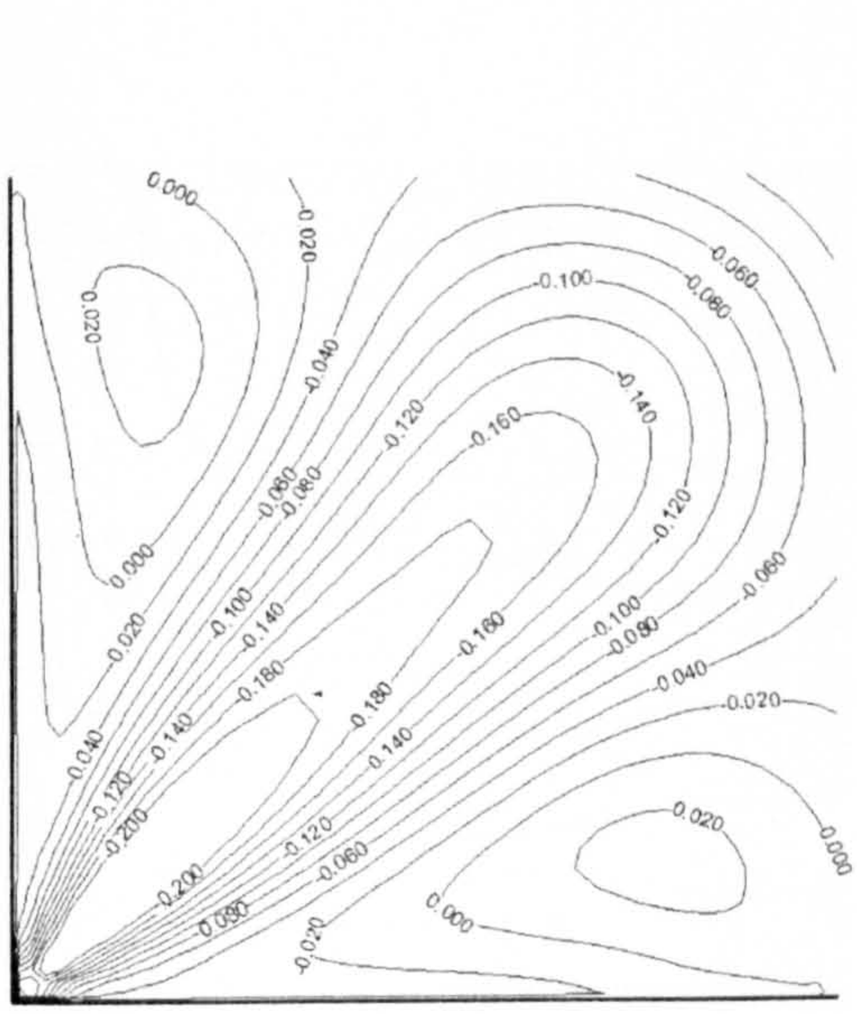

(b)

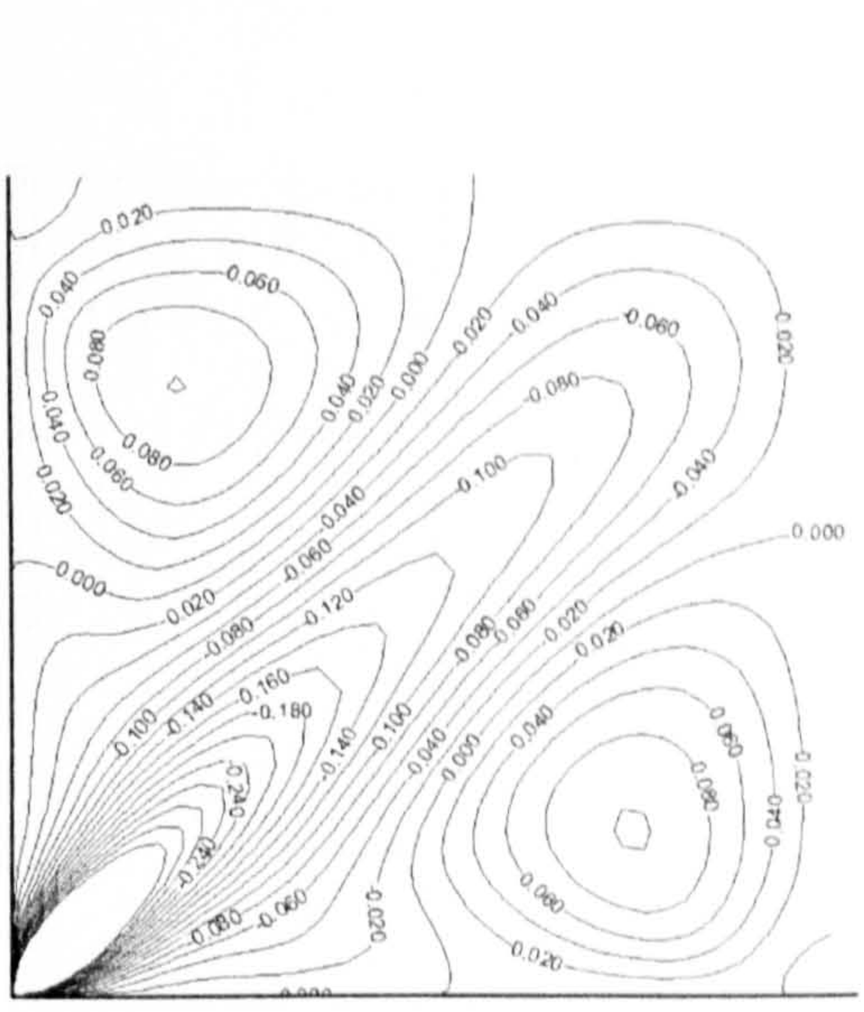

(c)

Figure 6.6: Prediction of Reynolds shear stresses $-\overline{vw}$ normalised by U_*^2 with (a) the LY model (b) the NLKE model and (c) the NR model in a closed duct.

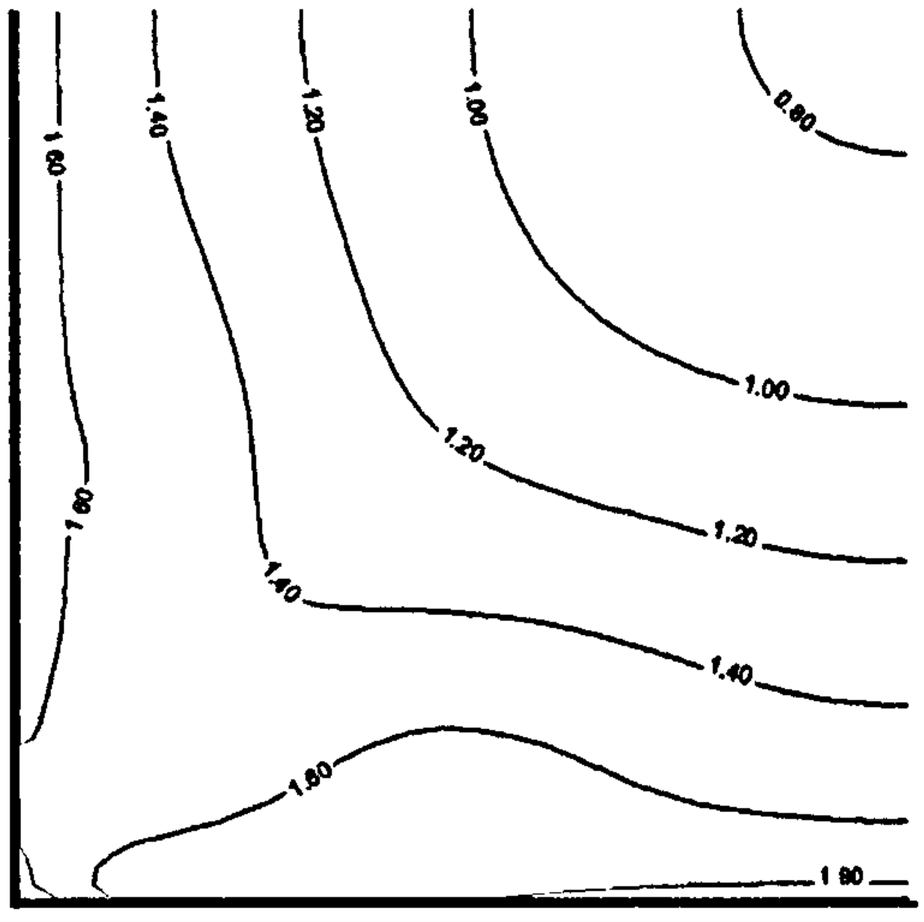

(a)

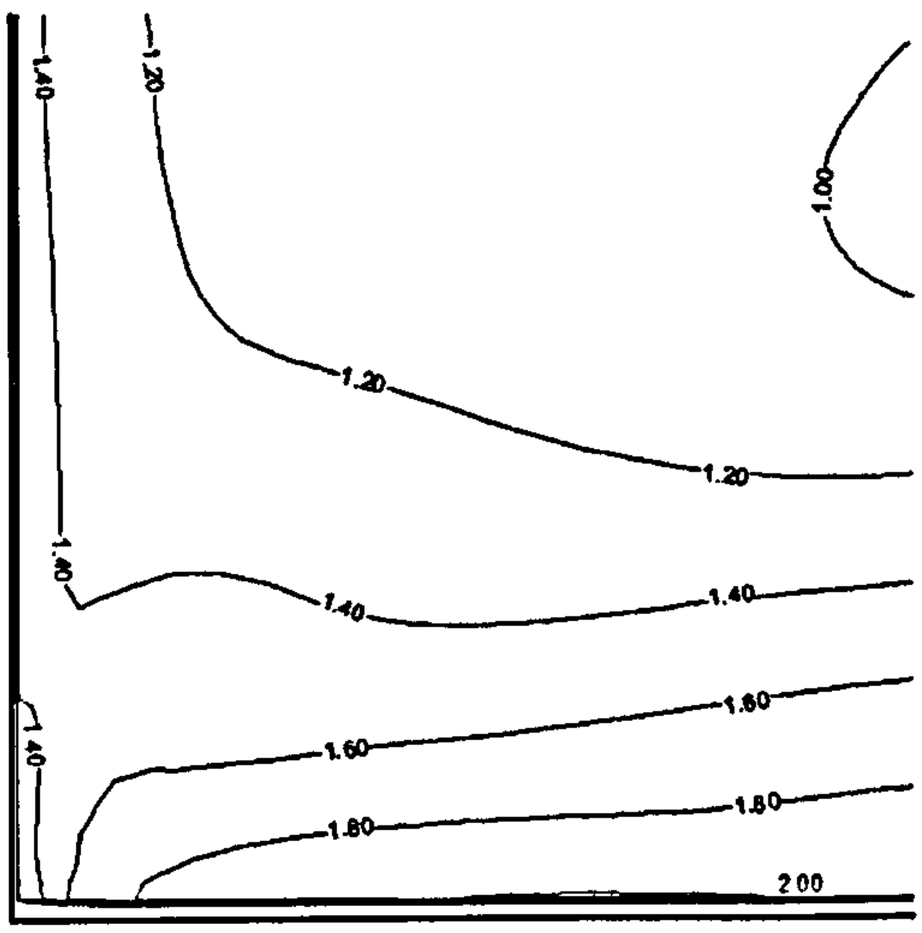

(b)

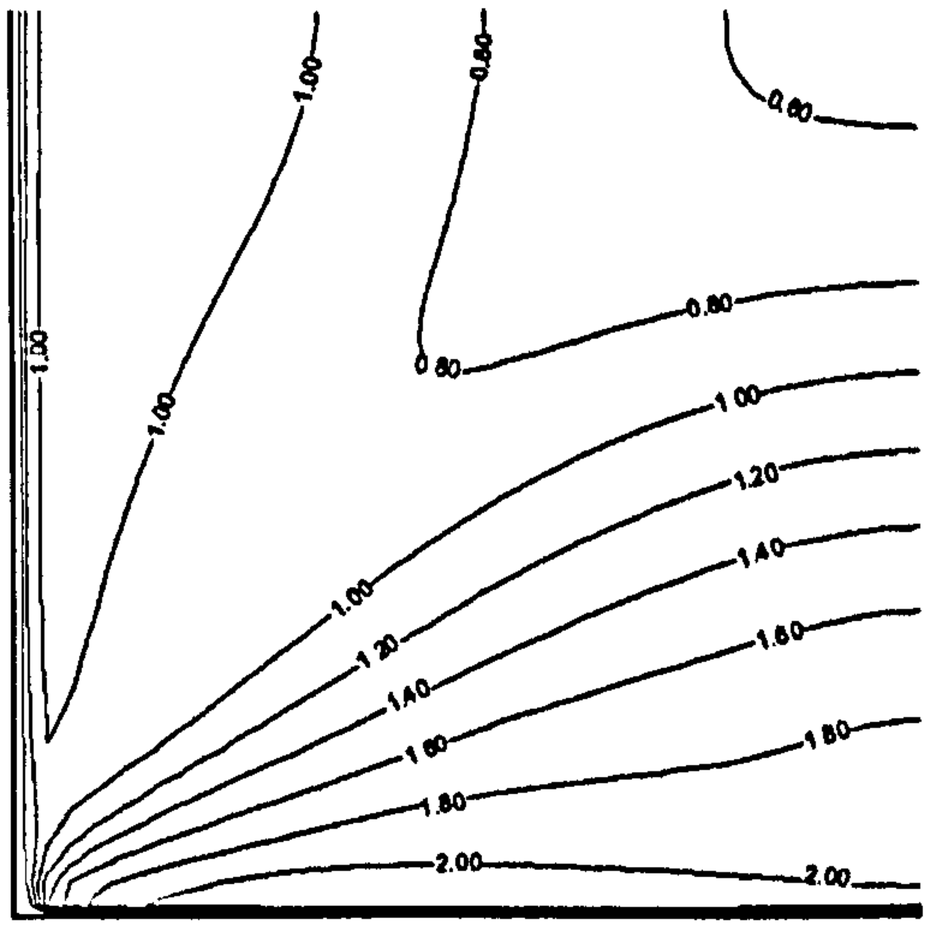

(c)

Figure 6.7: Prediction of Reynolds normal stresses $-\overline{vv}$ normalised by U_*^2 with (a) the LY model (b) the NLKE model and (c) the NR model in a closed duct.

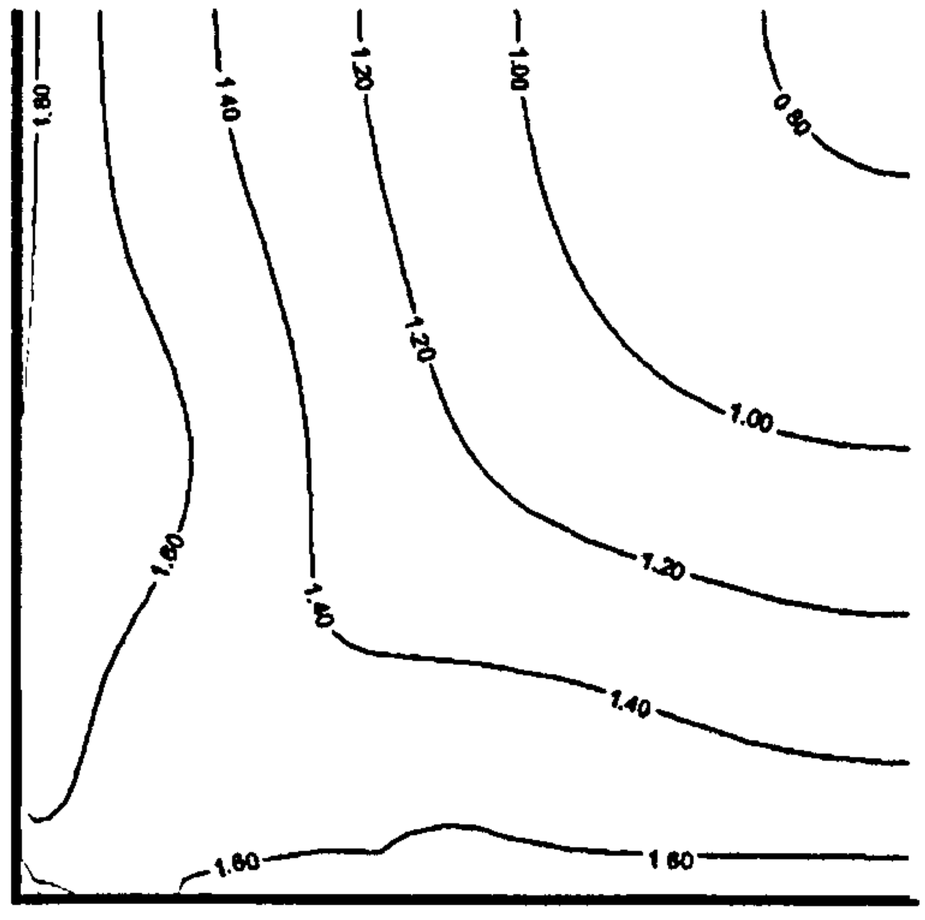

(a)

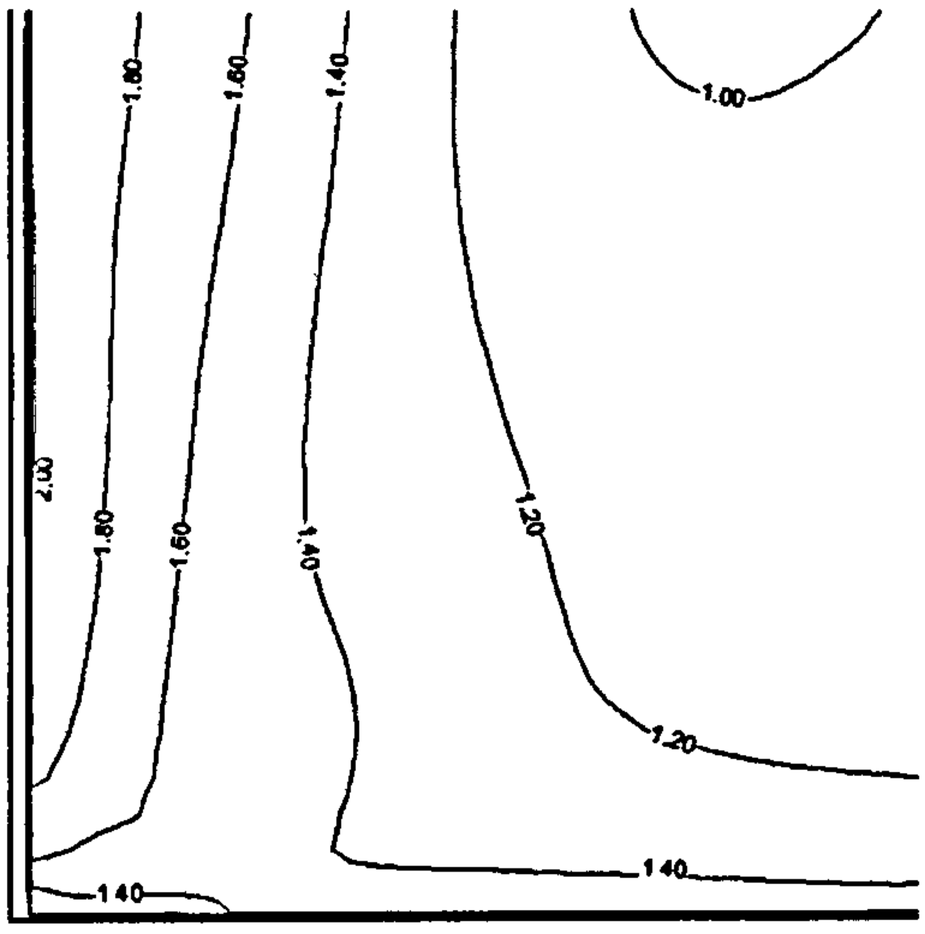

(b)

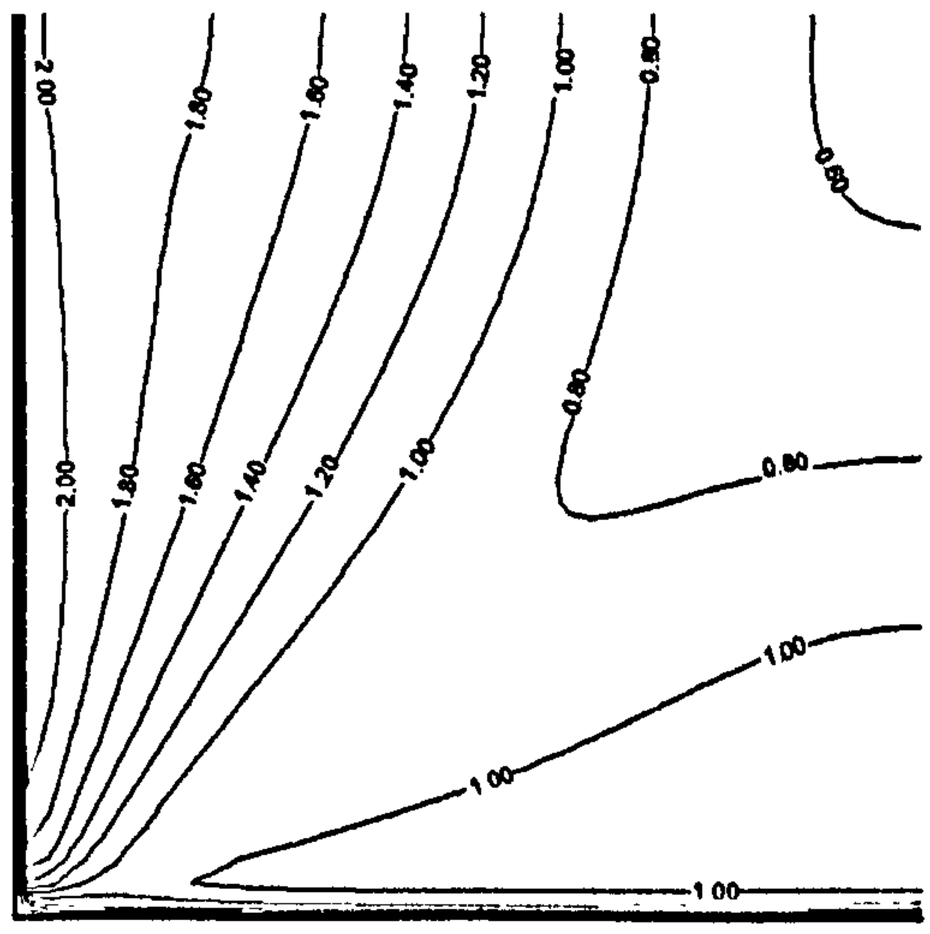

(c)

Figure 6.8: Prediction of Reynolds normal stresses $-\overline{ww}$ normalised by U_*^2 with (a) the LY model (b) the NLKE model and (c) the NR model in a closed duct.

to the symmetry boundary condition applied at both top and right sides of the quadrant. From the produced results it can be said that all the models are able to reproduce the separation between the vertical and transverse component, which drives the secondary currents and match reasonably well with the previous work of Nezu and Nakagawa (1993), Naot and Rodi (1982), Launder and Ying (1973) and others. The NR model has a more refined function for the distance of wall influence, and the effect of the free surface and symmetry. Hence, lateral fluctuations close to the horizontal symmetry boundary are enhanced, and damped close to the vertical ones compared to the LY model.

From these observations, it can be concluded that the prediction of the mean velocity distribution and secondary currents closely match with the previous literature. The implemented ASMs capture all the essential behaviour of the flow when the symmetry boundary condition is imposed at the top and right of the domain to simulate the flow in a closed channel. In terms of the secondary currents pattern, magnitude and its effects of the mean velocity profile, the NR model is found to predict the flow behaviour with the most accuracy in comparison with experimental data and will be carried forward to simulate open channel and compound channel flows.

6.2.2 Open Channel

In modelling open channel flow, it is assumed that the horizontal plane of symmetry in a duct flow is analogous to the free surface due to the fact that there is zero shear stress. However, the important difference is that in open channel flow, the vertical component of turbulent intensity is damped out at the free surface and the longitudinal turbulence intensity is increased (see Section 3.5.2 for details). This difference has been captured by imposing a free surface boundary condition, which can be expressed as

$$\varepsilon_{top} = \frac{C_\mu^{3/4}}{\kappa} k_{top}^{3/2} \left(\frac{1}{y'} + \frac{1}{0.07H} \right) \tag{6.3}$$

where κ is the von Karman constant, H is the depth of water and y' is the distance from the nearest wall. In this section the model is validated by reproducing the essential flow behaviour of open channel flow with the help of NR model and comparing with experimental data.

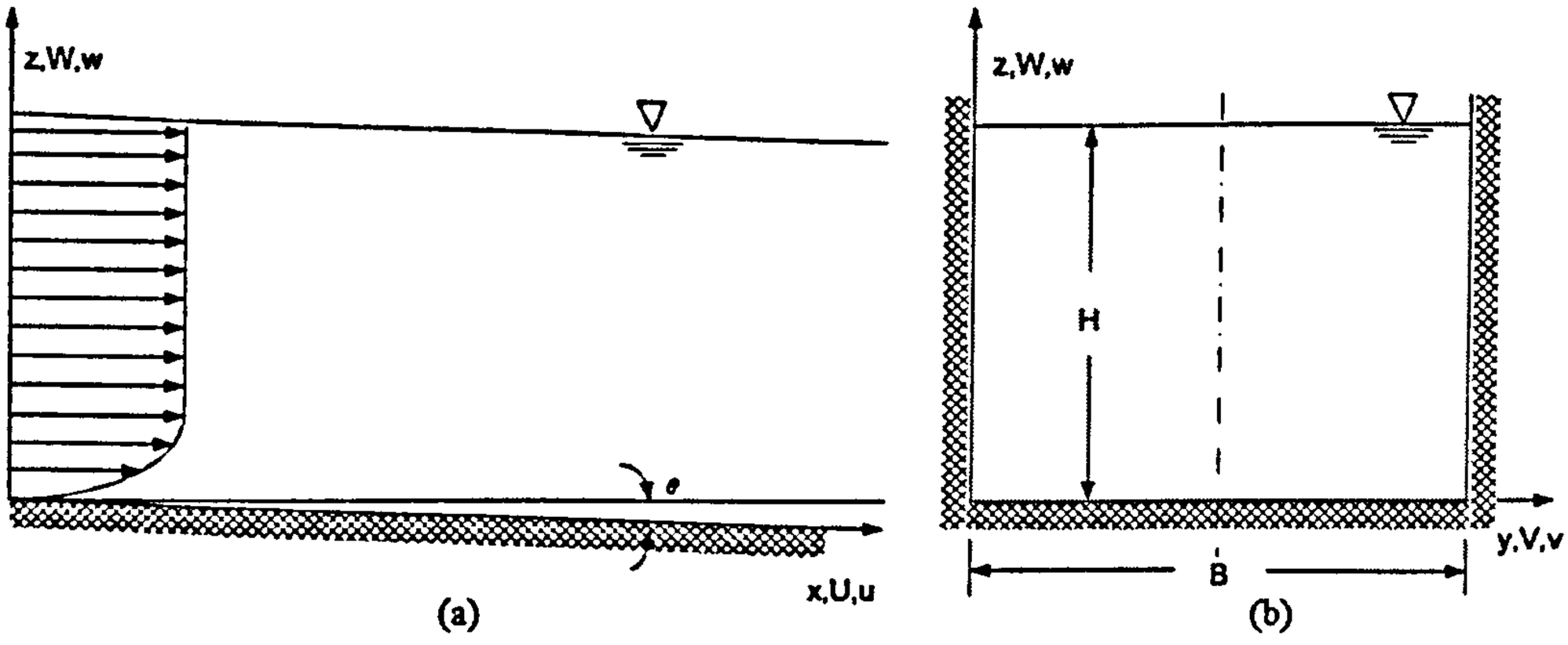

Figure 6.9: Typical sketch of an open channel: (a) longitudinal view (b) cross sectional view, where L = length, B = breadth, H = height of the open channel. U, V and W are mean velocities in x, y and z coordinates respectively and θ is the channel slope. For simulations, only half of the open channel considered due to the channel axisymmetry.

Figure 6.9 shows a sketch of the straight open channel with aspect ratio 2.0, which is used frequently for benchmarking in the literature (Naot and Rodi (1982), Nezu and Nakagawa (1993) and others). The channel slope and other non-dimensional hydraulic conditions are described in Table 6.1. As the geometry is symmetric about the z axis, only the left side of the channel is simulated. The numerical grid used for the closed channel, shown in Figure 6.2, is also used for open channel flow simulations. From the results of the closed channel simulations with different turbulence models, it was clear that the NR model produces better results as compared to the LY and NLKE models. Hence, only the NR model is carried forward for the simulation of open channel flow. In Figure 6.10 experimental observations of Nezu and Nakagawa (1993) for open channel (aspect ratio=2.0) is illustrated which shows (a) the longitudinal mean velocity contours

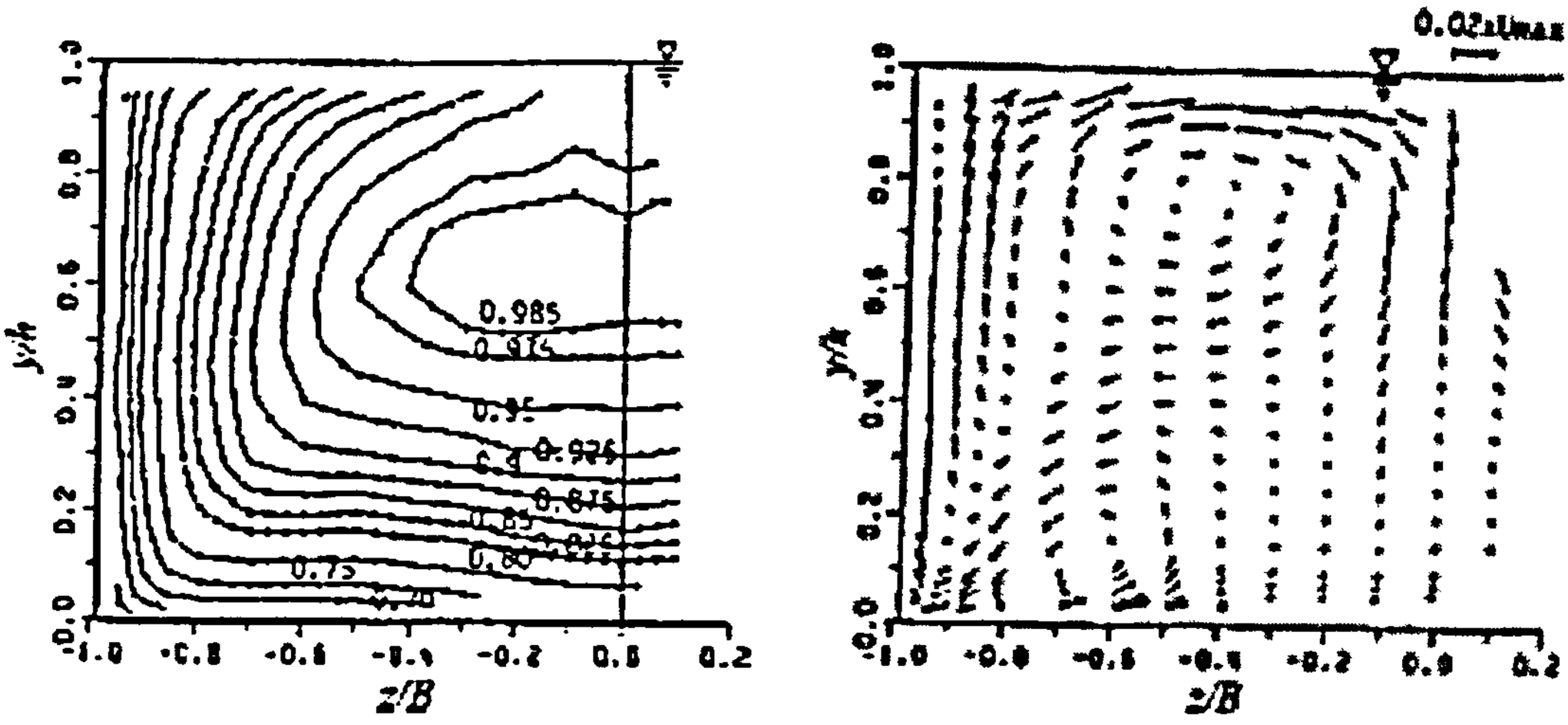

(a) (b)

Figure 6.10: Flow patterns in closed channel observed experimentally by Nezu and Nakagawa (1993): (a) Longitudinal velocity isovels (b) Secondary currents.

and (b) secondary currents. These results will be used to validate the model performance.

Figure 6.11 (a) shows the isovel lines of mean velocity (U) normalised with cross sectional average velocity (U_s). It can be seen from the figure that the isovel lines bulg toward the side wall, and they indicate a large retardation near the free surface. The maximum velocity is located not at the channel centre like duct flow but slightly below the free surface at $z/H = 0.6$. This effect, known as *the velocity dip effect* as discussed in Section 2.2, is captured well with the model in comparison to the experimental data shown in Figure 6.10 (a). The locations of points of local maximum streamwise velocity along the vertical line, generally known as max-line, is found along $z/H = 0.55$, which also match with the experimental data.

In Figure 6.11 (b) the velocity vectors of secondary currents are shown. The magnitude of the arranged secondary current is 2% of U_s, which is similar to that of the closed channel case. It can be observed from the figure that a strong vortex

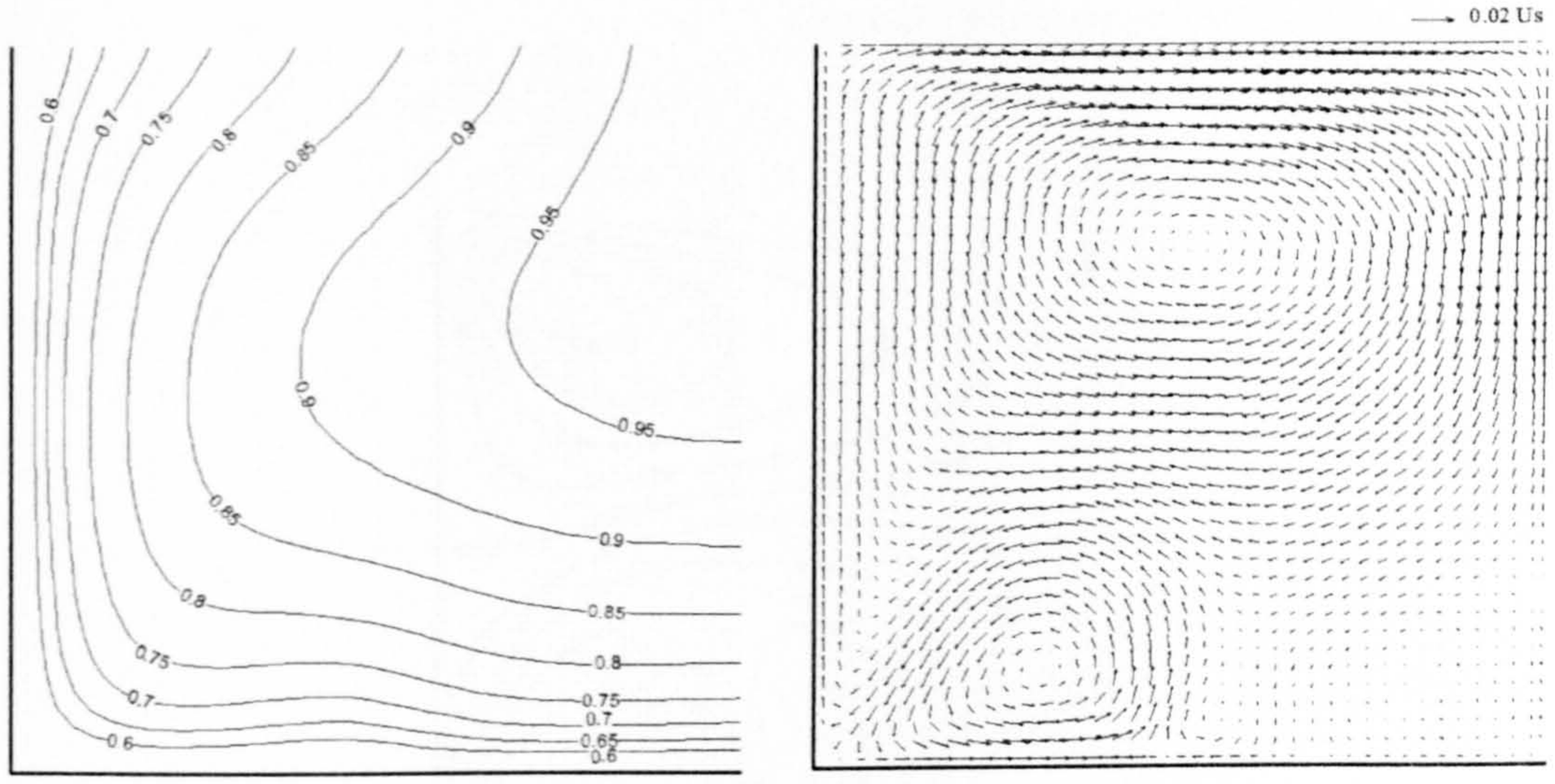

(a) (b)

Figure 6.11: Prediction of (a) mean velocity distribution normalised by $Umax$ and (b) secondary currents with help of the NR model in an open channel. The isovel lines bulge toward the sidewall and retardation near the free surface. The free surface damps fluctuations normal to it which causes a strong vortex near the free surface. The maximum magnitude of the currents is $0.02 \times U_s$.

occurs in the upper layer and is paired with a much small size vortex near the bed. These vortices are known as the *free-surface vortex* and the *bottom vortex* respectively. The presence of the free surface, dampens the vertical component of velocity and causes a strong free surface vortex. Moreover, the free-surface vortex is much stronger than the bottom vortex. The strong down flow occurring at the channel centre causes the velocity dip as longitudinal momentum is transferred from the free surface towards the mid-depth. The behaviour of the predicted secondary currents match reasonably well with the experimental data of Nezu and Nakagawa (1993) as shown in Figure 6.10 (b).

Figure 6.12 shows the Reynolds stresses normalised by U_*^2 using the NR model. From the profile of Reynolds shear stresses $-\overline{vw}/U_*^2$ [Figure 6.12(a)], it can be seen that near the water surface, there is a large area of positive $-\overline{vw}/U_*^2$ values.

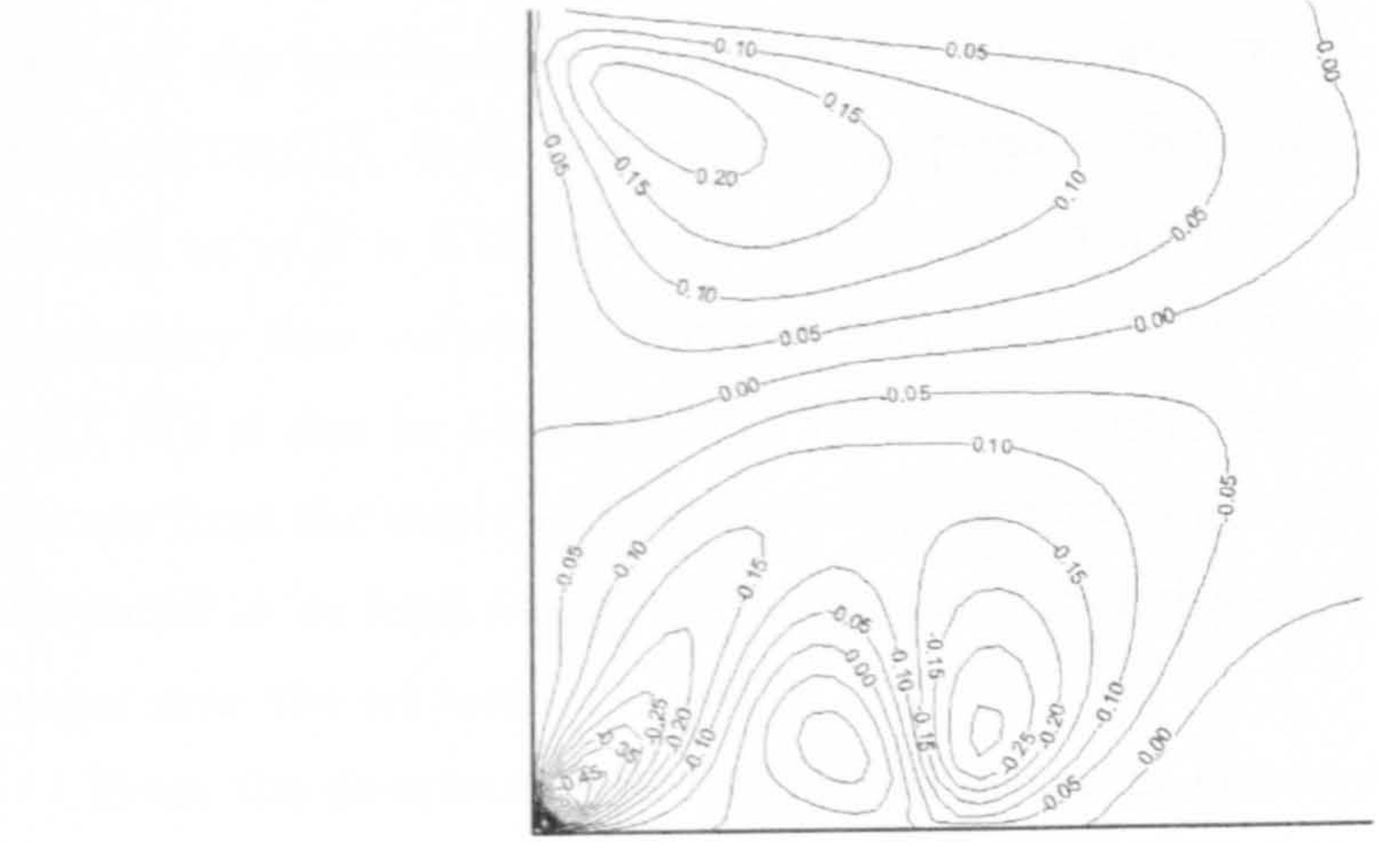

(a) (b) (c)

Figure 6.12: Prediction of Reynolds stresses with the NR model in open channel flows (a) $-\overline{vw}/U_*^2$ (b) $-\overline{vv}/U_*^2$ and (c) $-\overline{ww}/U_*^2$.

This is the only area of positive $-\overline{vw}/U_*^2$ in the channel and corresponds to the clockwise rotation of secondary flow (*free-surface vortex*) in the region $0.5 < z/H$, where as in close channel case [see Figure 6.6 (c)] positive values of $-\overline{vw}/U_*^2$ are seen at the junctions of symmetry boundary and walls. The largest negative value of $\overline{vw}/U_*^2$, -0.45, occurs where approximately $y/B = 0.15$ and $z/H = 0.15$ as well as $y/B = 0.15$ and $z/H = 0.55$, which corresponds to the anti-clockwise secondary flow vortex. On the examination of the secondary flow [see Figure 6.11 (b)] it can be observed that there is a strong current directed towards the corner from the water surface at an approximate angle of 45° to the bed, which is responsible for high negative value in the corner region compared to the positive value near the surface.

From the distribution of $-\overline{vv}/U_*^2$ as shown in Figure 6.12 (b) it can be seen that, similar to closed channel flow (See Figure 6.7 (c)), values are positive at the bed and gradually reduce toward the channel surface. However, values at side wall are less in magnitude (0.8) in the case of open channel compared to the closed channel (1.4), which is due to the free surface effect in open channel. The distribution of $-\overline{ww}/U_*^2$ calculated from NR model is illustrated in Figure 6.12 (c). It can be seen from the figure that, similar to the closed channel flow case (Figure 6.8 (c)), the values of vertical intensity are high at the side wall and reduces towards the free surface as well as towards the symmetry boundary. However, compared to the closed channel case, values of vertical intensity are less intense (1.8) compared to the closed channel (2.0). This is because in an open channel the vertical intensity is dampened due to the presence of free surface as explained earlier in beginning of this section.

The profiles of Reynolds stresses computed from the NR model are in good agreement with previous experimental (Naot and Rodi (1982), Kearney (2000)) and numerical findings (Naot *et al.* (1993b), Sugiyama *et al.* (1995)).

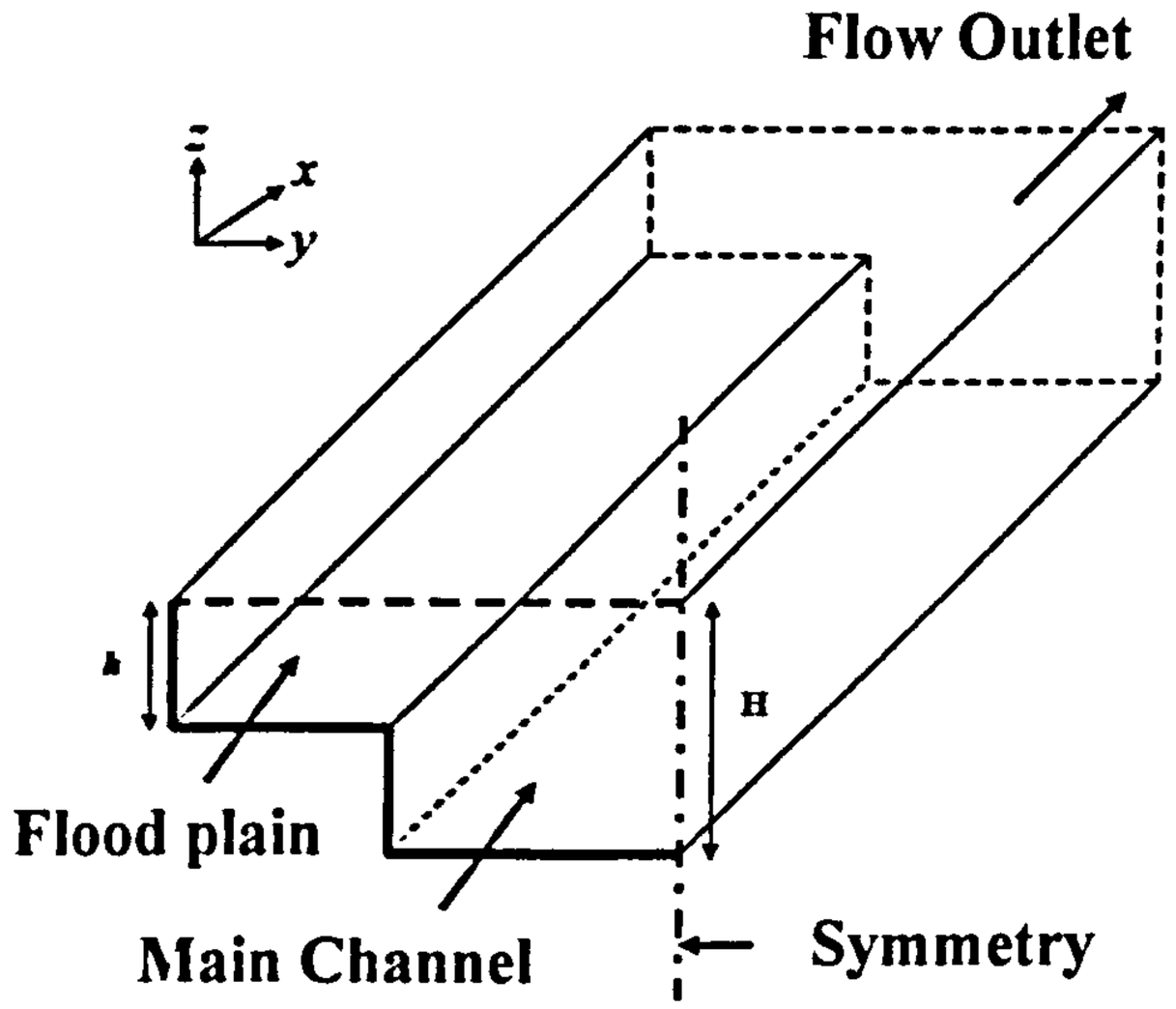

Figure 6.13: Typical 3D sketch of a compound channel showing the floodplain and the main channel. H is the total height of a compound channel and h is the height of a floodplain. The relative depth of a compound channel is define as Dr=h/H.

6.3 Compound Channel

A compound channel consists of a main channel and a floodplain. The flow in the main channel is faster than the flow in the floodplain. This difference in velocity generates shear layer and as well as secondary circulations in the cross-section, which ultimately influence the primary mean velocity field in the same way as in square and rectangular channels (Tominaga and Nezu (1990), Bradshaw (1987)).

In computations the cross section of the channel is modified with the help of the masking array concept to produce the compound channel cross-section. The compound channel geometry is created by blocking off unwanted CVs as discussed in Section 4.7.3.2. The purpose of this section is to assess the performance of the masking array concept by simulating closed and open compound channel flows. In this section, mean velocity profiles, secondary currents and Reynolds stresses, produced from the NR model are presented.

Figure 6.13 shows a sketch of the compound channel representing the main

Table 6.2: Non-dimensional hydraulic parameters considered for compound channel flow simulations

	Closed channel	Open channel
Floodplain height (h)	0.3	0.15
Floodplain width (b)	0.5	0.5
Total height (H)	0.8	0.4
Total width (B)	1.0	1.0
Relative depth (h/H)	0.375	0.375
Reynolds number (Re ($\times 10^4$))	10.0	10.0
Channel slope (θ)	0	1/2000

channel section, floodplain and flow configurations. For simulation purposes a narrow channel with relative depth (h/H) equal to 0.375 is considered to assess the model's ability to reproduce the compound channel flow behaviour. The computed results, especially the mean velocity profile and secondary currents are compared with the published results of Naot *et al.* (1993a). The non-dimensional flow parameters such as channel dimensions, Reynolds number and channel slope are shown in Table 6.2. The uniform finite volume grid generated for simulations is shown in Figure 6.14. The numerical grid comprised of 38 and 24 CVs in the lateral and vertical directions respectively. The highlighted portion is the blocked-off region in which no computations are performed.

6.3.1 Closed Channel

Similar to the simple channel flow case, discussed in Section 6.2, the compound closed channel is first simulated to check the model capability whilst applying a symmetry boundary condition at the top, coupled with the masking array concept.

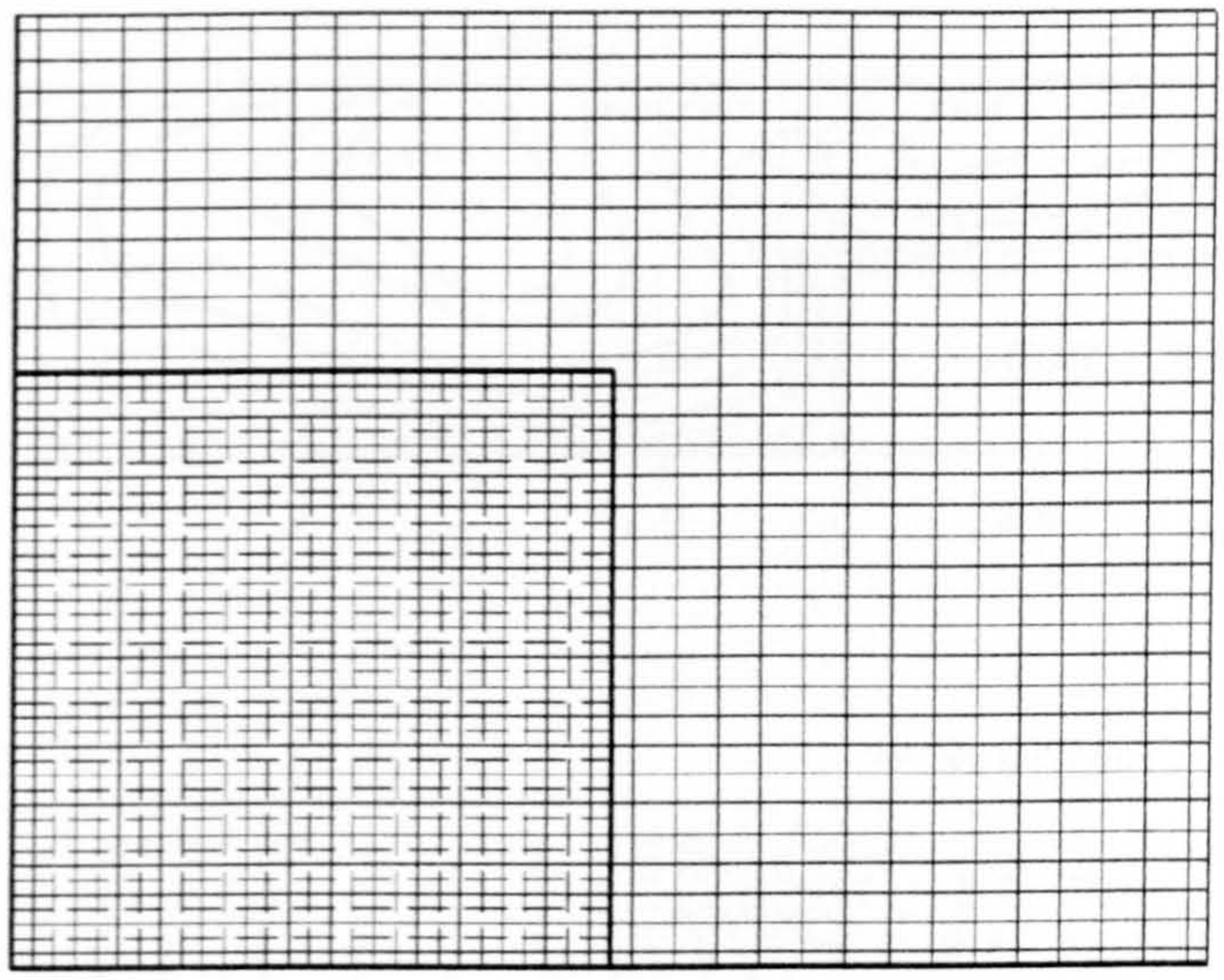

Figure 6.14: Uniform numerical grid of a compound channel. The highlighted bottom left corner is blocked off during computations. Number of CVs are (y, z) = (32,28). The relative depth, $h/$H, of a compound channel considered for numerical simulations is 0.375.

The longitudinal velocity distribution and secondary flow currents for the compound closed channel case computed from the NR model are shown in Figure 6.16.

Figure 6.16 (a) shows the longitudinal velocity distribution normalised by the sectional averaged velocity. Strong bulging in the contour lines is observed in the junction area between the main channel and the floodplain. On the left side on the channel $y/B < 0.5$ are higher than the rest of the channel. On the floodplain near the side wall, the longitudinal velocity decreases as the water surface is approached. This behaviour matches schematically with the experiments as shown in Figure 6.15 (a) and is further explained by the secondary currents.

Secondary currents for the compound closed channel are shown in Figure 6.16 (b). It can be observed that a vortex pair is formed in the main channel floodplain junction area. These vortices move fluid with low momentum from the junction towards the water surface, decreasing the velocity in this region and consequently causing the bulging in the longitudinal velocity contour. The vortex formed on the

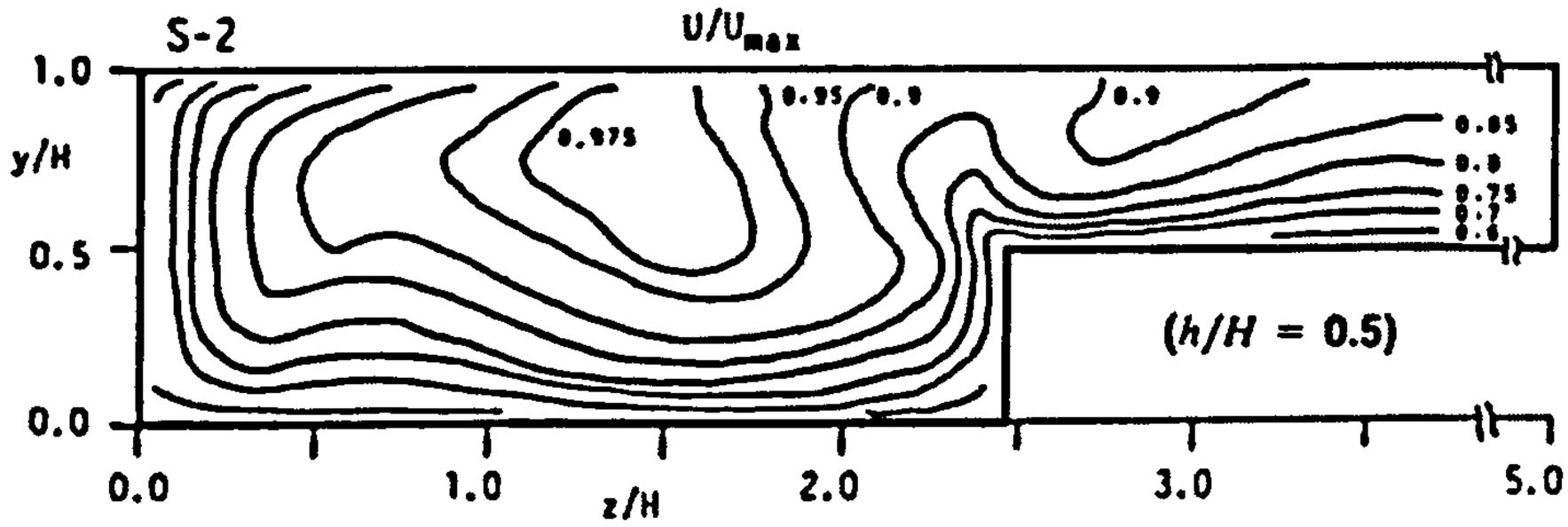

(a)

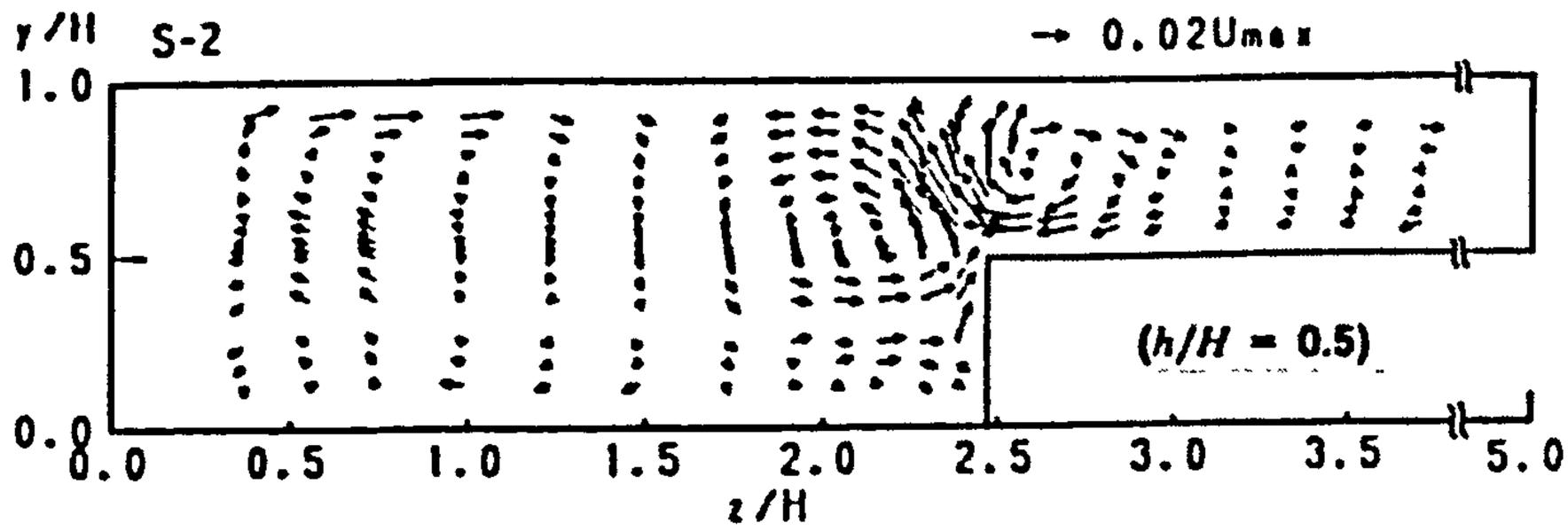

(b)

Figure 6.15: Flow patterns observed in compound open channel ($h/H = 0.5$) observed experimentally by Tominaga and Nezu (1990): (a) Longitudinal velocity contours (b) Secondary currents.

right hand side of the junction, moves downward after reaching the water surface, and carries fluid with high momentum toward the sidewall/corner of the main channel. The distortion of the longitudinal velocity (Figure 6.16 (a)) matches very well the current pattern in the region. The vortex formed on the floodplain, after reaching the water surface transfers high momentum fluid from the water surface region towards the corner of the floodplain. Due to the downward movement of this vortex toward the corner of the floodplain, another vortex is formed on the floodplain which occupies the rest of the part of floodplain. This behavior of secondary currents is also in good agrement with experimental data as shown in Figure 6.15 (b).

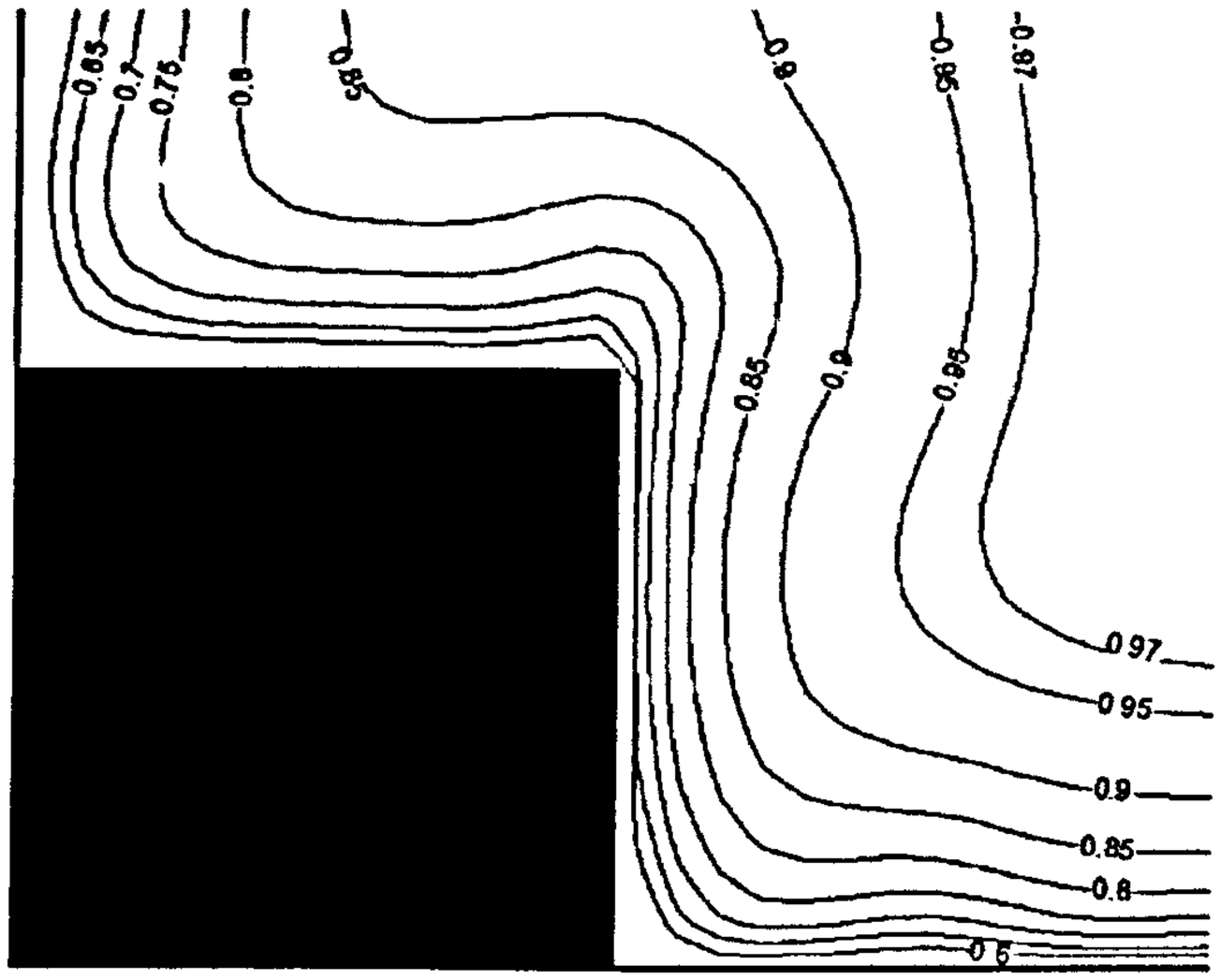

(a)

(b)

Figure 6.16: Prediction of (a) mean velocity distribution normalised by $Umax$ and (b) secondary currents in a compound duct using the NR model. The velocity difference between the main channel and the floodplain causes momentum exchange between them. This velocity difference also generates the shear layers and hence the vertical vortices along the interface between the main channel and the floodplain. The magnitude of secondary currents is found to be 2% of the U_s.

The maximum magnitude of secondary currents is about 2% of cross-sectional mean velocity. This value is in accordance with the values observed by Tominaga and Nezu (1990).

Figures 6.17 (a) shows the distribution of Reynolds shear stresses ($\overline{vw}$) normalised by the squared friction velocity U_*^2 calculated from the NR model. From the figure it can be seen that negative values of $-\overline{vw}/U*^2$ are observed in the corners of floodplain and main channel with a highest value of -0.10 in the main channel corner. At the side wall-symmetry boundary on the floodplain positive values are observed, which corresponds to a small clockwise circulation observed at the same location. At the main channel-floodplain junction, a clockwise circulation exists as well as an anticlockwise circulation, hence positive and negative values of $-\overline{vw}/U_*^2$ prevails at the same location.

From the profile of $\overline{vv}/U_*^2$ [see Figure 6.17 (b)], it can be seen that in a similar way to the simple channel flow, values are highest at the bottom of main channel (0.7) and floodplain (0.6) and gradually decrease toward the main channel-floodplain junction and symmetry boundaries. For $-\overline{ww}/U_*^2$, values are highest at side walls of main channel (0.6) and floodplain (0.5) and gradually decreasing towards the main channel-floodplain junction and symmetry boundaries as shown in Figure 6.17 (c).

The flow mechanism predicted by the NR model for the compound closed channel captures its essential behaviour, which is similar to that of the compound open channel shown in Figures 6.15. The results show that the concept of a masking array works with reasonably good accuracy and is able to reproduce the essential characteristics of compound closed channel flow.

6.3.2 Open Channel

Simulating compound open channel flow is the last step to be performed before simulating compound meandering channel flow. Hence, the purpose of this section is to validate the model, especially the masking array concept with the free surface

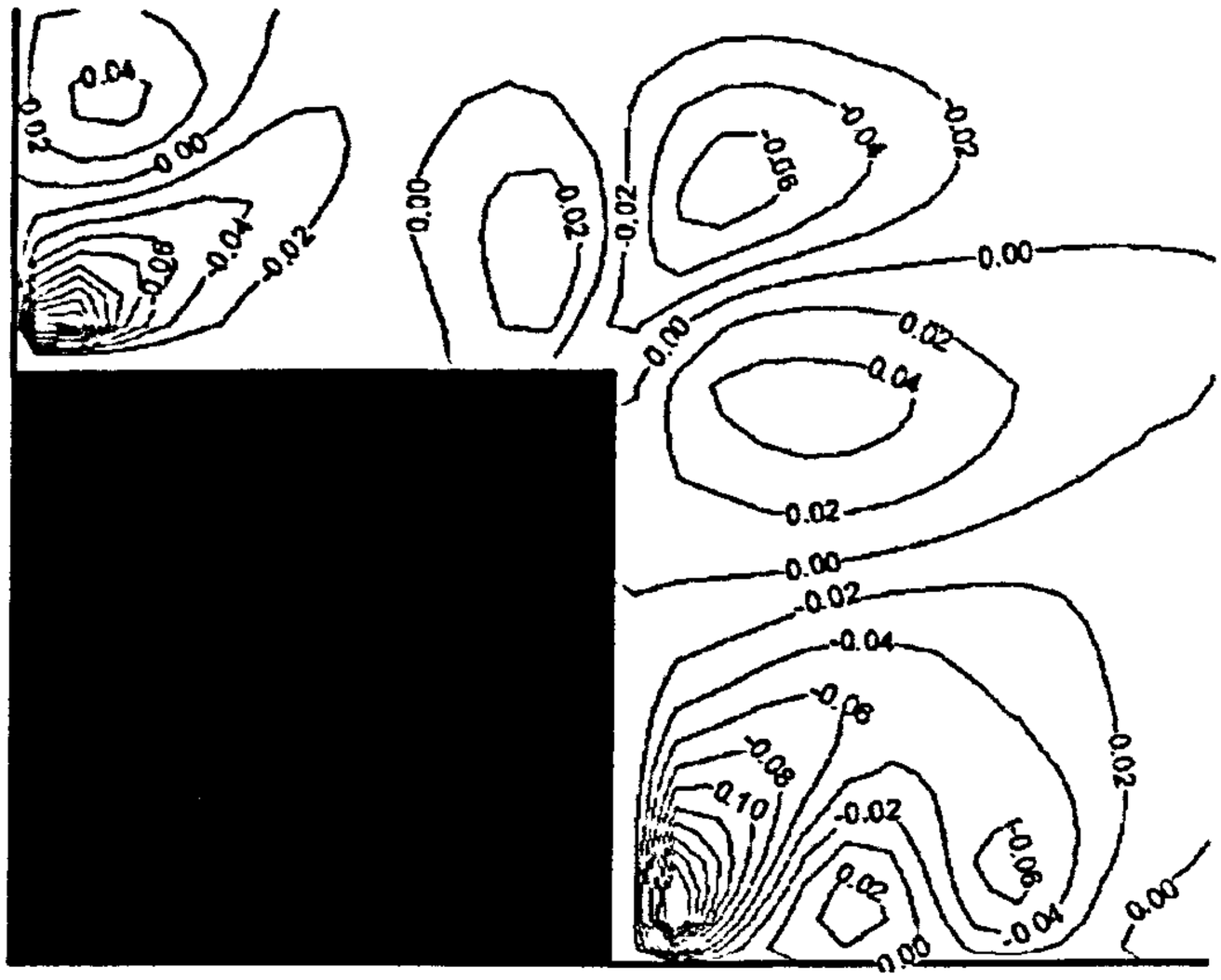

(a)

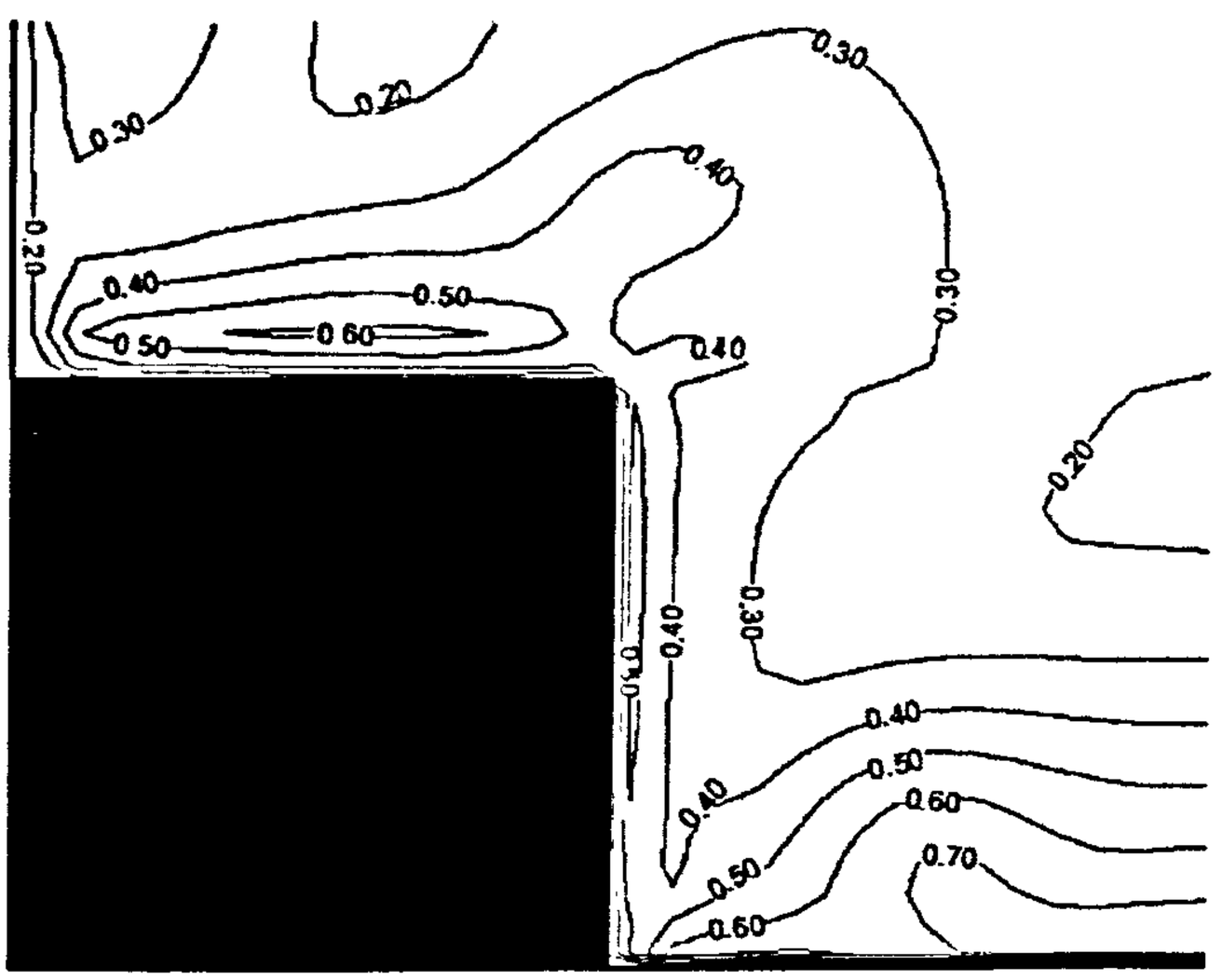

(b)

Figure 6.17: Prediction of $-\overline{vw}/U*^2$ and $-\overline{vv}/U*^2$ in a compound duct using the NR model.

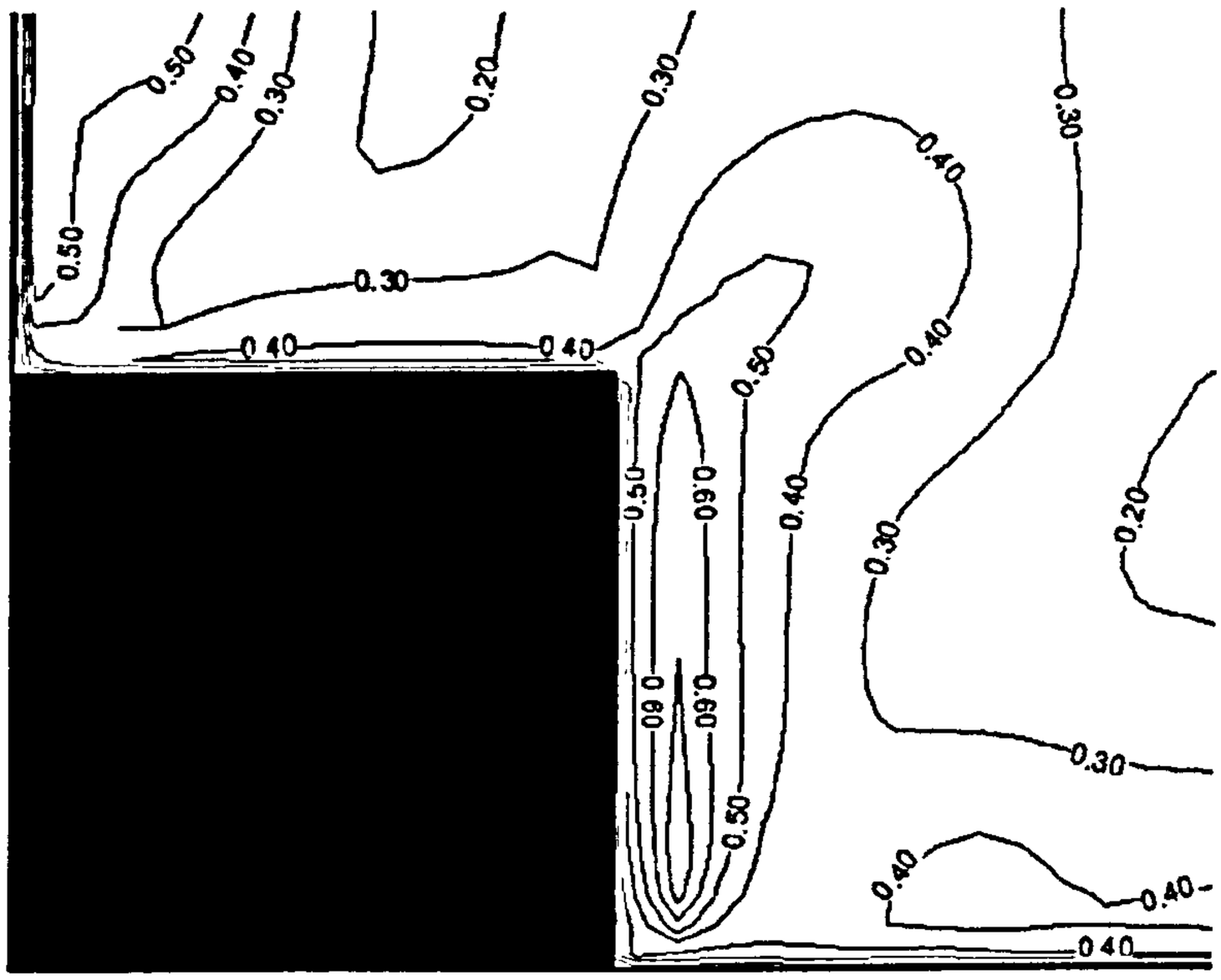

(a)

Figure 6.18: Prediction of $-\overline{ww}/U*^2$ in a compound duct using the NR model.

boundary condition, by reproducing compound open channel flow characteristics. The non-dimensional parameter are adopted for simulations are listed in Table 6.2. The numerical grid is the same as that used for the compound closed channel, shown in Figure 6.14.

The longitudinal velocity distribution and secondary flow currents for the compound open channel case computed from the NR model are shown in Figure 6.19.

The profile of longitudinal velocity (U) normalised by cross-sectional average velocity (U_s), shown in Figure 6.19 (a), is similar to the compound closed channel [see Figure 6.16 (a)], except on the floodplain and at the channel step. It can be seen that the longitudinal velocity decreases as it approaches the water surface on the floodplain ($y/B \leq 0.3$) and the effect is stronger compared to the closed channel case. At the floodplain main channel junction the bulging of longitudinal velocity is stronger towards water surface compared to the closed channel. In

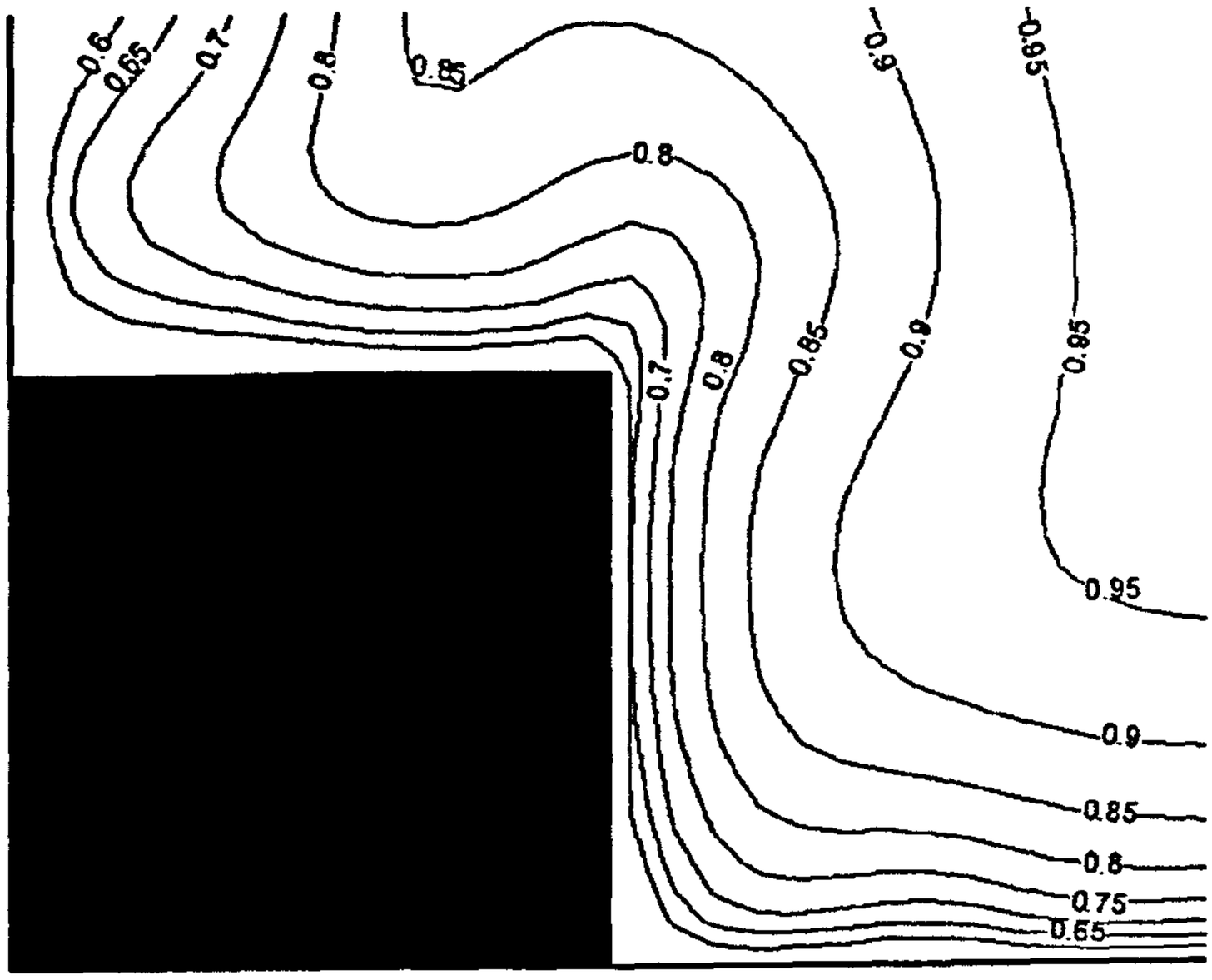

(a)

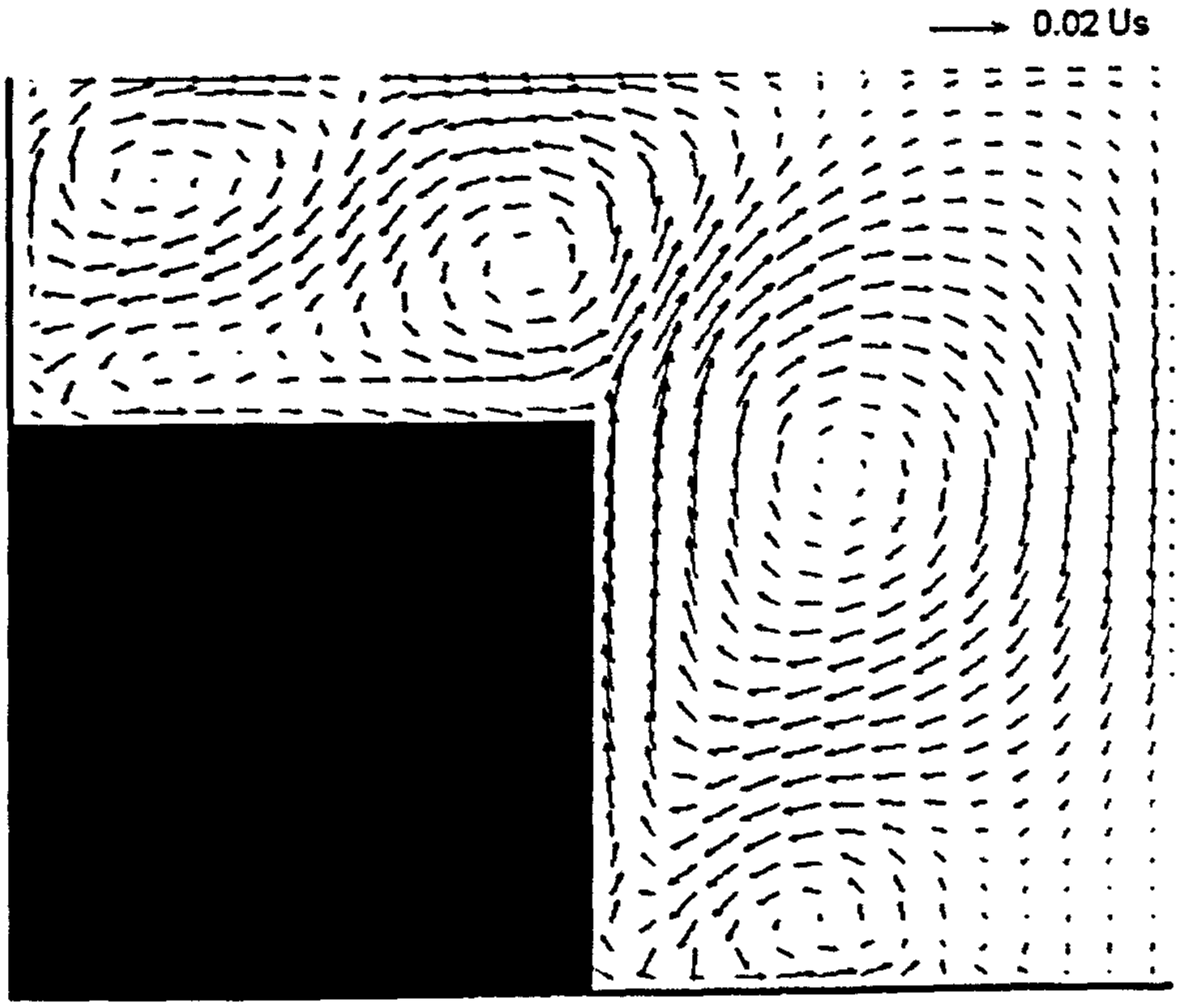

(b)

Figure 6.19: Prediction of (a) mean velocity distribution normalised by $Umax$ and (b) secondary currents in a compound channel (Dr=0.375) using the NR model. The magnitude of secondary currents is found to be 2% of the U_s.

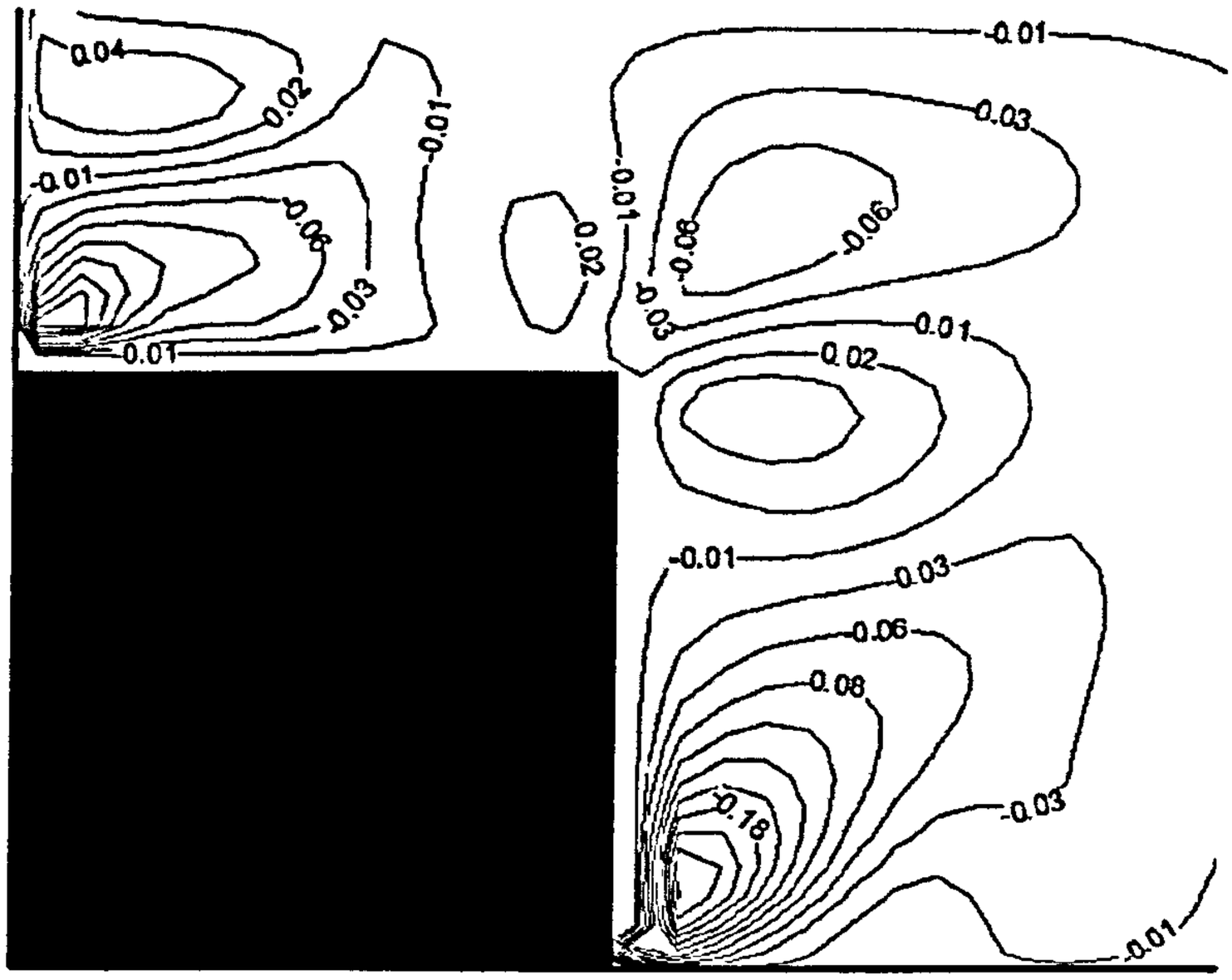

(a)

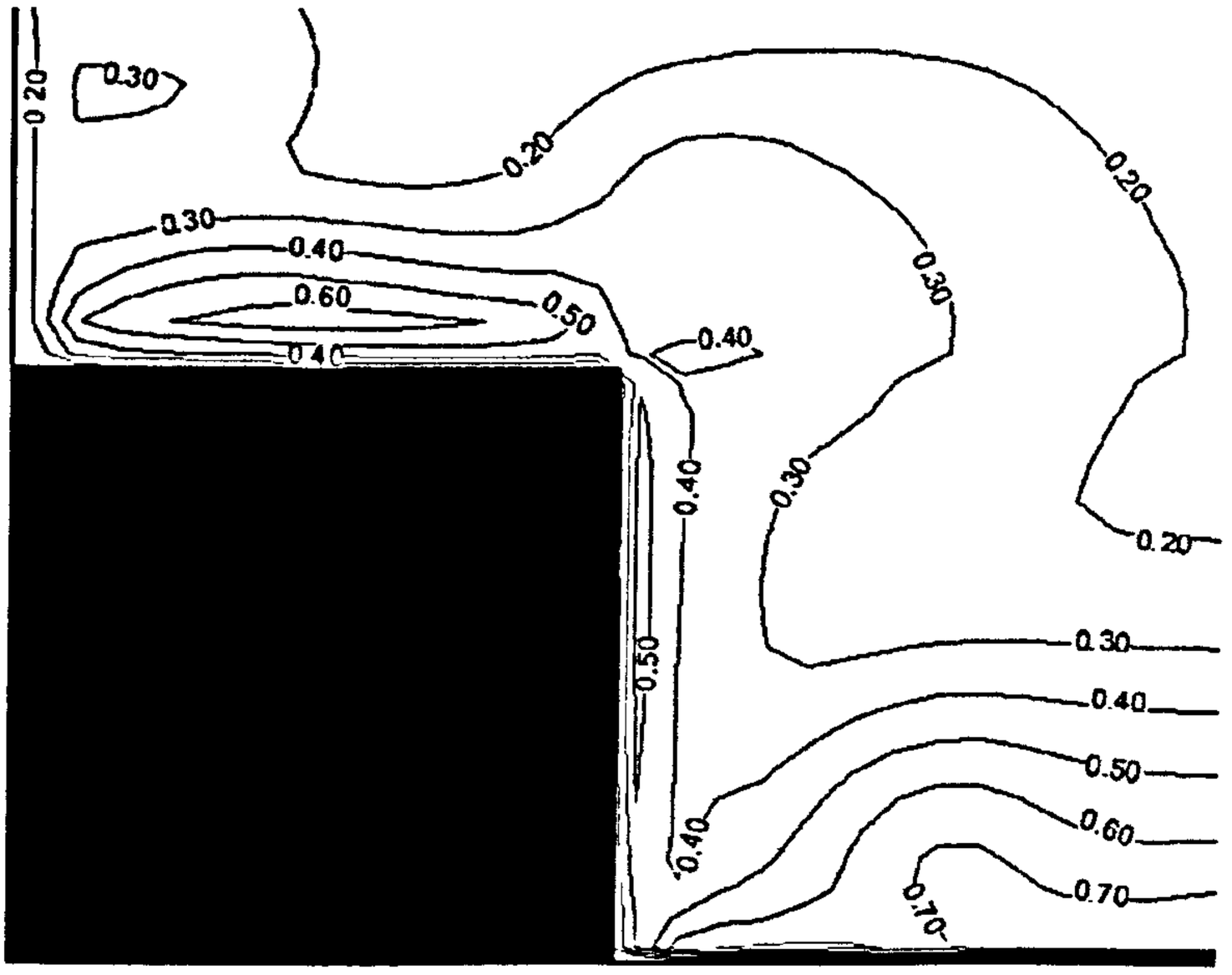

(b)

Figure 6.20: Prediction of (a) $-\overline{vw}/U*^2$ and (b) $-\overline{vv}/U*^2$ in a compound channel (Dr=0.375) using the NR model.

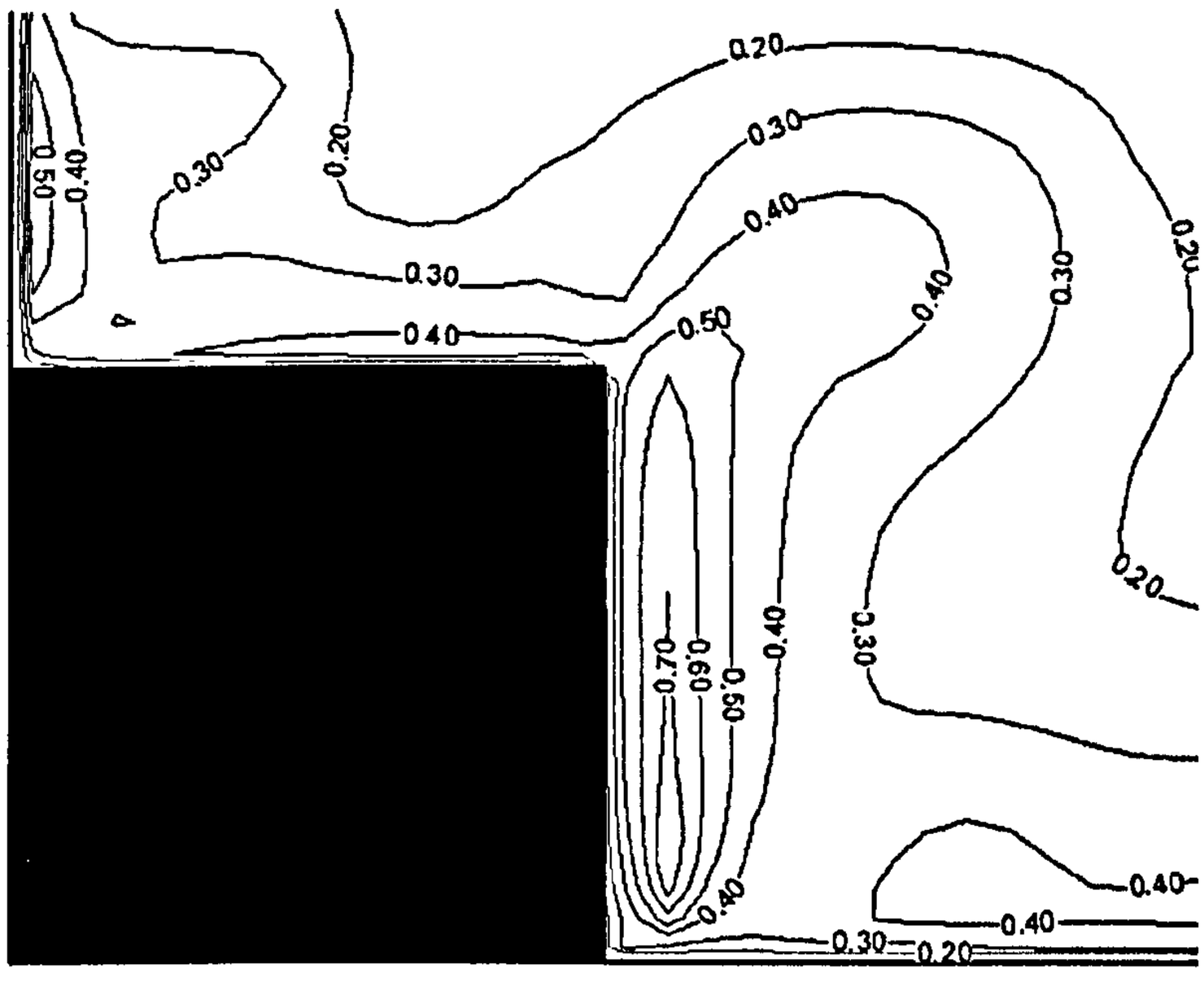

(a)

Figure 6.21: Prediction of $-\overline{ww}/U*^2$ in a compound channel (Dr=0.375) using the NR model.

the rest of the channel ($y/B > 0.5$), the distribution found similar to the closed channel. In general, the profile of longitudinal velocity distribution matches well with the experimental data as shown in Figure 6.15 (a).

The secondary currents for the compound open channel computed from the NR model are shown in Figure 6.19 (b). From the figure it can be observed that the small vortex at floodplain sidewall/free surface junction, observed in the case of compound closed channel [Figure 6.16 (b)], becomes stronger in the case of compound open channel flow. The floodplain vortex is observed strong compared to the closed channel case, which transfer the low momentum fluid from the junction towards the water surface causing the strong bulging at junction. The rest of the secondary current patterns remain similar to those of the compound closed channel. As discussed in Section 2.2 the presence of the free surface in the compound open channel reduces the turbulence length scale, retards the vertical

movement and increases the horizontal flow towards the channel center. This increases the strength of the small vortex at free surface-side wall junctions on floodplain. This behaviour of the secondary currents in compound open channel flow matches well with the experimental work shown in Figure 6.15 (b).

The Reynolds shear stresses, $-\overline{vw}$, normalised by squared friction velocity U_*^2 is shown in Figure 6.20. There is negative value in the region of the twin secondary flow vortices at the channel step. On the floodplain, the maximum negative value of $-\overline{vw}/U_*^2$ is -0.06 the the bottom region, corresponds to a anticlockwise circulation of secondary flow. In the free surface floodplain side wall region, $-\overline{vw}/U_*^2$ peaks at 0.04 correspond to a clockwise circulation. Compared to compound closed duct flow case [see Figure 6.17 (a)], the area of positive values at the free surface floodplain side wall region seems expanded, due to the stronger clockwise circulation at the same location. Within the area of main channel, no positive values are observed, which are seen in the compound close duct case, which may be due to the stronger secondary flow towards the main channel sidewall/corner and weaker pairing vortex, rotating anticlockwise, at the main channel corner.

Figure 6.20 (b) shows the distribution of $-\overline{vv}/U_*^2$ for compound open channel flow computed from the NR model. The peak intensity occur on the floodplain (0.6) and main channel (0.7) beds similar to the compound duct flow case [see Figure 6.17 (b)], which reduces rapidly at the free surface and channel center. In Figure 6.18, the square of vertical turbulent intensity normalised by friction velocity ($-\overline{ww}/U_*^2$) computed from the NR model is plotted. A noticeable difference between the values for closed duct case and open duct case is at the floodplain side wall free surface region. The presence of free surface in open channel dampens the vertical intensity and reduces the intensity of $-\overline{ww}/U_*^2$. This effect can be observed near the free surface, where $-\overline{ww}/U_*^2$ equal to 0.3 and 0.5 in the open channel case and closed channel case respectively as shown in Figure 6.18.

For masking arrays, secondary flow and other parameters in the corners of compound channels seem to be not quite same as simple channel cases. It may

be affected by setting boundary conditions differently from the simple channel case. However, this difference has not affected the flow behaviour in significant manner.

From the predicted results for the case of compound open channel flow using the NR model, it can be said that the masking array concept with free surface boundary condition captures the essential behaviour of the flow structures similar to produced by Tominaga and Nezu (1990) experimentally as shown in Figure 6.15. Hence it can be concluded that the concept of masking array coupled with a free surface boundary condition works with reasonably good accuracy.

6.4 Compound Meandering Channels

The flow in a compound meandering channel is characterised by the presence of strong helical secondary flow circulations in the streamwise direction and the variation of the flow parameters along the meander wavelength. The interaction between the main channel and floodplain flows also plays a crucial part in the flow behaviour.

In this section, the concept of orthogonal coordinates (see Chapter 5) is applied to reproduce the compound meandering flow behaviour. The objective of this section is to check the performance of the governing equations in orthogonal coordinates coupled with a masking array by simulating compound meandering channel flows. The complicated flow mechanism within compound meandering channels is governed by the sinuosity of the channel and relative depth of the flow besides other parameters. Therefore, three different cases of sinuosity with three different relative depths of flow are simulated and discussed in terms of the effect of sinuosity on floodplain flows.

Figure 6.22 shows an idealised sketch of the compound meandering channel in which the sinuosity (s) is defined as the ratio of curved channel length to straight valley length. The algorithm to generate orthogonal grids is discussed

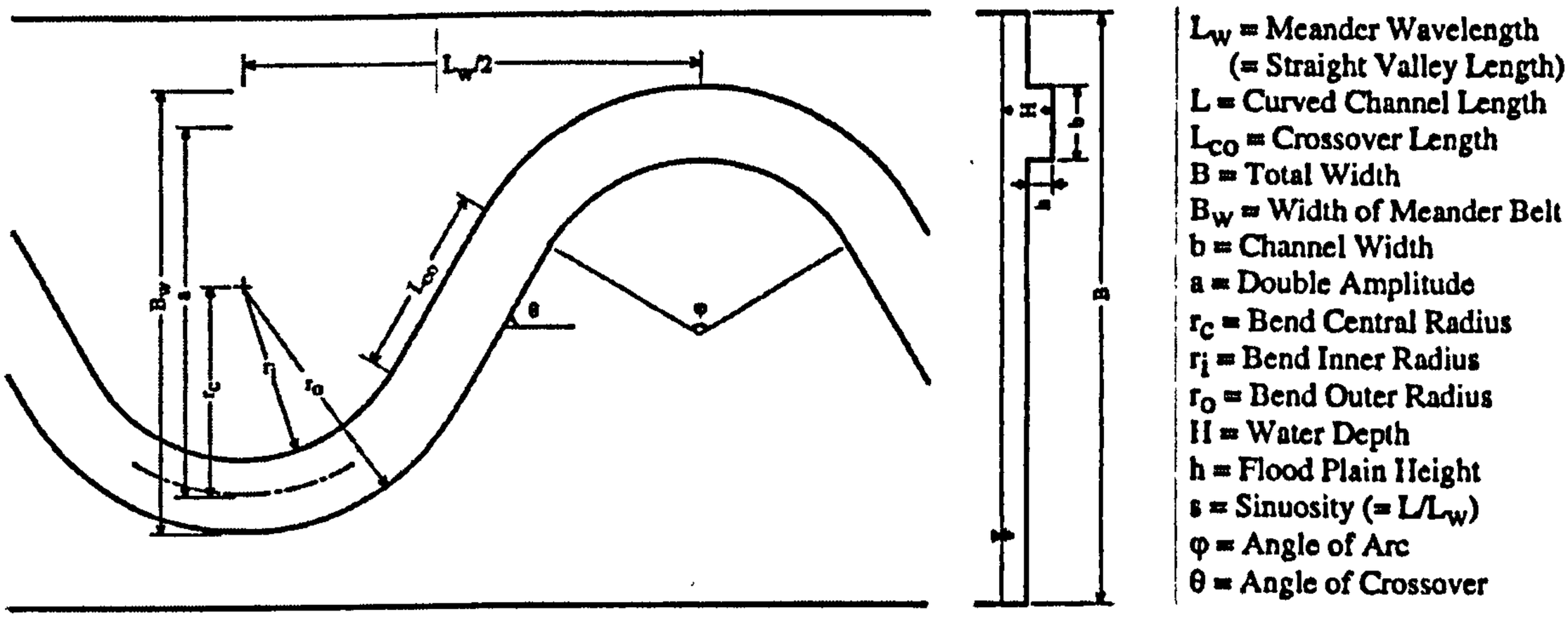

Figure 6.22: Sketch of an idealised compound meandering channel explaining various terms (after Muto (1997)). The sinuosity of a meandering channel is define as the ratio of curved channel length to straight valley length. The starting point of a meandering wavelength is known as the apex region. Inner apex and outer apex regions are at r_i and r_o respectively. Three different cases of sinuosity (s = 1.093, s = 1.370 and s = 1.570) are simulated in the this research.

in detail in Section 4.7.3.3. Simulating a compound meandering channel involves the following steps:

1. Generate an orthogonal grid of a compound meandering channel.
2. Generate corresponding cartesian grid and calculate transformation parameters.
3. Perform simulations on a cartesian grid (see Figure 4.3).
4. Transfer or plot the computed results on the orthogonal grid.

Muto (1997) collected high quality data for compound meandering channels with varying sinuosity and relative depth. In this research, these data are used to validate the model. Table 6.3 describes the meander parameters such as sinuosity and channel dimensions used during experiments and are adopted for the numerical simulations.

Table 6.3: Meander parameters for experimental and modelled channels

	Case 1	Case 2	Case 3
Sinuosity (s)	1.093	1.370	1.571
Angle of arc ($\varphi°$)	60	120	180
Meander Wavelength (L_w, mm)	1502	1848	1700
Total width (B, mm)	1200	1200	1200
Width of meander (B_w, mm)	452	900	1000
Bend radius (r_c, mm)	425	425	425
Crossover length (L_{co}, mm)	376	376	0
Crossover angle ($\theta°$)	30	60	90
Channel width (b, mm)	150	150	150
Flood plain height (h, mm)	53	53	53

In this section, depth averaged and cross-sectional profiles are discussed for nine different cases. In absence of the experimental data, the computed results are used to discuss the depth averaged longitudinal velocity, velocity vectors and pressure. The flow behaviour on the cross-sectional plains are discussed based on the experiments.

6.4.1 Case 1: Sinuosity = 1.093

The model was initially applied to simulate the turbulent flow in a compound meandering channel with sinuosity 1.093. The aim of this section is to validate the model by comparing computed results for three different relative depths with the experimental data of Muto (1997).

In Figure 6.23 a sketch of the compound meandering channel (s=1.093) is shown, where S1, S3, S5, S7 and S9 are measuring locations, where the view point of data comparison is the same as the direction of flow. The experimental

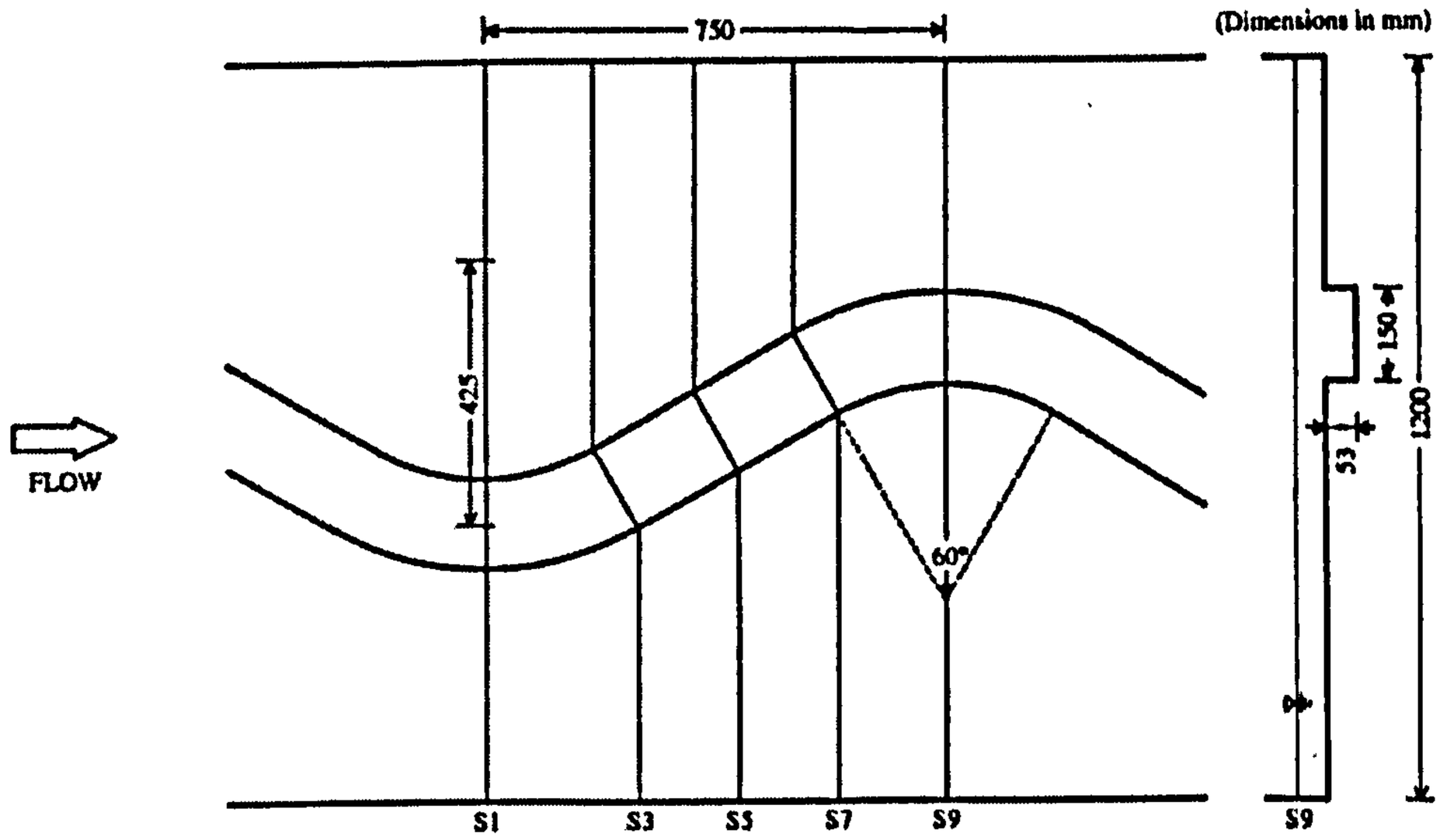

Figure 6.23: Sketch of the physical domain of a compound meandering channel (sinuosity = 1.093) representing dimensions and measuring locations. Simulation results are compared for locations S1, S3, S5, S7 and S9 with experimental data. The view point of the cross section is same as the direction of flow.

data are collected in curvilinear space. Though the computations are performed on cartesian computational domain, the results are mapped backed on to the curvilinear physical domain; making the comparison possible.

The hydraulic conditions such as relative depth, discharge and Reynolds number for each of these cases are represented in Table 6.4. With the help of this hydraulic data, the orthogonal grid for the channel is generated, which involves following steps:

1. Generate an orthogonal grid for main channel only, as shown in Figure 6.24 (b). This grid gives the boundary data required to generate top and bottom floodplains.

2. Generate a grid for the top floodplain with the help of specific geometrical boundary conditions, which is shown in Figure 6.24 (a). The grid is generated based on the algorithm discussed in Section 4.7.3.3.

Table 6.4: Hydraulic conditions for channels with s = 1.093

	Case 1(a)	Case 1(b)	Case 1(c)
Relative depth (Dr=(H-h)/H)	0.0	0.15	0.5
Water depth (H)	0.0525	0.0633	0.1078
Mean velocity (U_s, m/s)	0.237	0.157	0.352
Discharge (Q, m^3/s)	1.876	3.102	25.755
Friction velocity (u_*, m/s)	0.0166	0.0121	0.0225
Reynolds number (Re ($\times 10^4$))	2.63	0.82	6.26

3. Similarly, generate a grid for bottom floodplain, as shown in Figure 6.24 (c).

4. Combine all of these grids to get grid points for the compound meandering channel, which is represented in Figure 6.25.

In Figure 6.25, a plan view of the computational orthogonal grid is presented, which comprises 120 and 78 CVs in longitudinal and lateral direction respectively. The cross-sectional view of the grid at apex section (S1 of Figure 6.23) is shown in Figure 6.26, which comprises 78 and 36 CVs in lateral and vertical direction respectively. The deviation from orthogonality of the generated grid is shown in Figure 6.27. It can be seen from the figure that the highest deviation of 10° is found near the apex sections. However, the mean deviation from orthogonality is calculated to be roughly 2.8°. Moreover, from Figures 6.24 (a) and 6.24 (c) it can be seen that the grids of the two floodplain sides are not completely similar, which is also reflected in Figure 6.27. This is because top and bottom floodplains are exposed to the different geometrical boundary conditions. The top floodplain is geometrically constrained on two sides, for which two side boundaries are narrow as compared to the bottom floodplain. This deviation from orthogonality of the

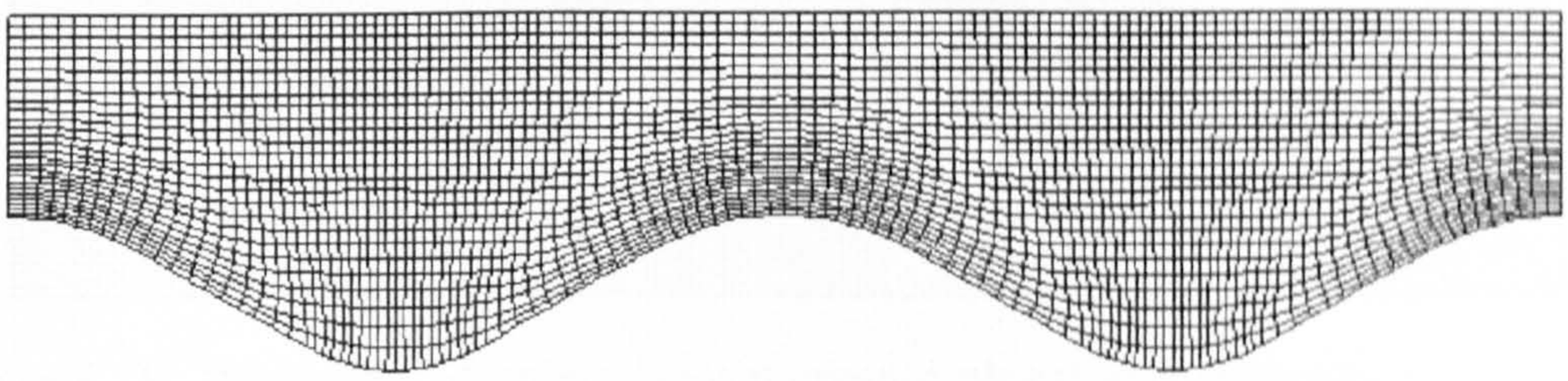

(a) Top of the floodplain

(b) Main channel

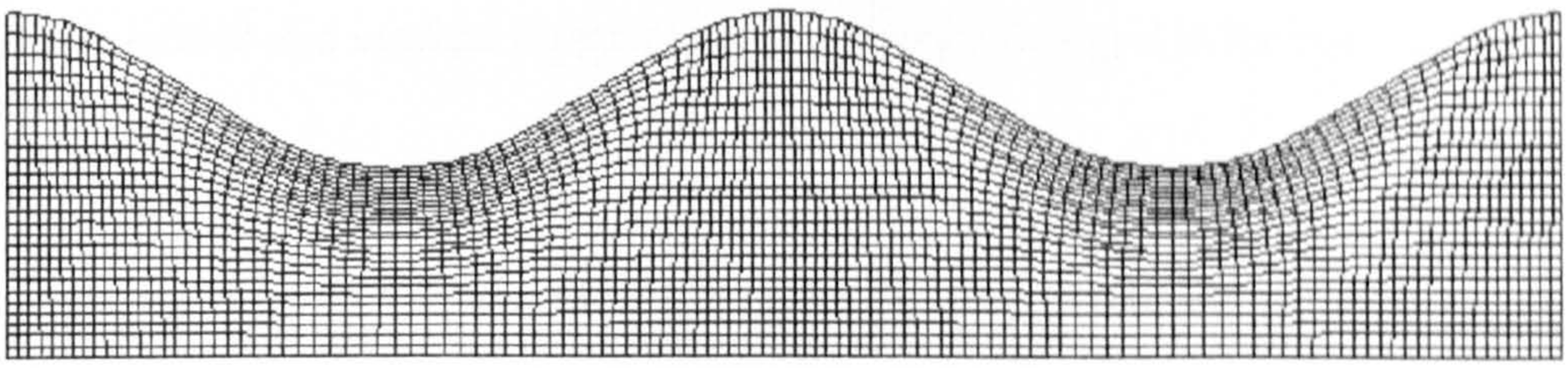

(c) Bottom of the floodplain

Figure 6.24: Different portions of a compound meandering channel. First, the main channel grid is generated. Floodplain grids are generated in two steps in such a way that the boundary point coordinates of main channel match with inner boundary of floodplains.

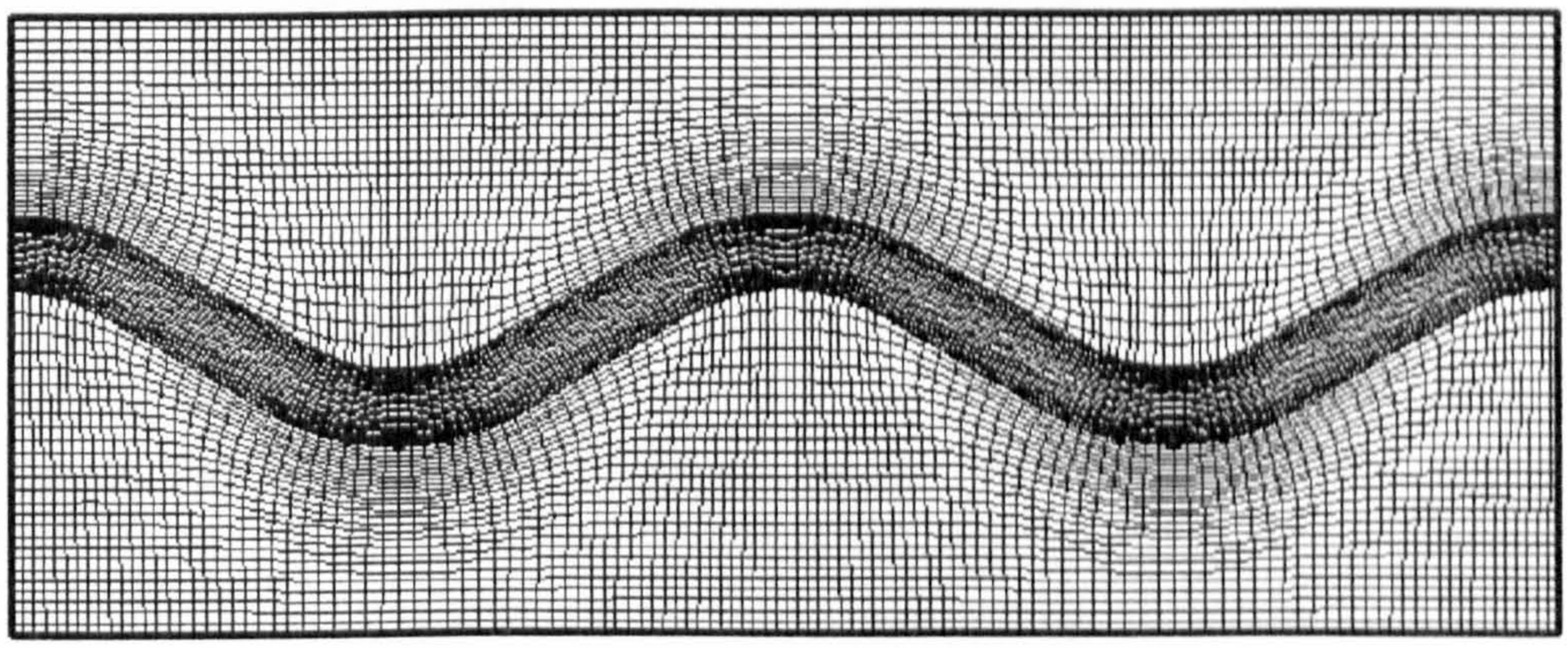

Figure 6.25: Plane view of an orthogonal computational grid (sinuosity = 1.093) of two meanders. No. of CVs are in horizontal (x) and lateral (y) directions are 120 and 78 respectively. In the main channel, no. of CVs are 26.

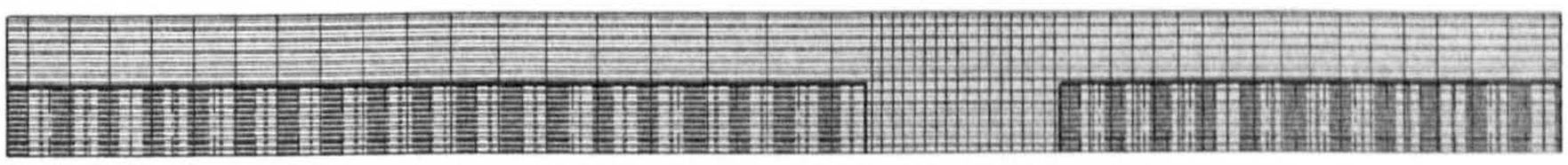

Figure 6.26: Cross-sectional view of the computational grid in (y,z) plane where y and z are lateral and vertical directions respectively. This grid is for the relative depth equal to 0.5.

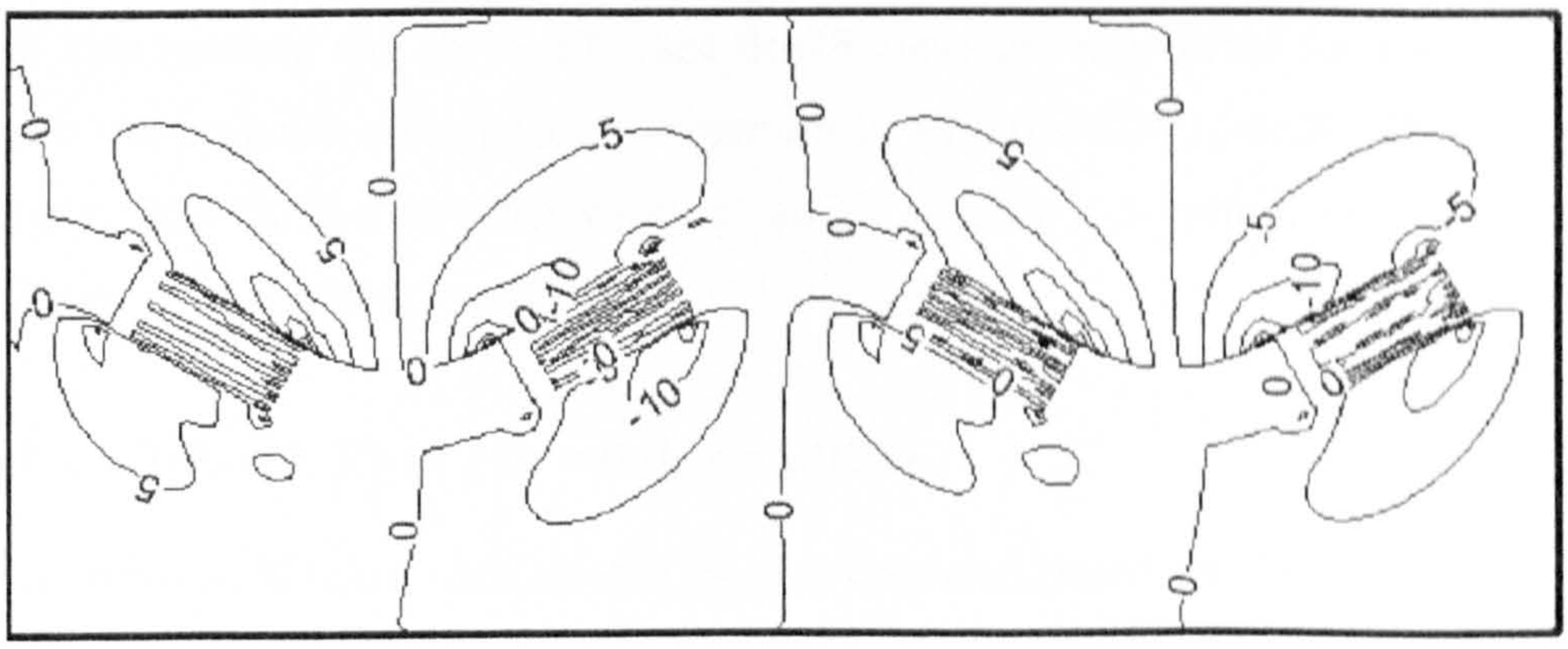

Figure 6.27: Contour lines showing the deviation from orthogonality of a numerical grid shown in Figure 6.25. Maximum deviation = 10°, Mean deviation = 2.67°

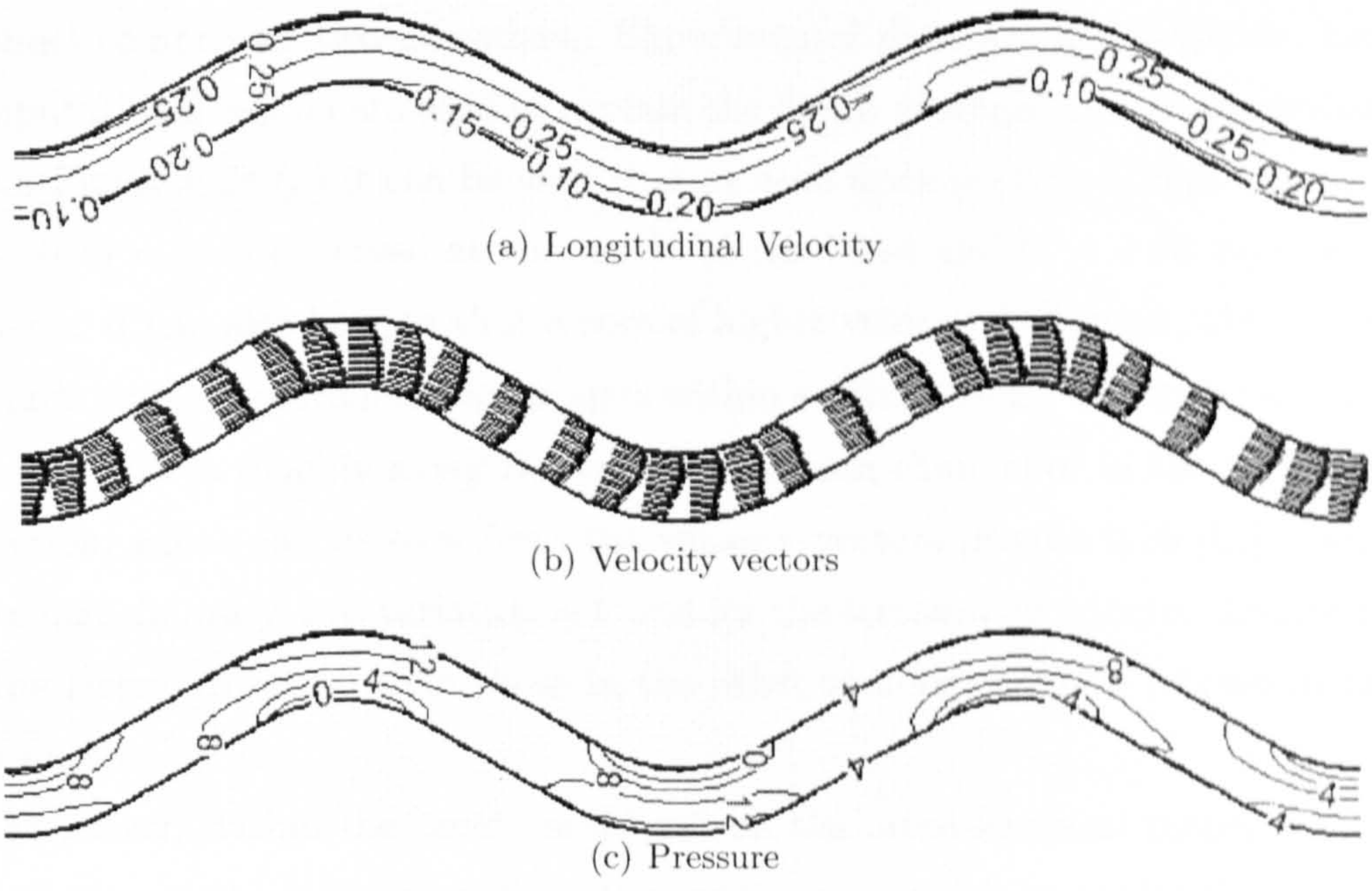

(a) Longitudinal Velocity

(b) Velocity vectors

(c) Pressure

Figure 6.28: S=1.093, Inbank flow: Plan view of (a) depth averaged mean velocity in m/sec, (b) velocity vectors and (c) pressure distribution in N/m^2. Due to the centrifugal forces the velocity is higher at inner side of the apex section, which causes low pressure at the same location. The pattern is repeated at each apex section.

grid and non-symmetry of the top and bottom floodplain grids causes additional numerical errors, which are discussed in the following sections.

In this section, the three different depth cases are simulated for the s=1.093, 60° arc, rectangular channel, are presented in Figures 6.28 to 6.38. This channel geometry has three characteristics: a) small sinuosity, b) small crossover angle (30°) and c) short bend reach (30°).

6.4.1.1 Inbank Flow (Dr=0.0, s=1.093)

In this section, 3D flow characteristics are discussed based on the depth averaged and cross-sectional profiles.

Figure 6.28 shows (a) the depth averaged mean velocity distribution, (b) the velocity vectors and and (c) the pressure distribution for inbank flow within a

channel comprising two meanders. Experimental data are not available, hence computational results are used to explain the depth averaged flow characteristics. From Figure 6.28 (a) it can be seen that at each apex section, a high velocity of $U = 0.25\ m/s$ is observed at the inside of the bend and $U = 0.20\ m/s$ on the outside. It can also be seen that a core of higher velocity is formed, which moves towards outer apex from the inner apex within a bend radius. The direction of the primary flow is roughly along the wall of the main channel or in the streamwise direction, which can be seen from the velocity vectors [Figure 6.28 (b)]. Due to the small sinuosity, less variation is found for the streamwise velocity distribution in the lateral direction than those in the other sinuous channels (shown in later sections).

Moreover, within the bend curvature, on the cross-sectional plane, the flow moves toward the outer apex from the inner apex, which increases the pressure near the outer apex wall and decreases near inner apex as shown in Figure 6.28 [c]). The behaviour of the pressure field and its resulting effect on the free surface is known as the "*super elevation effect*" and the "*depression effect*" respectively. Based on the hydrostatic pressure assumption, the difference in the depth averaged pressure field (ΔP) between inner and outer bend can be connected to the difference in height of the water level (ΔH) by the following equation:

$$\Delta P = \rho g \Delta H \qquad \text{or} \qquad \Delta H = \frac{\Delta P}{\rho g} \tag{6.4}$$

With the help of Equation 6.4, the difference in water level (ΔH) is found equal to 1.223 mm for the pressure difference (ΔH) of 12 N/m^2. It is difficult to measure 1.223 mm in experiments, but computation at least shows 1.223 mm of super elevation occurred at the outside of the bend.

The situation is reversed at the next apex section, and a similar pattern can be seen at alternate apex sections throughout the channel, which is due to the repetitive channel geometry. Due to the channel curvature, the flow experiences a centrifugal force, which is responsible for the higher velocity at the inner bank

of the apex. In the governing equations, this force is described in the U and V momentum equations as an additional source term (see Equations 5.35 and 5.36).

Figure 6.29 shows the predicted and measured cross sectional distributions of the streamwise velocity along the channel meander (sections S1 to S9 of Figure 6.23). It can be seen from the measured data that the maximum velocity, with magnitude over 20% larger than U_s is located near the inner wall of the main channel at the bend apex (Section 1). As the flow goes through the latter half of the bend, the core starts to shift towards the outer wall and the velocity distribution becomes more uniform during its path through the crossover section (S3 to S7). The maximum velocity is observed at the end of crossover region and the beginning of the next bend (Section 7). The mirror images of these velocity distributions are attained between consecutive bend apices (Sections 1 & 9).

For the computed results, it can be seen that the path traveled by the maximum velocity core is similar to that of the experimental data. From sections S5 to S9 the core is found to be below the free surface. This may be due to the presence of a strong secondary circulation, rotating in an anticlockwise direction, near the free surface-left wall junction, which is discussed in the following paragraphs.

The growth and decay process of secondary flow through the bend is represented in Figure 6.30, which compares the prediction with measured values. From the measured data it can be seen that, the magnitude of secondary the currents is noticed to be 10% of U_s. From the figure, it can be seen that there is no large secondary cell occupying the majority of the cross section, which is observed in apex section of s=1.37 and s=1.57 channels (discussed in following sections). Instead, a clockwise circulation starts to develop at S1, which strengthens at S3 but weakens as it reaches S5. Finally, at S9 the clockwise circulation attains its maximum potential and occupies half of the cross section, which is opposite to S1.

From the computed secondary currents, it can be seen that, similar to the experimental data, a clockwise circulation starts to grow at S1 but it does not develop completely. However, from S1 to S9 a circulation, rotating anticlockwise,

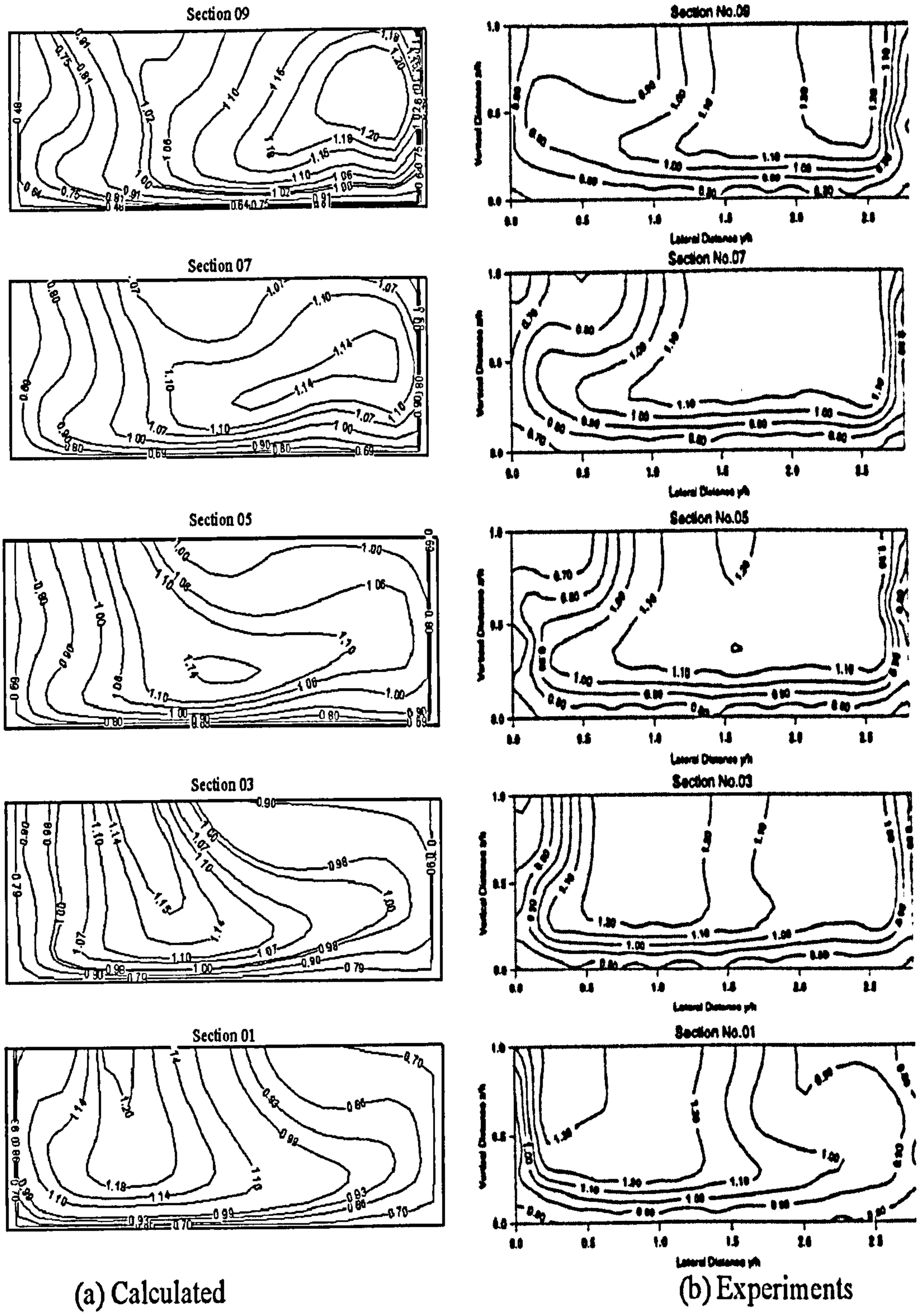

(a) Calculated (b) Experiments

Figure 6.29: S=1.093, Inbank flow: Comparison of simulated U/U_s with experimental data collected by Muto (1997) at different sections. For section configuration in the channel, see Figure 6.23.

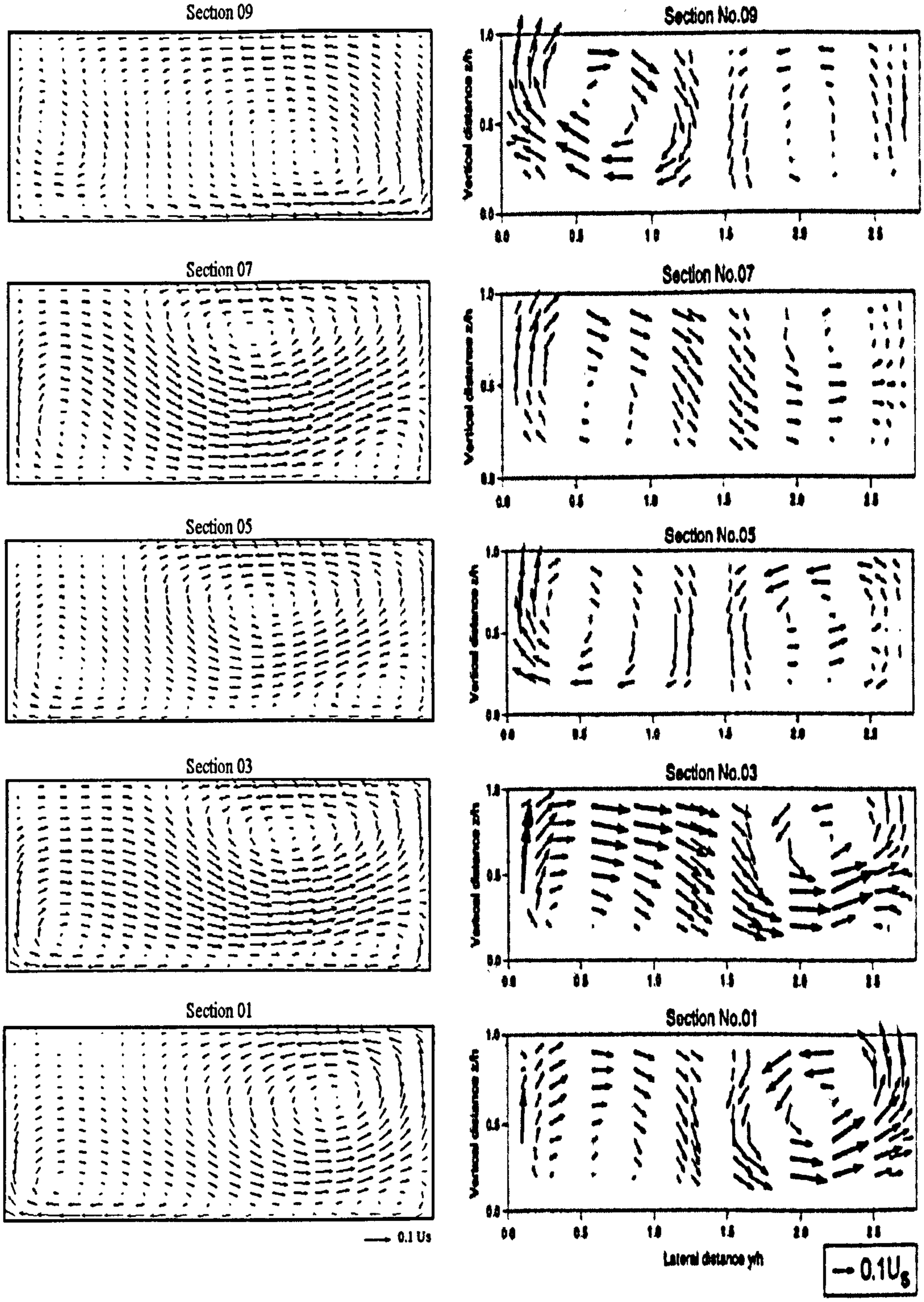

(a) Calculated (b) Experiments

Figure 6.30: S=1.093, Inbank flow: Comparison of simulated secondary currents with experiments data collected by Muto (1997) at different sections. For section configuration in the channel, see Figure 6.23. Strength of secondary current is around 10% of the mean velocity.

is seen at the free surface-left wall junction. This circulation drives the momentum transfer from the left wall towards the free surface, which forces the maximum velocity core below the free surface.

Although the secondary flows near surface in various sections over predicted, the model is able to reproduce the essential behaviour of the meandering channel inbank flow for s=1.093. The predicted results are in reasonably good agreement with the experimental data.

6.4.1.2 Overbank Flow (Dr=0.15, s=1.093)

Once the inbank flow was simulated successfully, the model was then applied to simulate overbank flow with Dr=0.15. It is clear from the previous investigations, discussed in Section 2.4, that due to flooding or overbank flow, the flow structures in the main channel are significantly affected by floodplain flow (Shiono and Muto (1998)). In this section, the flow characteristics of overbank flow are discussed and the predicted depth-averaged velocity, cross-sectional mean velocity and secondary circulations patterns are compared with experimental data.

Figure 6.31 shows the prediction of (a) depth averaged longitudinal velocity, (b) velocity vectors and (c) pressure for s=1.093 channel with Dr=0.15. From the depth averaged velocity plot it can be observed that on the right and left floodplains (side walls), the value of mean velocity is observed to be 0.01 m/s and 0.02 m/s respectively. High velocity contour lines at the inner bend of apex section is also noticed. In comparison to inbank flow (see Figure 6.28), the flow pattern is altered slightly in the crossover region.

From the vector plot [Figure 6.31 (b)], the flow in the main channel tends to follow the streamwise direction while on the floodplain it follows the longitudinal direction. Moreover, the magnitude of the velocity vectors are higher in the main channel compared to the flood plain. Due to this difference in the direction of flow, complex flow behaviour is created, especially from the crossover region to the first half of the following bend. It can also be seen that in the crossover region

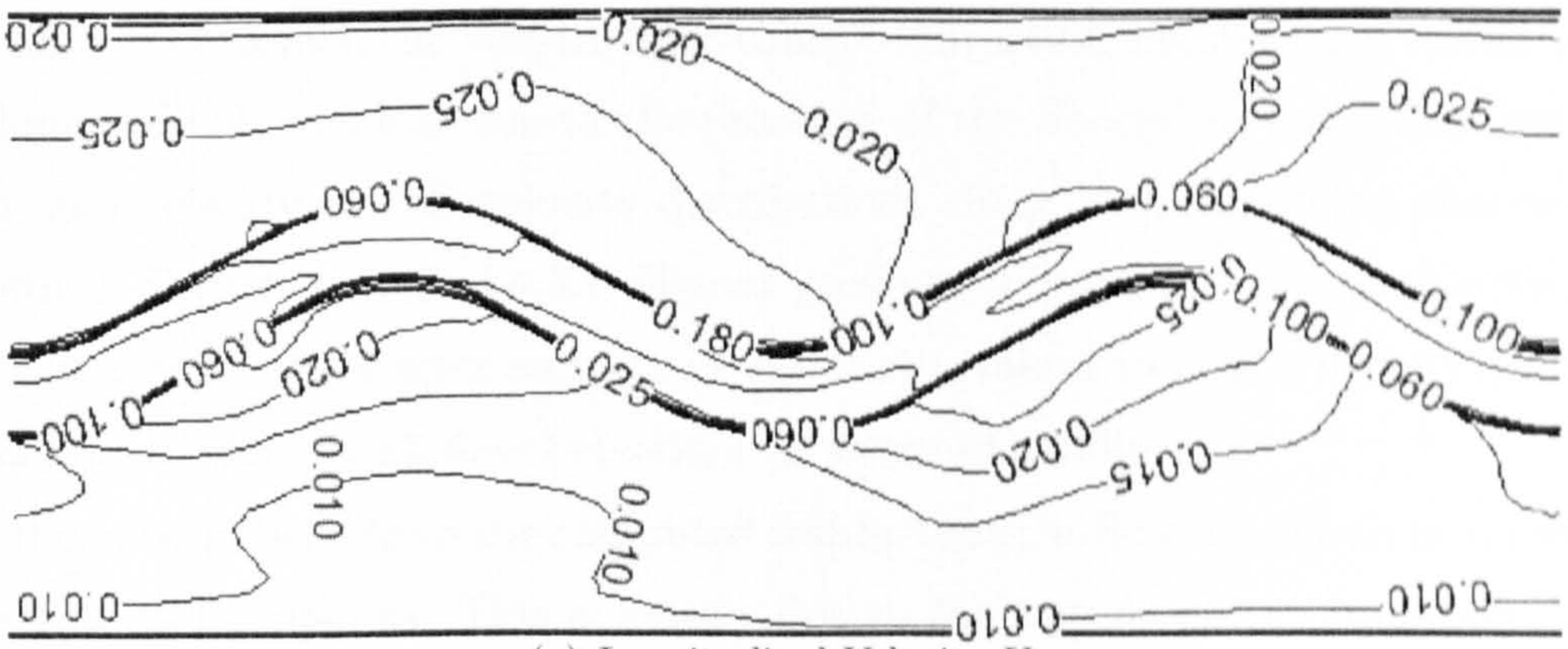

(a) Longitudinal Velocity U

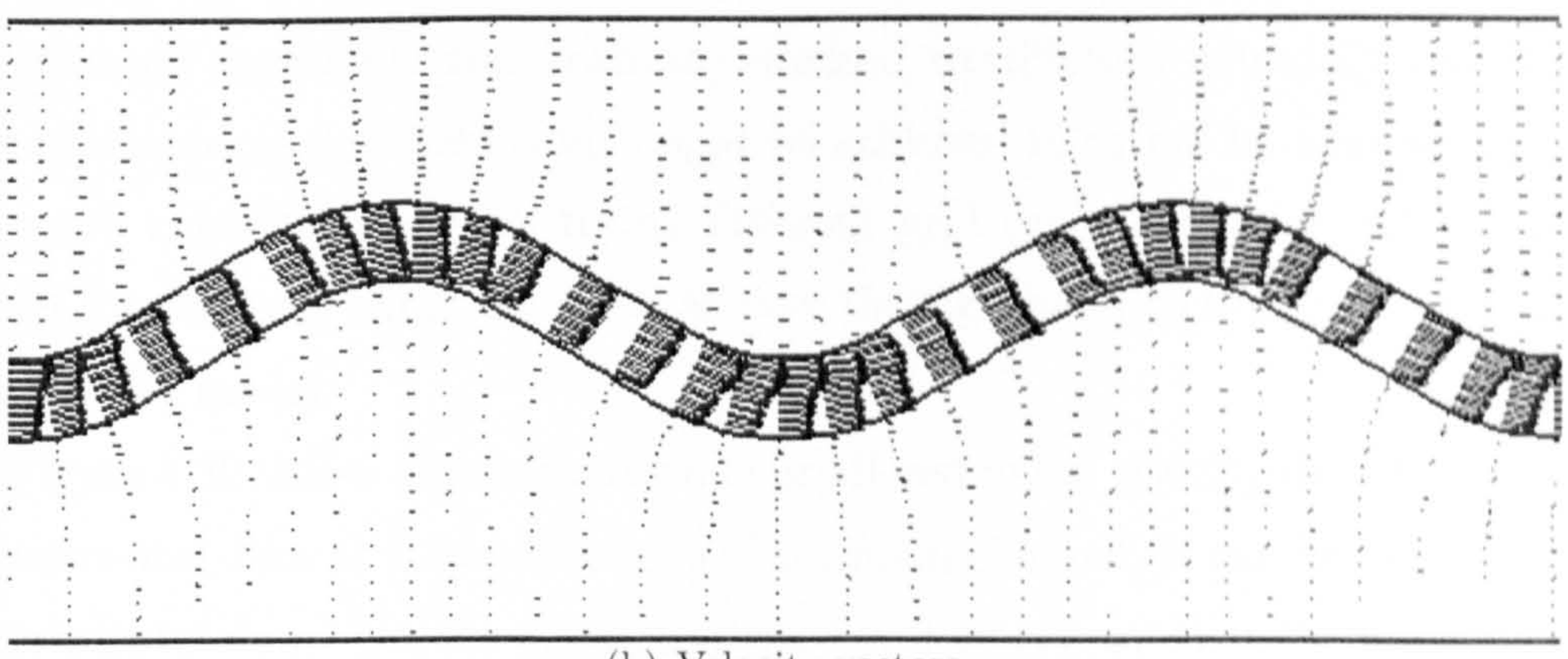

(b) Velocity vectors

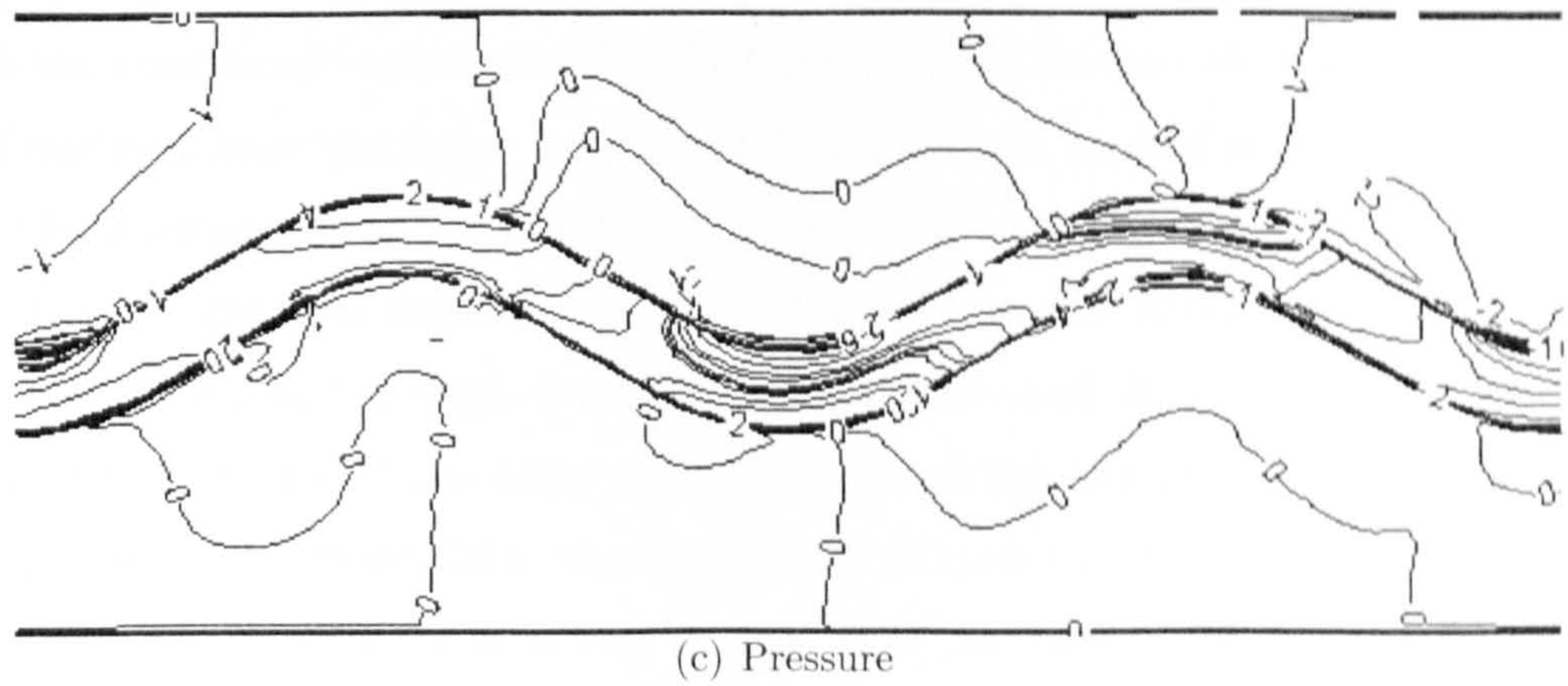

(c) Pressure

Figure 6.31: S=1.093, Dr=0.15: Plan view of depth averaged ((a) mean velocity in m/sec, (b) velocity vectors and (c) pressure distribution in N/m^2. Due to the centrifugal forces the velocity is higher at inner side of the apex section which causes low pressure at the same location. The pattern is repeated at next apex section.

of the main channel, the vectors have changed direction slightly from streamwise to longitudinal, which is due to the presence of the floodplain flow. This can be seen more clearly by 3-D velocity distributions along the meandering channel as shown in Figures 6.46 and 6.33. Higher pressure [Figure 6.31 (c)] is observed at the outer bend of the apex sections (2 N/m^2 equivalent to $\Delta H = 0.2mm$), which is similar to the inbank flow behaviour in terms of profile.

It can be noticed from the computed results that the flow behaviour is not symmetrical on floodplains. This is mainly due to the way in which floodplain grids are generated. As shown in Figure 6.24 the orthogonal grid for each floodplain is generated separately and both are exposed to different boundary conditions. The symmetrical flow behaviour might be achieved in future by simulating more than two channel meanders, trying different grid refinement and validating the model for different situations such as flow through bend to find out any manual error in the model.

Figure 6.32 shows the comparison of predicted mean velocity distribution with experimental data at various sections of the main channel. It can be seen from the experimental data that the maximum velocity core is formed at the inner bend of the apex section S1. This core starts to shift towards the other side as it enters into the next bend curvature (S7). At the next apex section S9, the core occupies the position near the inner bend, which is opposite to section S1. From S3 to S7, the intrusion of floodplain flow into the main channel can be seen. However, the velocity gradient between the main channel flow and floodplain flow is not as steep at S5 where the angle between main channel and floodplain is the highest. Moreover, higher U/U_s is observed within the main channel along the meander compared to the floodplain, showing the dominance of the main channel flow. From the predicted results, it can be said that the mean velocity distribution is captured well by the model.

The growth and decay pattern of the secondary currents is shown in Figure 6.33. It can be seen from the experimental data that a secondary circulation exists rotating in an anticlockwise direction, with magnitude of 20% of U_s at the

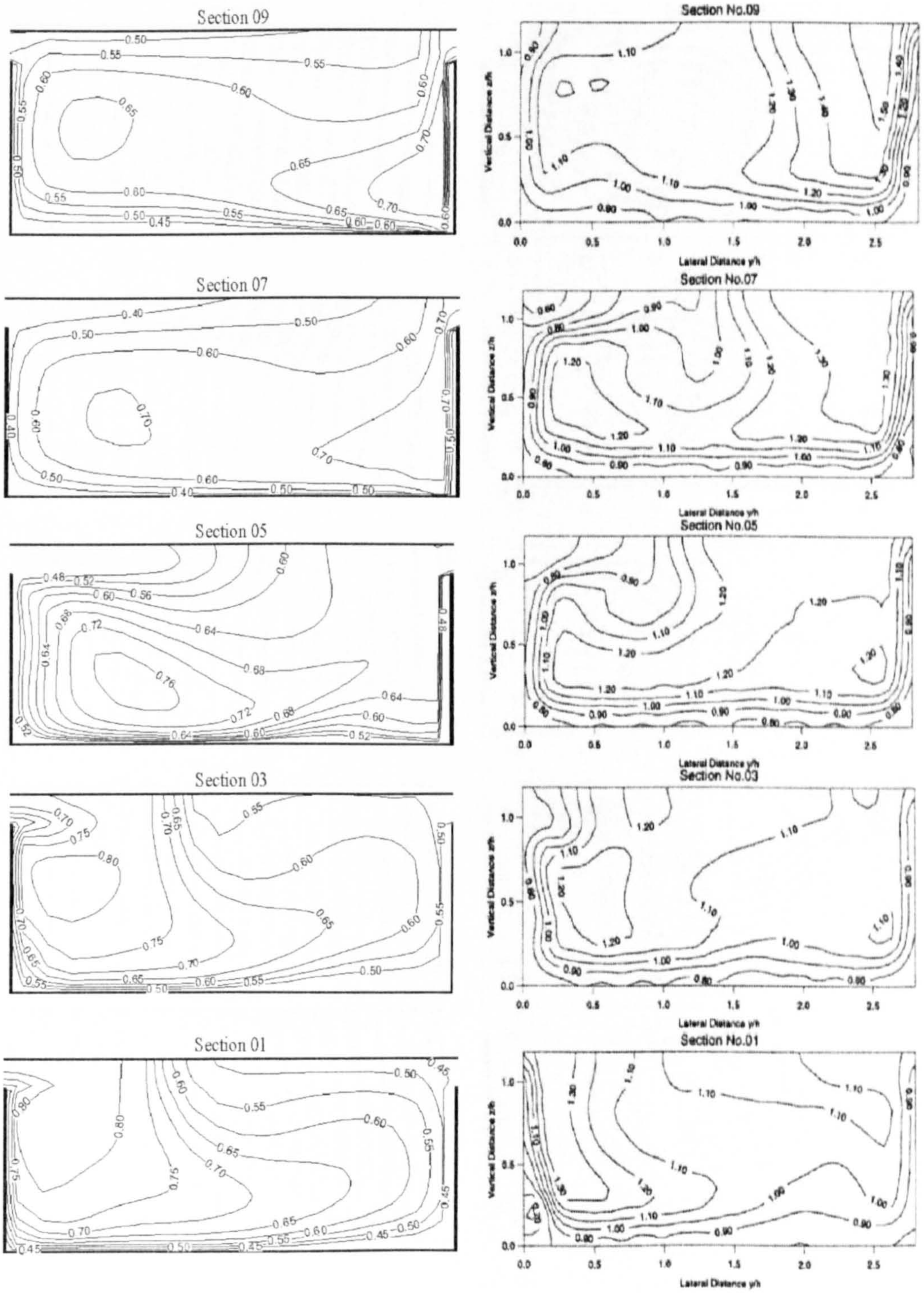

Figure 6.32: S=1.093, Dr=0.15: Comparison of simulated U/U_s with experimental data collected by Muto (1997) at different sections. For section configuration in the channel, see Figure 6.23.

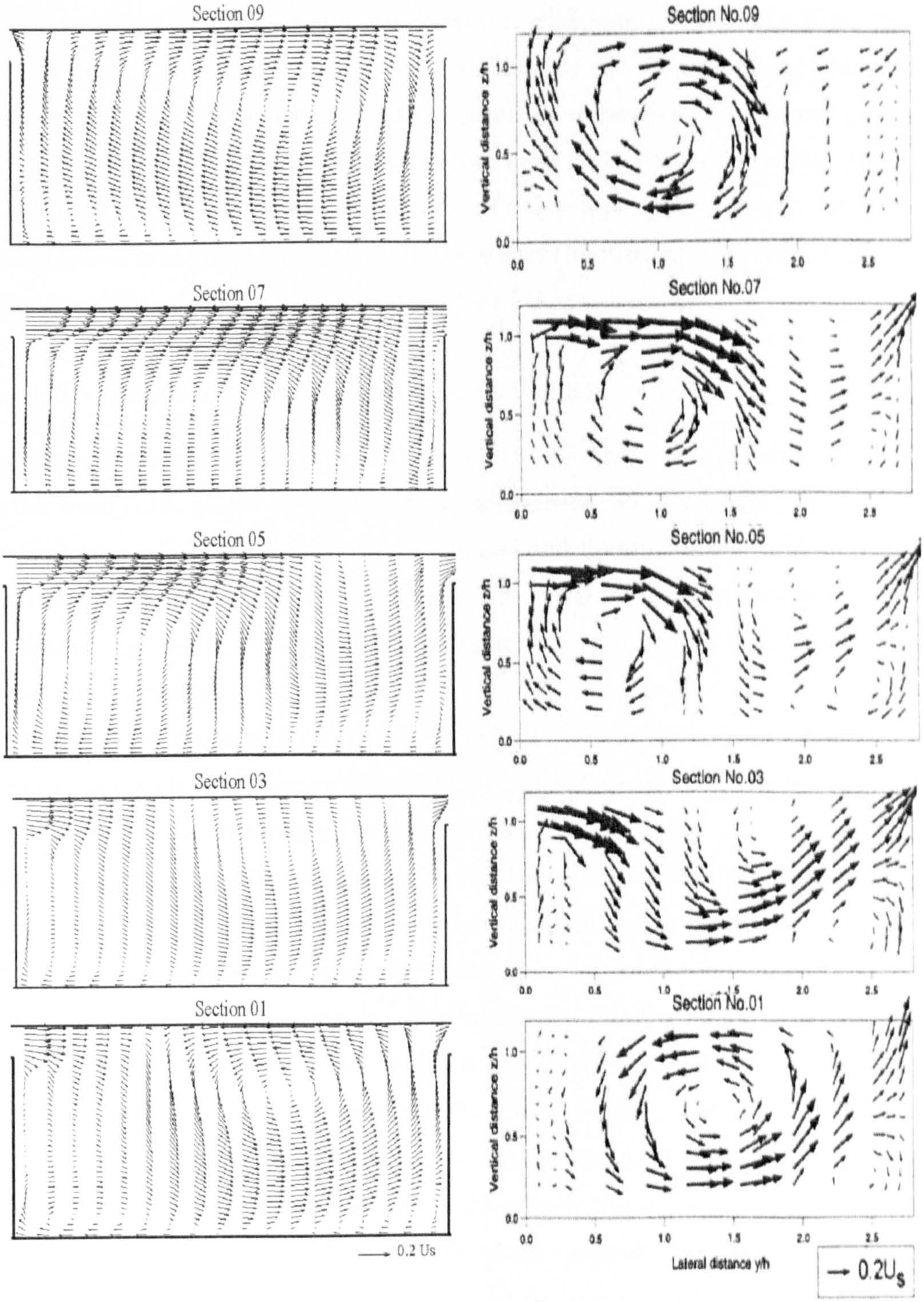

(a) Calculated (b) Experiments

Figure 6.33: S=1.093, Dr=0.15: Comparison of simulated secondary currents with experiments data collected by Muto (1997) at different sections. For section configuration in the channel, see Figure 6.23. Strength of currents are 20% of the mean velocity.

apex (section S1). This circulation, however, disappears within the bend (S1 to S5). A new clockwise circulation starts to form in the vicinity of the inner bend area at S3. This clockwise circulation grows as it reaches the crossover region. Then a large clockwise circulation occupies most of the cross section of the main channel. A clockwise rotating cell can be seen developing in crossover region (S5), which grows and gains strength as it travels to the next apex section (S9). This behaviour of circulation is also well captured by the model.

6.4.1.3 Overbank Flow (Dr=0.50, s=1.093)

By increasing the discharge (see Table 6.4), the relative depth is further increased to 0.5 from 0.15, which makes the flow mechanism more complex due to the increased interaction between the main channel and floodplain flow in the crossover section. In this section flow behaviour is discussed for the channel with Dr=0.5 by describing depth averaged parameters and cross-sectional mean velocity and secondary currents.

Figure 6.34 represents the prediction of (a) the depth averaged longitudinal mean velocity, (b) the velocity vectors and (c) the pressure distribution for Dr=0.5 case. From the depth averaged velocity profile a high velocity at the inner bend of the apex sections can be seen, which is similar to the behaviour found in inbank and Dr=0.15 cases. However, in the crossover region due to the increased plunging effect from the floodplain flow, the mean velocity profile is changed, which is discussed in the next paragraph. Similar to the Dr=0.15 case, the profiles on the two floodplains are different, which is due to the grid generation mechanism, as explained in the previous section. For the floodplain and main channel, the magnitude of vectors is roughly the same and in the same direction [Figure 6.34 (b)]. The main channel flow direction is affected by the strong overbank flow. The flow direction of the main channel is deviated partially from the streamwise to the longitudinal unlike the Dr=0.15 case. An increased pressure on the floodplain (20 N/m^2) and a high pressure at the outer bank (30 N/m^2) can also be observed

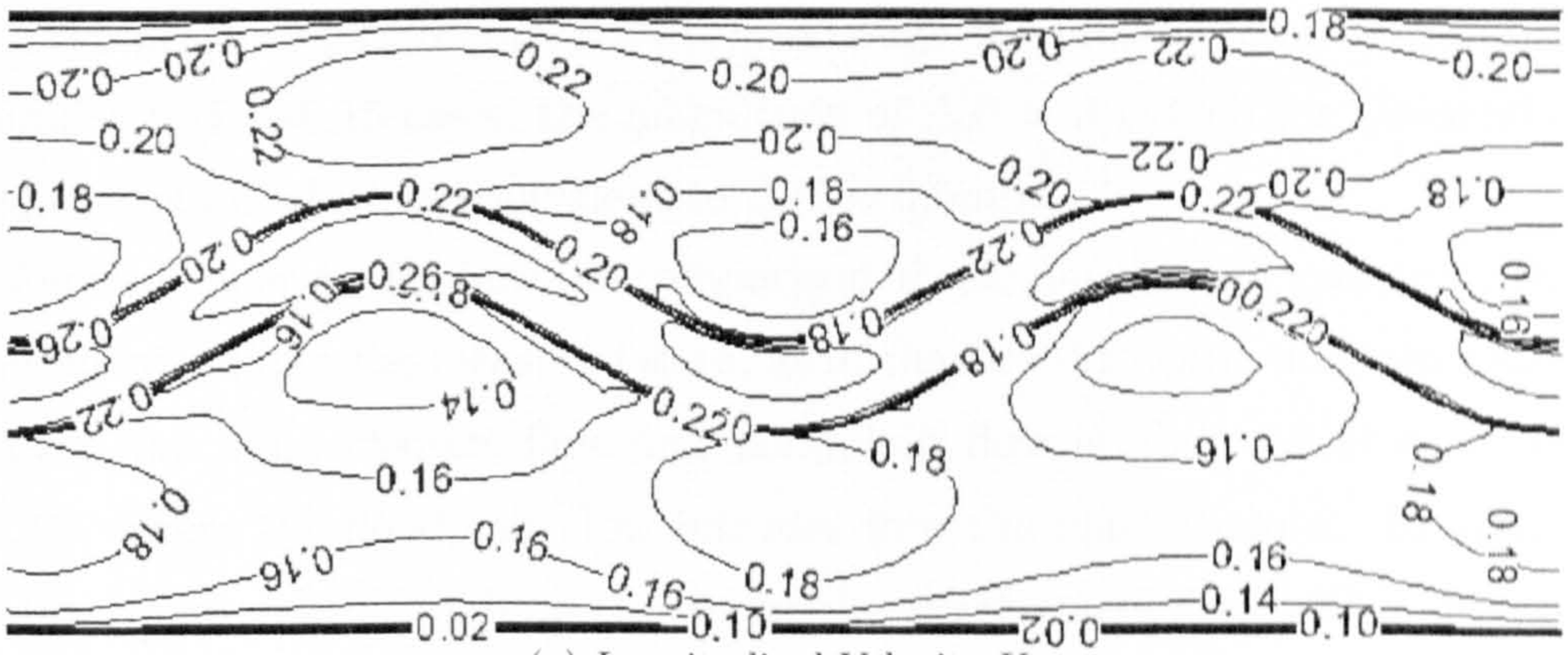

(a) Longitudinal Velocity U

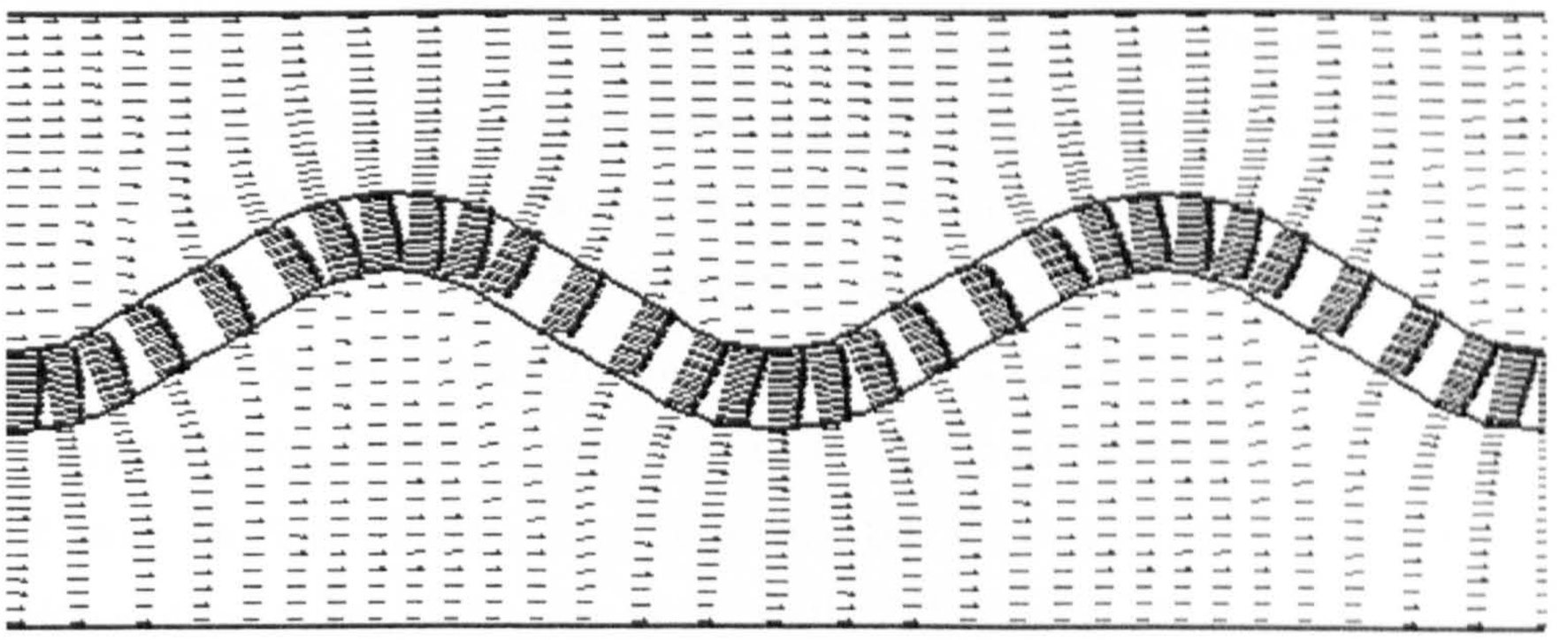

(b) Velocity vectors

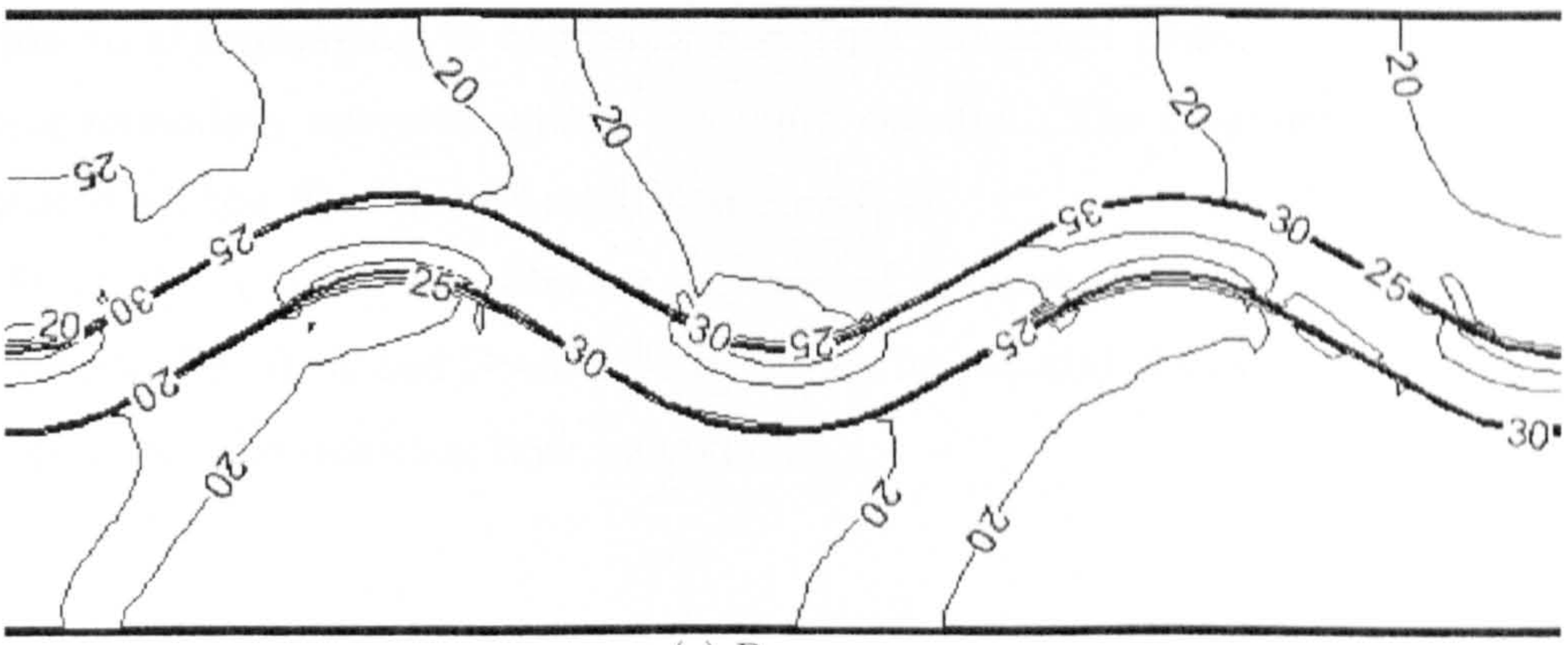

(c) Pressure

Figure 6.34: S=1.093, Dr=0.50: Plan view of depth averaged (a) mean velocity in m/sec, (b) velocity vectors and (c) pressure distribution in N/m^2. Due to the centrifugal forces the velocity is higher at inner side of the apex section which causes low pressure at the same location. The pattern is repeated at next apex section.

from the pressure plot [Figure 6.34 (c)]. Though the pressure distribution profile is similar to Dr=0.15 cases, the magnitude of $\Delta P = 5$ is high for Dr=0.50 case at apex section which is equivalent to $\Delta H = 0.5mm$.

Figure 6.35 and 6.36 show the comparison of calculated mean velocity with the experiments. From the measured data, as in the Dr=0.15 case, no steep gradient between the main channel flow and floodplain flow is observed at sections 03 and 05, where the floodplain flow intrudes into the main channel. In addition, the maximum velocity is found to be in the overbank region, which shows the dominance of floodplain flow. The flow below the bankfull level has a value of U/U_s=1.0 along the meander compared to 1.2 in the overbank region, which suggests that the flow in the overbank region in stronger than that in the main channel. This behaviour is successfully predicted by the model.

In Figures 6.37 and 6.38 the secondary currents at different sections are compared for Dr=0.5 case. From the measured data, it can be noticed that at section 01, a large anticlockwise circulation with a magnitude of 50% of U_s occupies the whole cross section, disappearing at section 03. From section 03, a clockwise circulation starts to form from the inner wall of the bend, which grows in strength as it travel across the crossover region till it reaches next bend apex (S9). This is due to the plunging of overbank flow into the main channel, which induces strong secondary currents within the main channel. The computed results have captured all the flow characteristics successfully.

From the computed results for the case of the meandering channel (s=1.093) for inbank, Dr=0.15 and Dr=0.5 flows, it can be concluded that the model is able to reproduce the essential flow behaviour.

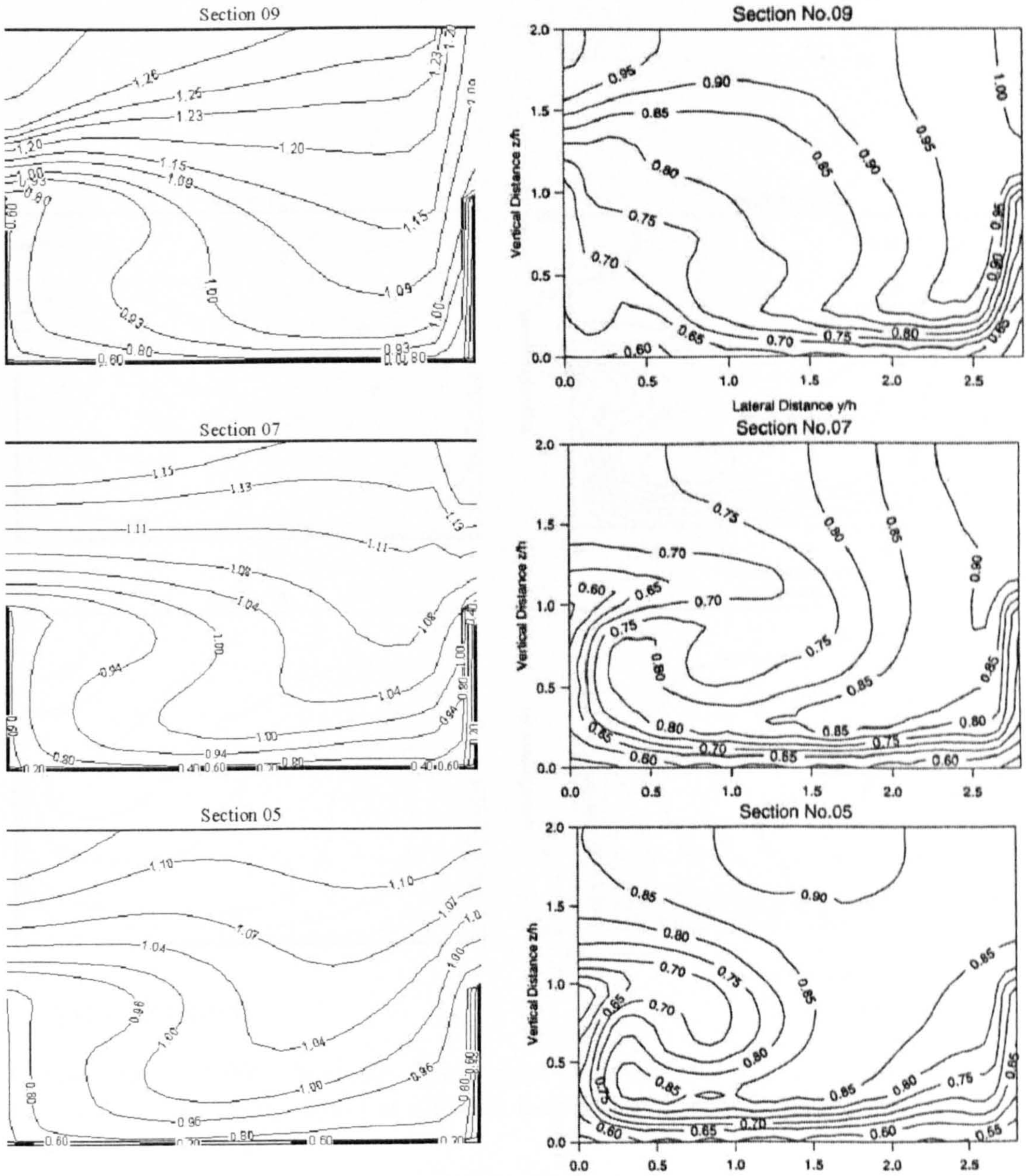

(a) Calculated (b) Experiments

Figure 6.35: S=1.093, Dr=0.50: Comparison of simulated U/U_s with experimental data collected by Muto (1997) at different sections. For section configuration in the channel, see Figure 6.23.

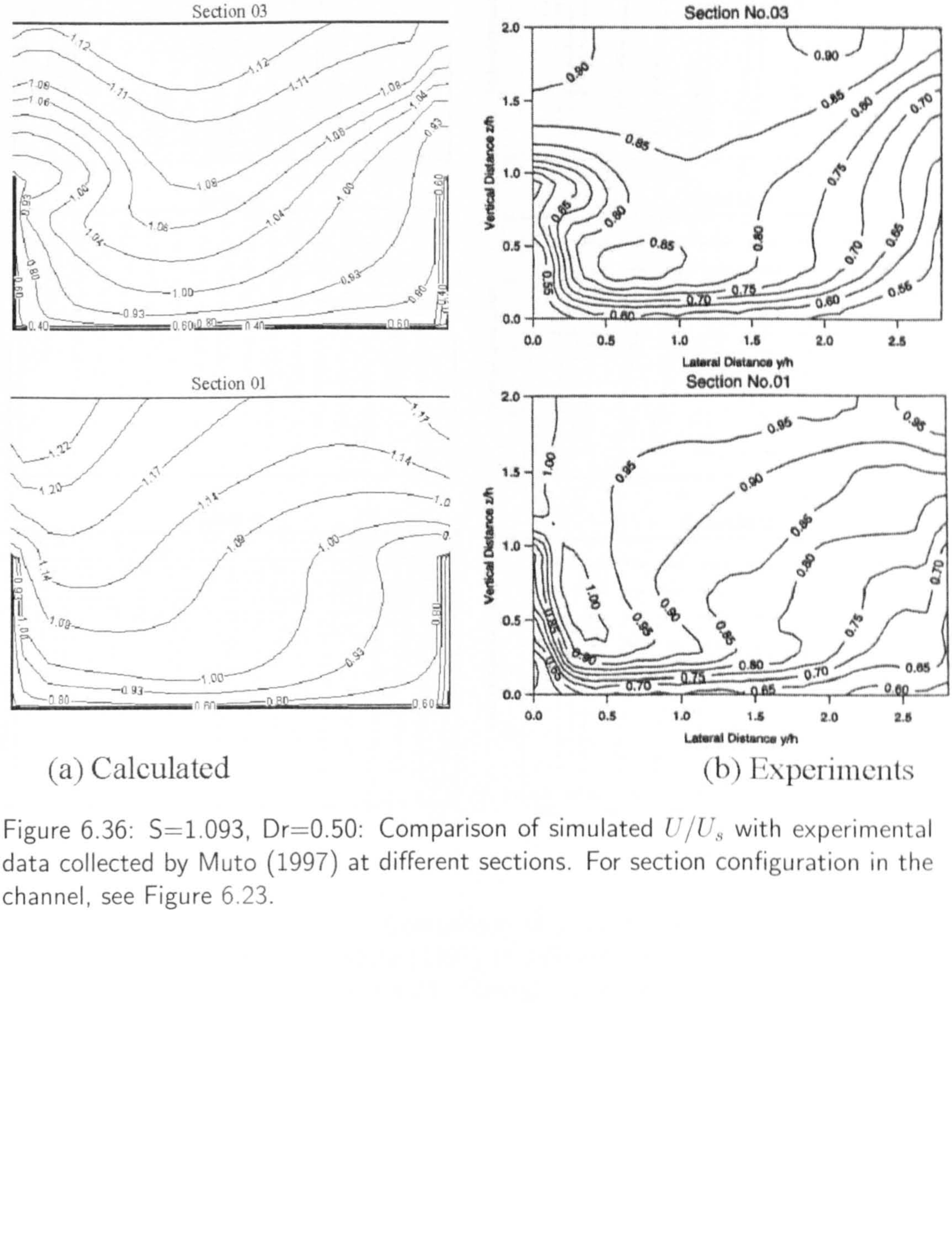

Figure 6.36: S=1.093, Dr=0.50: Comparison of simulated U/U_s with experimental data collected by Muto (1997) at different sections. For section configuration in the channel, see Figure 6.23.

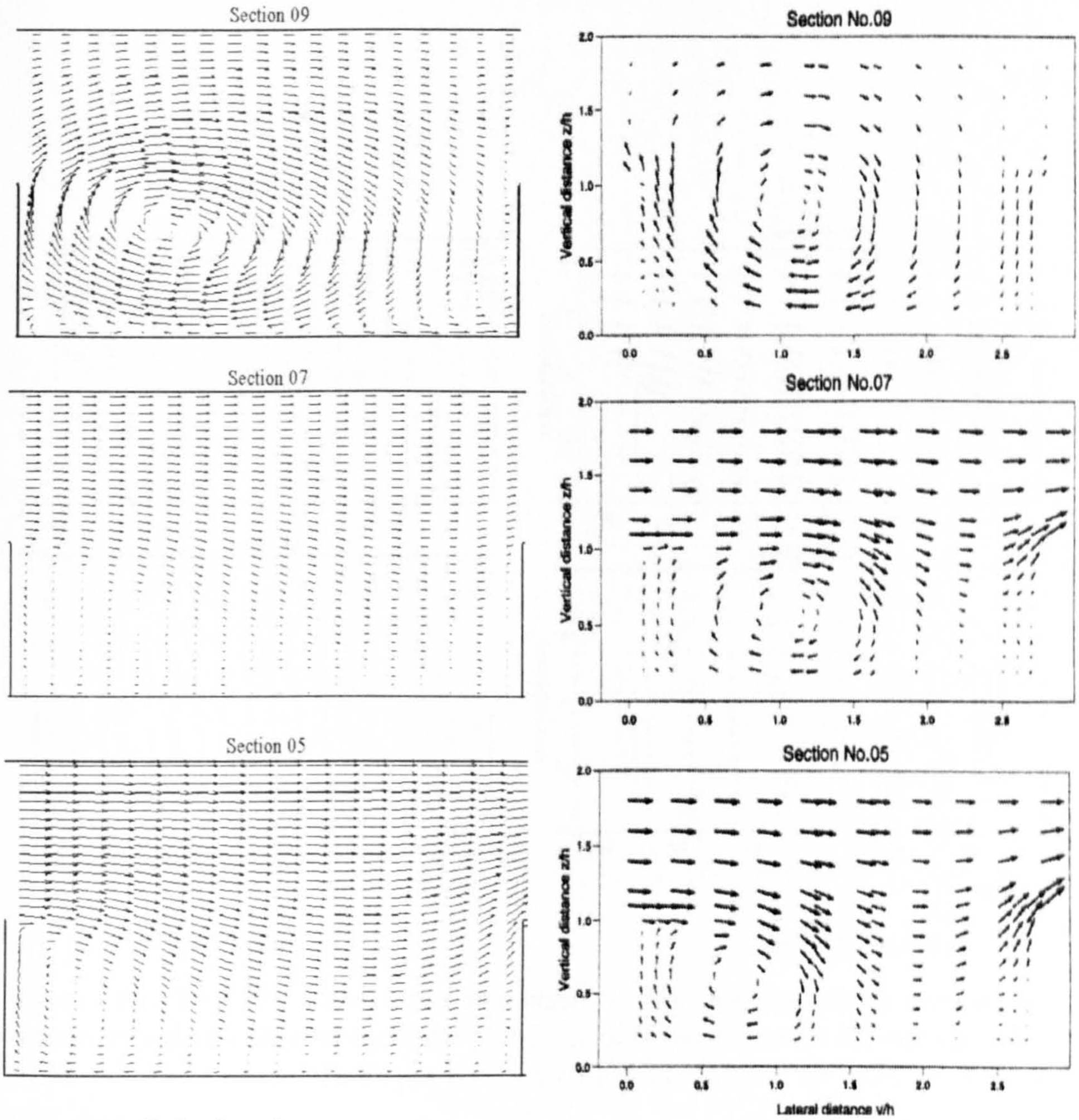

(a) Calculated (b) Experiments

Figure 6.37: S=1.093, Dr=0.50: Comparison of simulated secondary currents with experiments data collected by Muto (1997) at different sections. For section configuration in the channel, see Figure 6.23. Strength of currents are 50% of the mean velocity.

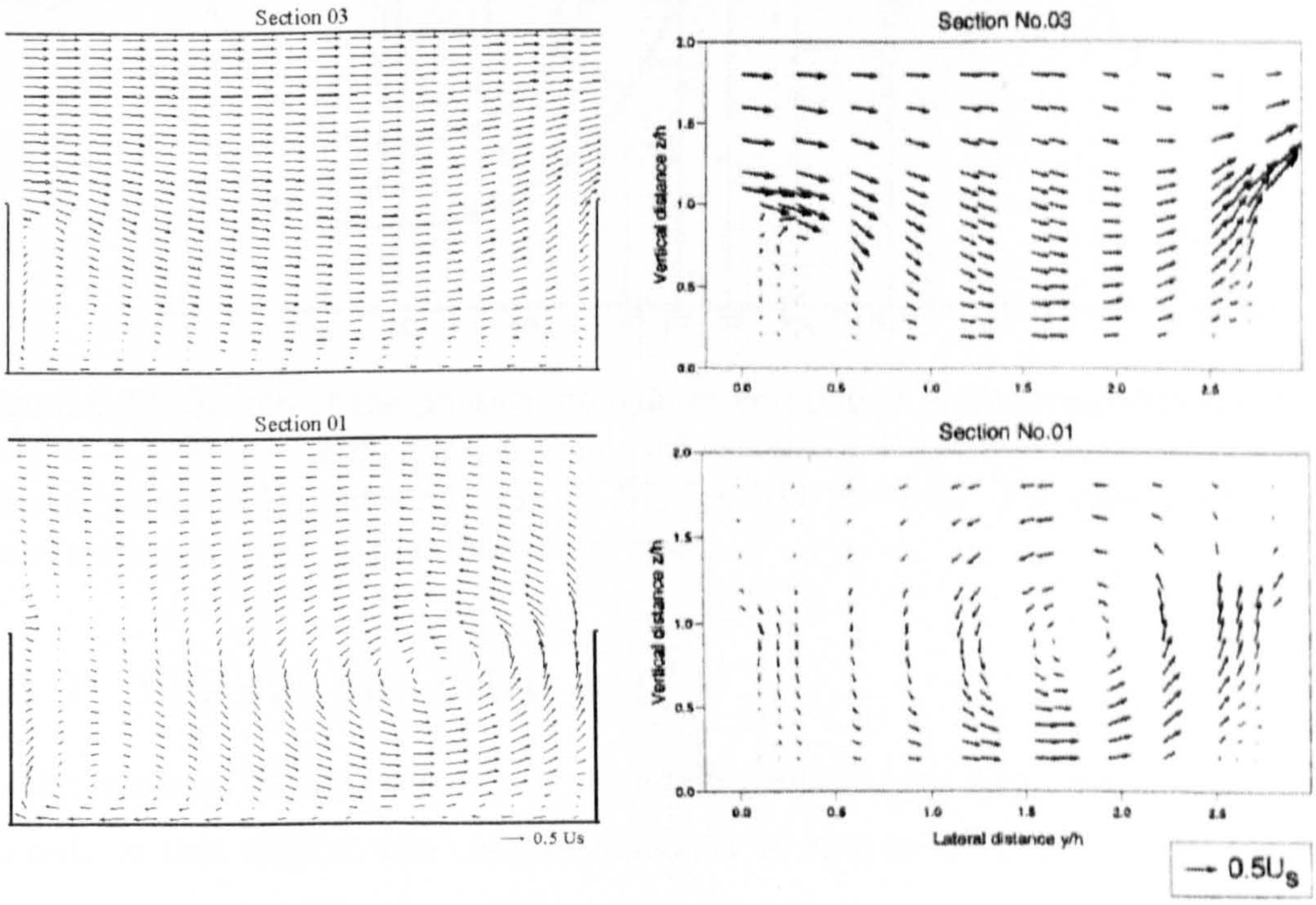

(a) Calculated (b) Experiments

Figure 6.38: S=1.093, Dr=0.50: Comparison of simulated secondary currents with experiments data collected by Muto (1997) at different sections. For section configuration in the channel, see Figure 6.23. Strength of currents are 50% of the mean velocity.

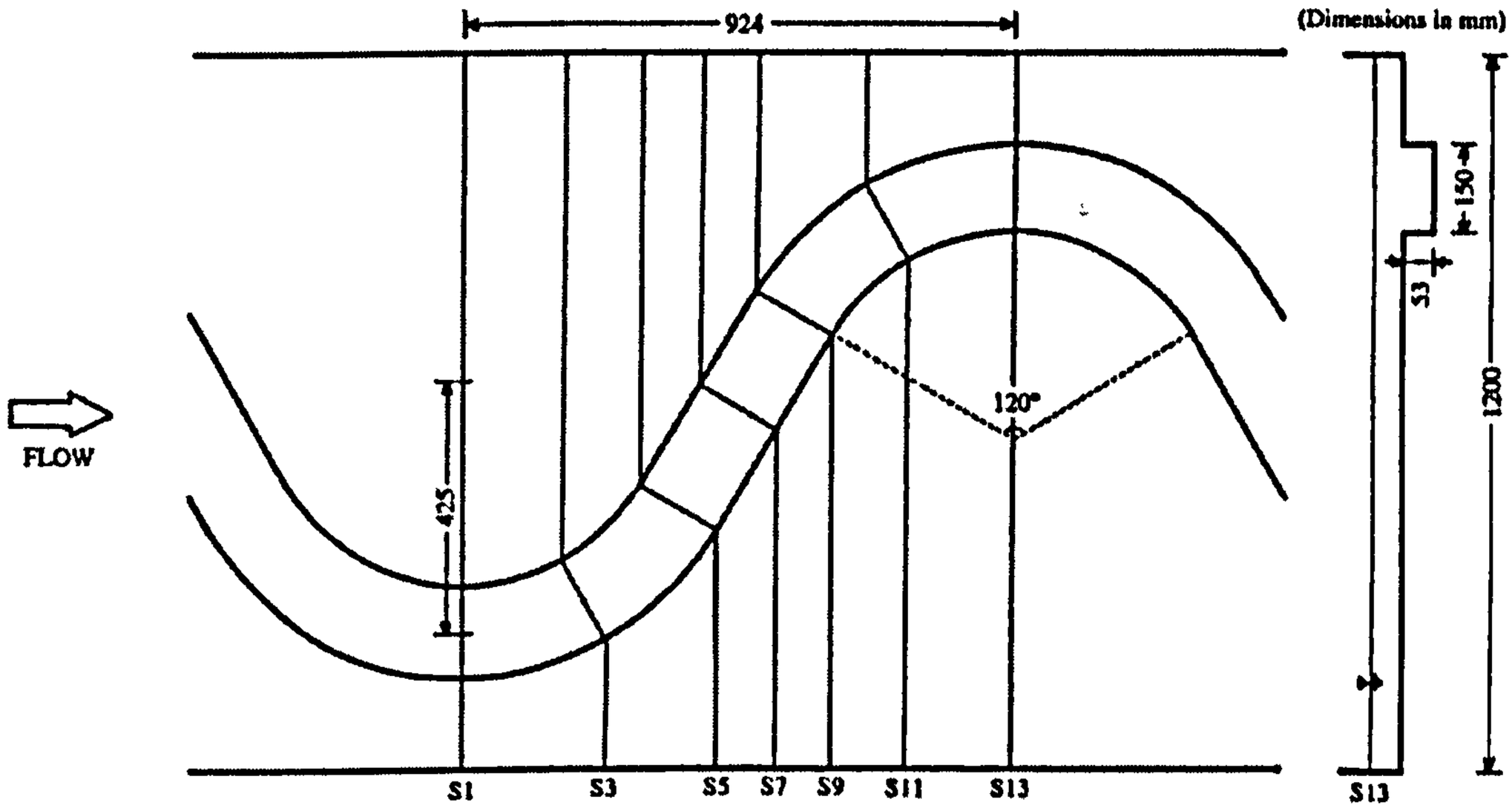

Figure 6.39: Sketch of the physical domain of compound meandering channel (sinuosity = 1.370) representing dimensions and measuring locations. Simulation results are compared for locations S1, S3, S5, S7, S9, S11 and S13. The view point of the cross section is same as the direction of flow..

6.4.2 Case 2: Sinuosity = 1.37

In the previous section, a compound meandering channel with s=1.093 was simulated. In this section, the channel sinuosity is increased to s=1.37 and simulations are carried out for three different relative depths; inbank flow, Dr=0.15 and Dr=0.5.

A sketch of the compound meandering channel with s=1.370, 120° arc and rectangular cross section, is shown in Figure 6.39 where S1, S3, S5, S7, S9, S11 and S13 are measuring locations. An orthogonal computational grid of two meanders corresponding to the physical domain is represented in Figure 6.40. In Figure 6.41 the deviation from orthogonality is presented. It can be seen that the maximum deviation is around 10° and the average deviation is 3.2°, which is greater than in the s=1.093 case. It can be also noticed that the deviation is not symmetric due to the way in which the grid is created (see Section 6.4.1). The hydraulic parameters adopted for simulations are presented in Table 6.5, which describes

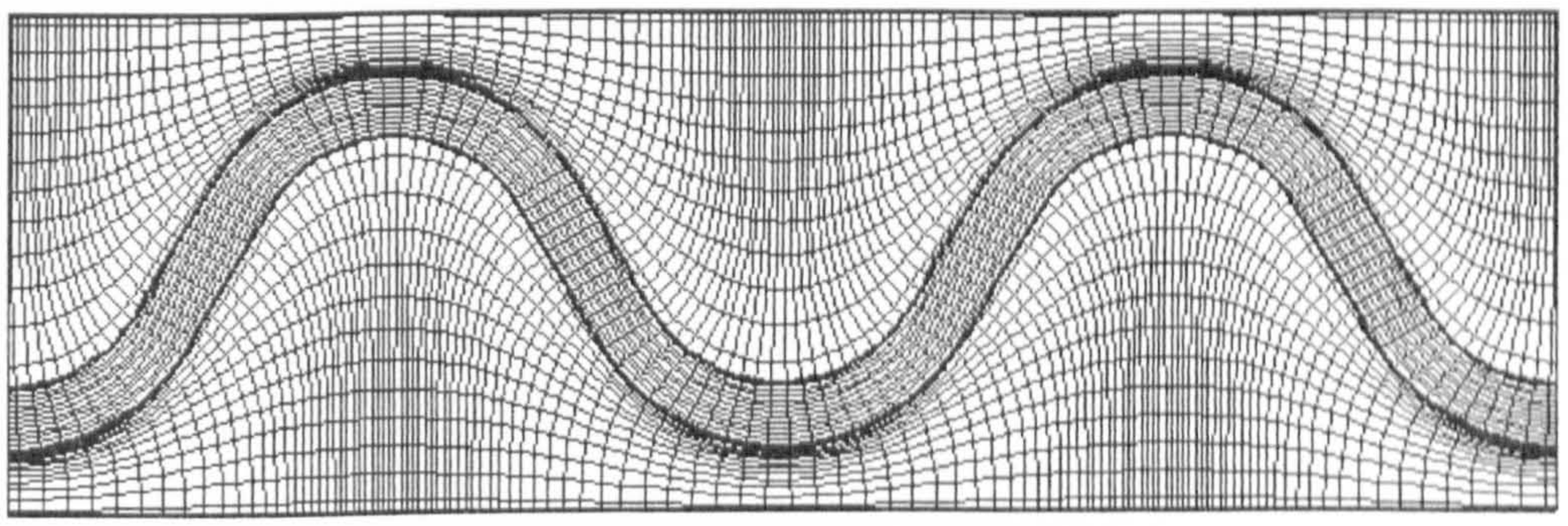

Figure 6.40: Plane view of an orthogonal computational grid (sinuosity = 1.37) of two meanders. No. of CVs are in horizontal (x) and lateral (y) directions are 120 and 36 respectively. In the main channel, no. of CVs are 12.

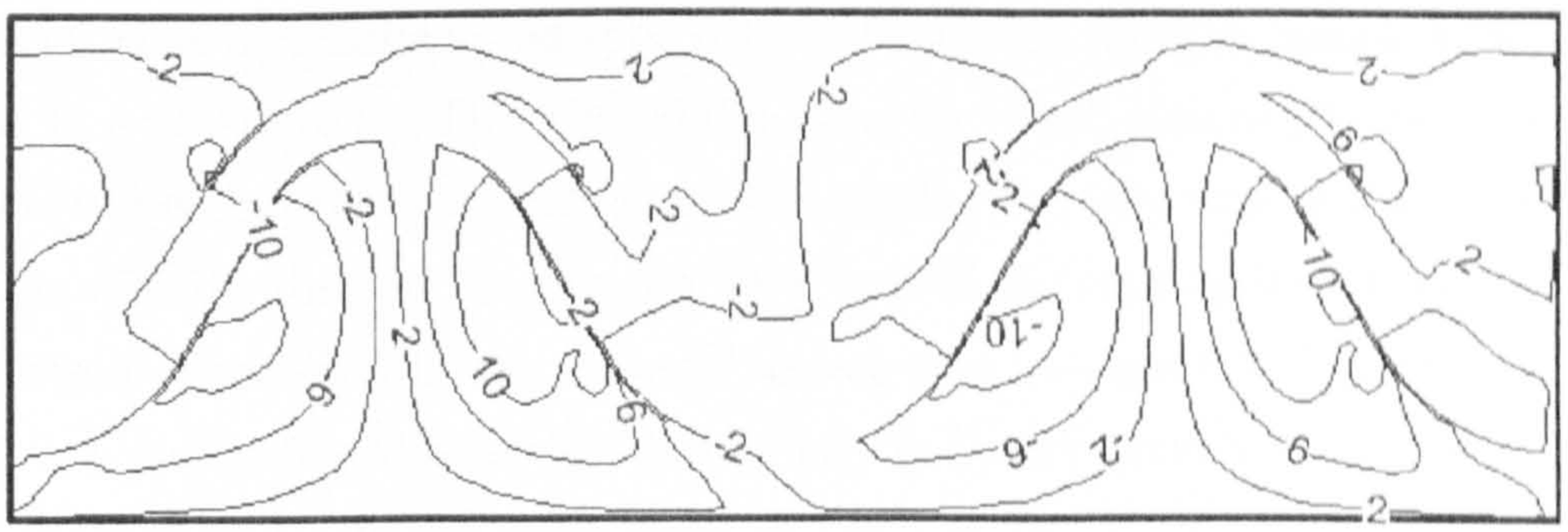

Figure 6.41: Deviation of a numerical grid (shown in Figure 6.40) from orthogonality: Maximum deviation = 10°, Mean deviation = 3.2°

Table 6.5: Hydraulic conditions for channels with s = 1.370

	Case 2(a)	**Case 2(b)**	**Case 2(c)**
Relative depth (Dr=(H-h)/H)	0.0	0.15	0.5
Water depth (H)	0.0519	0.0630	0.1059
Mean velocity (U_s, m/s)	0.197	0.129	0.282
Discharge (Q, m^3/s)	1.556	2.513	19.996
Friction velocity (u_*, m/s)	0.0148	0.0120	0.0221
Reynolds number (Re ($\times 10^4$))	2.19	0.66	4.92

parameters such as flow discharge and Reynolds numbers for the three relative depths.

In this section, the flow mechanisms are discussed by describing depth averaged parameters, cross-sectional mean velocity and secondary currents for the three different relative depths. The model performance is also assessed by comparing computed results with experimental data.

6.4.2.1 Inbank Flow (Dr=0.0, s=1.37)

Figure 6.42 (a) shows the predicted depth averaged mean velocity profile for the inbank flow of meandering channel (s=1.37). From Figure 6.42 (a) it can be seen that a maximum velocity core (0.2 m/s) is formed, which is smaller than in s=1.093 case. This core shifts from the inner side of the bend to the outer wall within the bend curvature and reaches the side wall of the cross over region. Finally, the core reaches the inner side of the next apex section. Similar behaviour is reflected in the velocity vectors plot as shown in Figure 6.42 (b). The flow direction is streamwise, particularly in the crossover region, as it follows the channel wall. At the inner bend of the apex section high velocity vectors are clearly observed, which also suggests the formation of a maximum velocity core at the same location. Figure 6.42 (c) shows the depth averaged pressure distribution for the inbank flow case. From the figure it can be seen that at the inner bend, where the high velocity core formation is observed, a low pressure region exists and at the outer bend, a high pressure region can be seen, which is smaller in profile to s=1.093 case. However, in the crossover region no pressure variation is noticed. In terms of the free surface elevation effect, the difference in the water level is found to be $1.325mm$ corresponding to $\Delta P = 13$ (see Equation 6.4), which is greater than in s=1.093 case.

The mean velocity profiles for different cross sections (S1 to S13 of figure 6.39) obtained from the model and from experiments are produced in Figure 6.43. From the measured data it can be seen that the maximum velocity, the magnitude of

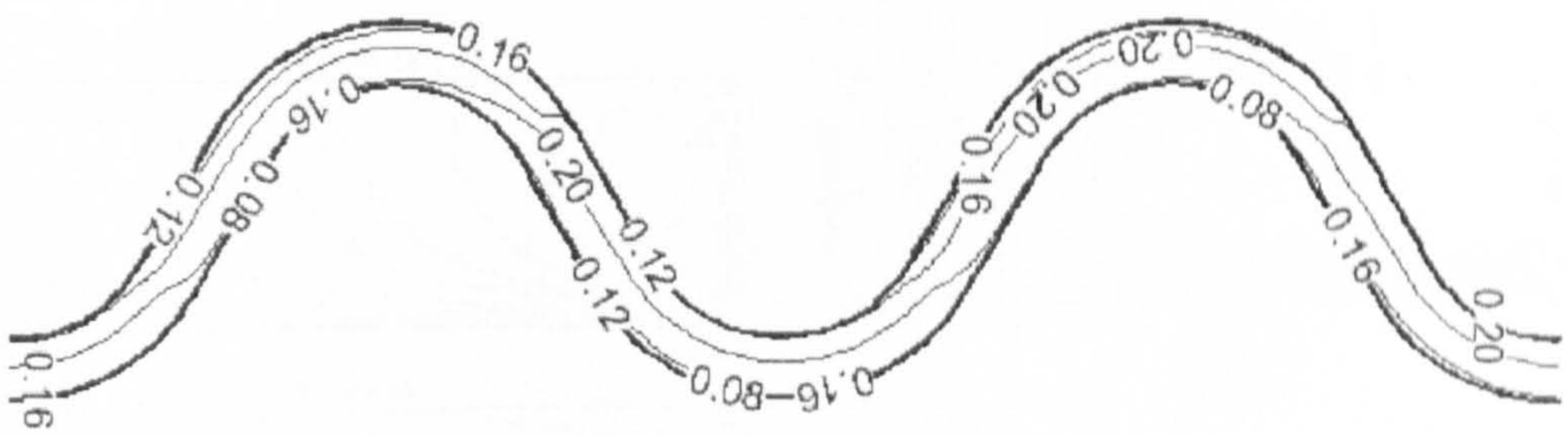

(a) Longitudinal Velocity U

(b) Velocity vectors

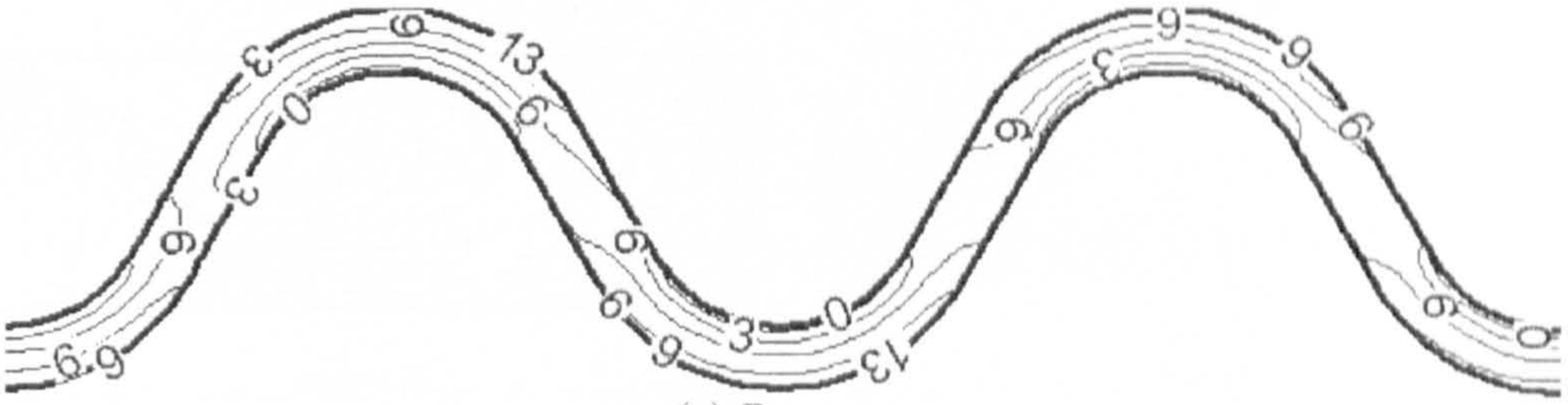

(c) Pressure

Figure 6.42: S=1.370, Inbank flow: Plan view of depth averaged (a) mean velocity in m/sec, (b) velocity vectors in m/sec and (c) pressure distribution in N/m^2. Due to the centrifugal forces the velocity is higher at inner side of the apex section which causes low pressure at the same location. The pattern is repeated at next apex section but in opposite manner.

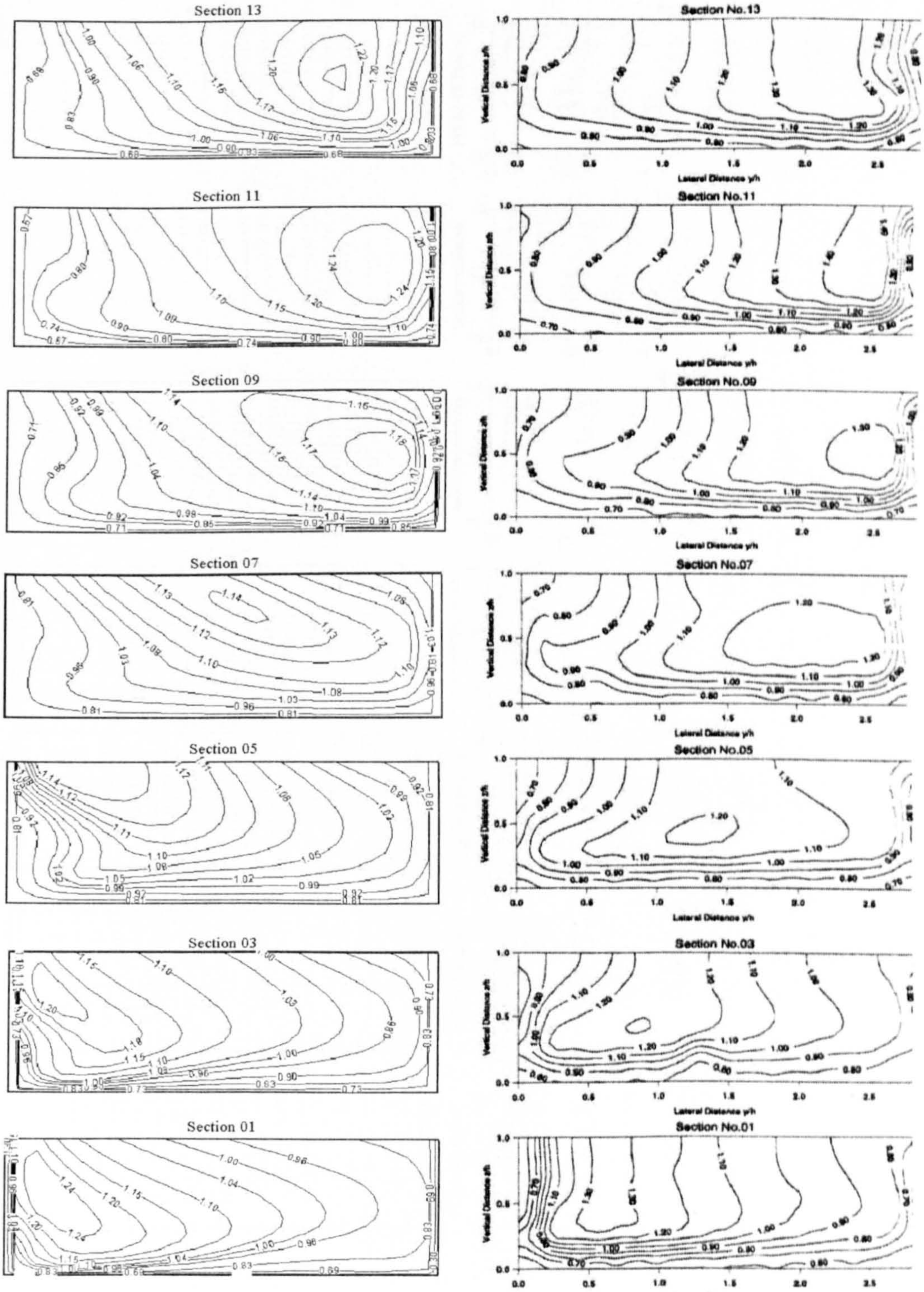

(a) Calculated (b) Experiments

Figure 6.43: S=1.370, Inbank flow: Comparison of simulated U/U_s with experimental data collected by Muto (1997) at different sections. For section configuration in the channel, see Figure 6.39.

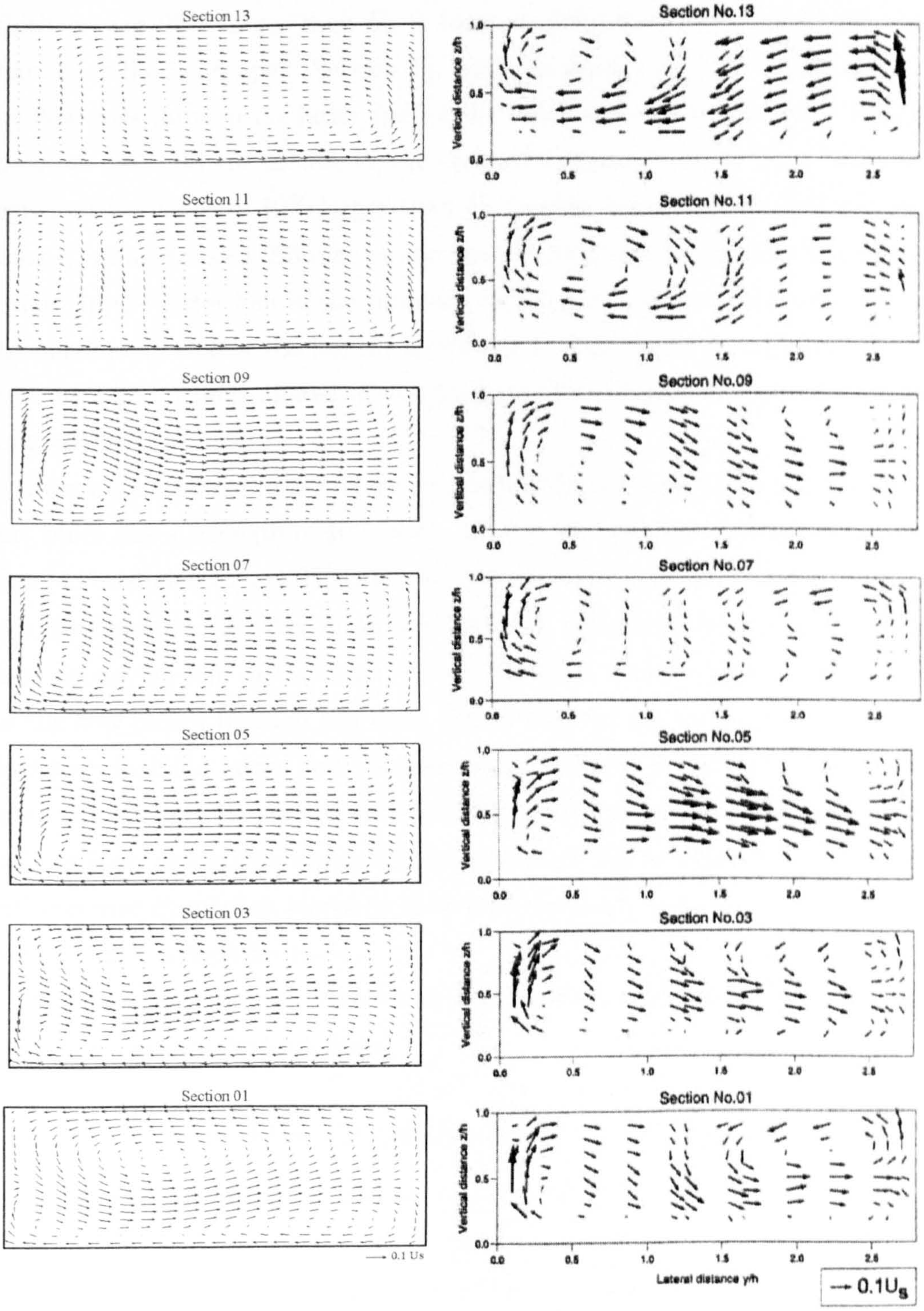

(a) Calculated (b) Experimental

Figure 6.44: S=1.370, Inbank flow: Comparison of simulated secondary currents with experiments data collected by Muto (1997) at different sections. For section configuration in the channel, see Figure 6.39. Strength of currents are 10% of the mean velocity.

which is over 20% larger than U_s is located along the inner wall of the main channel at the bend apex (Section 1), which is similar to the s=1.093 case. As the flow goes through the latter half of the bend, the core region moves towards the outer wall. In the middle of the crossover region (Section 7), a faster flow region with a velocity 10% larger than U_s reaches the right side wall and runs along it, whilst for s=1.093 case profile remains uniform throughout the crossover region. In the latter half of the meander (Section 11), same as the s=1.093 case the maximum velocity reaches up to 25% of U_s and starts to shift towards the inner wall and attains almost mirror image at S13. This behaviour is very well captured by the model.

Figure 6.44 shows the secondary circulations for different sections of the meander, which has a strength of 10% of U_s. The magnitude and circulation patterns found to be similar to s=1.093 case. At apex section S1 two currents, one rotating in a clockwise and another in an anticlockwise direction, are observed, each of them occupying half of the cross section, which is similar to the s=1.093 case. As the flow passes through the bend (S1 to S5), the circulation rotating in the clockwise direction grows and transfers away momentum from the inner to the outer wall. Within the crossover region (S5 to S9), the circulation tries to stabilize. As soon as the flow enters the latter half of the meander (S9 to S13), the anticlockwise circulation starts to grow and dominate most of the cross section at S13, which is opposite to S1.

The secondary currents reproduced by the model are in reasonably good agreement with the experimental data.

6.4.2.2 Overbank Flow (Dr=0.15, s=1.37)

Figure 6.45 shows the plan view of (a) the depth averaged mean streamwise velocity, (b) velocity vectors and (c) the pressure distribution for a compound meandering channel with s=1.370, Dr=0.15. The flow structures found similar to those of s=1.093 (Dr=0.15) case. However, the important difference can be described as follow.

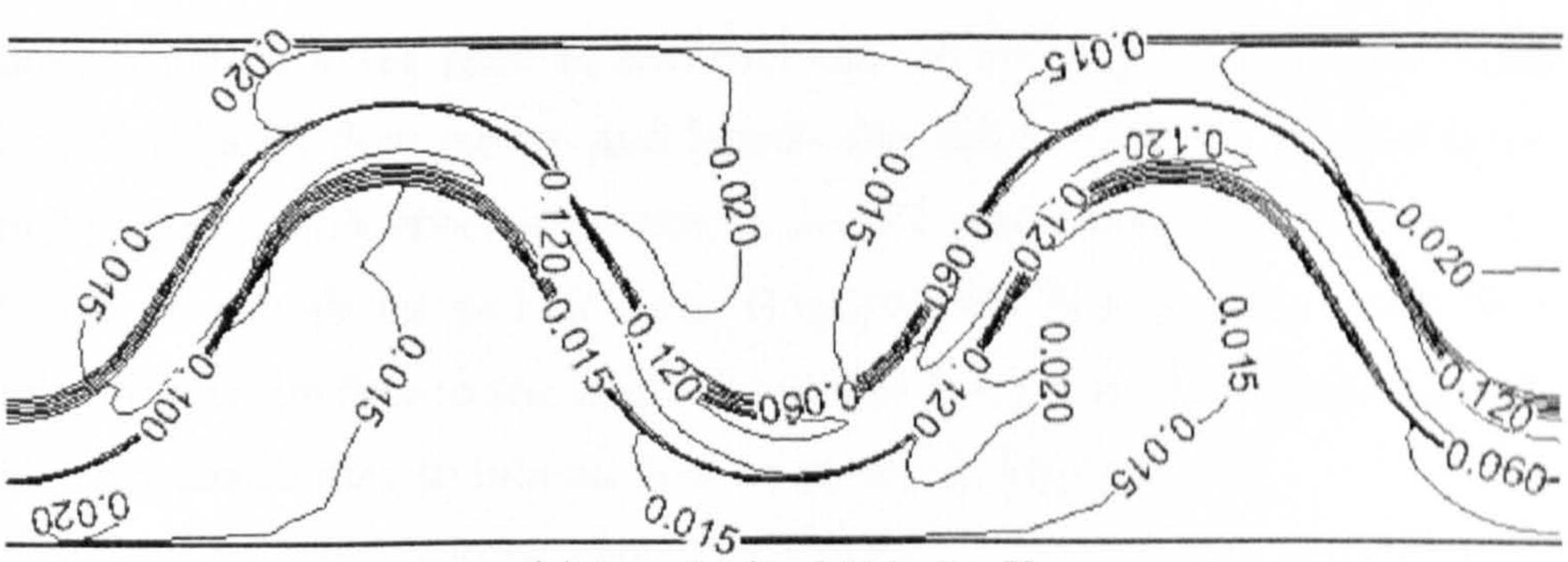

(a) Longitudinal Velocity U

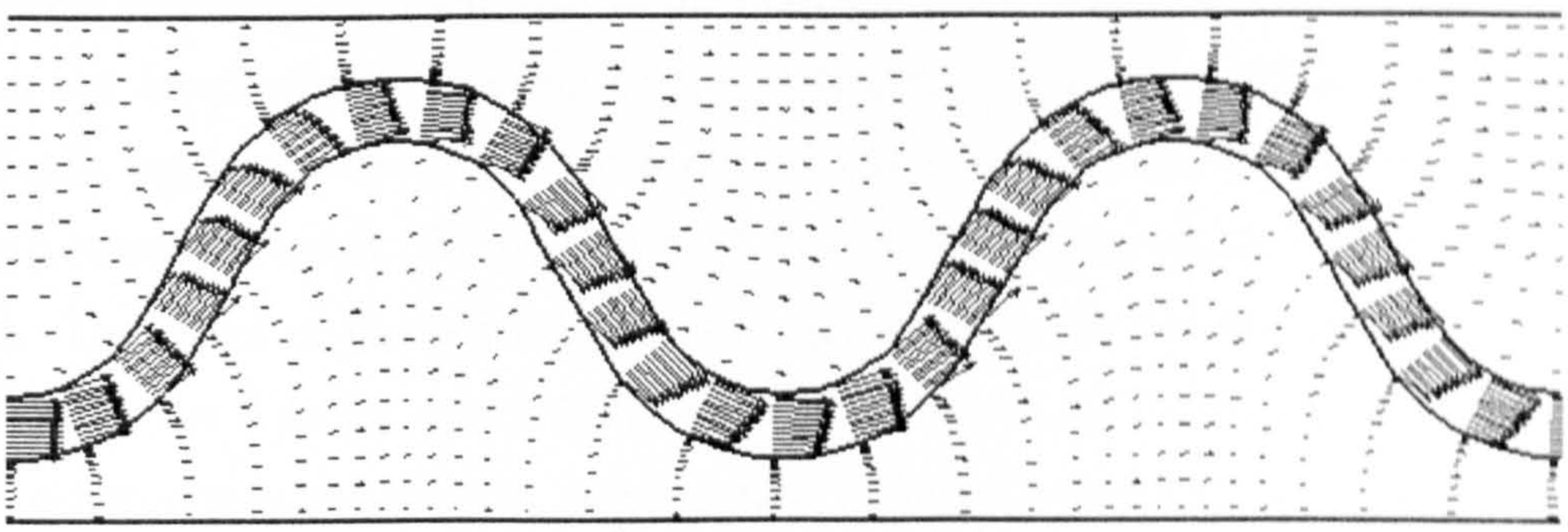

(b) Velocity vectors

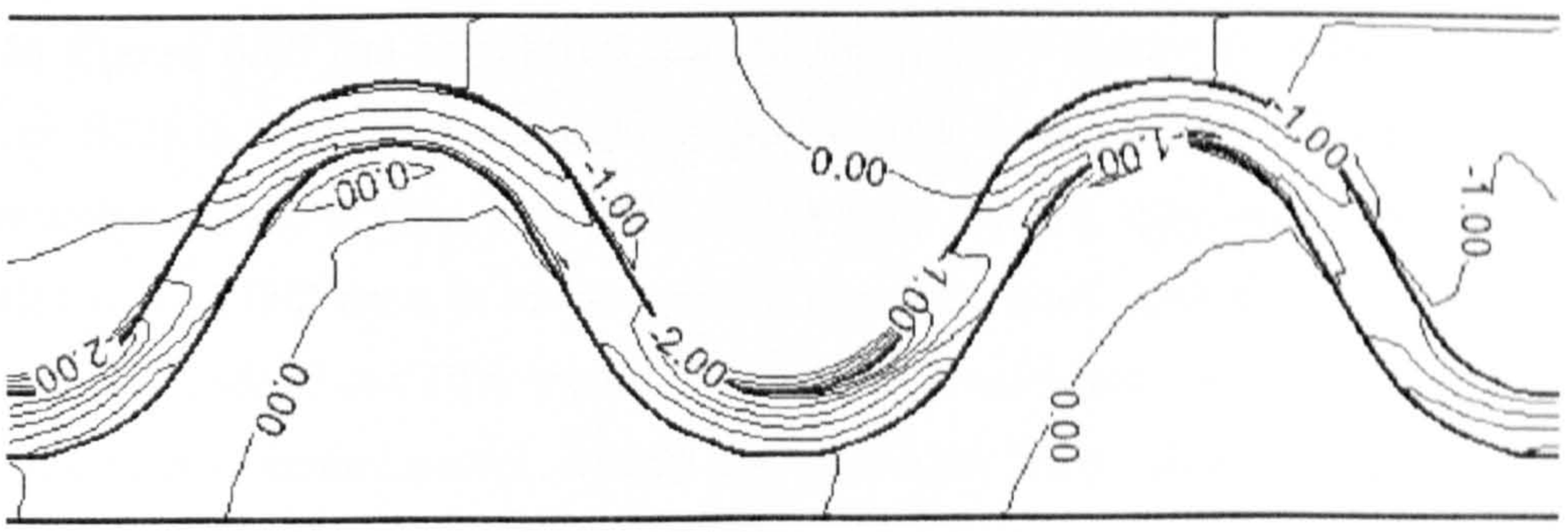

(c) Pressure

Figure 6.45: S=1.370, Dr=0.15: Plan view of depth averaged (a) mean velocity in m/sec, (b) velocity vectors and (c) pressure distribution in N/m^2. Due to the centrifugal forces the velocity is higher at inner side of the apex section which causes low pressure at the same location. The pattern is repeated at next apex section.

From the depth averaged velocity profile (see Figure 6.45 (b)) it can be seen that the maximum velocity of 0.12 m/s is observed at the inner bend of the apex section, which is lower than in s=1.093 case ($0.18m/s$). Within the crossover region, floodplain flow enters and leaves the main channel, which causes the plunging effect. This effect is greater in s=1.37 case than in s=1.093 due to the high crossover angle for s=1.37 case. However, the flow pattern is not changed significantly as the flow in the main channel is dominant. The main channel flow profile remains similar to inbank flow as shown in Figure 6.42.

From the velocity vectors, shown in Figure 6.45 (b), it can be observed that the flow entering from the upstream floodplain into the main channel deviates from the longitudinal direction to the streamwise direction. This is due to the stronger main channel flow. However, at the main channel-floodplain junction near crossover region, the deviation of flow is slightly stronger than in s=1.093 case. The effect of the centrifugal force on the pressure distribution can also be seen in Figure 6.45 (c), which is almost similar to s=1.093 case in terms of profile. The difference in pressure at apex section is found equal to 3 N/m^2 (equivalent to $\Delta H = 0.31mm$), which is greater than s=1.093 case.

In Figure 6.46 the calculated normalised mean velocity at different sections (S1 to S13) is compared with the experimental data. It can be seen from the experimental results that at bend apex section (S1), a maximum velocity core, similar to s=1.093 case, is seen to develop at the inner wall of the bend, which has a magnitude about 10% higher than the cross sectional average velocity. This core remains at same location within the bend curvature. However, as soon as the flow enters into the crossover region, the core shifts towards the other side wall and remains at same location till it reaches the next apex section. For s=1.093 case, the core shifts at the middle of crossover region. In addition, the slowly moving floodplain flow intrudes into the main channel in which the flow is fast. This causes a high velocity gradient at the main channel-floodplain junction (S5), which is less visible in s=1.093 case. An increasing area is getting affected due to the intruding flow along the crossover sections (S5 to S9). It can also be noticed

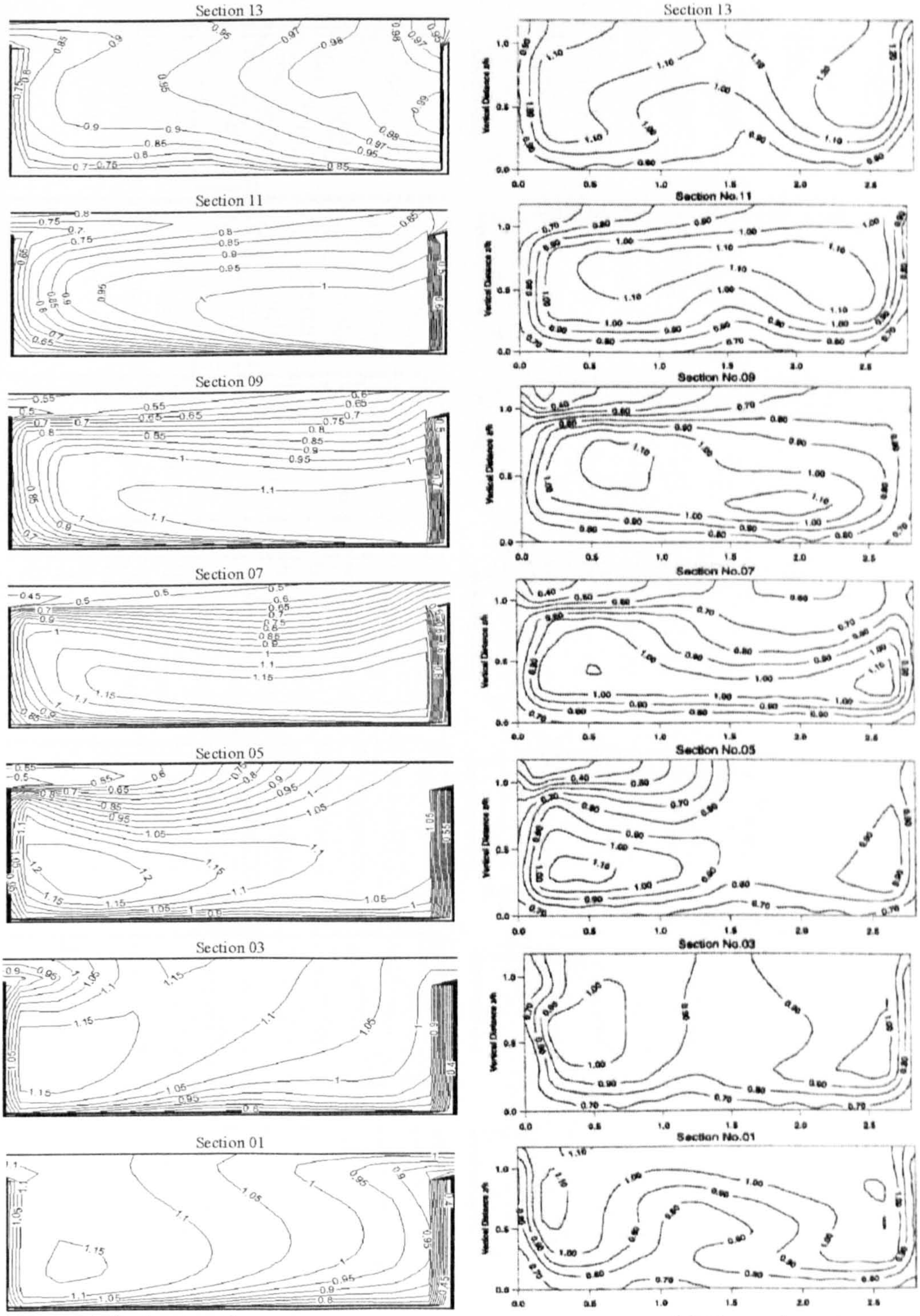

Figure 6.46: S=1.370, Dr=0.15: Comparison of simulated U/U_s with experimental data collected by Muto (1997) at different sections. For section configuration in the channel, see Figure 6.39. Accumulation of contour lines near right side wall in computed results is due to the node arrangement in the same vicinity.

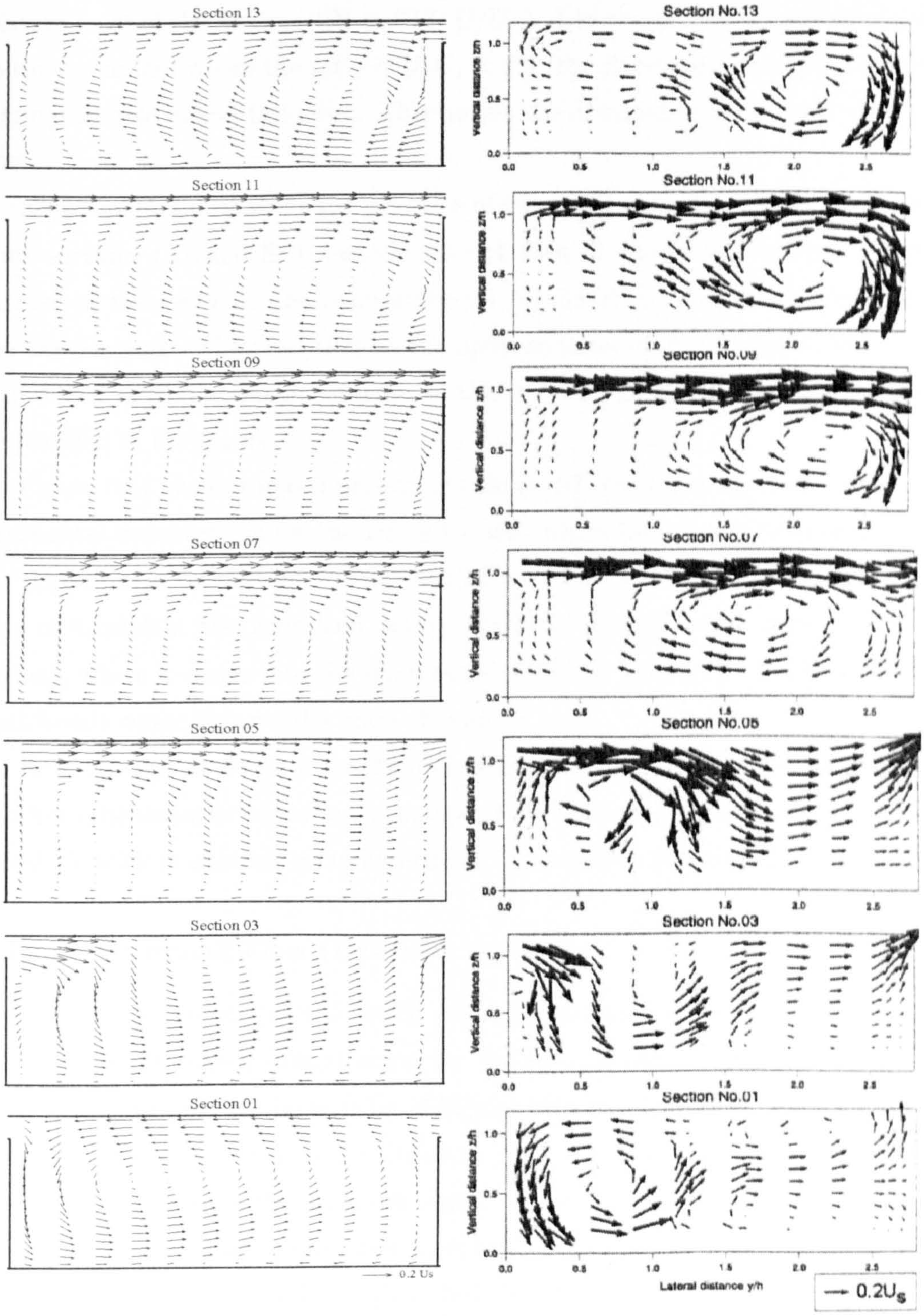

(a) Calculated (b) Experiments

Figure 6.47: S=1.370, Dr=0.15: Comparison of simulated secondary currents with experiments data collected by Muto (1997) at different sections. For section configuration in the channel, see Figure 6.39. Strength of currents are 20% of the mean velocity.

that, in most of the sections (S1 to S13) $U/U_s > 1$ in the main channel, compared to the floodplain where the ratio is $U/U_s < 0.8$ (the floodplain flow is not clearly distinguishable in s=1.093 case). This proves the dominance of the main channel flow.

Experimental data show the presence of two maximum velocity cores at both apex sections (S1 and S13), which are not seen in the computational results. In rest of the sections, the computational results match reasonably well with the experiments. The deviation at the apex sections might be due to the error introduced by the non-orthogonality of the grid and grid refinement, which can be justified in the future.

Figure 6.47 shows the comparison of calculated secondary currents to the experimental investigation for the Dr=0.15 case, which has a magnitude of 20% of U_s. The circulation pattern remains similar the s=1.093 case. However, the presence of floodplain flow is noticed clearly at section S5 (beginning of the crossover region), where it enters into the main channel and at section S11 (begging of the next bend) where it leave the main channel.

From the model results it can be noticed that the computed results have again captured the essential behaviour of compound meandering channel flow (s=1.37), Dr=0.15, with reasonably good agreement compared to the experimental data.

6.4.2.3 Overbank Flow (Dr=0.50, s=1.37)

Figure 6.48 represents (a) the depth averaged streamwise velocity, (b) velocity vectors and (c) pressure distribution for the Dr=0.5 case. From the depth averaged velocity profile, the bulging of higher velocity (0.25 m/s) is observed at apex sections. Compared to the Dr=0.15 case, the intrusion of floodplain flow is even more visible in the crossover region. It can be noticed that the profile is not symmetrical at two consecutive apex sections. Moreover, the velocity profile on both sides of overbank is roughly similar but not symmetrical. Flow on the top floodplain is found faster than on the bottom floodplain. This may be due

to the way in which the orthogonal grid (refer Figure 6.40) is generated. As discussed in Section 6.4.1, two separately generated overbank grids have different deviation from orthogonality and hence are prone to non-orthogonality errors of differing magnitude. The magnitude of error is observed to be the same for different relative depths.

From the vector plot (see Figure 6.48 (b)) it can be seen that flow on the floodplain is dominant. The main channel flow, especially in the crossover region, is affected by the strong floodplain flow. Hence, the flow direction of the flow in the main channel deviates partially from streamwise to longitudinal unlike the Dr=0.15 case. The magnitude of the vectors becomes roughly equal for flood plain and main channel flows.

From the pressure plot, Figure 6.48 (c), it can be noticed that there is a formation of high pressure on the floodplain near each apex section, which is due to the fact that the floodplain width reduces on the approach to the apex section. One of the reasons for this might be that the flow in the main channel is slightly faster (0.2 m/s) than the floodplain flow (0.15 m/s). Therefore, the flow on floodplain converges and increases the pressure as it approaches the apex section. There, the floodplain flow suddenly enters the main channel and releases the pressure. At apex section, $\Delta P = 10\ N/m^2$ which is equivalent to 1.02 mm of ΔH and greater than s=0.15 case.

Figures 6.49 and 6.50 shows a comparison of the calculated mean velocity with the experiments. From the experimental data it can be seen that similar to the Dr=0.15 case, a steep gradient is observed at section 05 where the floodplain flow intrudes into the main channel, which is less visible in s=1.093 case. A slower velocity, roughly 60% of U_s is observed on the outer wall of bend sections. The flow below the bankfull level has a value of U/U_s less than 1.0 throughout the meander, which suggests that the main channel, in this case act as a resistance to the overall flow. Contrary to this, in s=1.093 case, no significant difference noticed between the velocities of main channel and floodplain flow. From the

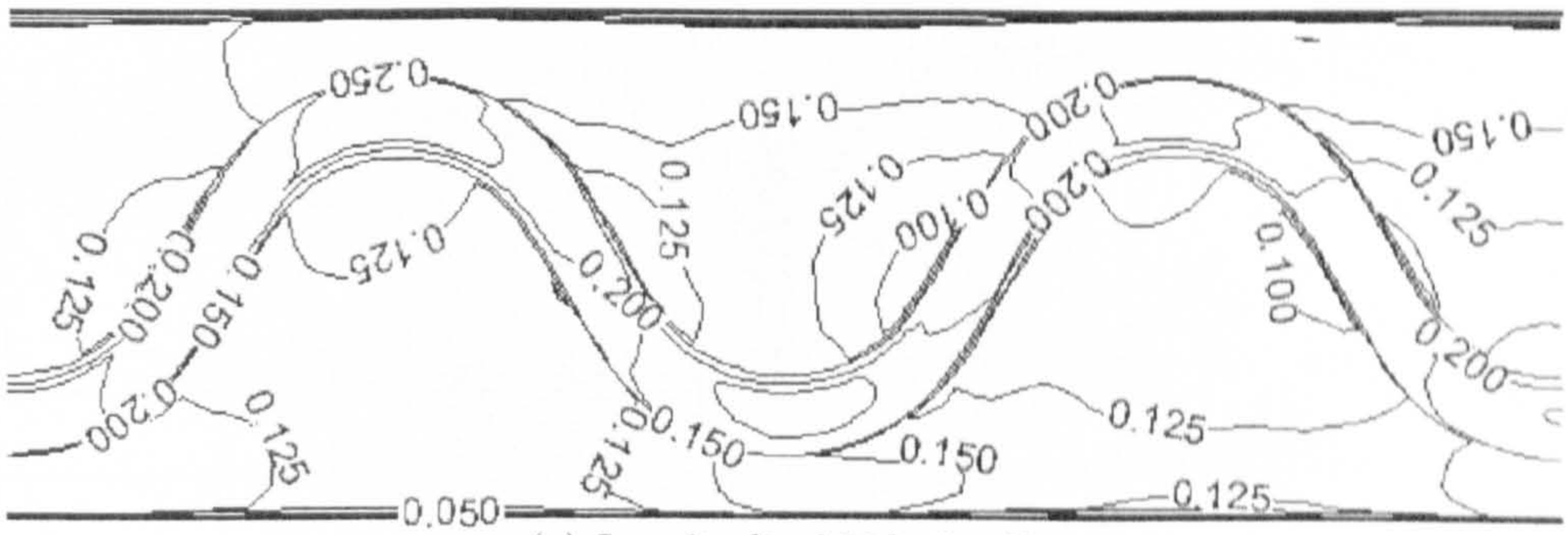

(a) Longitudinal Velocity U

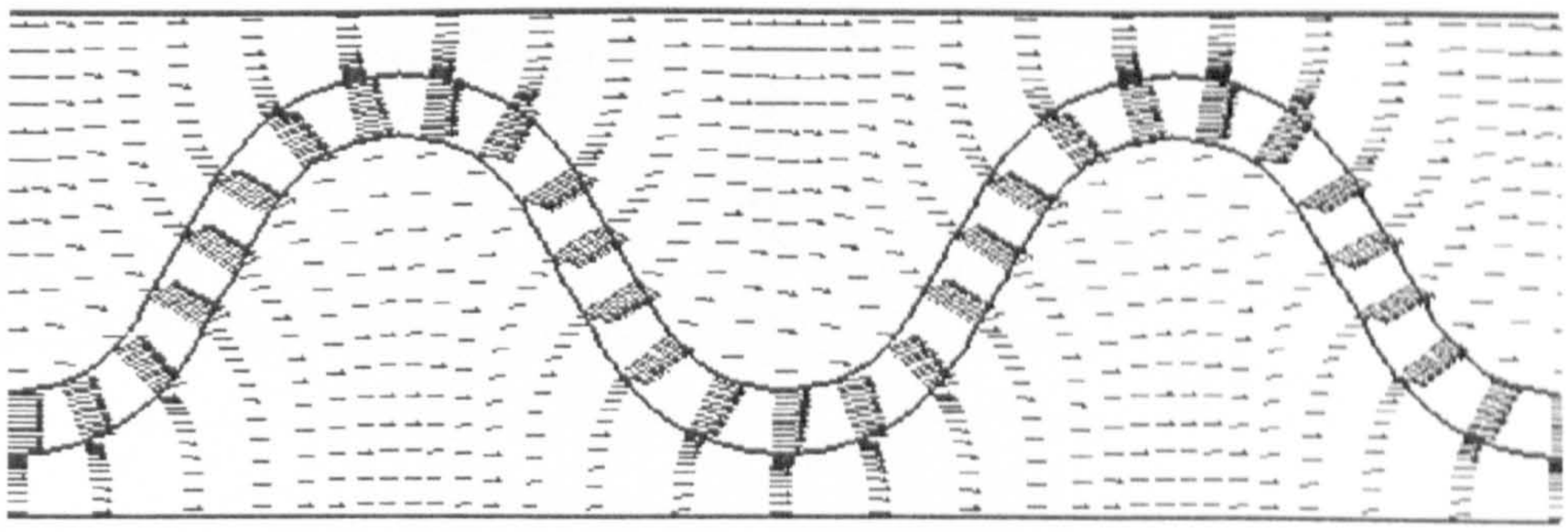

(b) Pressure

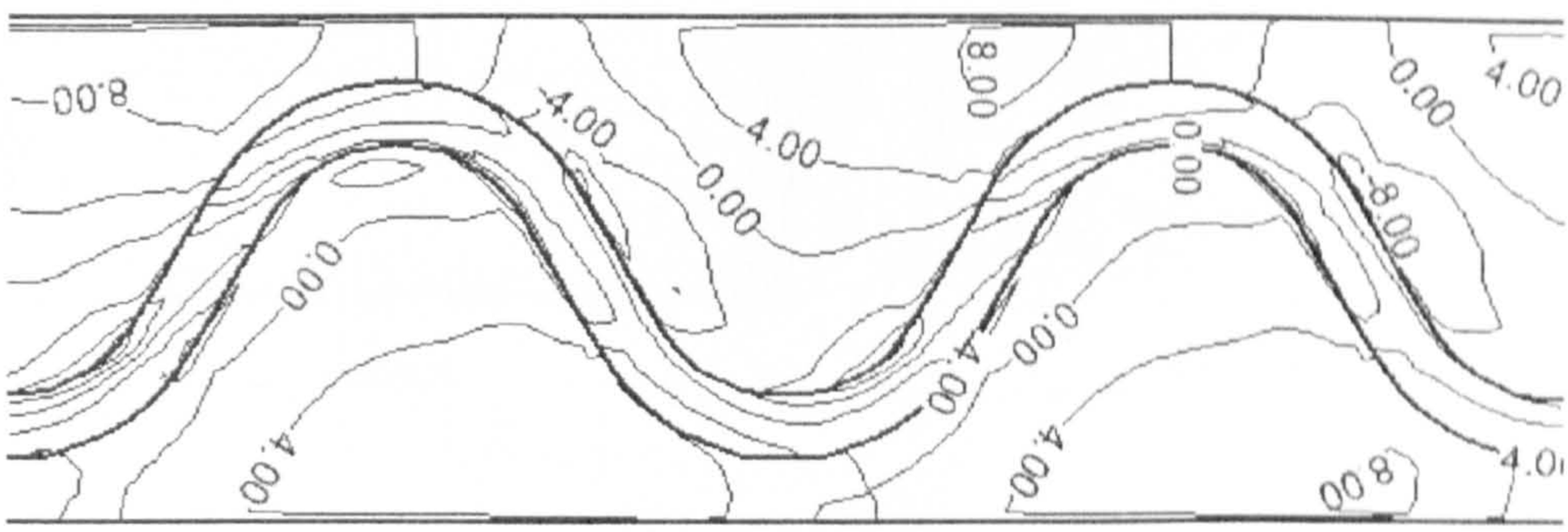

(c) Velocity vectors

Figure 6.48: S=1.370, Dr=0.50: Plan view of depth averaged (a) mean velocity in m/sec, (b) velocity vectors and (c) pressure distribution in N/m^2. Due to the centrifugal forces the velocity is higher at inner side of the apex section which causes low pressure at the same location. The pattern is repeated at next apex section.

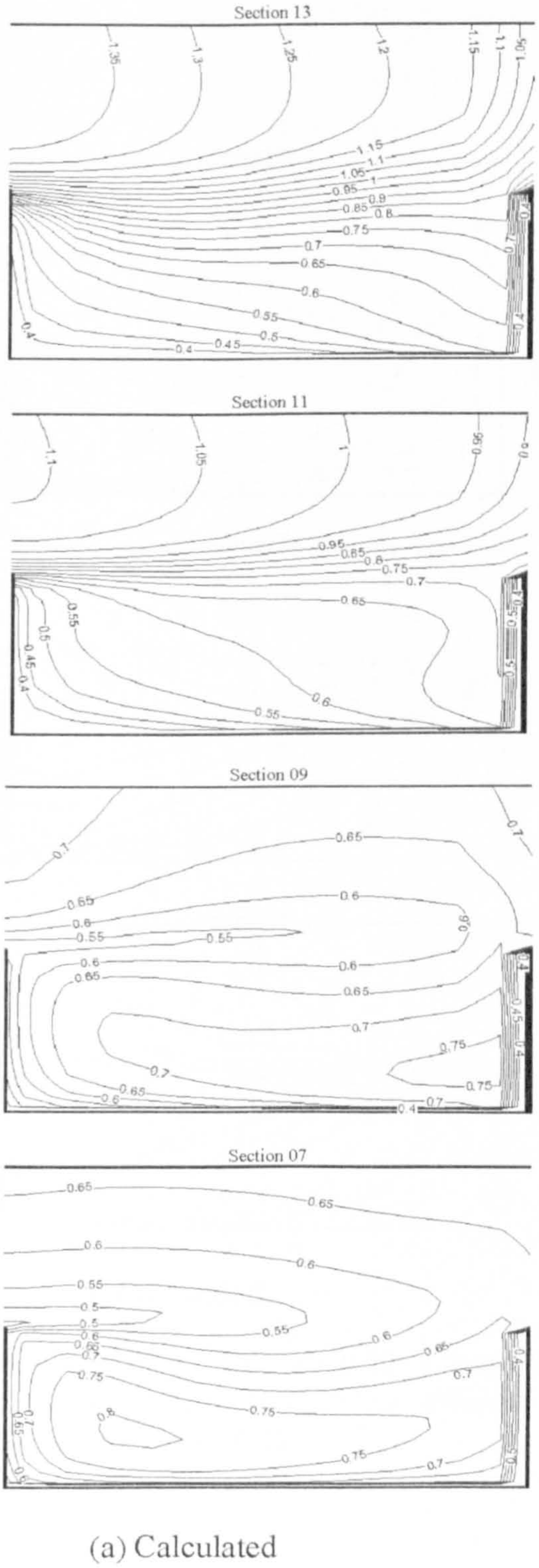

(a) Calculated (b) Experiments

Figure 6.49: S=1.370, Dr=0.50: Comparison of simulated U/U_s with experimental data collected by Muto (1997) at different sections. For section configuration in the channel, see Figure 6.39. Accumulation of contour lines near right side wall in computed results is due to the node arrangement in the same vicinity.

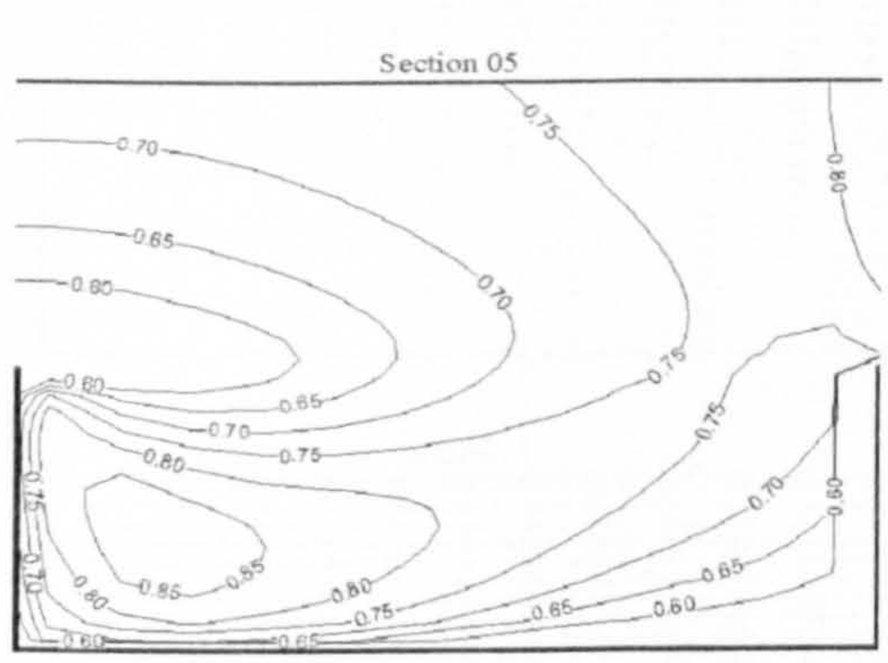

(a) Calculated (b) Experiments

Figure 6.50: S=1.370, Dr=0.50: Comparison of simulated U/U_s with experimental data collected by Muto (1997) at different sections. For section configuration in the channel, see Figure 6.39.

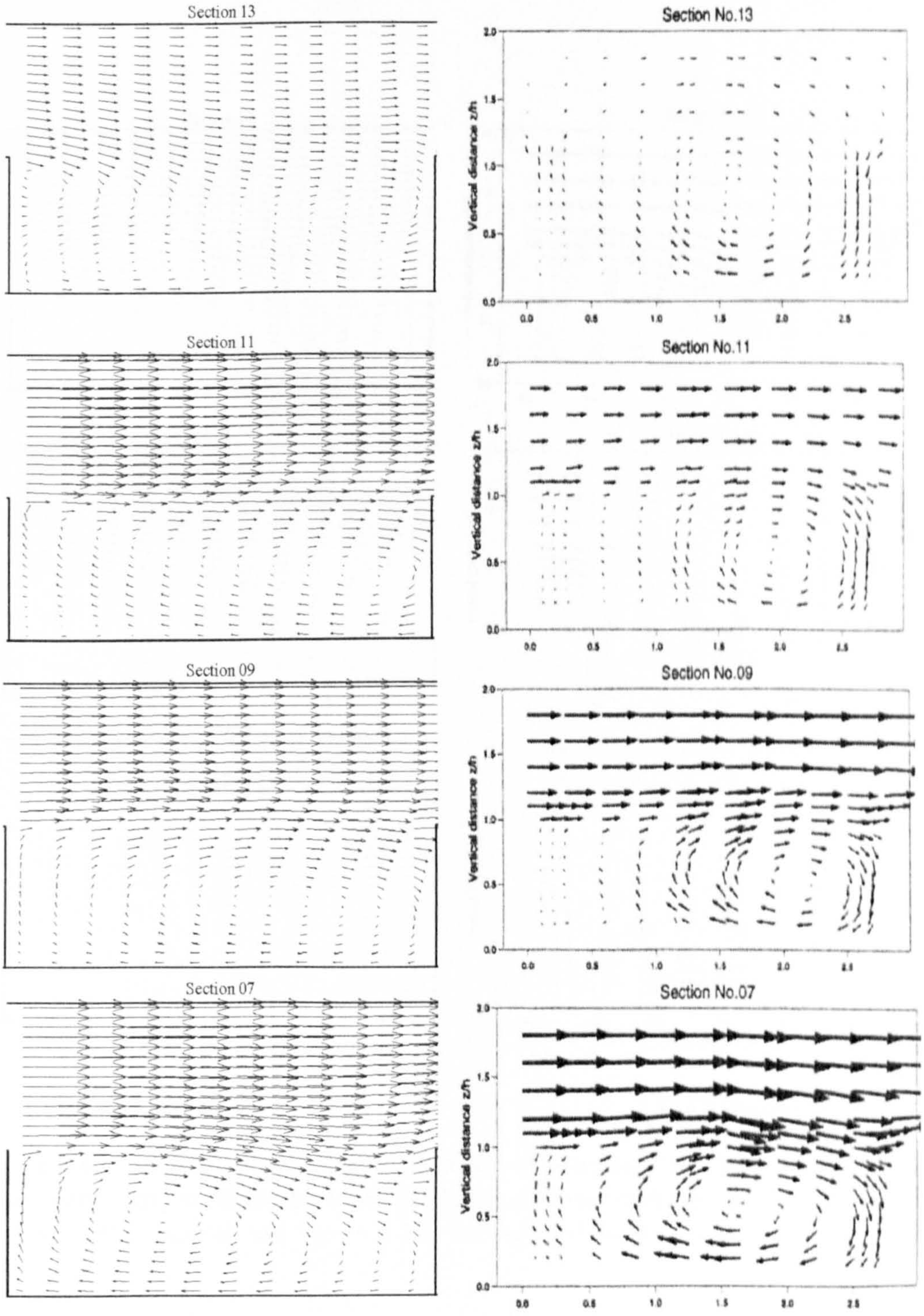

(a) Calculated (b) Experiments

Figure 6.51: S=1.370, Dr=0.50: Comparison of simulated secondary currents with experiments data collected by Muto (1997) at different sections. For section configuration in the channel, see Figure 6.39. Strength of currents are 50% of the mean velocity.

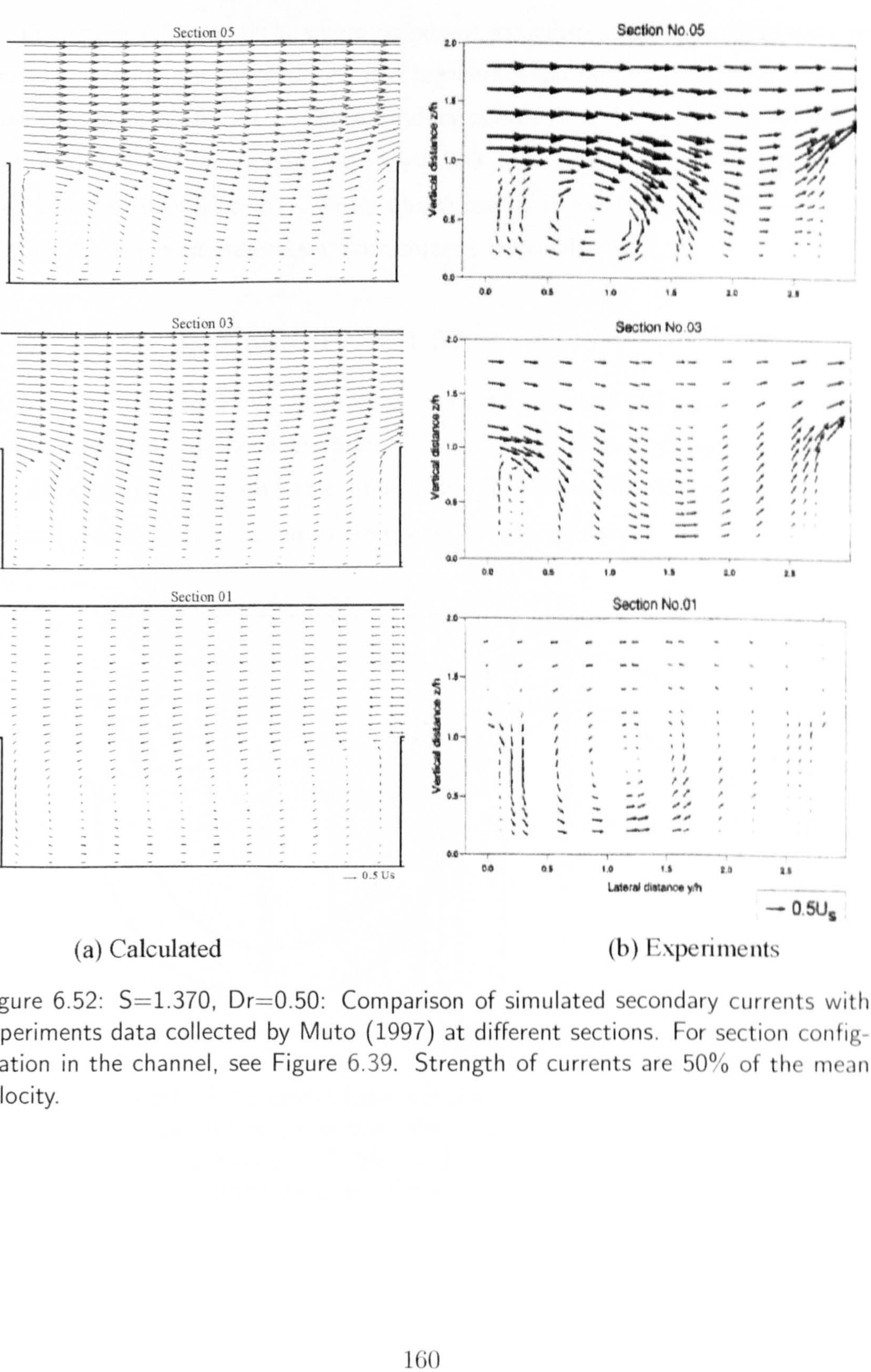

(a) Calculated (b) Experiments

Figure 6.52: S=1.370, Dr=0.50: Comparison of simulated secondary currents with experiments data collected by Muto (1997) at different sections. For section configuration in the channel, see Figure 6.39. Strength of currents are 50% of the mean velocity.

produced results it can be seen that the mean velocity profiles are captured very well by the model.

In Figures 6.51 and 6.52, a comparison of secondary currents at different sections is made between predictions and measurements for the Dr=0.5 case, which have strength of 50% of U_s. The secondary circulations pattern found similar to s=1.093 case. However, compared to s=1.093 case, very strong floodplain flow is seen from sections S5 to S11. From above results it can be said that the model is able of capture the secondary flow pattern reasonably well.

6.4.3 Case 3: Sinuosity = 1.57

After simulating compound meandering channels with s=1.093 and s=1.37, in this section simulation results are validated for a channel with a stronger sinuosity of s=1.57. Compared to previous channels, s=1.57 channel has the highest angle of arc and crossover angle, equal to 180° and 90° respectively.

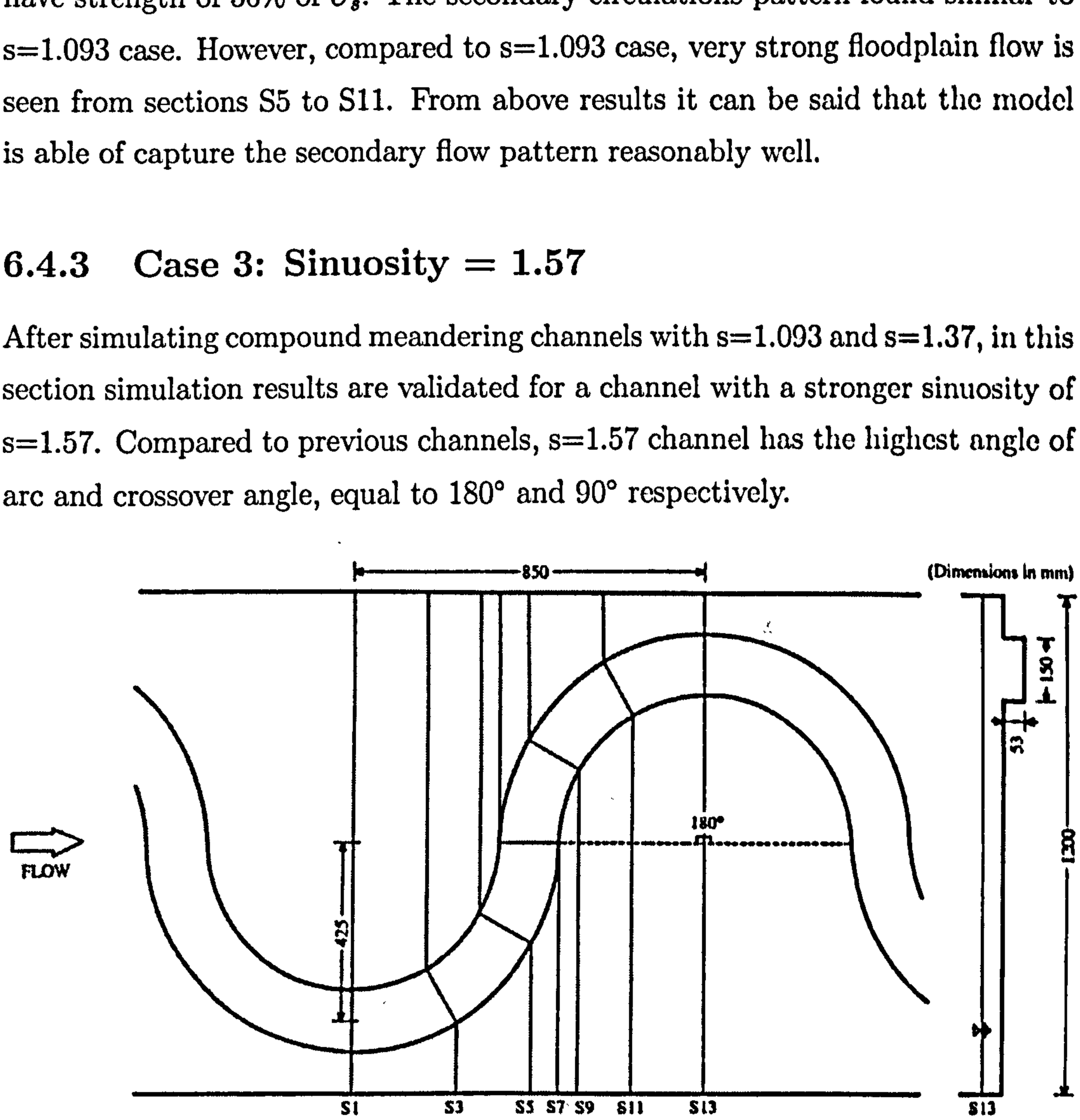

Figure 6.53: Sketch of the physical domain of compound meandering channel (sinuosity = 1.573) representing dimensions and measuring locations. Simulation results are compared for locations S1, S3, S5, S7, S9, S11 and S13. The view point of the cross section is same as the direction of flow

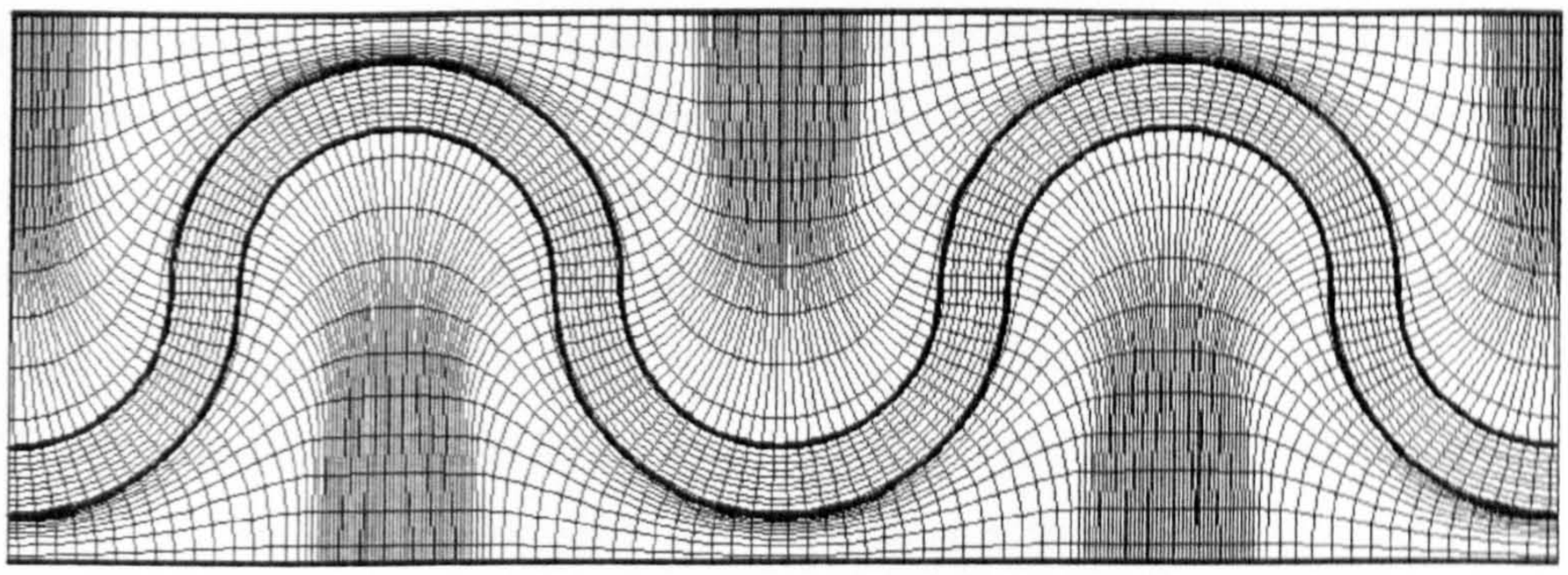

Figure 6.54: Plane view of an orthogonal computational grid (sinuosity = 1.093) of two meanders. No. of CVs are in horizontal (x) and lateral (y) directions are 160 and 30 respectively. In the main channel, no. of CVs are 10.

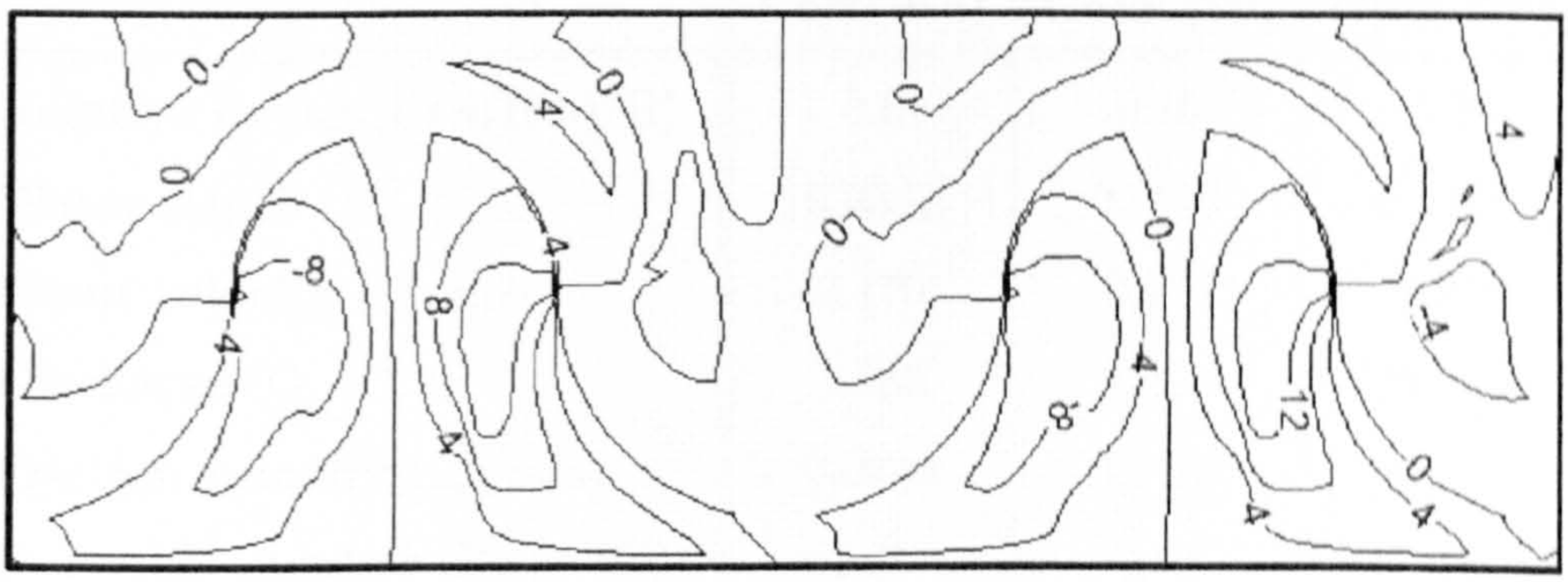

Figure 6.55: Deviation of a numerical grid (shown in Figure 6.54) from orthogonality: Maximum deviation = 12°, Mean deviation = 3.8°

Figure 6.53 shows a sketch of the physical domain of this compound meandering channel (s=1.57) describing the dimensions and experimental data comparison points (S1 to S13). In Figure 6.54 the corresponding computational orthogonal grid is shown, which comprises 160 and 30 CVs in the longitudinal (x) and spanwise (y) directions respectively. This is the most curved channel, making it difficult to generate the orthogonal grid, which can be seen by observing the aspect ratio of CVs. The maximum deviation and mean deviation from orthogonality are 12° and 3.8° respectively, which is shown in Figure 6.55; both of these

quantities are higher than s=1.093 and s=1.37 grids. This deviation seems non-symmetric on both floodplains, which is due to the way in which the orthogonal grid is generated, since the top floodplain side boundaries are less constrained compared to the bottom floodplain. Hence, more deviation is observed in the bottom floodplain region.

The hydraulic conditions for inbank flow, Dr=0.15 and Dr=0.50, are presented in Table 6.6. In this section, the flow mechanism is discussed for inbank flow, Dr=0.15 and Dr=0.5 cases and for each case computational results are compared with experimental data to assess the performance of the model.

Table 6.6: Hydraulic conditions for channels with s = 1.571

	Case 3(a)	Case 3(b)	Case 3(c)
Relative depth (Dr=(H-h)/H)	0.0	0.15	0.5
Water depth (H)	0.0532	0.0631	0.1087
Mean velocity (U_s, m/s)	0.170	0.113	0.268
Discharge (Q, m^3/s)	1.382	2.204	19.881
Friction velocity (u_*, m/s)	0.0140	0.0120	0.0226
Reynolds number (Re ($\times 10^4$))	1.95	0.62	5.16

6.4.3.1 Inbank Flow (Dr=0.0, s=1.57)

Figure 6.56 shows (a) the depth averaged mean velocity, (b) velocity vectors and (c) the pressure distribution for the inbank flow (s=1.57) case. Compared to the s=1.37 and s=1.57 cases, the channel has a greater bend length and crossover angle but a smaller crossover length as shown in Table 6.3.

In the depth averaged velocity profile (Figure 6.56 (a)) the maximum velocity core is formed at the beginning of the bend and within the bend, the core shifts towards the other side wall. The vector profile (Figure 6.56 (b)) and pressure

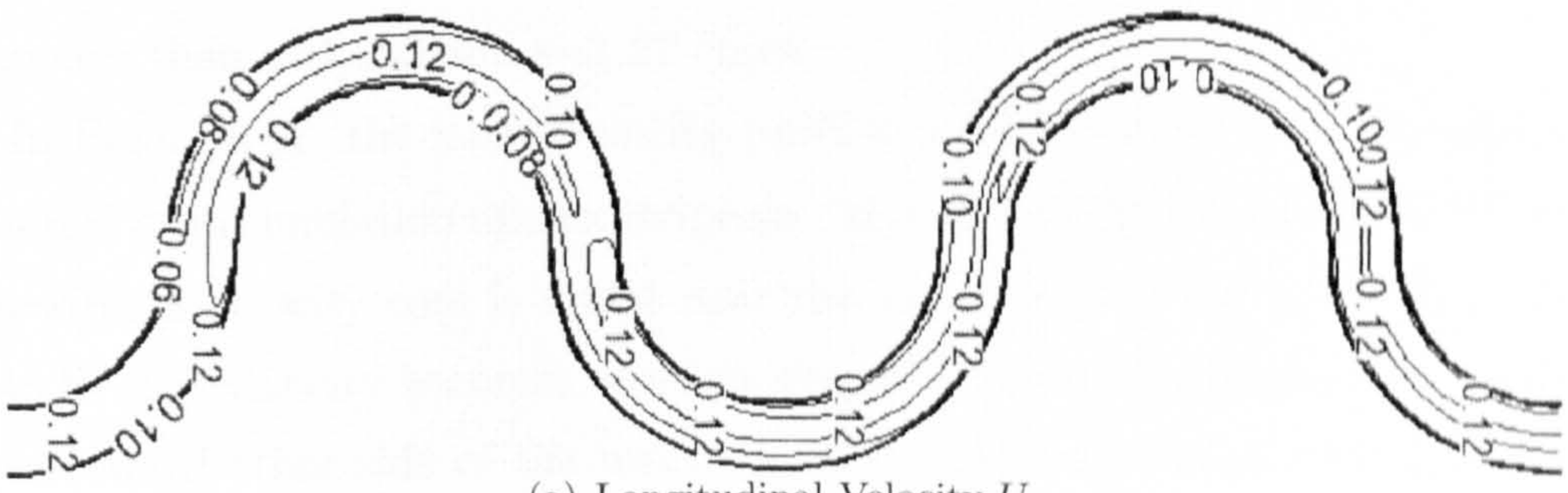

(a) Longitudinal Velocity U

(b) Velocity vectors

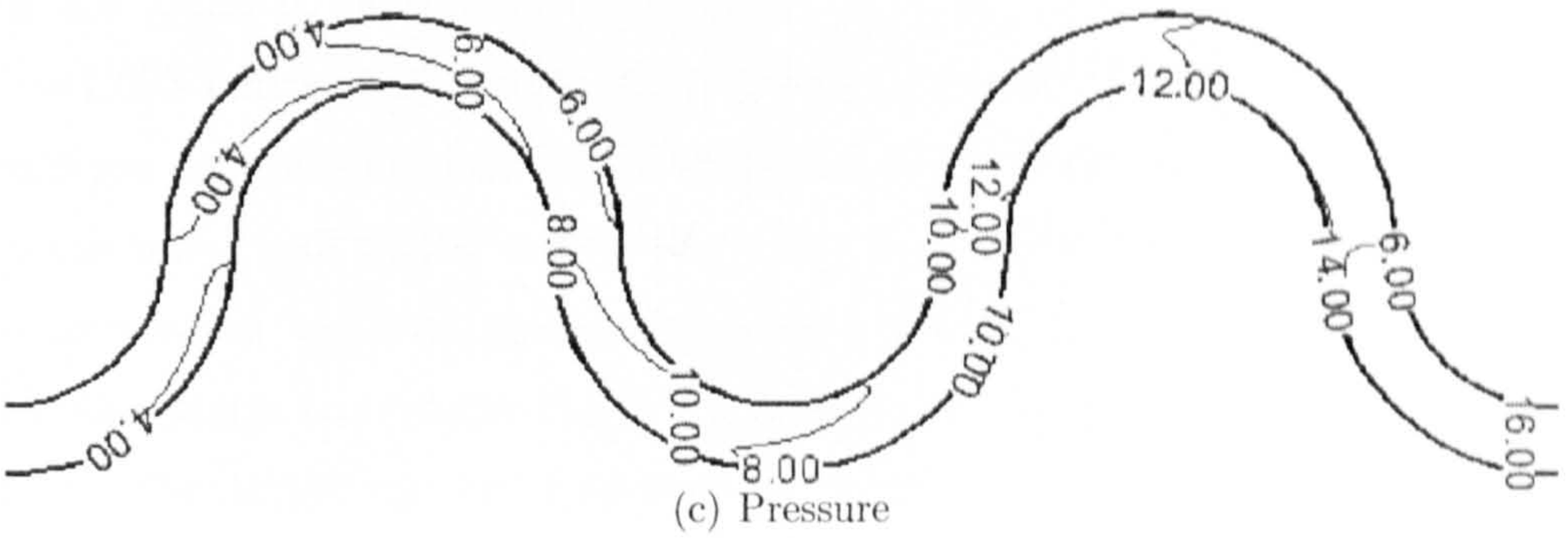

(c) Pressure

Figure 6.56: S=1.570, Inbank flow: Plan view of depth averaged (a) mean velocity in m/sec, (b) velocity vectors and (c) pressure distribution in N/m^2. Due to the centrifugal forces the velocity is higher at inner side of the apex section which causes low pressure at the same location. The pattern is repeated at next apex section.

profile (Figure 6.56 (c)) are almost similar in terms of the distributions to the inbank flow, s=1.37 channel (Section 6.4.2). However, in terms of magnitude ΔP is found equal to 14 N/m^2, equivalent to 1.43 mm of super elevation effect, which is greater than s=1.093 and s=1.37 cases.

In Figure 6.57, the mean velocity profiles at different sections are shown as obtained from simulation and experiment. As with the inbank flow (s=1.37) case, a maximum velocity core is found near the inner bend of the apex (S1). From S3 to S7, the velocity becomes uniform and the maximum velocity core starts to move toward other side of the wall, which is similar to the s=1.37 case. From the results, it can be concluded that the computed results for mean velocity are in good agreement with experimental data. Importantly, the model is able to capture the bulging of velocity in the corner of the main channel especially at S5 and S7 with good accuracy.

The secondary currents at various sections are shown in Figure 6.58. It can be seen that a dominating clockwise circulation is seen at S1 along with a small anticlockwise circulation at the outer bend/free surface junction. Both circulations are found to be of equal magnitude of 10% of the U_s, which is similar to the s=1.093 and s=1.37 cases. As the flow moves within the bend, a clockwise circulation occupies most of the cross section transferring momentum and energy from the inner wall to the outer. Once the flow enters into next bend the clockwise circulation weakens and anticlockwise circulation starts to gain strength, which also starts to transfer the momentum from the inner to the outer wall. At S13, the circulation pattern becomes opposite to that of S1. From the plotted results, it can be concluded that the computed results are in good agreement with experiments and the model works reasonably well for the inbank flow case (s=1.57).

6.4.3.2 Overbank Flow (Dr=0.15, s=1.57)

In Figure 6.59 (a) the depth averaged mean velocity, (b) velocity vectors and (c) the pressure distribution are shown for the Dr=0.15 case. The overall flow

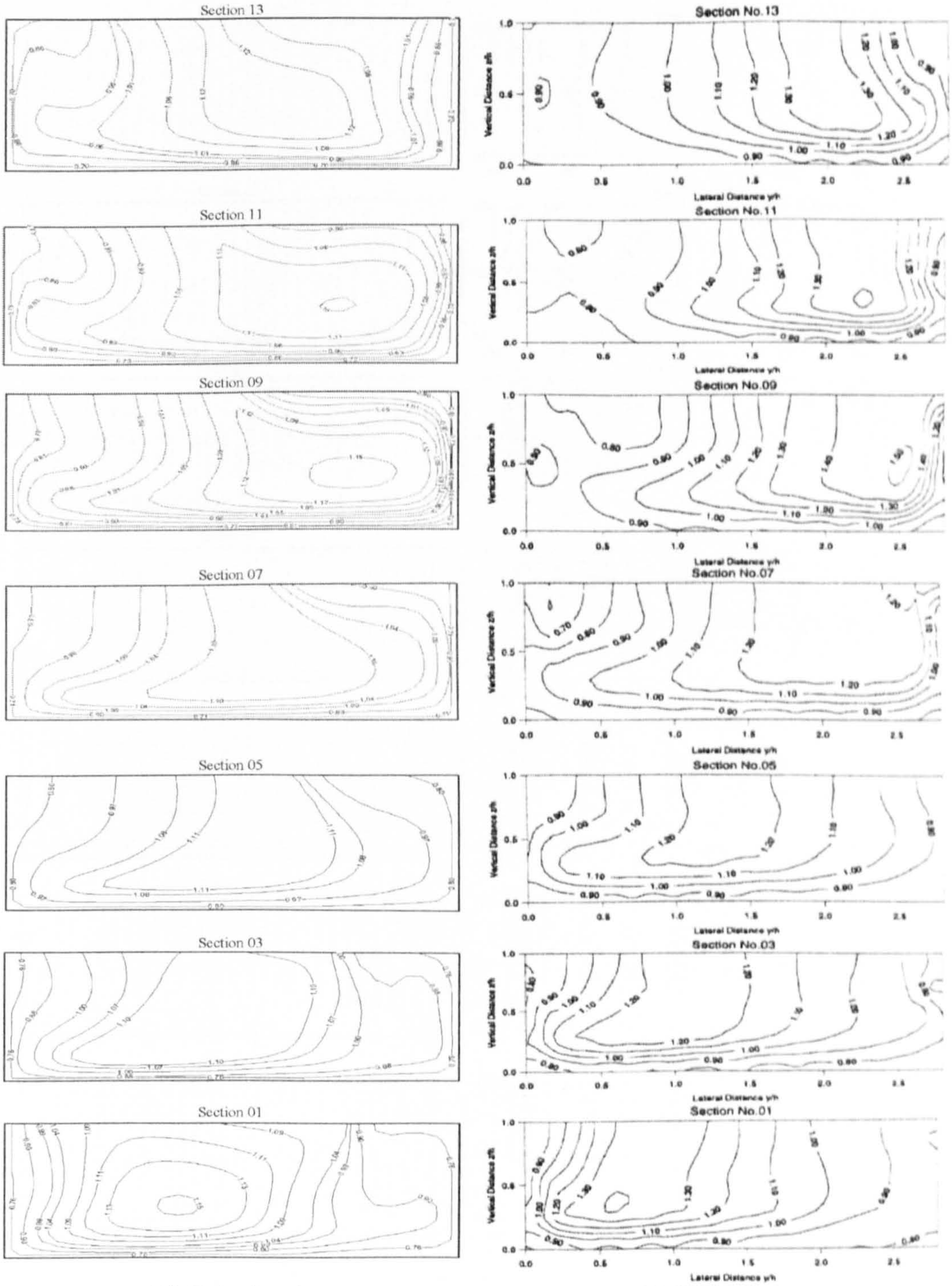

(a) Calculated (b) Experiments

Figure 6.57: S=1.570, Inbank flow: Comparison of simulated U/U_s with experimental data collected by Muto (1997) at different sections. For section configuration in the channel, see Figure 6.53.

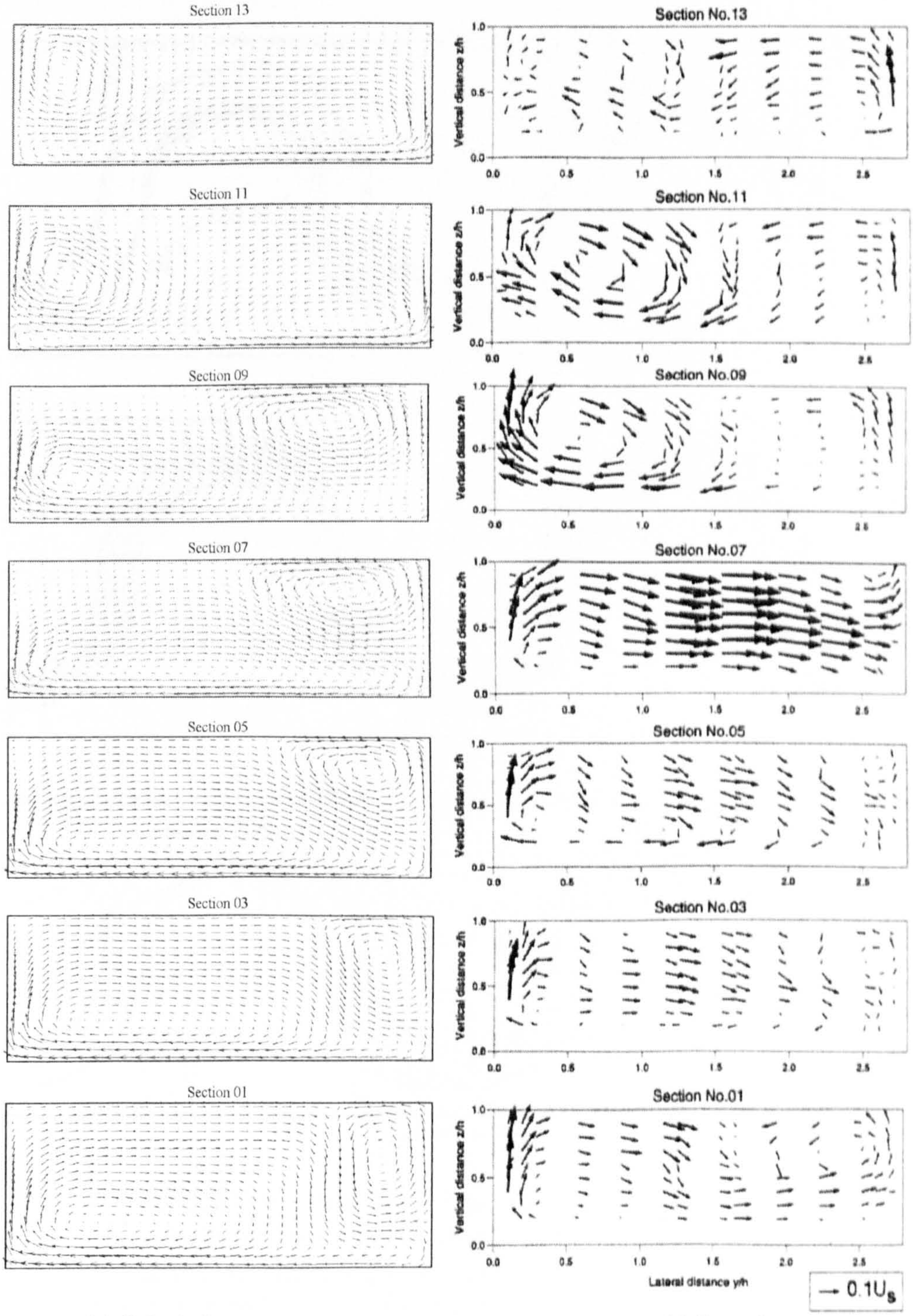

(a) Calculation (b) Experiments

Figure 6.58: S=1.570, Inbank flow: Comparison of simulated secondary currents with experiments data collected by Muto (1997) at different sections. For section configuration in the channel, see Figure 6.53. Strength of currents are 10% of the mean velocity.

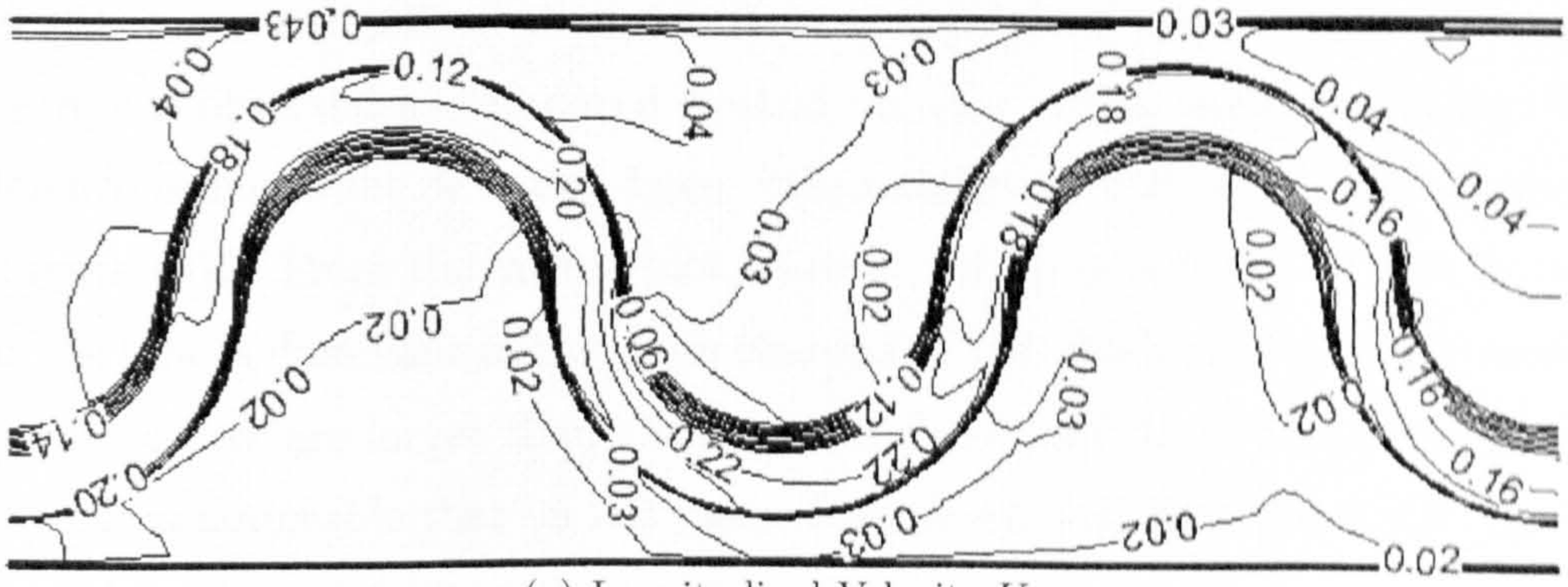

(a) Longitudinal Velocity U

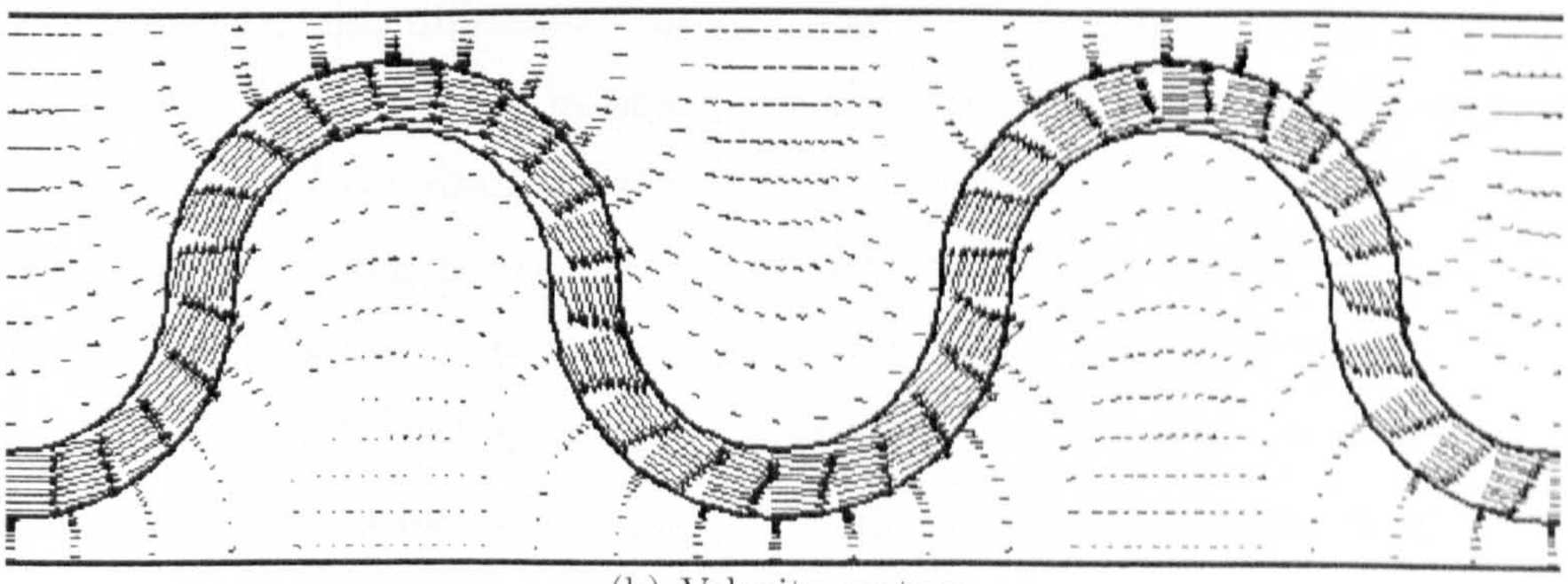

(b) Velocity vectors

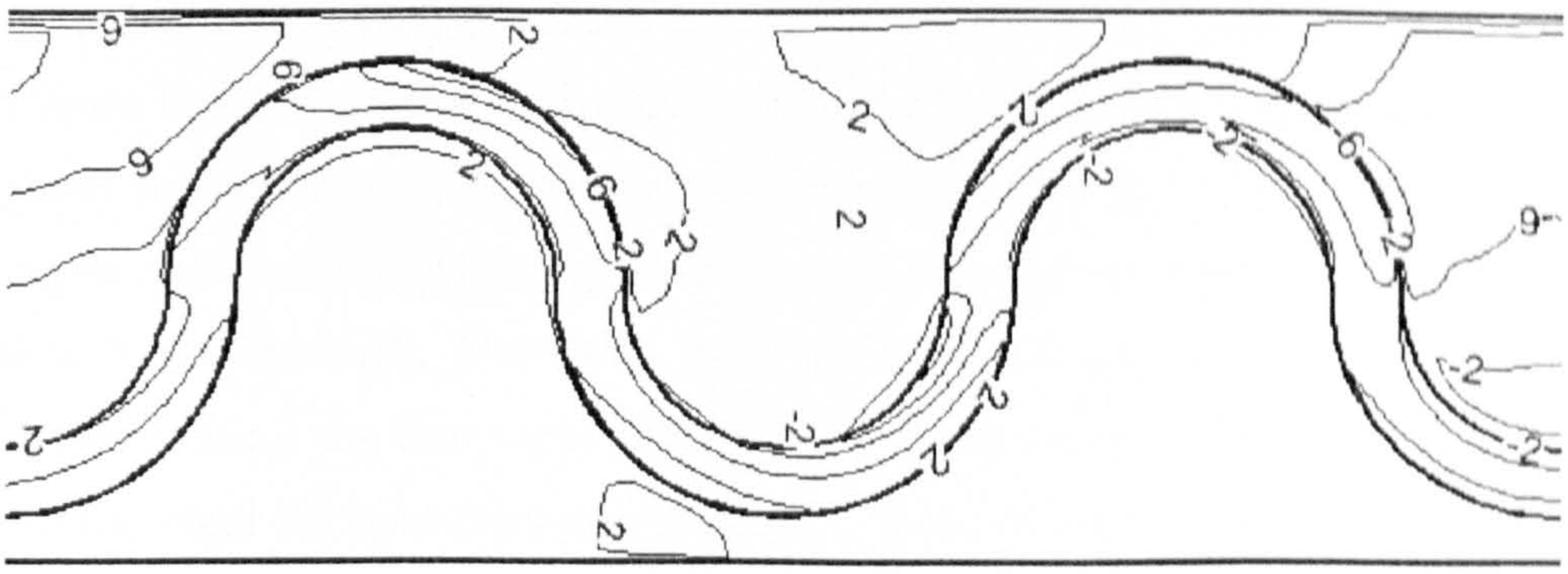

(c) Pressure

Figure 6.59: S=1.570, Dr=0.15: Plan view of depth averaged (a) mean velocity in m/sec, (b) velocity vectors and (c) pressure distribution in N/m^2. Due to the centrifugal forces the velocity is higher at inner side of the apex section which causes low pressure at the same location. The pattern is repeated at next apex section.

mechanism remains similar to the s=1.37 (Dr=0.15) case. However, from Figure 6.59 (a) it can be noticed that on the top floodplain a maximum velocity of 0.04 m/s is observed as compared to 0.03 m/s for the bottom floodplain. This difference is due to the deviation from orthogonality of both floodplains as shown in Figure 6.55. From the vector plot, shown in Figure 6.59 (b), it can be seen that the flow is dominant in the main channel as the flow direction is streamwise and the vectors are larger than those of the floodplain flow. From the velocity vectors it is noticeable that on left part of the floodplain flow velocity is slightly slower than the velocity on the right part of floodplain. As the main channel flow is dominant, this difference has not caused any significant effect on the main channel flow. The difference in pressure distribution at apex section found equal to 6 N/m^2 or $\Delta H = 0.6mm$, which is greater than s=1.37 and s=1.093 cases.

The flow behaviour is expected to be different in the crossover region due to difference in crossover angle as compared to s=1.37, which is shown in Figure 6.60. At Section 07, a steep velocity gradient is seen between the floodplain and main channel flows, which is due to the plunging of slowly moving floodplain flow into the main channel. Near the right side wall, no contour value is seen in the computed results, which is due to the coarse nature of the computational grid.

Figure 6.61 shows the comparison between the calculated and experientially obtained velocity vectors at different sections. With respect to the s=1.37 case, a strong secondary circulation is seen at Section 09 rotating clockwise, which causes erosion of the channel. Moreover, in experimental data at S7, the flow is seen to be penetrating the free surface, which is not observed in the computed results due to the rigid lid boundary condition, for pressure, at the top.

Based on a comparison between the computed results and experimental results for cross-sectional mean velocity and secondary currents, it can be concluded that the computed results are in good agrement with the experimental data. Hence, the model is able to capture the essential flow behaviour for a channel of s=1.57 with Dr=0.15.

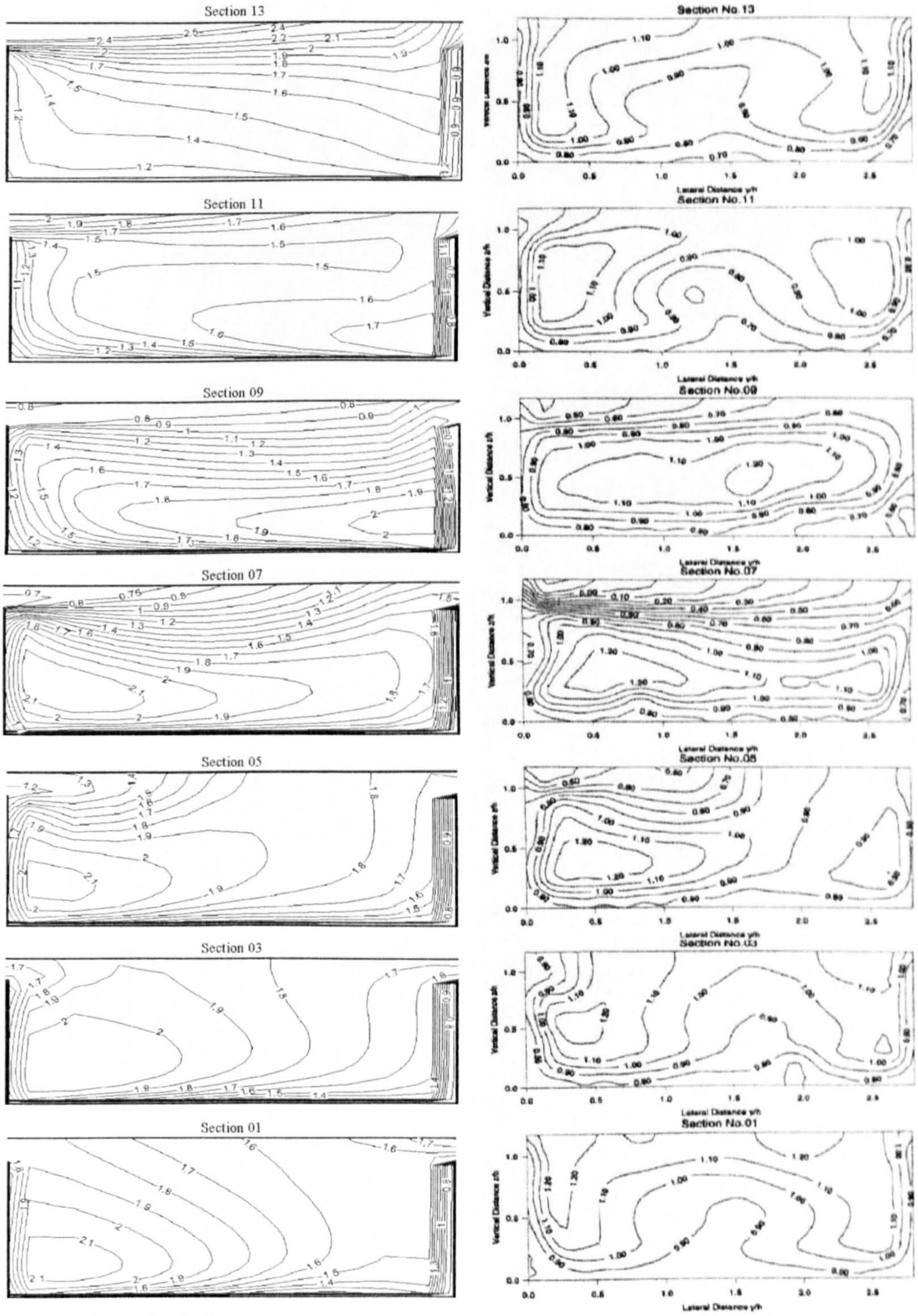

(a) Calculation (b) Experiments

Figure 6.60: S=1.570, Dr=0.15: Comparison of simulated U/U_s with experimental data collected by Muto (1997) at different sections. For section configuration in the channel, see Figure 6.53. Accumulation of contour lines near right side wall in computed results is due to the node arrangement in the same vicinity.

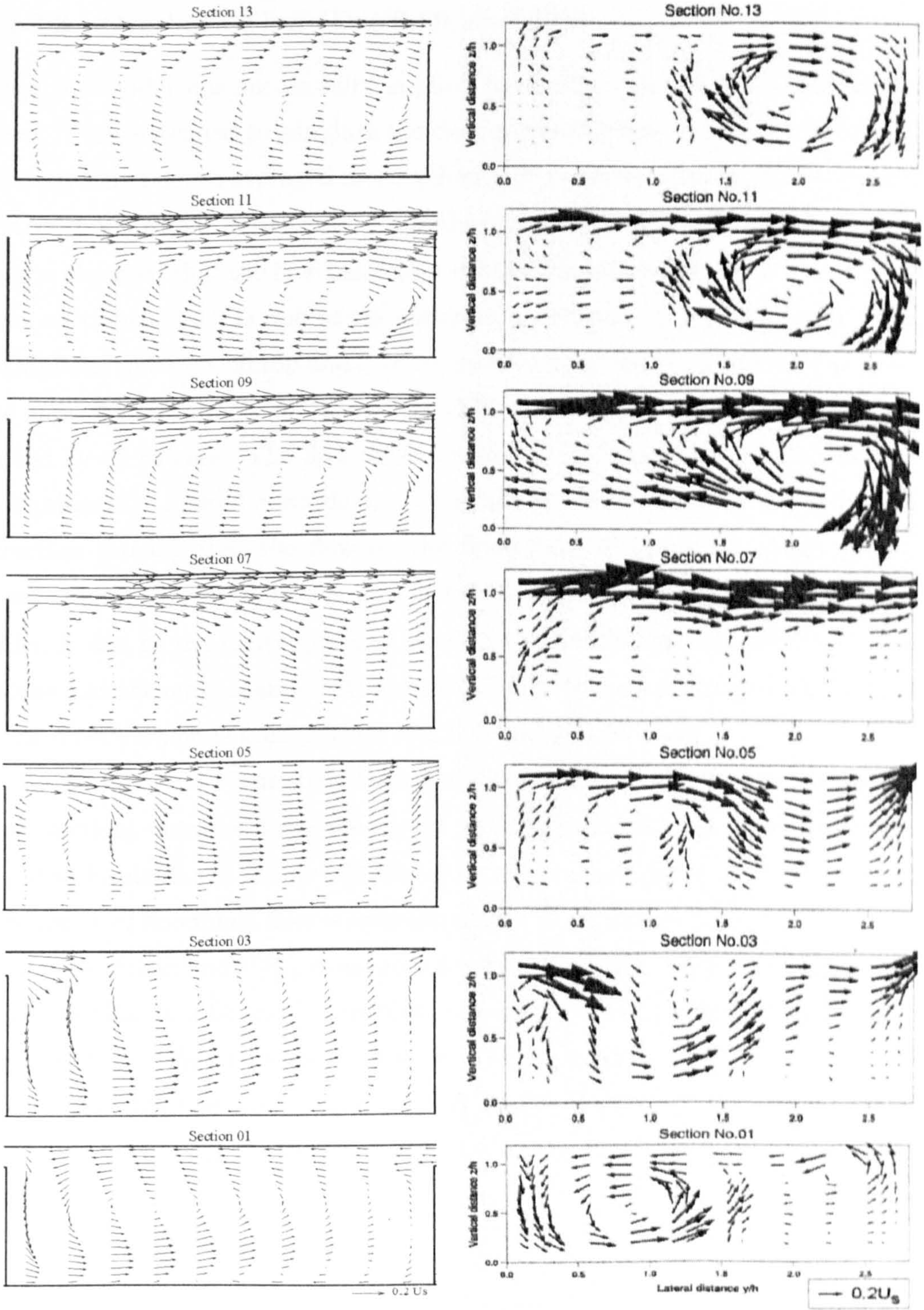

(a) Calculation (b) Experiments

Figure 6.61: S=1.570, Dr=0.15: Comparison of simulated secondary currents with experiments data collected by Muto (1997) at different sections. For section configuration in the channel, see Figure 6.53. Strength of currents are 20% of the mean velocity.

6.4.3.3 Overbank Flow (Dr=0.50, s=1.57)

Once the model was successfully applied to simulate inbank flow and Dr=0.15 cases, it was extended to simulate the deeper Dr=0.5 case. Figure 6.62 shows (a) distribution of depth averaged mean velocity (b) velocity vectors and (c) pressure distribution for the Dr=0.5 case. From the depth averaged mean velocity profile it can be observed that the flow behaviour is not symmetrical at the two consecutive apex sections, which is due to the different magnitude of mean velocity on the floodplains (0.2 m/s on top and 0.18 m/s on bottom) interacting with the flow in the main channel at apex sections. This difference seems to be improved compared to the Dr=0.15 case. The flow direction in the main channel (Figure 6.62 (b)) is significantly altered towards the longitudinal direction from the streamwise direction proving that the flow on the floodplain is dominant. High pressure zones (Figure 6.62 (c)) are seen just before the apex sections on the floodplains, which is due to the convergence of flow on the floodplains and then its sudden release into the main channel. At apex section, within main channel, ΔP is found to 12 N/m^2, which is greater than s=1.093 and s=1.37 cases.

Figure 6.63 and Figure 6.64 show the mean velocity distributions at different cross sections obtained from the model and experiments. The flow behaviour is found to be similar to the s=1.37, Dr=0.5 case as discussed in Section 6.4.2. The dominance of floodplain flow is seen across all the sections with U/U_s equal to 0.8 on the floodplain and U/U_s equal to 0.5 within the main channel. Secondary circulations (Figure 6.65 and Figure 6.66) are also found to be similar to the s=1.37 case. No free surface effect is observed at S7 compared to Dr=0.15 (s=1.57) case.

Results obtained from the developed model are found to be in reasonably good agreement with experimental results for the Dr=0.5, Dr=0.15 and inbank flow cases.

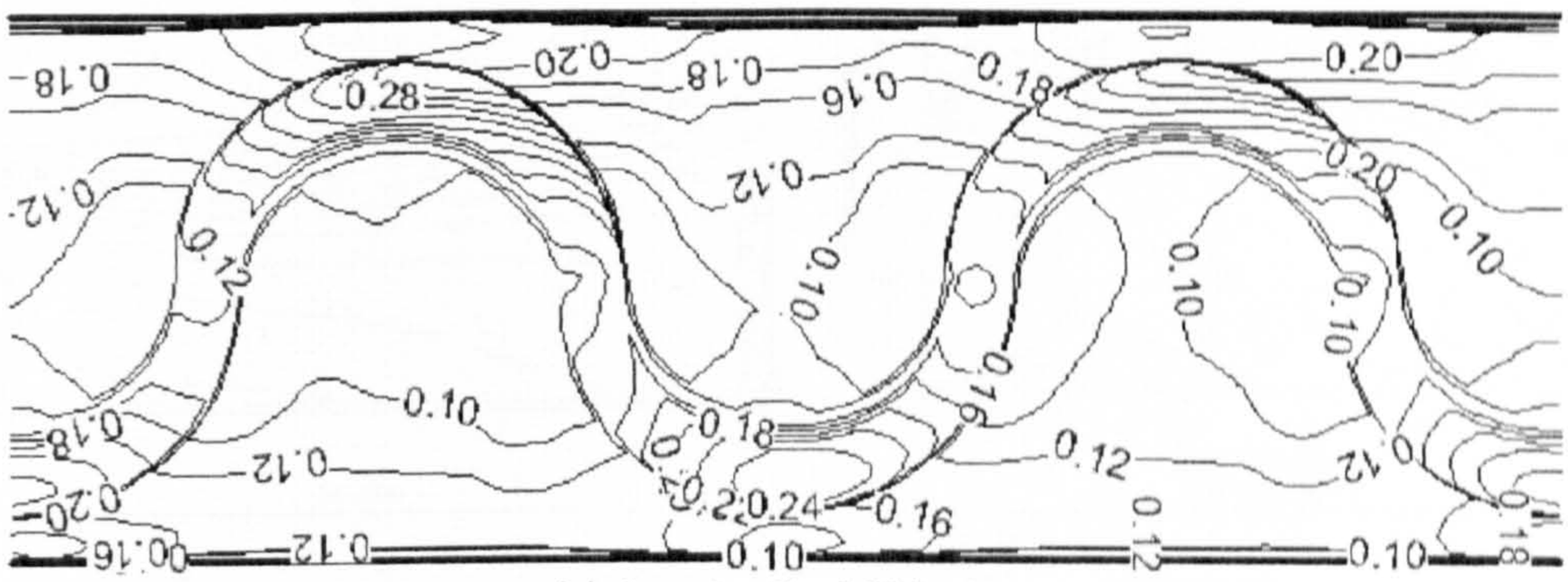

(a) Longitudinal Velocity

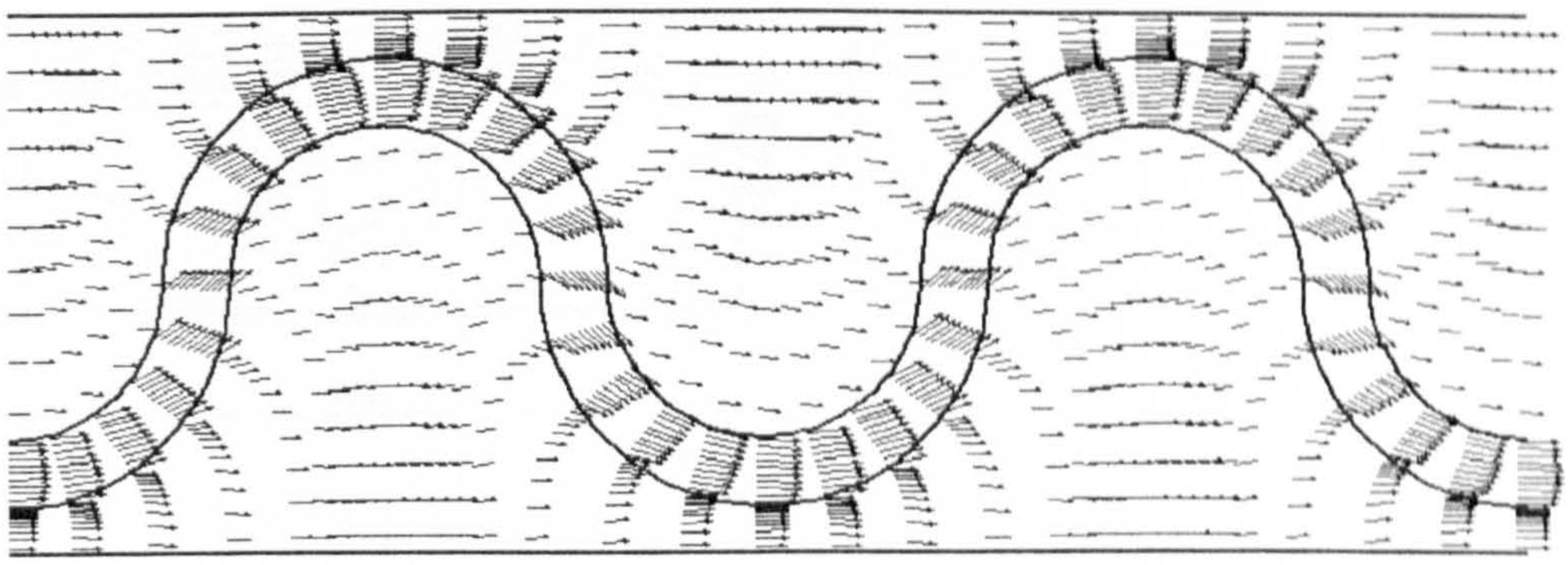

(b) Velocity vectors

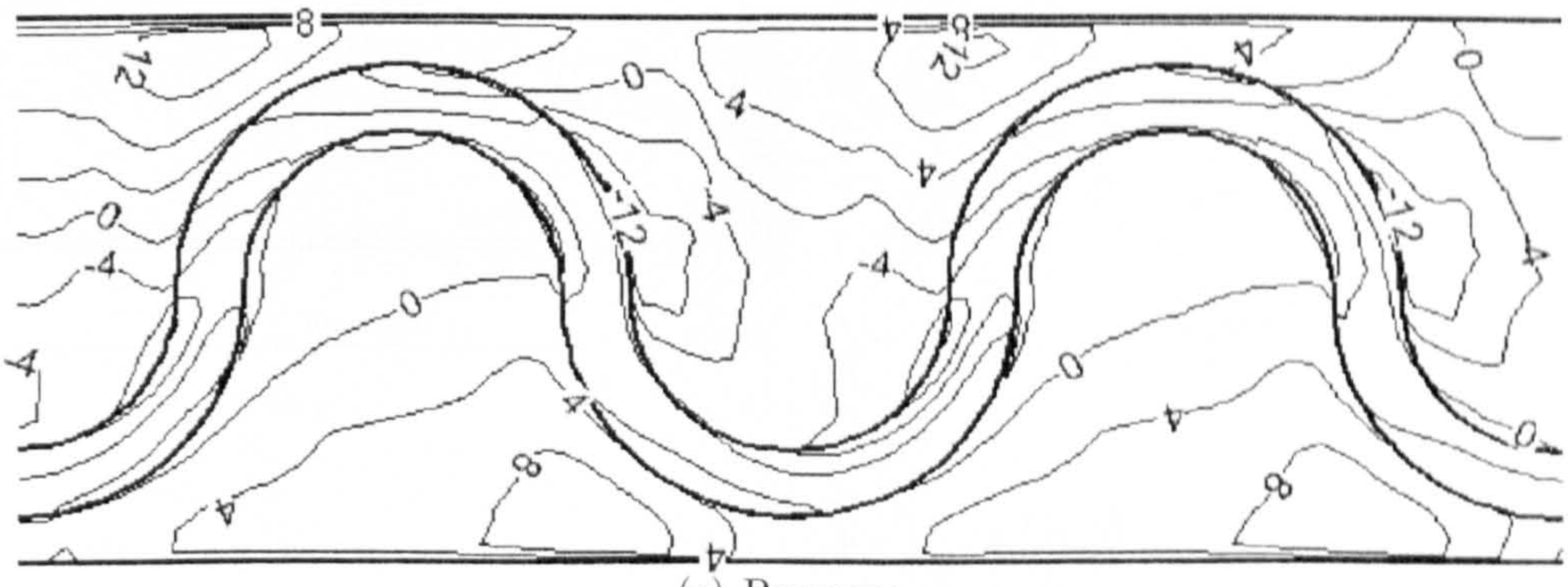

(c) Pressure

Figure 6.62: S=1.570, Dr=0.50: Plan view of depth averaged (a) mean velocity in m/sec, (b) velocity vectors and (c) pressure distribution in N/m^2. Due to the centrifugal forces the velocity is higher at inner side of the apex section which causes low pressure at the same location. The pattern is repeated at next apex section.

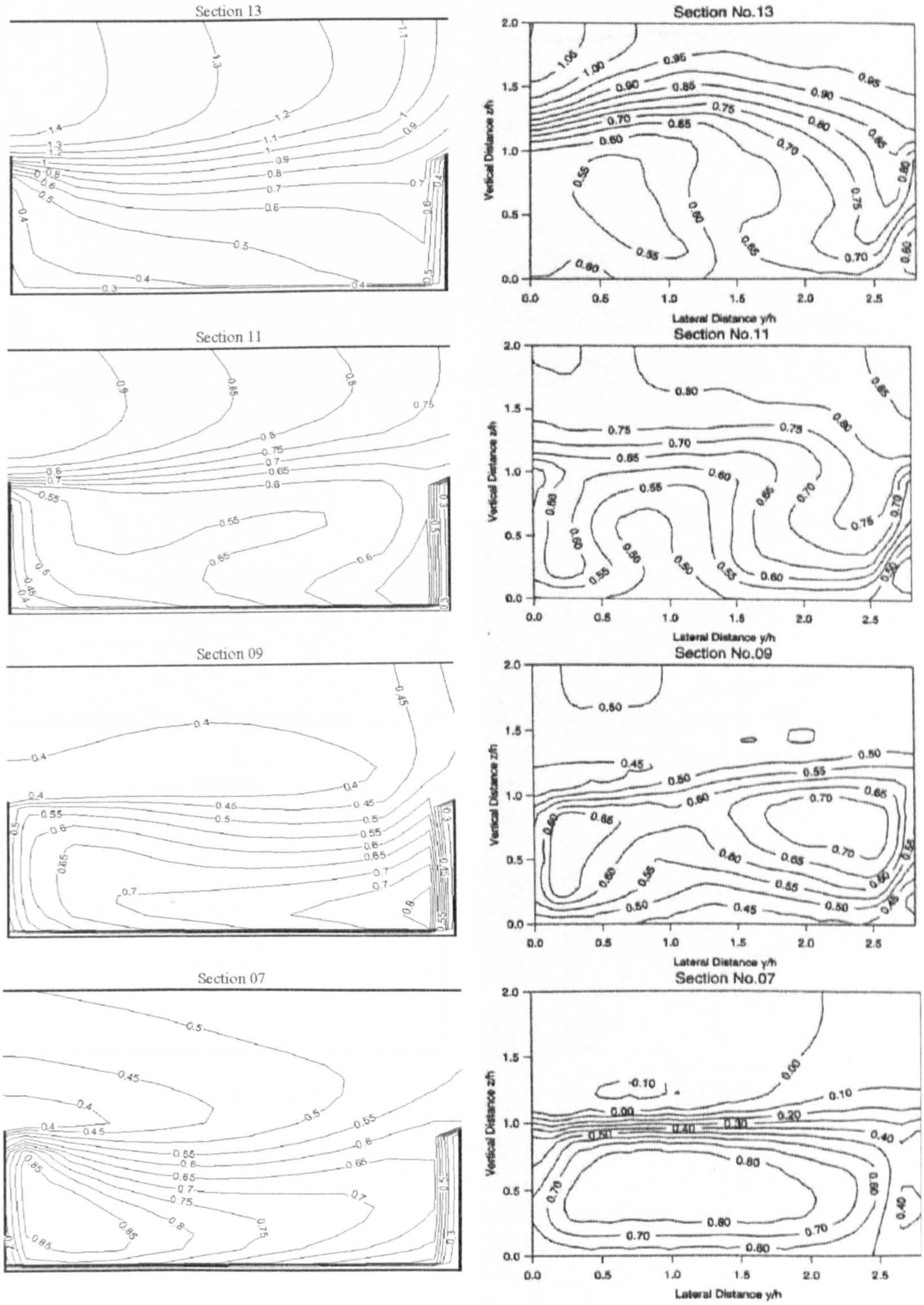

(a) Calculation (b) Experiments

Figure 6.63: S=1.570, Dr=0.50: Comparison of simulated U/U_s with experimental data collected by Muto (1997) at different sections. For section configuration in the channel, see Figure 6.53. Accumulation of contour lines near right side wall in computed results is due to the node arrangement in the same vicinity.

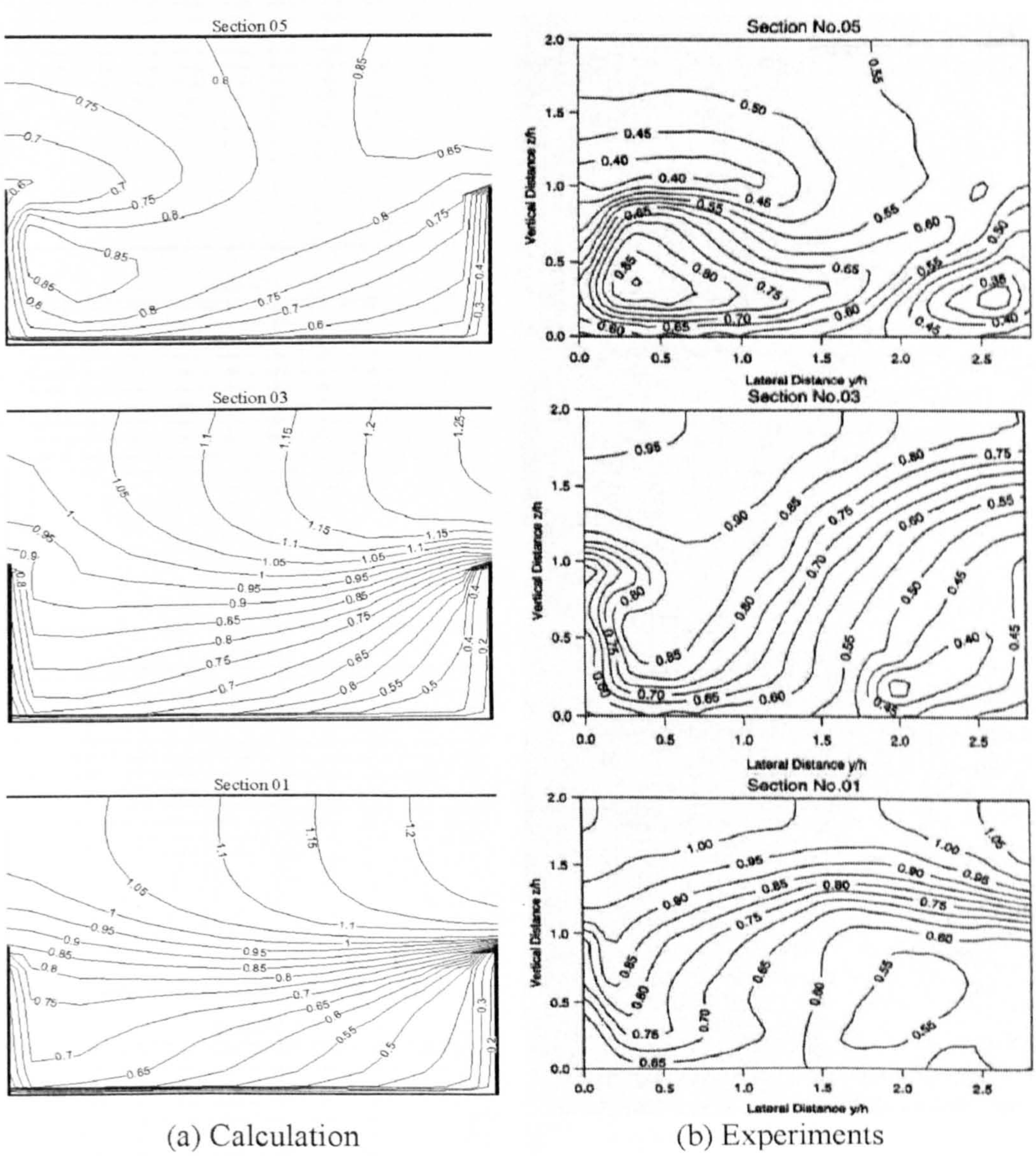

(a) Calculation (b) Experiments

Figure 6.64: S=1.570, Dr=0.50: Comparison of simulated U/U_s with experimental data collected by Muto (1997) at different sections. For section configuration in the channel, see Figure 6.53. Accumulation of contour lines near right side wall in computed results is due to the node arrangement in the same vicinity.

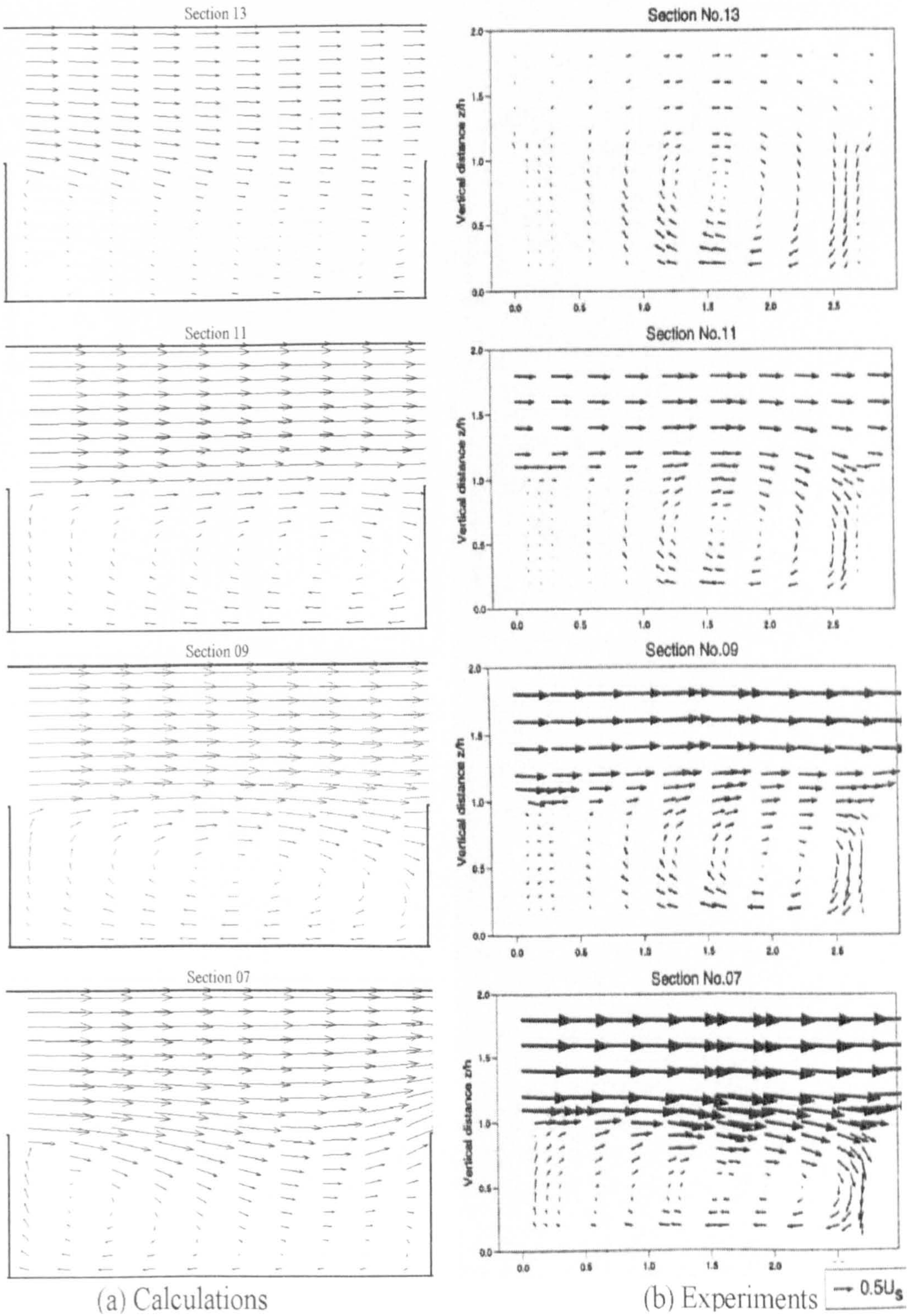

Figure 6.65: S=1.570, Dr=0.50: Comparison of simulated secondary currents with experiments data collected by Muto (1997) at different sections. For section configuration in the channel, see Figure 6.53. Strength of currents are 50% of the mean velocity.

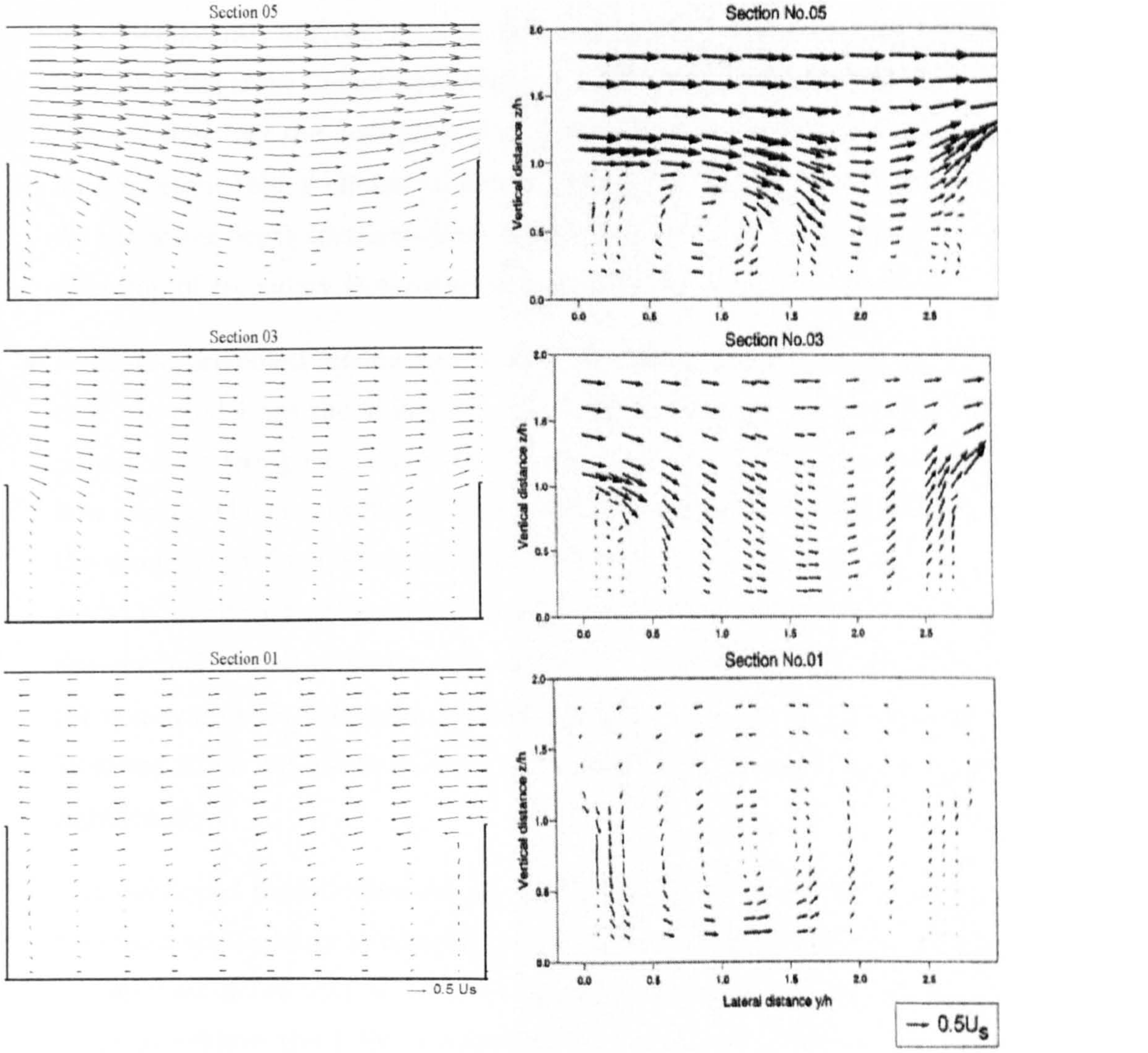

(a) Calculations

(b) Experiments

Figure 6.66: S=1.570, Dr=0.50: Comparison of simulated secondary currents with experiments data collected by Muto (1997) at different sections. For section configuration in the channel, see Figure 6.53. Strength of currents are 50% of the mean velocity.

6.4.4 Summary

- For overbank flow it was found that the magnitude and direction of velocity were significantly changed around the bankfull level where a strong 3D type flow occurred along the meander channel. The interaction between the main channel flow and the floodplain flow in the crossover region found to play an important role of change of flow structure for the overbank conditions. As the water depth increases from inbank to overbank flow a change in the direction of secondary flow rotation was observed at the bend section.

- From the presented results produced from the model it can be concluded that the model has the ability to reproduce the flow mechanisms for compound meandering channels with varying sinuosity and relative floodplain flow depth. The mean velocity distribution is captured well especially when the plunging of floodplain flow into the main channel (s=1.37 and s=1.57 cases) is significant. The generation and decay of secondary currents across the channel meander is also well captured. Due to the orthogonality error non-symmetric behaviour is observed in the profiles of floodplain flows. However, it has not affected the essential flow behaviour in the main channel significantly.

- The developed model offers unique advantages in terms of faster computations and applicability to complex geometries. The computation is very fast (roughly six hours with a standard personal computer for s=1.57, Dr=0.5 case) to achieve the fully developed flow conditions. The model can be adopted easily to analyse estuaries and river flows. In terms of disadvantages, the orthogonal grid for high sinuous channels (s=1.57) has shown a higher degree of deviation from orthogonality, which has introduced additional errors. However, this may be overcome by trying different options such as simulating more than two meanders, adopting grids with different densities and trying different ways of generating orthogonal grids.

6.5 Engineering Applications

6.5.1 Aim

Meandering channel flows are widely seen in nature, hence indepth understanding can help us prevent or minimize the effects of flooding. In Section 6.4, meandering channel flow simulations were discussed. The linear $k-\varepsilon$ model was used for computations, which is not able to capture the turbulence driven secondary currents. Secondary circulations in meandering channel flows are, generally, pressure driven but in less sinuous channel the effect of anisotropic turbulence may play an important role, as in the cases of straight simple and compound channels. Therefore, the aim of this section is to investigate the effects of anisotropy using the anisotropic turbulence model to simulate a compound meandering channels; the least sinuous, s=1.093, case among the cases studied in the previous sections.

6.5.2 Methodology

In this section, flow characteristics are discussed for a compound meandering channel s=1.093, apex section S9 (see Figure 6.23). The results produced from the $k-\varepsilon$ model and anisotropic LY model are presented. The LY model is selected due to its simplicity of implementation in orthogonal coordinates as compared to the NR model in which the wall and free surface functions in orthogonal coordinates were complex to implement. Three different flow situations are analysed; inbank flow, Dr=0.15 and Dr=0.5. For each case, the following parameters are discussed:

- Secondary currents and mean velocity distribution - comparison of computed results with experimental data
- Reynolds shear stress ($-\overline{vw}/U_*^2$) - comparison of $k-\varepsilon$ model with LY model
- Wall shear stress ($-\overline{uv}/U_*^2$) - comparison of $k-\varepsilon$ model with LY model
- Bed shear stress (ρU_*^2) - comparison of $k-\varepsilon$ model with LY model

The governing model equations for the standard $k-\varepsilon$ and LY models in an orthogonal coordinate system are discussed in Sections 5.4.4 and 5.4.5 in detail.

6.5.3 Discussions

Inbank flow: Figure 6.67 shows the mean velocity profile, secondary currents, $-\overline{vw}/U_*^2$, $-\overline{uv}/U_*^2$ and bed shear stress distributions at apex section S9 (see Figure 6.23 for the location of S9) calculated from the linear $k-\varepsilon$ model and the LY model. The mean velocity and secondary currents obtained from the experiments are shown in Figures 6.29 and 6.30. It can be seen that a maximum velocity core exists at inner wall (right side) for both models; this behaviour is similar to that observed in the experiments. However, for both cases the bulging is less intense at the outer wall (left side).

Two secondary circulations are seen, rotating in both clockwise and anticlockwise directions. The circulation rotating in anticlockwise direction seems dominant, which is not seen in experiments. From the circulations it can be observed that the secondary currents are stronger in the LY model prediction and match closely with measured data than the $k-\varepsilon$ model. This may be due to the fact that the LY model adds the contribution of Reynolds stresses generated from the turbulence anisotropy; giving the additional strength to the currents. The effect of stronger circulation for LY model case can be clearly seen in the Reynolds shear stress ($-\overline{vw}/U_*^2$) distributions. The highest value of -0.06 is observed near free surface in the LY model case compared to -0.04 in the $k-\varepsilon$ model case. The magnitudes of wall shear stresses $-\overline{uv}/U_*^2$ found to be 1.0 near the left wall and 3.0 the near right wall for both the LY and $k-\varepsilon$ model cases. However, for the LY model case the magnitude is higher near the right wall. The magnitude of bed shear stress (ρU_*^2), similar to the distribution of wall shear stress, is 1.0 near the left wall and gradually increasing to about 2.5 near the right wall. However, the distribution is more wavier in the case of LY model

Linear $k-\varepsilon$ Model **Inbank Flow** LY Model

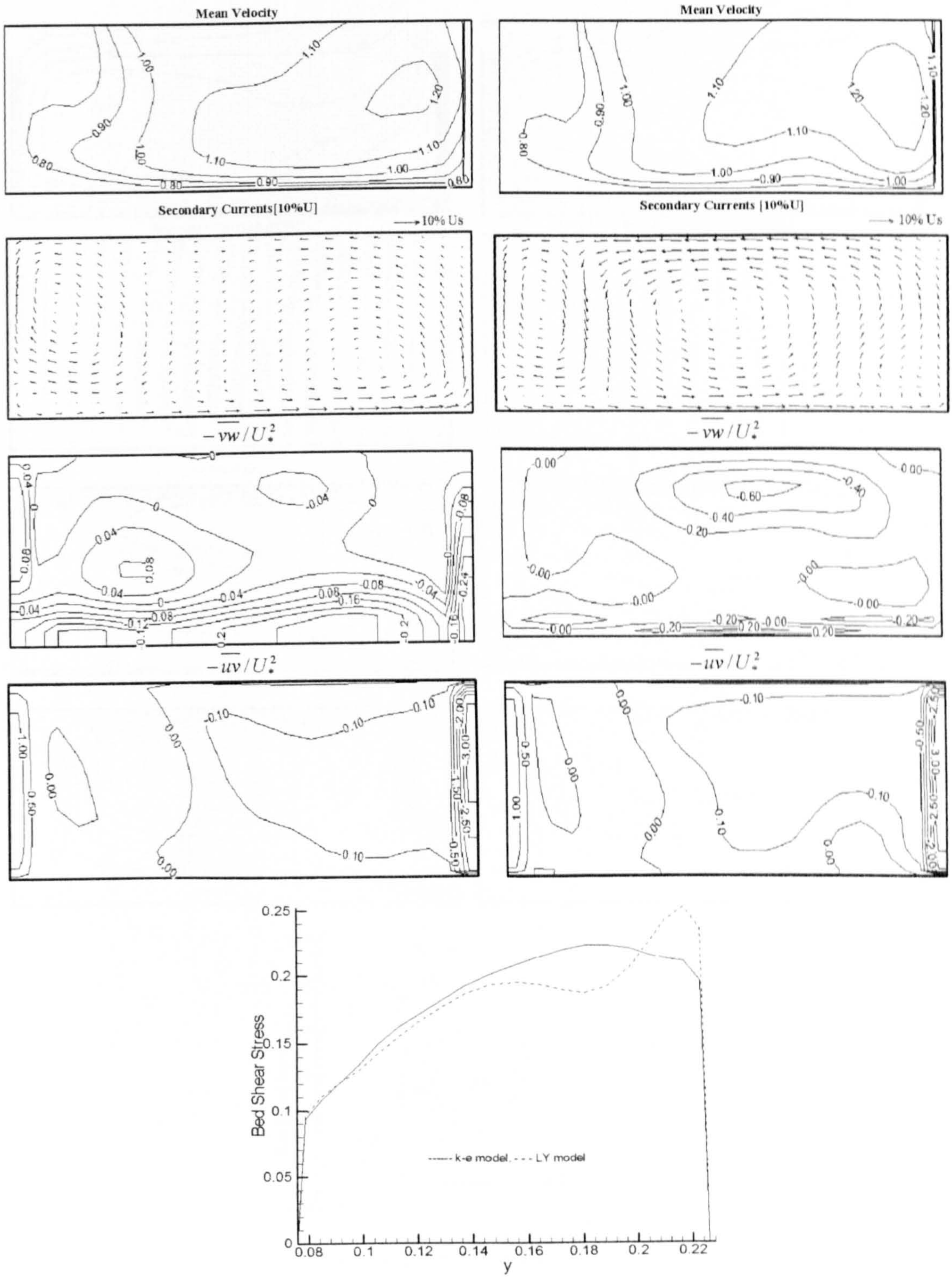

Figure 6.67: S=1.093, Inbank flow: Comparison of normalised flow parameters computed from linear $k-\varepsilon$ model and the LY model

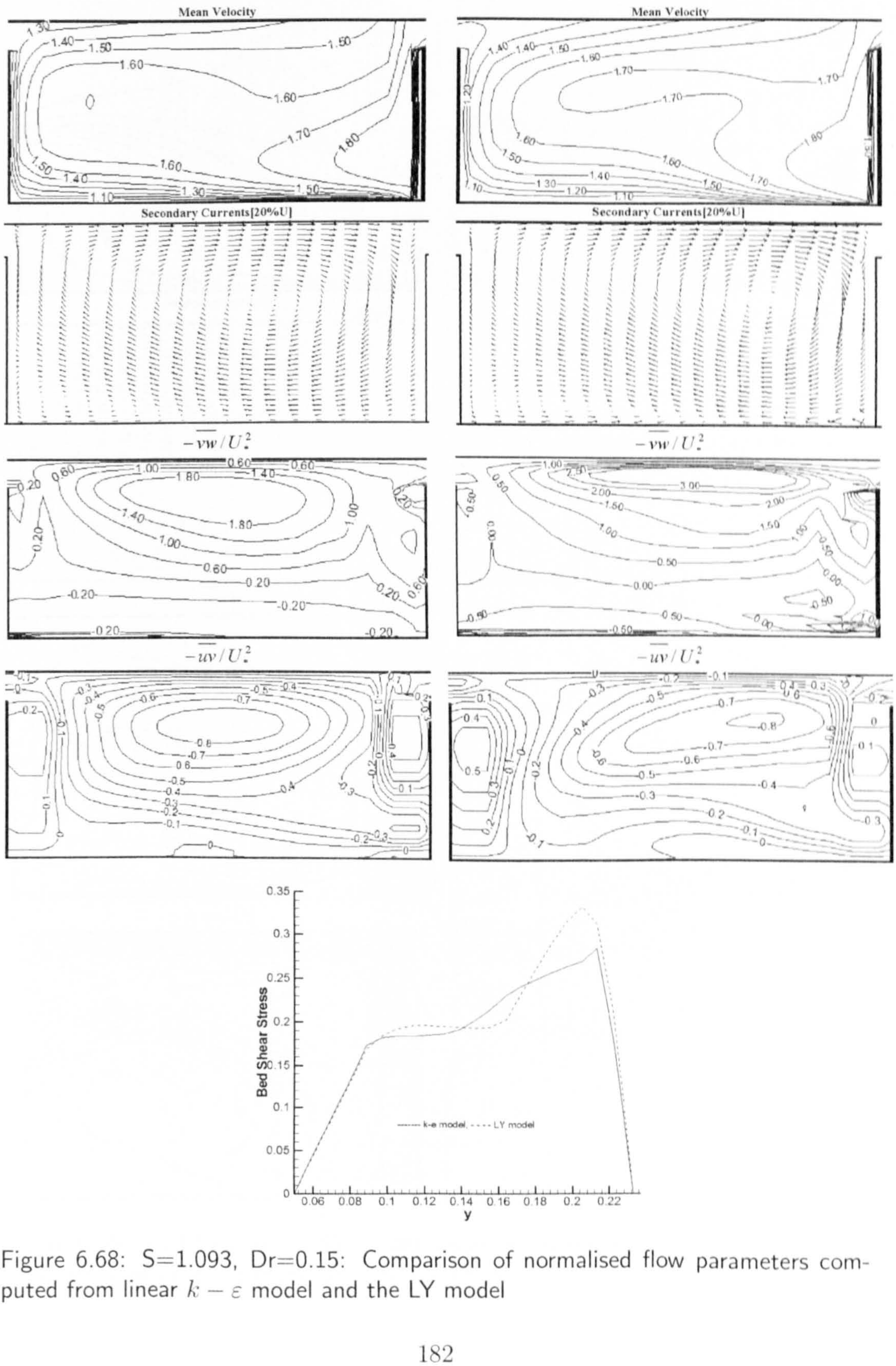

Figure 6.68: S=1.093, Dr=0.15: Comparison of normalised flow parameters computed from linear $k-\varepsilon$ model and the LY model

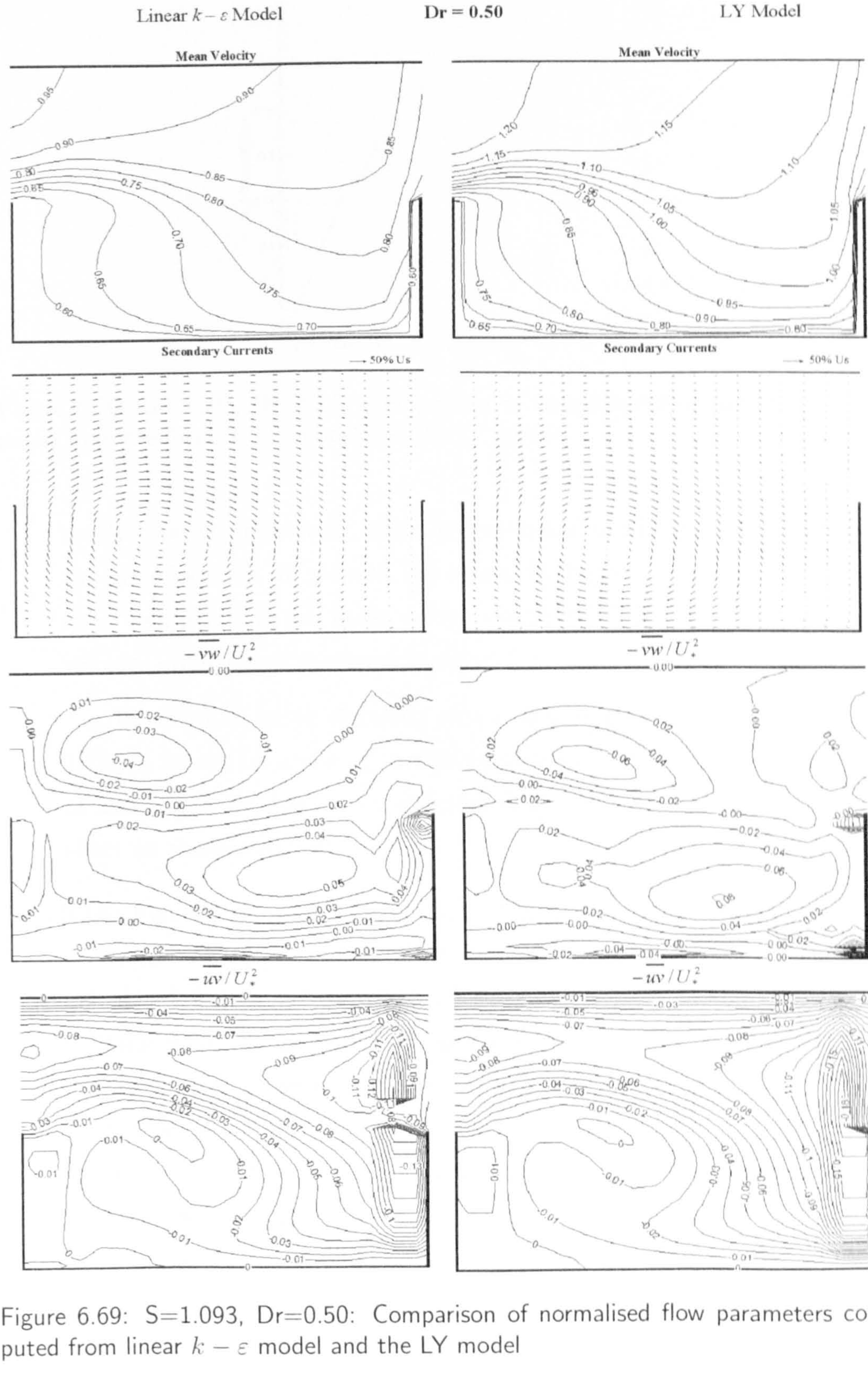

Figure 6.69: S=1.093, Dr=0.50: Comparison of normalised flow parameters computed from linear $k-\varepsilon$ model and the LY model

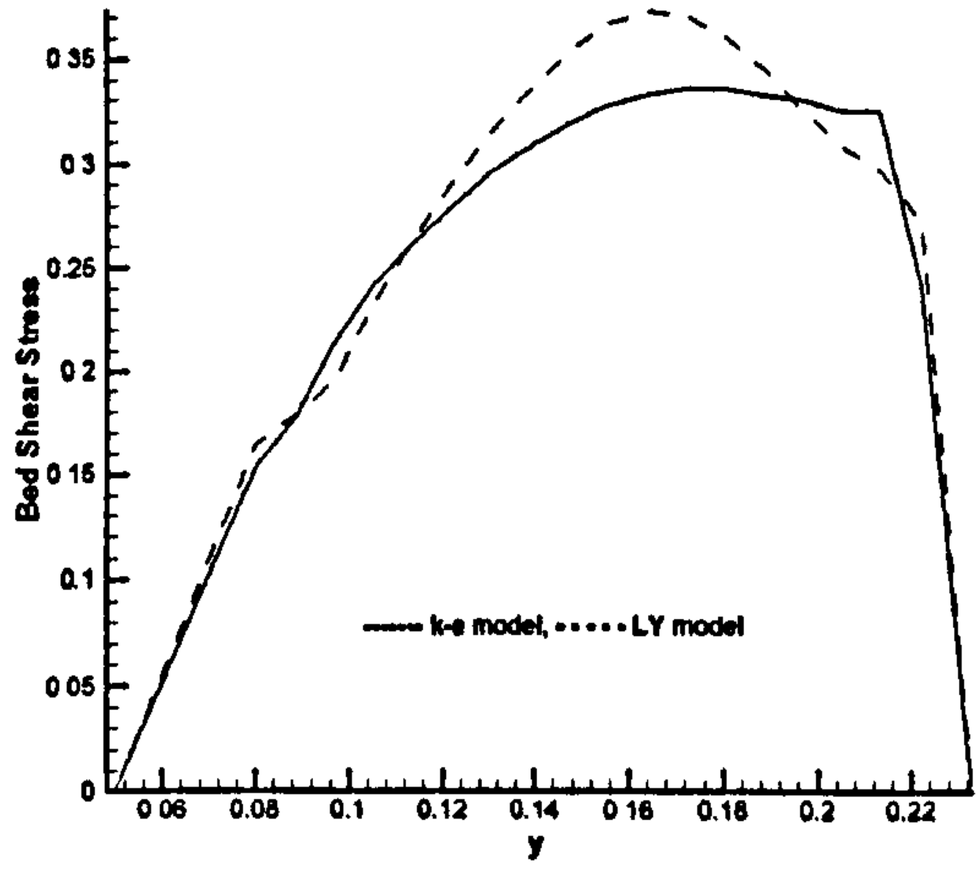

Figure 6.70: S=1.093, Dr=0.50: Comparison of normalised flow parameters computed from the linear $k-\varepsilon$ model and the LY model

results near the right wall, which is correspond to the circulation patter at the same location. In general, the reason for higher shear stresses near the right wall is due to the faster mean velocity (U/U_s) and consequent steep velocity gradients at the same location.

In terms of super elevation effect, ΔH is found to be $1.72mm$ and $1.22mm$ for the LY and $k-\varepsilon$ models respectively. Slightly higher magnitude of ΔH might be due to the stronger secondary currents and subsequent effect on the pressure distribution.

Dr=0.15: Figure 6.68 represents the mean velocity profile, secondary currents, $-\overline{vw}/U_*^2$, $-\overline{uv}/U_*^2$ and bed shear stress distributions at apex section S9 calculated from the linear $k-\varepsilon$ model and the LY model. In Figures 6.32 and 6.33, the mean velocity and secondary currents obtained from the experiments are shown. From the mean velocity profile it can be seen that both models are able to capture the maximum velocity core location at the inner wall of the channel, similar to the experiments. In the case of the secondary circulations, the magnitude of currents captured by the LY model seem slightly stronger compared to those from the linear $k-\varepsilon$ model

similar to the inbank flow case. A dominant clockwise circulation is shifted more towards the floodplain/main channel junction at the inner wall in the case of the LY model as compared to the linear $k-\varepsilon$ model.

Similar to inbank flow case, the magnitude of Reynolds shear stresses ($-\overline{vw}/U_*^2$) is higher in the case of the LY model (-3.0 near the surface) than the $k-\varepsilon$ model (-0.6). The wall shear stresses distribution ($-\overline{uv}/U_*^2$) found increasing gradually from the left wall toward the right wall for both the LY model and the the linear $k-\varepsilon$ model cases. However, steep gradients noticed at the walls. The profiles of bed shear stresses found gradually increasing from the left wall toward the right wall similar to the wall shear stresses. No significant difference is observed for the super elevation effect ($\Delta H = 0.2$ for both cases) in the results from the LY model and the linear $k-\varepsilon$ model.

Dr=0.50: Figures 6.69 and 6.70 show the mean velocity profile, secondary currents, $-\overline{vw}/U_*^2$, $-\overline{uv}/U_*^2$ and bed shear stress distributions calculated from the linear $k-\varepsilon$ model and the LY model. In Figures 6.35, 6.36, 6.37, and 6.38, the mean velocity and secondary currents obtained from the experiments are shown. It can be seen from the mean velocity and secondary current profiles that the model predictions are in good agrement with the experiments. One dominating cell, rotating in the clockwise direction is seen in both cases, however for the LY model the origin of the cell is shifted towards the bottom wall and is also greater in strength.

The maximum value of $-\overline{vw}/U_*^2$ is found to be 0.08 and 0.05 for the LY model case and the linear $k-\varepsilon$ model case respectively. Similar to inbank flow and Dr=0.5 cases wall shear stress increases from the left wall (0.13) toward the right wall (0.3). The bed shear stresses, similar to the wall shear stress increases gradually from the left wall towards the right wall. No significant difference ($\Delta H = 0.5$ for both cases) is observed in terms in super elevation effects.

6.5.4 Summary

- In terms of the secondary current pattern, the linear $k-\varepsilon$ model results are slightly closer to the experimental data, but in terms of the current's strength, the LY model seems closer to the data.

- The magnitude of the Reynolds shear stress ($-\overline{vw}/U_*^2$) is found to be stronger for the LY model in the inbank and Dr=0.15 cases as compared to the linear model.

- Though no significant difference in $-\overline{uv}/U_*^2$ distribution is observed, bed shear stress distribution found to be wavier using the LY model as compared to the linear $k-\varepsilon$ model for inbank flow, Dr=0.15 and Dr=0.5 cases.

- As relative depth increases difference between the LY model and the $k-\varepsilon$ model for mean velocity and Reynolds stresses distribution decreases. This shows that the flow structures depends on the plunging effects and the geometrical effects than the anisotropy of turbulence for overbank flows.

- From the analysis, it can be said that to see the effects of anisotropic turbulence on flow structure, the sinuosity need to reduce.

CHAPTER 7

Summary, Conclusions and Future Work

7.1 Summary

A novel three-dimensional computational model has been developed to simulate the complex turbulent flows within simple channels, compound channels and compound meandering channels. Various stages of this research can be summarised as follows:

Identifying the Research Gap: From the literature review discussed in Chapter 2, it was found that the linear $k-\varepsilon$ model is often used for the simulations of compound meandering channel flows. The computational models developed so far are based on methods such as finite element[1], finite volume and finite difference. The non-orthogonal grid is also used frequently for numerical simulations[2]. The computational time for these methods to achieve uniform flow condition in the meandering channel is dramatically

[1]Refer the publication Olsen (2003) and weblink: http://www.telemacsystem.com/

[2]SSIIM developed by Norwegian University of Science and Technology is based on the non-orthogonal grid method (http://folk.ntnu.no/nilsol/ssiimwin/).

high[1]. Based on this investigation, an opportunity was identified to develop a model, which is computationally efficient and able to capture the anisotropy of turbulence in compound meandering channels.

The Model Development Process: A computer model developed by Lilek *et al.* (1995) created to simulate the three-dimensional lid driven cavity flow was adopted as a starting point[2]. The reasons behind the selection of this model are discussed in Chapter 4. The following enhancements were introduced to achieve the objectives of the research (Section 1.3) .

1. Turbulence models: The governing equations were modified to Reynolds-Averaged Navier-Stokes (RANS) equations by incorporating the isotropic $k-\varepsilon$ model of Launder and Spalding (1974) to simulate the turbulent flows in a simple channel (Chapter 3). To capture the secondary currents and its effects on the streamwise velocity, the algebraic stress models of Launder and Ying (1973), Speziale (1987) and Naot and Rodi (1982) were added to compute the Reynolds stresses.

2. Masking array concept (Blocked cells): The geometry of a simple channel was modified by masking (blocking off) the unwanted arrays during computations. Logical arrays were created and binary numbers, one (=perform) and zero(=not to perform), were specified for simulations. This is one of the most efficient way to prevent the computations to occur in specified CVs. Mathematical modifications implemented for the blocked off region are discussed in Section 4.7.3.2. Then, the isotropic $k-\varepsilon$ model and anisotropic NR model were tested to check the performance of the masking array concepts by simulating the flow through compound duct and open channels.

[1]Telemac2D used by research colleagues took more than two days to achieve uniform flow condition for compound meandering channels on a 512MB RAM and 2.1GIIz desktop computer.

[2]The computer code **3dc** is available online at ftp://ftp.springer.de/pub/technik/peric/.

3. Curvilinear coordinates: In the final stage of development, governing equations including RANS equations, isotropic model equations and anisotropic model equations were converted into the curvilinear coordinate system (Chapter 5). The channel geometry was modified to the compound meandering channels by generating orthogonal curvilinear grid and using masking array concept. The grid generation method for channels with different sinuosity and forcing functions used to prevent the grid line collapsing are discussed in Section 4.7.3.3. According to author's knowledge, though the orthogonal grids are often used for two-dimensional ocean flow modelling, it has never been tested for three-dimensional compound meandering channel flows[1].

7.2 Conclusions

In this work, the new computational approach is developed to simulate the complex turbulent flows within simple channel, compound channel and compound meandering channels. The performance of the model for each type of the channel can be concluded as follow.

Simple Channel: The implemented ASMs were first tested to simulate the simple duct flow (Section 6.2). It is found that the ASMs reproduced all the essential behaviour of the flow when the symmetry boundary condition is imposed at the top and the right of domain to simulate the flow in the bottom left quarter of a closed channel. The NR model is found to predict the flow behaviour (secondary currents and mean velocity distribution) more closely with the previous literature among all the ASMs (Section 6.2.1). For open channel flow simulations free-surface boundary condition for ϵ

[1]GRIDGEN, a MATLAB-based tool developed by United States Geological Survey department, is developed to construct orthogonal curvilinear grids for ocean circulation models, which is available online at http://woodshole.er.usgs.gov/operations/modeling/gridgen/index.html.

was imposed at the top which causes the highest longitudinal velocity to be below the free surface. This behaviour was also reproduced reasonably well with the NR model (Section 6.2.2). The periodic boundary conditions used to achieve the uniform flow condition worked successfully and helped to reduce computational time.

Compound Channel: The masking arrays concept adopted for compound channel grid generation was able to reproduces the compound closed and compound open channel flow behaviour. The exchange of momentum between the floodplain and main channel flows and resulting formation of secondary currents on lateral plan was reproduced with the NR model with good accuracy (Section 6.3). An additional circulation was noticed on the floodplain in compound open channel compared to compound closed channel. This is due to the presence of free surface in compound open channel flow.

Compound Meandering Channels: The orthogonal grids with steep curvatures (s=1.37 and s=1.57) were created successfully using forcing functions. These functions provided the control to prevent the grid line collapsing near the curved regions. In terms of flow behaviour, secondary currents and mean velocity distributions computed from the model for s=1.093, s=1.37 and s=1.57 cases matched reasonably well with the experimental data of Muto (1997) (Section 6.4). The effects of varying sinuosity and relative depths on the flow behaviour in terms of secondary currents and plunging of floodplain flow into the main channel were reproduced with good accuracy. It was noticed that for the overbank flow situations, non-symmetric flow behaviour was observed on both floodplains, which was due to the different deviations from orthogonality of the grid for top and bottom floodplains (Section 6.4.1). The difference in deviation tends to increase as channel sinuosity increases. Though this different grid property had caused faster flow on one floodplain than the other, it had not affected the main channel

flow significantly. The non-symmetry on both floodplains in terms of deviation from orthogonality and speed of the flow might be improved in the future by working on different way to generate orthogonal grid, simulating more than two meanders, trying different grid refinement and finding out any manual error (*bug*) into the model.

Anisotropy in the Compound Meandering Channel: Finally, a unique and a new study was carried out to understand the turbulence effect within compound meandering channel and to demonstrate the capability of the developed model. The anisotropic LY model was applied to the less sinuous case of compound meandering channel s=1.093 and results were compared with the linear $k-\varepsilon$ model. Three different flow conditions, namely, the inbank flow, Dr=0.15 and Dr=0.5, were investigated for the s=1.093 case. Flow characteristics such as secondary currents, mean velocity distribution, Reynolds shear stresses, wall shear stress and bed shear stresses were discussed (Section 6.5). It was noticed that in terms of secondary current pattern, the linear model result was slightly closer to the experimental data; but in terms of strength the LY model result seemed closer to the data. The magnitude of Reynolds shear stress was found to be stronger for the LY model in inbank and Dr=0.15 cases compared to the linear model. Bed shear stress distribution found slightly higher in magnitude near the right wall for all inbank flow, Dr=0.15 and Dr=0.5 cases compared to the linear $k-\varepsilon$ model. No significant difference in wall shear stress distribution was observed by using the LY model compared to linear model.

7.3 Future Work

The developed model has enormous capabilities of dealing with complicated geometries coupled with higher order anisotropic turbulence modelling, which can

be applied to solve a wide variety of problems in a computationally efficient manner. The following are few of the potential areas in which the developed model could be extended:

1. **Engineering Applications**

   - In case of flooding the flow through a river inundates the river bank, which is, in real life, occupied by trees (vegetation) and other civilian constructions. A replica of a similar situation has been set up at Loughborough University's Department of Civil and Building Engineering laboratory as shown in Figure 7.1. The developed model can be modified to tackle a similar situation by extending the concept of masking arrays (Section 4.7.3.2). Thereafter, the model can be used to predict the flow discharge under different vegetation conditions, which can help to work out a floodplain management strategies and to minimize the flooding consequences.
   - The river flow causes the erosion of banks and transports as well as deposits the sand and debris to various locations. By incorporating the concept of varying bathymetry and sediment transport into the model, this phenomena can be understood thoroughly.
   - The discharge of pollutants from various sources into a river is a frequently encountered problem in the real world. With the help of the model, coupled with a scheme for solving an additional scaler transport equation, the optimum location of pollutant discharge can be worked out by specifying the location of the pollutant source in the channel.

2. **Understanding the Complicated Flow Physics**

   - The developed model is based on the assumption of a rigid lid at the free surface. The rigid lid boundary condition can be modified by incorporating the concept of the "σ" coordinate in the vertical

direction. This will help to understand the free surface variation of the flow, its effect on bed shear stress and the effect of sloshing.

- Turbulent flow through a compound meandering channel is one of the most complex flow phenomena as it comprises various flow regimes generated due to the nature of geometry and the turbulent nature of flow. The computational tool can easily be adapted to understand these regimes such as the location of turbulent energy production and dissipation, the secondary flow generation and decay thoroughly. The concept of *Large Eddy Simulations* can also be coupled with the model for the similar purposes.

3. Computational Efficiency Enhancement

- For numerical simulations, the computer programme was developed in FORTRAN 90, which represents one of the latest versions in FORTRAN compiler series. Advanced features of FORTRAN 90 like modules and dynamic memory allocation can be implemented to make the programme less memory intensive. In addition, the programming style can be modified to take the advantage of parallel processing, which would reduce the computation time drastically.

- Finally, a user-friendly front-end can be created for data input in MATLAB or Visual Basic of Applications to make the computer model easier to operate. The use of MATLAB can also be extended for post-processing of the numerical results.

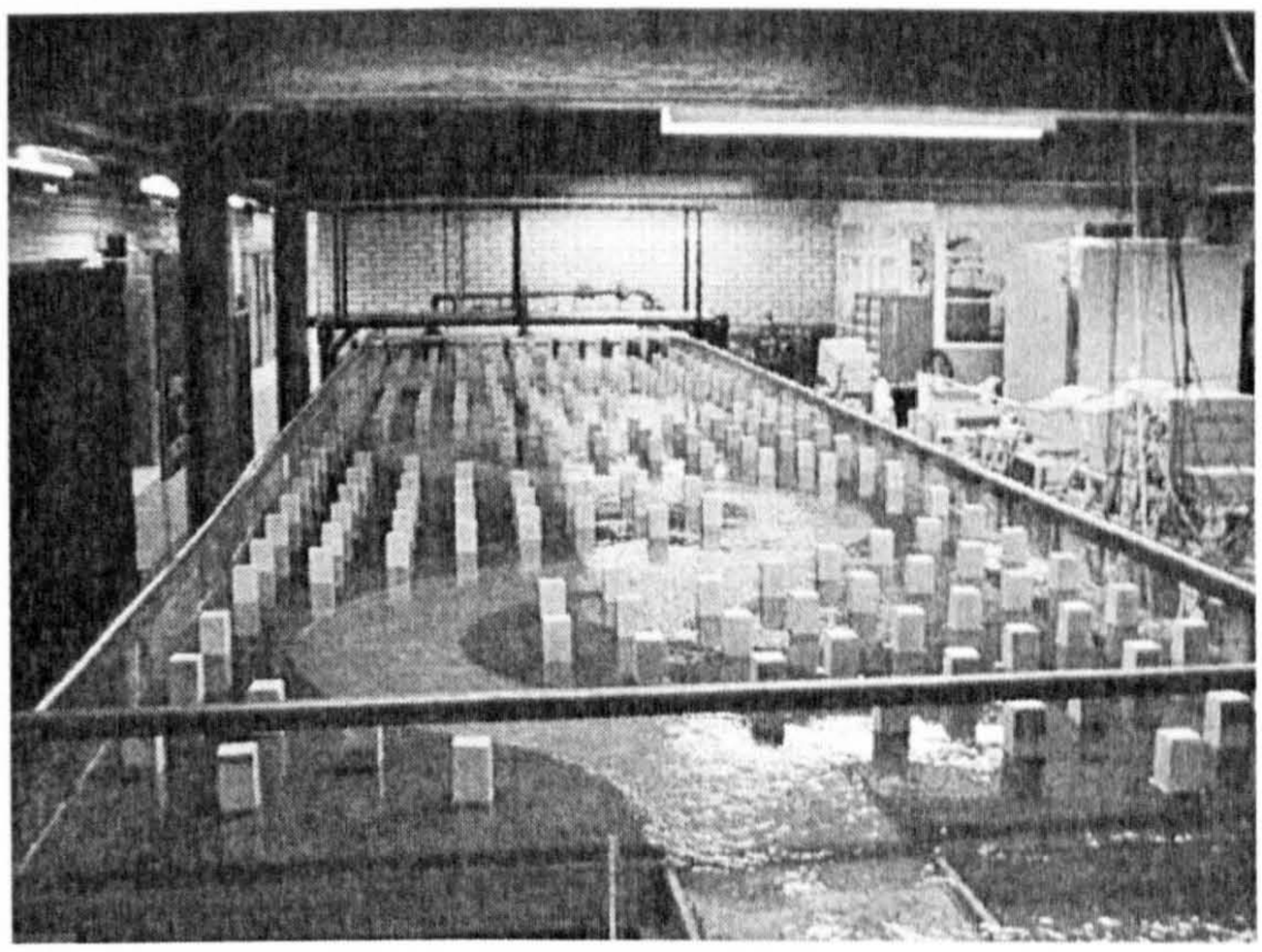

(a)

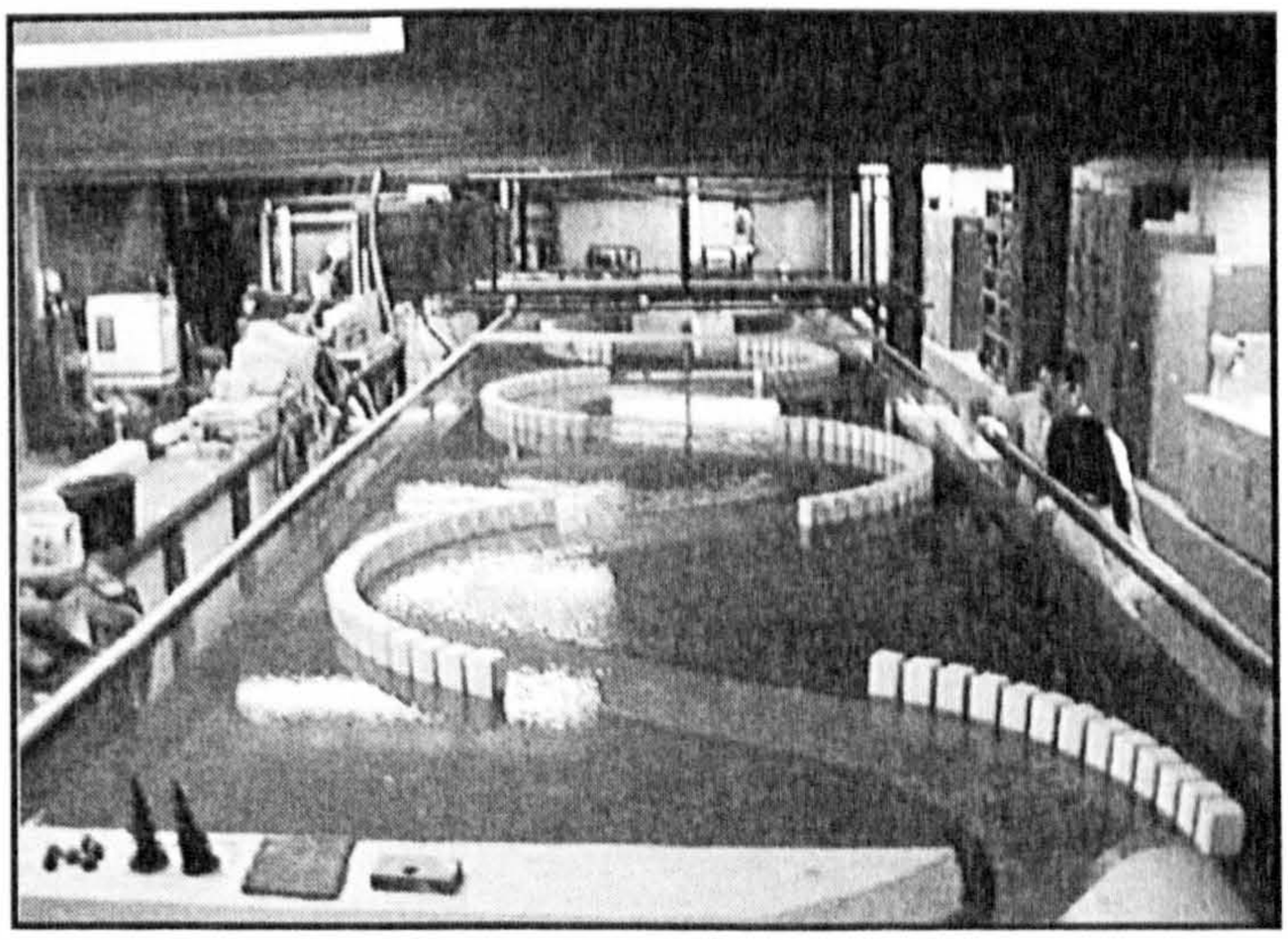

(b)

Figure 7.1: Meandering channel flume at Loughborough University, UK. The model could be extended to simulate (a) overbank flow with trees (b) trees on the edge of main channel. (after Prof. Shiono's presentation)

References

ABOTT, M.B. AND BASCO, D.R. (1989). *Computation Fluid Dynamics: An introduction for engineers*. John Wiley & Sons, New York, USA. 3.1

AKCELIK, V., JARAMAZ, B. AND GHATTAS, O. (2001). Nearly orthogonal two-dimensional grid Generation with aspect ratio control. *J. Comp. Phy.*, **171**, 805–821. 4.7.3.3, 4.7.3.3, 4

BOUSSINESQ (1887). Esai sur la theories des eaux courantes. In *Memories Prcsente par Divers Savants al' Academie des Science,*, vol. 23, 1–680. 3.2.1, 5.4.2.4

BRADSHAW, P. (1987). Turbulent secondary flows. *Annu. Rev. Fluid Mech.*, **19**, 53–74. 2.2.1, 6.3

BRUNDRETT, E. AND BAINES, W.D. (1964). The production and diffusion of vorticity in duct flow. *Annu. Rev. Fluid Mech.*, **19**, 375–394. 2.3.2.1

COKLJAT, D. (1991). Mathematical modeling of turbulent flows in two stage channels. Transfer report, Department of Civil Engineering, City University, London, UK. 2.3.3, 3.4.2

COKLJAT, D. AND YOUNIS, B. (1995). Second order closure study of open-channel flows. *J. Hydraul Engi, ASCE*, **95**, 94107. 1.1, 2.3.2

ECA, L. (1996). 2D orthogonal grid generation with boundary point distribution control. *J. Comput. Phys.*, **125**, 440. 4.7.3.3, 4.7.3.3

ERVINE, D.A. AND ELLIS, J. (1987). Experimental and computational aspects of overbank floodplain flow. *Transaction of the Royal Society of Edinburgh: Earth Sciences*, **78**, 315–325. 2.4.2.1

ERVINE, D.A. AND JASEM, H.K. (1995). Observations on flows in skewed compound flows. In *Proc. Instn. Civ. Engrs., London*, vol. 112, 249–259. (document), 2.4.2.1, 2.9

FARHANIEH, B. AND DAVIDSON, L. (1993). Employment of second moment colsure for calculation of turbulent recirculating flows in complex geometries with collocated variable arrangement. *Int. Jou. Num. Meth. Fluid*, **16**, 525–544. 1

FERZIGER, J.J. AND PERIĆ, M. (1995). *Law of flow in rough pipes*. Nat. Advis. Comm. On Aero. Tehc. Mem. 1292, Washington D.C, USA. 3.1, 4.2, 4.4, 5.5

FLETCHER, C. (1989). *Computational Techniques for Fluid Dynamics*. Springer-Verlag, London, 1988. 2^{nd} volume. 5.2

GESSNER, F.B. AND JONES, J.B. (1965). On some aspects of fully developed turbulent flow in rectangular channels. *J. Fluid Mech.*, **23**, 689–713. 2.3.2.1

GHOSH, S.N. AND KAR, S.K. (1975). River flood plain interaction and distribution of boundary shear stress in a meander channel with flood plain. In *Proc. Civil Eng., London*, vol. 59(2), 805–811. 2.4.3

HARLOW, F.H. AND WELSH, J.E. (1965). Numerical calculation of time dependent viscous incompressible flow with free surface. *Phy. Fluids*, **8**, 2182–2189. 4.7.1

HUR, N., S.THANGAM AND SPEZIALE, C.G. (1990). Numerical study of turbulent secondary flows in curved ducts. *J. Fluid Eng.*, **112**, 205–211. 1.2

IMAMOTO, H., ISHIGAKI, T. AND FUJISAWA, H. (1982). On the characteristics of open channel flow in bends with flood plains. *Annuals DPRI, Kyoto University, (in Japanese)*, **25B-2**, 529–543. 2.4.2.1

JENKINS, G.A. AND KELLER, R.J. (1992). On the numerical modelling of flows in natural rivers. In *Proc. 24th IAHR Cong., Madrid, Spain*, C229–C238. 2.4.4

KEARNEY, D. (2000). *Turbulent diffusion in channels of complex geometry.* Ph.D. thesis, Loughborough University, UK. 6.2.2

KNIGHT, D.W. AND SHIONO, K. (1990). Turbulence measurements in a shear layer region of a compound channel. *J. Hydraul. Res.*, **28**, 175–196. 2.3.2

KNIGHT, D.W., YUAN, Y.M. AND FARES, Y.R. (1992). Boundary shear in meandering channels. In *Proc. Int. Symp. Hyd. Res. Nature and Laboratory, Yangtze River Scientific Research Institute, China*, vol. 2, 102–107. 2.4.3

KRISHNAPPA, B.G. AND LAU, Y.L. (1986). Turbulence Modelling of Floodplain Flows. *J. Hydraul. Eng., ASCE*, **112**, 251–266. 1.1

LAI, Y.G., WEBER, J. AND PATEL, V.C. (2003). Nonhydrostatic three-dimensional model for hydraulic flow simulation. I: formulation and verification. *J. Hydrau. Engi.*, **129**, 196–204. 2.4.4

LAUNDER, B.E. AND SPALDING, D.B. (1974). The Numerical computation of turbulent flows. *Comput. Methods Appl Mech. Eng.*, **3**, 269–289. 3.5.3, 1

LAUNDER, B.E. AND YING, W.M. (1973). Prediction of flow and heat transfer in ducts of square cross section. *Proc. Instn. Mech. Engrs*, **187**, 455–461. 1.2, 2.2.1, 3.4.1, 6.2.1, 1

LILEK, Z., MZAFERIJ, S. AND PERIC, M. (1995). Efficiency and accuracy aspects of a full-multigrid SIMPLE algorithm for three-dimensional flows. *Numerical Heat Transfer, Part B*, **31**, 23–42. 4.1, 7.1

LIN, B. AND SHIONO, K. (1994). Three-dimensional numerical modelling of rectangular open channel flows. *J. Hydraul. Engi., Chinese Hydraulic Engineering Society*, **3**, 47–58. 2.3.2

LORENA, M. (1992). *Meandering compound flow*. Ph.D. thesis, University of Glasgow, UK. 2.4.3

MORVAN, H., PENDER, G., WRIGHT, N.G. AND ERVINE, D.A. (2002). Threedimensional hydrodynamics of meandering compound channels. *J. Hydrau. Engi.*, **128**, 674–682. 1.1

MUTO, Y. (1997). *Turbulent flow in two-stage meandering channels*. Ph.D. thesis, University of Bradford, UK. (document), 2.4.3, 6.22, 6.4, 6.4.1, 6.29, 6.30, 6.32, 6.33, 6.35, 6.36, 6.37, 6.38, 6.43, 6.44, 6.46, 6.47, 6.49, 6.50, 6.51, 6.52, 6.57, 6.58, 6.60, 6.61, 6.63, 6.64, 6.65, 6.66, 7.2

NAOT, D. AND RODI, W. (1982). Calculation of secondary currents in channel flow. *J. Hydrau. Div., ASCE*, **111**, 116–125. 1.2, 2.2.2, 2.3.2.1, 3.4.2, 3.4.2, 3.4.3, 3.5.2, 6.2.1, 6.2.2, 6.2.2, 1

NAOT, D., NEZU, I. AND NAKAGAWA, H. (1993a). Calculation of compound-open-channel flow. *J. Hydrau. Engi.*, **119**, 1418–1426. 6.3

NAOT, D., NEZU, I. AND NAKAGAWA, H. (1993b). Hydrodynamic behaviour of compound rectangular open channels. *J. Hydrau. Engi.*, **119**, 390408. 1.1, 1.2, 6.2.2

NEZU, I. (2005). Open-channel flow turbulence and its research prospect in the 21^{st} century. *J. Hydrau. Engi.*, **131**, 229–246. 2.2.2

NEZU, I. AND NAKAGAWA, H. (1993). *Turbulence in Open-Channel Flows*. IAHR Monograph, Rotterdam, Balkema, USA. (document), 2.2.2, 2.2.2, 2.2, 6.2.1, 6.3, 6.2.1, 6.2.2, 6.10, 6.2.2

NEZU, I. AND RODI, W. (1993). Experimental study on secondary currents in open channel flow. *J. of Hydrau. Engi.*, **119**, 390408. 2.2.2, 2.2.2

NEZU, I., SAGARA, Y. AND IKETANI, K. (1999). Secondary currents and bcd shear stress in compound open channel flows with shallo flood plains. In *Proc.*, 28^{th} *IAHR Congress, Gratz, Austria*, vol. D6, 1–8. 2.3.3

NIKURADSE, J. (1933). *Laws of flow in rough pipes, NACA TM 1292, 1950. Translated from "Strmungsgesetze in rauhen Rohren.* Forsch. Arb. Ing.-Wes. No. 361. 2.2.1

OLSEN, N.R.B. (2002). SSIIM user's manual. Www.bygg.ntnu.no/ nilsol/ssiimwin; Norwegian Univ. of Science and Technology. 2.4.4

OLSEN, N.R.B. (2003). Three-dimensional CFD modelling of self-forming meandering channel. *J. Hydraul. Eng.*, **12**, 336–372. 2.4.4, 1

PATANKAR, S.V. (1980). *Numerical heat transfer and fluid flow.* Hemisphere, New York, USA. (document), 4.2, 4.3

PATANKAR, S.V. AND SPALDING, D.B. (1972). A calculation procedure for heat, mass and momentum transfer in three-dimensional parabolic flows. *Int. J heat and Mass Transfer*, **15**, 1787–1806. 4.1, 4.6.1

PATRA, K.C., KAR, S.K. AND BHATTACHARYA, A.K. (2004). Flow and velocity distribution in meandering compound channels. *J. Hydraul. Eng.*, **130**, 398–411. 2.4.1

PERIC, M. (2004). Email Corrospondence with author. 1

PERIC, M., RUEGER, M. AND SCHEUERER, G. (1989). A finite volume multigrid method for calculating turbulent flows. In *Proc. 7th Symp. on Turbulent Shear Flows*, vol. 1. 4.1

PEZZINGA, G. (1994). Velocity Distribution in Compound Channels by Numerical Modelling. *J. Hydraul. Engng. ASCE*, **120**, 1176–1198. 1.1

PRESTON, J.H. (1954). The determination of turbulent skin friction by means of Pitot tube. *J. Roy. Aeronau. Soc.*, **58**, 109–121. 2.4.3

RAJARATNAM, N. AND AHMADI, R.M. (1979). Interaction between main channel and flood-plain flows. *J. Hydr. Div., Proc. ASCE*, **105**, 573–588. 2.3.1

RAMESHWARAN, P. AND NADEN, P.S. (2004). Three-dimensional modelling of free surface variation in a mearnding channel. *J. Hydrau. Res.*, **42**, 603–615. 2.4.4, 2.4.4

RAMESHWARAN, P. AND SHIONO, K. (2002). Predictions of velocity and boundary shear stress in compound meandering channel. In *Proc. of River Flow, International Conference on Fluvial Hydraulics, Louvain-la-Neuve, Belgium, (BOUSMAR D. and ZECH Y (eds)), September 4-6*, vol. 1, 223231. 1.1

RAMESHWARAN, P. AND SHIONO, K. (2003). Computer modelling of two-stage meandering channel flows. In *Proc. of the Inst. of Civil Engineers, Water and Maritime Engineering*, vol. 156, 326339. 1.1, 2.4.4

RAMESHWARAN, P. AND WILLETTS, B.B. (1999). Conveyance prediction for meandering two-stage channel flows. In *Proc. of the Inst. of Civil Engineers Water, Maritime & Energy*, vol. 136, 153–166. 1.1

RODI, W. (1993). *Turbulence models and their application in hydraulics: a state-of-the-art review*. IAHR Monograph, Rotterdam : Balkema, NETHERLAND. 3.1, 3.3, 3.3

SELLIN, R.H.J. (1964). A laboratory investigation into the interaction between flow in the channel of a river and that of its flood plain. In *La Houille Blanche, Grenoble, France*, vol. 7, 793–801. 2.3.1

SELLING, R.H.J., ERVINE, D.A. AND WILLETTS, B.B. (1993). The behaviour of two-stage channels. *Proc., Instn. Civ. Engrs., Water, Maritime and Energy, London*, **101**, 99–112. (document), 2.4.2.1, 2.8

SHAO, X., WANG, H. AND CHEN, Z. (2003). Numeircal modeling of turbulent flow in courved channels of compound cross-section. *Adv. Water Resou.*, **26**, 525–539. 2.4.4, 5.1, 5.4

SHIONO, K. AND KNIGHT, D.W. (1989). Transverse and vertical Reynolds stress measurements in a shear layer region of a compound channel. In *Proc., 7th Symp. on Turbulent Shear Flows, Stanford Univ.*, 28.1.1–28.1.6. (document), 1.1, 2.3.2, 2.6

SHIONO, K. AND KNIGHT, D.W. (1990). Mathematical models of flow in two or multi-stage straight channels. In *Proc., Int. Conf. on River Flood Hydraulics, W. R. White, ed., Wiley, New York, Paper GI,*, 229–238. 1.1

SHIONO, K. AND KNIGHT, D.W. (1991). Turbulent open-channel flows with variable depth across the channel. *J. Fluid Mech.*, **222**, 617–646. (document), 2.3, 2.4

SHIONO, K. AND LIN, B. (1995). Numerical modelling of solute transport in compound channel flows. *J. Hydraul. Res. IAHR*, **33**, 773–788. 1.1

SHIONO, K. AND MUTO, Y. (1998). Complex flow mechanisms in compound meandering channels with overbank flow. *J. Fluid Mech.*, **376**, 221–261. (document), 2.4.1, 2.7, 2.4.2.2, 2.4.2.2, 2.10, 2.4.2.2, 2.11, 6.4.1.2

SHIONO, K., MUTO, Y., IMAMOTO, H. AND ISHIGAKI, T. (1994). Flow structure in meandering compound channel for overbank. In *7^{th} International Symposium on Application of Laser Techniques to Fluid Mechanics , 2 , Lisbon, Portugal*, vol. 376, 28.2.1–28.2.8. 2.4.2.1

SHIONO, K., AL-ROMAIH, J.S. AND KNIGHT, D.W. (1999). Stage-discharge assessment in compound meandering channels. *J. Hydraul. Eng.*, **125**, 66–77. 2.4.3

SHUKLA, D.R. (2006). *Three-dimensional Computatinal Investigations of Flow Mechanisms in Compound Meandering Channels*. Ph.D. thesis, Loughborough University, UK. 2.4.4, 2.4.4

SHUKRY, A. (1949). Flow around bends in an open flume. *Trans. ASCE*, **115**, 751–779. 2.4

SOFIALIDIS, D. AND PRINOS, P. (1999). Numerical study of momentum exchange in compound open channel flow. *J. Hydraul. Eng.*, **125**, 152–165. 1.1, 2.3.3

SPEZIALE, C.G. (1987). On Nonlinear $k-l$ and $k-\epsilon$ models of turbulence. *J. Fluid Mech.*, **178**, 459–475. (document), 1.2, 2.1, 2.2.1, 3.4, 3.4.3, 1

STEIN, C.G. AND ROUV, G. (1989). 2D depth-averaged numerical predictions of the flow in a meandering channel with compound cross section. *Hydrosoft*, **2**, 2–7. 2.4.4

SUGIYAMA, H. AND SAITO, T. (2002). Numerical study of turbulent in compound meandering open-channel. In *Proc. of JSCE*, 712/II-60, 25–43. (document), 2.4.4, 2.12, 5.1

SUGIYAMA, H., AKIYAMA, M., MATSUBARA, T. AND HIRATA, M. (1995). Numerical analysis of three-dimensional turbulent structure in open channel flow. *Jou. of Comp. Fluid Dynamics*, 4, 236–262. 6.2.2

SUGIYAMA, H., AKIYAMA, M. AND SATO, R. (1999). Numerical study of turbulent stucture in rectengular meandering channel flow. In *Proc. of JSCE. No 628/II-48*. 2.4.4

THOMAS, T.G. AND WILLIAMS, J.J.R. (1995). Large Eddy Simulation of Turbulent Flow in an Asymmetric Compound Open Channel. *J. Hydraul. Res. IAHR*, **33**, 27–41. 1.1

THOMPSON, J.F., WARSI, Z.U.A. AND MASTIN, C.W. (1985). *Numerical grid generation*. North-Holland, New York, USA. 4.7.3.3, 5.1

THOMSON, J. (1876). On the origin of windings of rivers in alluvial plains, with remarks on the flow of water round bends in pipes. In *Proc. Roy. Soc. London.*, vol. 25, 5–8. 2.4

TOEBES, G.H. AND SOOKY, A. (1967). Hydraulics of meandering rivers with floodplains. *J. Waterw. Harbors Div., Am. Soc. Civ. Eng.*, **93**, 1053–1066. 2.4.2.1

TOMINAGA, A. AND NEZU, I. (1990). Turbulence measurements in compound open channels. In *Mem. Fac. Eng., Kyoto Univ*, vol. 52. (document), 2.3, 2.2.2, 2.5, 2.3.2.1, 6.3, 6.15, 6.3.1, 6.3.2

TOMINAGA, A. AND NEZU, I. (1991). Turbulent structure in compound open-channel flows. *J. Hydraul. Eng.*, **117**, 21–41. 2.3.1

TOMINAGA, A., EZAKI, K. AND NAKAGAWA, H. (1989). Threedimensional turbulent structure in straight open-channel flows. *J. Hydraul. Res.*, **27**, 149–173. 2.2.2, 2.3.1, 2.3.2.1

VERSTEEG, H.K. AND MALALASEKERA, W. (1995). *An introduction to Computational Fluid Dynamics: The Finite Volume Method*. Longman Scientific and Technical, England, UK. 3.1, 4.2

WARSI, Z. (1998). *Fluid Dynamics: Theoretical and Computational Approaches*. 2^{nd} edition, CRC Press, Inc.,. 5.4

WENKA, T., VALENTA, P. AND RODI, W. (1992). Depth-averaged calculation of flood flow in a river with irregular geometry. In *Proc. 24th IAHR Cong.*, A225–A232. 2.4.4

WILLETTS, B.B. AND HARDWICK, R.I. (1993). Stage dependency for overbank flow in meandering channels. In *Proc. Inst. Civ. Eng., Waters. Maritime Energ.*, vol. 101, 45–54. 2.4.2.1

WILSON, C.A.M.E., BATES, P.D. AND HERVOUET, J.M. (2002). Comparison of turbulence models for stage-discharge rating curve prediction in reachscale compound channel flows using two-dimensional finite element methods. *J. Hydrol.*, **257**, 42–58. 1.1

WORMLEATON, P. AND EWUNETU, M. (2006). Three-dimensionla $k - \varepsilon$ numerical modelling of overbank flow in a mobile bed meandering channel with floodplains of different depth, roughness and planform. *J. Hydraul. Res.*, **44**, 18–32. (document), 2.4.4, 2.12, 5.1

YE, J. AND MCCORQUODALE, J.A. (1997). Depth-averaged hydrodynamic model in curvilinear collocated grid. *J. Hydraul. Eng.*, **123**, 380–388. 2.4.4, 5.4

YE, J. AND MCCORQUODALE, J.A. (1998). Simulation of curved open channel flow by 3D hydrodynamic model. *J. Hydraul. Eng.*, **124**, 687–697. 2.4.4, 5.1, 5.4